



SAFETY ASPECTS OF LITHIUM ION BATTERIES

Thesis submitted by:

MALCOLM STEWART WISE

For the degree of Doctor of Philosophy

Newcastle University

School of Chemical Engineering and Advanced Materials

June 2023

Abstract

Lithium-ion batteries (LiBs) are the highest energy density battery and are essential to the transition away from fossil fuels, and hence the decarbonisation of the planet. LiBs find major application in electric vehicles (EVs) and Battery Energy Storage Systems (BESS). LiBs in BESS can store energy from intermittent renewable generators (the sun doesn't always shine or the wind blow) to support national grids.

The high energy density of LiBs comes at a price: they contain flammable solvents, and if this chemical energy is released in an uncontrolled manner, through abuse, defects, or contamination, they generate gases which can undergo thermal runaway and ignite producing flare-like flames or explode. LiBs are comprised of cells: a cell in thermal runaway can cause other cells to enter thermal runaway (thermal propagation). Large LiBs, i.e. those in EVs (10- 100kWh), can re-ignite hours, days or weeks after apparently being extinguished and many times.

This thesis is essentially in two parts, the first part, Chapters 3, 4 & 5 report on experiments carried out on single LiB modules and stacks of modules from the Nissan Leaf 2 EV. In Chapters 3 & 4 the module(s) were sent into thermal runaway by abuse to investigate the fire characteristics, gases, and provide a demonstration of LiB fires and re-ignition to emergency responders. It was found that the emitted gases can easily be confused for smoke and/or steam when they actually contain toxic and flammable components. Chapter 5 introduces a novel method to estimate the Heat Release Rate (HRR) from a single module fire using optical cameras. It was found that using this method, approximately twice the heat released was accounted for.

The second part, Chapter 6 follows the experiments in Chapters 3 & 4 and is a report written for the Department of Business & Industrial strategy (BEIS) concerning the safety of LiBs in domestic BESS (DLiBESS). The aim was to understand if there are additional risks associated with the use of second-hand LiBs in DLiBESS and if the current codes and standards are adequate. Part of the conclusion was that consideration should also be given to whether stricter requirements are needed for home-built ("DIY") DLiBESS that use second-life batteries, similarly to the USA.

Acknowledgements

The experiments in this Thesis were conducted with the ReLiB and SafeBatt groups of the Faraday Institution, and Dr Francesco Restuccia of Kings' College London.

The experiments were too large to be conducted alone and Professor Paul Christensen, Dr Simon Lambert, Dr Zoran Milojevic, Dr Mohamed Ahmeid, Dr Pierrot Attidekou, Dr Wojciech Mrozik, Mr Joseph McDonald and Mr Neville Dickman helped design and set up the experiments.

Mr Neville Dickman designed and built the first battery rig and built all the additions in the later experiments.

Gas analysis was performed by Dr Wojciech Mrozik.

Technical help was provided by Dr Francesco Restuccia in the video analysis.

Table of Contents

Abstract	i
Acknowledgements	ii
List of Publications	viii
My contributions to publications	ix
List of Tables	x
List of Figures	xii
Glossary	xix
CHAPTER 1 . INTRODUCTION	22
1.1. Composition and structure of a lithium-ion battery	22
1.2. Charge and discharge	29
1.3. A summary of the history of lithium-ion batteries	32
1.4. Safety systems	32
1.4.1. The solid electrolyte interface (SEI)	32
1.4.2. The battery management system	34
1.4.3. Physical safety systems	37
1.4.4. Chemical additives	39
1.5. Thermal runaway of cells	42
1.6. Abuse and malfunction of cells causing thermal runaway	44
1.6.1. Thermal abuse	44
1.6.2. Electrical abuse	45
1.6.3. Mechanical abuse	47
1.7. Accidents and scope (BEIS)	47
1.8. Summary of Chapter	50
1.9. Outline of Thesis	50
1.10. References	51

CHAPTER 2 . EXPERIMENTAL	63
2.1. The Envision-AESC cells and modules.	63
2.2. The battery and camera rigs	64
2.3. The optical cameras	69
2.4. The thermal cameras	71
2.5. The thermocouples, voltage cables and DAQ	71
2.6. The gas sensors	71
2.7. The GC-MS	72
2.9. The experimental methods	72
2.9.1. Charging a cell	72
2.9.2. Thermal abuse experimental method	74
2.9.3. Nail penetration experimental method	74
2.10. The experiments	75
2.11. References	91
CHAPTER 3 . MECHANICAL ABUSE	92
3.1. Introduction	92
3.2. Results	93
3.2.1. Experiment A1.	93
3.2.2. Experiments A2, A3 & A4.	98
3.2.3. Experiments B1 & B2.	109
3.3. Discussion	122
References	130
CHAPTER 4 . THE JANUARY 2020 (DNV 1) EXPERIMENTS (CONTINUED) AND SPRING 2021 (DNV 2)	135
4.1 Introduction	135

4.1 Overcharge experiments at DNV January 2020	135
4.1.1 Experiment A6 (overcharge of a single module)	135
4.1.2 Experiment A7 (single module overcharge in stack of three).	148
4.2 Nail penetration experiments at DNV April/May 2021	163
4.2.1 Experiment C4	164
4.2.1 Experiments C5 – C7	170
4.3. Conclusions	181
References	182
CHAPTER 5 . CALCULATING HEAT RELEASE RATES FROM LITHIUM-ION BATTERY FIRES: A METHODOLOGY USING DIGITAL IMAGING	186
5.2. Image Processing	190
5.2.1 Black and White recording method	191
5.2.2 Greyscale recording	194
5.2.3 RGB Recording	195
5.3. Image Processing of lithium-ion battery fires	196
5.3.1 Comparing different camera resolutions and camera speeds	196
5.3.2 Removing the fish-eye effect from recorded images	199
5.3.3. Surface area of a rapidly changing, irregularly shaped flame	214
5.4. Measuring the flames and resulting Heat Release Rate	216
5.5. Conclusions	220
5.6. References	220
5.7. Appendix 5.1	222
5.8. Appendix 5.2	227
5.9. Appendix 5.3	229
CHAPTER 6 DEPARTMENT OF BUSINESS ENERGY & INDUSTRIAL STRATEGY REPORT: A STUDY ON THE SAFETY OF SECOND-LIFE BATTERIES IN BATTERY ENERGY STORAGE SYSTEMS.	231

6.1. Introduction	235
6.1.1. Overview	236
6.1.2. Study objectives and scope	237
6.2. Overview of lithium-ion cells	238
6.2.1. Physical characteristics	238
6.2.2. Applications	239
6.2.3. Composition and electrochemistry	239
6.3. The market for second-life LiBESS	240
6.3.1. The market for DLiBESS	241
6.3.2. Environmental and economic drivers for second-life LiBs	243
6.3.3. The availability of second life LiBs	244
6.3.4. Factors determining the price of second-life LiBs	248
6.4. Summary of the general hazards associated with LiBESS	249
6.4.1. Electric shock	249
6.4.2. Electrolyte spillage	249
6.4.3. Thermal runaway	250
6.5. The risks and hazards specific to second-life LiBs	256
6.5.1 The effect of ageing and unknown stress and/or abuse	257
6.5.2. Consumers purchasing or building their own SLDiBESS	261
6.6. Gateway testing of second-life LiBs	262
6.6.1. State of health, state of safety and remaining useful life	262
6.6.2. Examples of gateway testing	265
6.7. Analysis of mitigating measures for LiBs and DLiBESS	267
6.7.1. Safety systems at cell level	268
6.7.2. Safety systems external to DLiBESS	272
6.7.3. Installation and maintenance	274
6.8. Codes, standards, and regulations	275
6.8.1. Second-life LiBs and type tests	276
6.8.2. Standards in the UK and Europe	277
6.8.3. Codes, standards, and regulations outside the UK and Europe	282
6.8.4. Second-life LiBs as waste	286
6.8.5. The sale and transport of second-life LiBs	287
6.8.6. The EU batteries regulation	289

6.9. Conclusions	292
6.10. References	295
6.11. Appendix 6.1: A case study: the explosion of the McMicken LiBESS, Surprise, Arizona	310
6.11.1. The LiBESS	310
6.11.2. Timeline	310
6.11.3. The cause of thermal runaway	311
6.11.4. References	312
6.12. Appendix 6.2: The BSI committees and their remits	314
6.13. Appendix 6.3: Survey of LIB suppliers on EBay	315
CHAPTER 7 . FUTURE WORK	319

List of Publications

1. Paul A. Christensen, Paul A. Anderson, Gavin D.J. Harper, Simon M. Lambert, Wojciech Mrozik, Mohammad Ali Rajaeifar, Malcolm S. Wise, and Oliver Heidrich. Risk management over the life cycle of lithium-ion batteries in electric vehicles. *Renewable and Sustainable Energy Reviews*, Volume 148, 2021, 111240, ISSN 1364-0321, <https://doi.org/10.1016/j.rser.2021.111240>.
2. P.A. Christensen, Z. Milojevic, M.S. Wise, M. Ahmeid, P.S. Attidekou, W. Mrozik, N.A. Dickmann, F. Restuccia, S.M. Lambert, and P.K. Das. Thermal and mechanical abuse of electric vehicle pouch cell modules. *Applied Thermal Engineering*, Volume 189, 2021, 116623, ISSN 1359-4311, <https://doi.org/10.1016/j.applthermaleng.2021.116623>.
3. Wojciech Mrozik, Paul Christensen, Zoran Milojevic, Mohamed Ahmeid, Malcolm Wise, Pierrot S. Attidekou, Neville Dickman, Simon Lambert, and Prodip Das. Hazards and Pollution Released from Abused and Burnt Industrial Lithium-Ion Batteries. International Union of Pure and Applied Chemistry General Assembly and the World Chemistry Congress with the Canadian Chemistry Conference and Exhibition. 13 Aug 2021 → 20 Aug 2021. <https://www.research.ed.ac.uk/en/publications/hazards-and-pollution-released-from-abused-and-burnt-industrial-1>
4. Wojciech Mrozik, Malcolm Wise, Neville Dickman, Mohamed Ahmeid, Zoran Milojevic, Prodip Das, Simon Lambert, and Paul Christensen. Abuse of Lithium-ion Batteries: emergence, composition, and toxicity of vapour cloud. Book of Abstracts, Nordic Fire & Safety Days. 21st June 2022. https://eprints.ncl.ac.uk/file_store/production/286871/674F1013-3739-4E45-9DE4-F987D03BEC6B.pdf
5. P. A. Christensen, W. Mrozik, and M. S. Wise. A Study on the Safety of Second-life Batteries in Battery Energy Storage Systems. Department for Business, Energy & Industrial Strategy, Office for Product Safety & Standards, January 2023. https://assets.publishing.service.gov.uk/government/uploads/system/uploads/attachment_data/file/1133213/safety-of-second-life-batteries-in-bess.pdf

6. Malcolm Wise, Paul Christensen, Neville Dickman, Joe McDonald, Wojciech Mrozik, Simon Lambert, and Francesco Restuccia. Calculating Heat Release Rates from Lithium-Ion Battery Fires: A Methodology Using Digital Imaging. Submitted to Fire Technology, Springer Science + Business Media, LLC. Under review, June 2023

My contributions to publications

1. Text editing, referencing.
2. Experimental design and operation, optical video analysis, text writing and editing.
3. Experimental design and operation.
4. Experimental design and operation, optical video analysis.
5. Second-hand LiB availability research, text editing, referencing.
6. Experimental design and operation, optical video correction and analysis, text writing and editing, referencing.

List of Tables

Table 1.1. Chemical formulas and structures for common electrolyte components.....	24
Table 1.2. Chemical formulas and structures for SEI components.....	34
Table 1.3. Chemical names, abbreviations, formulae, and structures for selected redox shuttles.	41
Table 1.4. Chemical names, abbreviations, formulas, and structures for selected shutdown additives.....	42
Table 1.5. The boiling points for common electrolyte solvents [115].....	45
Table 1.6. A brief list of some notable portable equipment lithium-ion safety incidents.	47
Table 1.7. A brief list of some notable electric vehicle lithium-ion safety incidents.	48
Table 1.8. A brief list of some notable aviation lithium-ion safety incidents.....	49
Table 1.9. A brief list of some notable recycling facility lithium-ion safety incidents.	49
Table 1.10. A brief list of some notable Battery Energy Storage Systems (BESS) lithium-ion safety.....	50
Table 2.1. The cells and modules employed in the work presented in this thesis.	64
Table 2.2. The setup options for the GoPro Hero 7 Black optical cameras.....	69
Table 2.3. The setup options for the GoPro Hero 9 Black optical cameras.....	70
Table 2.4. The setup options for the Vmotal GSV8560 optical cameras.	70
Table 2.5. The setup options for the Crosstour CT7000 optical cameras.....	70
Table 2.6. The setup options for the Apexcam M80 Air optical cameras.	70
Table 2.7. The Draeger gas sensors.	71
Table 2.8. A list of experiments conducted at DNV 1.....	75
Table 2.9. A list of experiments conducted at FSC 1.	75
Table 2.10. A list of experiments conducted at DNV 2.....	76
Table 2.11. A list of experiments conducted at DDFRS, all at >100 % SoC.	76
Table 2.12. The nail penetration rig and polyethylene blast wall positions in the DNV 2 experiments using the arrangement in figure 2.11.....	83
Table 3.1. Maximum sensor readings and times observed during experiment B2.	117
Table 3.2. Immediate effects thresholds and first lethal effects thresholds for various gases produced by lithium ion cells during the thermal runaway.....	123
Table 4.1. The SoCs and voltages at which the various regions and points in figure 4.6 occur for the overcharge experiments along with the maximum temperature changes recorded by the thermocouple under the overcharged module.....	162

Table 6.1. An overview of the research framework.....237
Table 6.2. Various listings of second hand lithium-ion batteries found on EBay.com. .318

List of Figures

Figure 1.1. Schematic of a lithium-ion cell.....	23
Figure 1.2. A schematic showing the components rolled in a cylindrical can.....	25
Figure 1.3. Schematic cross section of a typical 18650 cylindrical cell.	26
Figure 1.4. A schematic showing how the components are wound in a prismatic cell.	27
Figure 1.5. Schematic cross section of a prismatic cell.	27
Figure 1.6. A schematic showing the stacking of the electrodes and separator of a pouch cell.....	28
Figure 1.7. A schematic showing the ‘Z’ folding of the electrodes and separator of a pouch cell.	28
Figure 1.8. Schematic cross section of a pouch cell.	29
Figure 1.9. A simplified diagram of a charge/discharge cycle inside a LCO cell.	30
Figure 1.10. The charging and discharging of a lithium-ion cell.....	31
Figure 1.11. A schematic showing the electrochemical stability windows of the electrodes and electrolyte in lithium ion cells [10, 54].	33
Figure 1.12. Representation of a lithium-ion battery at (a) Beginning of Life, BoL, and (b) after ageing.....	35
Figure 1.13. An example of an OCV-SoC calibration curve, showing a difference in rest periods before measurements are made [79].	36
Figure 1.14. A comparison of different OCV-SoC curves for different cell chemistries, reproduced from ‘Cell state-of-charge inconsistency estimation for LiFePO ₄ battery pack in hybrid electric vehicles using mean-difference model, Zheng Y, et al.’ [83].	37
Figure 1.15. A cross section of a cylindrical cell; (a) with the blast cap in-tact; and (b) once the blast cap has operated and the electrical connection is broken.	39
Figure 1.16. Heat generation and heat dissipation (for illustration purposes).	44
Figure 2.1. The electronic configuration of an Envision AESC module for the Nissan Leaf 2 electric vehicle (a), the stacking of the cells inside the module (b) and the electrical connections on the front face of the module (c), not to scale.	63
Figure 2.2. The battery rig designed and built for the experiments: (a) plan view and (b) 3D view with a module attached.....	65
Figure 2.3. The rig with the hammer and arm attached (left side view).....	66
Figure 2.4. The rig with hammer, arm, chain, and skids attached.	67

Figure 2.5. The rig with arm, chain, skids, and a double hammer head, (a) front view and (b) 3D view.	68
Figure 2.6. A 3D view of the camera rig.	68
Figure 2.7. (a) The OCV SoC curve for an AESC Envision cell, marked at 40 % SoC and (b) the CCCV charging curve for an AESC Envision cell, with current when charging to 100 % SoC.	73
Figure 2.8. Positions of the nail penetration in the experiments.	77
Figure 2.9. Plan view of the experimental setup at DNV 1.	78
Figure 2.10. 3D view of the experimental setup at DNV 1.	78
Figure 2.11. A photograph of the experimental setup at DNV 1 (taken from Optical camera 1).	79
Figure 2.12. Plan view of the experimental setup at FSC.	80
Figure 2.13. 3D view of the experimental setup at FSC.	80
Figure 2.14. A photograph of the experimental setup at FSC.	81
Figure 2.15. Plan view of the experimental setup at FSC.	82
Figure 2.16. 3D view of the experimental setups at DNV 2.	82
Figure 2.17. A photograph of the experimental setup at DNV 2.	83
Figure 2.18. Plan view of the experimental setup at DNV 2 for experiment C8.	84
Figure 2.19. 3D view of the experimental setup at DNV 2 for experiment C8.	85
Figure 2.20. Front view of the 8 module stack, encased in steel plates, for experiment C8.	85
Figure 2.21. A photograph of the experimental setup at DNV 2, for experiment C8.	86
Figure 2.22. Plan view of the experimental setup at DNV 2, for experiments C9 and 10.	86
Figure 2.23. 3D view of the experimental setup at DNV 2, for experiments C9 and 10.	87
Figure 2.24. A photograph of the experimental setup at DNV 2, for experiments C9 and 10.	87
Figure 2.25. Front view of the 3 module stack used in experiment C10.	88
Figure 2.26. Plan view of the experimental setup at DDFRS.	89
Figure 2.27. 3D view of the experimental setup at DDFRS.	89
Figure 2.28. 3D view of the 5 module stack used in experiments at DDFRS.	90
Figure 2.29. A photograph of the experimental setup at DDFRS.	90
Figure 3.1. Frames from the optical videos taken during experiment A1.	93

Figure 3.2. Data from experiment A1, (a) flame lengths, (b) voltage and flame areas, and (c) flame areas, thermocouple, and IR temperature.	95
Figure 3.3. The voltage of the cells of the top quartet of the module, in Figure 3.2(b) and the first derivative from experiment A1.....	97
Figure 3.4. Frames from the optical videos taken during experiment A2.	102
Figure 3.5. A photograph of the underside of the module employed in experiment A2, showing the exit hole (arrowed) of the nail.	103
Figure 3.6. Data from experiment A2, (a) voltage, thermal imaging, and thermocouple, (b) voltage and the flame areas, and (c) thermal camera, thermocouple, and the flame areas.	106
Figure 3.7. The failure of the individual cells of the module during experiment A2 based on the voltage and flame area data in Figure 3.6(b), black represents undamaged cells, red represents failed cells from previous flare, and white represents dead cells.	107
Figure 3.8. Frames from the optical videos taken during experiment B1.....	112
Figure 3.9. Frames from the optical videos taken during experiment B2, they were collected at the times specified in the text.	114
Figure 3.10. Thermocouple, thermal camera, and concentrations of gases detected during experiment B2.....	116
Figure 3.11. Schematic showing the locations of the gas sensors in the FSC experiments.	117
Figure 3.12. Voltage, thermocouple, and thermocouple data recorded during experiment B2, and the first derivatives of thermocouple data.	119
Figure 3.13. Frames from the thermal camera taken during experiment B2.	121
Figure 3.14. Comparisons of flame measurements and SO ₂ concentrations from experiments A1-4, B1 and B2.....	124
Figure 4.1. Frames from the (a), (c), (e), (g), (i) and (k) front optical camera and (b), (d), (f), (h), (j) and (l) back optical camera, for experiment A6. They were collected at the times specified in the captions.	141
Figure 4.2 Thermal images taken (a) & (c) using the front thermal camera and (b) & (d) the rear thermal camera. (a) and (c) are 1 s apart, as are (b) and (d). All vertical axis are temperature in degrees Centigrade.....	143
Figure 4.3. Plots of the DAQ, thermal camera (the point employed to determine the latter is shown in the inset to (d)), and flame area data from experiment A6.	146

Figure 4.4. Frames from the videos taken during the overcharge of a single module in a stack of three at the DNV GL site (experiment A7). 156

Figure 4.5. The DAQ data and flame measurements for experiment A7, (a) all data, (b) the data leading up to thermal runaway and (c) – (e) after thermal runaway. 159

Figure 4.6. Generic representation of the voltage/time plot during overcharge. 159

Figure 4.7. Frames collected from the optical video in experiment C4 (a), (b), (c), (d), (e), (f), (g) and (h). The images were collected at the times specified in the text. 168

Figure 4.8. Plots of: (i) – (iv) the voltages of cell pairs 1 – 4, respectively, during experiment C5 in which one module at 40% SoC was penetrated with a nail, (v) the temperature of the thermocouple affixed to top of module. (1) Vapour cloud produced; (2) module ignites 60 s after penetration; and (3) blue/purple emission “flame” observed. . 171

Figure 4.9. Plots of: (i) – (iv) the voltages of cell pairs 1 – 4, respectively, on one module during experiment C6 in which two modules each at 35b % SoC were penetrated, and (v) the thermocouple above the module. 172

Figure 4.10. A frame taken during experiment C5 from an optical camera on the nail penetration rig, 16.2s after nail penetration. 172

Figure 4.11. Frames from the video taken by the GoPro camera mounted on the floor behind the module and under the frame of the nail penetration rig during experiment C6: (a), (b), (c), (d), (e) and (f). The images were collected at the times specified in the text. 175

Figure 4.12. Plots comparing the production of (a) HCN, (b) CO, (c) SO₂ and (d) H₂ in experiments C5, C6, and C7. (e) Shows plots of the concentrations of HCN, SO₂ and CO during experiment C7. 179

Figure 5.1. (a) A diagram of a candle and flame and (b) a cross section of the flame, showing the flame zone, unburnt fuel and oxygen moving towards the flame zone, not to scale. 187

Figure 5.2. A schematic showing how to measure the height of a candle flame. 188

Figure 5.3. The camera/observer view of measuring the width of a candle flame. 189

Figure 5.4. Representation of pixels for a given location in an image. 190

Figure 5.5. A colour still photo taken from an observation camera. 192

Figure 5.6. The image in figure 5.5 in black and white with different thresholds for light detection: threshold of: (a) 0, (b) 200, (c) 400, (d) 600, (e) 800 and (f) 1000. 192

Figure 5.7. A plot of the effect of minimum threshold on the outputted number of pixels with thresholds from 0 to 1000. 194

Figure 5.8. Three methods for accounting for the intensities of red, green and blue light: (a) all colours equal, (b) green twice the importance of blue and red and (c) a weighted scaling.	195
Figure 5.9. An example of a colour filter used with a CCD to produce colour digital images.	196
Figure 5.10. Camera G: (a) pre ignition; (b) ignition; (c) zoomed in (b); (d) & (e) thermal runaway; (f) differences in (c) & (d); Camera A: (g), (h) & (i) thermal runaway; (j) differences in (g) & (h); (k) differences in (g) & (i); and (l) zoomed in (g).	198
Figure 5.11. (a) The calibration image showing the full calibration box; (b) zoomed in version showing that the box has stretched in image and (c) calibration grid to account for image distortion.	200
Figure 5.12. The errors for horizontal powers from 1 to 9 and a vertical power of 1. ...	202
Figure 5.13. Vertical expansion factors for the whole image when using a highest power of 1 for the trendlines as described in Appendix 5.1, and a highest vertical power of 1 for the trendlines as described above.	203
Figure 5.14. Result of the expansion method used in Figure 5.28.	204
Figure 5.15. Vertical expansion factors for the whole image when using a highest power of 1 for the trendlines as described in Appendix 5.1, and a highest vertical power of 2 for the trendlines as described above.	204
Figure 5.16. Result of the expansion method used in Figure 5.30.	205
Figure 5.17. Vertical expansion factors for the whole image when using a highest power of 2 for the trendlines as described in Appendix 5.1, and a highest vertical power of 1 for the trendlines as described above.	206
Figure 5.18. Result of the expansion method used in Figure 5.32.	207
Figure 5.19. Vertical expansion factors for the whole image when using a highest power of 2 for the trendlines as described in Appendix 5.1, and a highest vertical power of 2 for the trendlines as described above.	208
Figure 5.20. Result of the expansion method used in Figure 5.34.	208
Figure 5.21. The same trendlines as in Figure 5.17, but with an imaginary mirror to reflect the points to the other side of the image.	209
Figure 5.22. The resulting expansion factors from Figure 5.36.	209
Figure 5.23. The resulting expansion factors from Figure 5.37, for the whole image. ...	210
Figure 5.24. The result of the expansion with an imaginary vertical mirror, for comparison see Figure 5.33.	211

Figure 5.25. The same trendlines as in Figure 5.21, but with an imaginary mirror to reflect the points to the other side of the image., note how the trendlines no longer converge. .212

Figure 5.26. The resulting expansion factors from Figure 5.40.....212

Figure 5.27. The resulting expansion factors from Figure 5.41, for the whole image. ...213

Figure 5.28. The result of the expansion in Figures 5.40 to 42, with an imaginary vertical mirror.214

Figure 5.29. (a) image of flame; (b) flame image in black and white; (c) maximum flame body; (d) minimum flame body; (e) differences in (b) and (c); (f) differences in (b) and (d); (g) and (h) changing red box based on flame body.....216

Figure 5.30. Plots of the heat release rate normalised, maximum, and minimum areas that can be calculated from the measured pixels of the flame. No correction factors were used.218

Figure 5.31. Plots of the heat release rate (mean) with and without the correction factor implemented.....218

Figure 5.32. Plots of total heat release with and without correcting for flame movement.219

Figure 5.33. The horizontal lines of the calibration box (black lines), with trendlines (red lines) overlaid when the equation shown was used to calculate the trendlines.222

Figure 5.34. The horizontal lines of the calibration box (black lines), with trendlines (red lines) overlaid when the equation shown was used to calculate the trendlines.223

Figure 5.35. The horizontal lines of the calibration box (black lines), with trendlines (red lines) overlaid when the equation shown was used to calculate the trendlines.223

Figure 5.36. The horizontal lines of the calibration box (black lines), with trendlines (red lines) overlaid when the equation shown was used to calculate the trendlines.224

Figure 5.37. The horizontal lines of the calibration box (black lines), with trendlines (red lines) overlaid when the equation shown was used to calculate the trendlines.224

Figure 5.38. The horizontal lines of the calibration box (black lines), with trendlines (red lines) overlaid when the equation shown was used to calculate the trendlines.225

Figure 5.39. The horizontal lines of the calibration box (black lines), with trendlines (red lines) overlaid when the equation shown was used to calculate the trendlines.225

Figure 5.40. The horizontal lines of the calibration box (black lines), with trendlines (red lines) overlaid when the equation shown was used to calculate the trendlines.226

Figure 5.41. The horizontal lines of the calibration box (black lines), with trendlines (red lines) overlaid when the equation shown was used to calculate the trendlines226

Figure 5.42. The expansion factors for each column when a trendline equation of $y = ax + b$ was used. 227

Figure 5.43. The expansion factors for each column when a trendline equation of $y = ax^2 + bx + c$ was used. 228

Figure 5.44. The expansion factors for each column when a trendline equation of $y = ax^3 + bx^2 + cx + d$ was used 228

Figure 5.61. The errors for horizontal powers from 1 to 9 and a vertical power of 1. 229

Figure 5.62. The errors for horizontal powers from 1 to 9 and a vertical power of 2. 230

Figure 5.63. The errors for horizontal powers from 1 to 9 and a vertical power of 3. 230

Glossary

Ageing	The loss of capacity due to, e.g. loss of lithium-ions or spallation of the anodes. This is due to time (calendar aging) and use (charging and discharging).
Anode	The negative electrode. In lithium-ion batteries this is most typically small particles of graphite.
ATF	Authorised treatment facility.
Battery (pack)	The complete energy storage unit consisting of a number of modules or strings.
BESS	Battery energy storage system.
BMS	Battery management system. This monitors and controls all the functions and the state-of-health of the battery.
BoL	Beginning of Life.
Calendar ageing	The changes in the cells of a LiB when in the passive state, i.e. not charging or discharging.
C-rate	The rate of charging or discharging expressed in terms of the capacity of the battery. A C-rate of 1 will charge/discharge a battery in 1 hour: thus, 1C discharge of a 60Ah battery requires 60A.
Capacity	The amount of charge stored in a battery or cell, usually specified in Amp hours (A h) or Watt hours (Wh). 1 A h = 3600 Coulombs (C).
Cathode	The positive electrode. These typically comprise lithium transition metal oxides: e.g. lithium nickel manganese cobalt oxide (LiNi _{0.33} Mn _{0.33} Co _{0.33} O ₂).
Cell	The smallest unit of a battery.
Current collector	The aluminium or copper foil on which is coated the cathode and anode material, respectively.
DIY SLDLiBESS	Do-It-Yourself second life domestic lithium-ion battery energy storage system
DLiBESS	Domestic lithium-ion battery energy storage system.
DMC	Dimethylcarbonate. One of the solvents used in the electrolyte.
DSR	Demand Side Response
EC	Ethylenecarbonate. One of the solvents used in the electrolyte.
EIS	Electrochemical impedance spectroscopy.
Electrolyte	In electrochemistry, this term can refer either to the inorganic salt (e.g. LiPF ₆) or to the salt + organic solvent in which it is dissolved.
End of Life (EoL)/ End of First Life (EoFL)	The point at which a battery ceases to be suitable for its current application. EoFL for automotive batteries is typically 75 – 80% State-of-Health.
End of Second-life (EoSL)	The final end of life of a lithium-ion battery, usually taken as 50 – 60% SoH.
Energy	The energy stored in a battery is specified in Watt hours (W h) or kiloWatt hours (kW h): 1 W h = 1 Amp Volt x 3600 secs = 3600 AVs = 3600 Joules.
Energy density	The energy per unit volume (litre) of battery.
EMC	Ethylmethylcarbonate. One of the solvents used in electrolyte.
EV	Electric vehicle
Galvanic cell	Usually just referred to as a cell. A device which when charged with electricity is in a higher energy state than when discharged. On

	discharge the chemical energy stored is released as an electrical current.
LCO cathode	Lithium Cobalt Oxide, LiCoO_2 .
LiB	LiB Lithium-ion Battery and general term for lithium-ion cells, modules and packs.
LFP cathode	Lithium iron (Ferrous) Phosphate, LiFePO_4 .
LiBESS	Lithium-ion battery energy storage system.
LiPF_6	Lithium hexafluorophosphate
LMO cathode	Lithium Manganese Oxide e.g. LiMn_2O_4 .
Module or string	Manufacturer-specific terms, e.g. collection of cells arranged in series and/or parallel.
MMO	Mixed metal oxide (cathode material).
NCA cathode	(Lithium) Nickel Cobalt Aluminium oxide, e.g. $\text{LiNi}_{0.8}\text{Co}_{0.15}\text{Al}_{0.05}\text{O}_2$.
NiCd	Nickel Cadmium
NMC cathode	(Lithium) Nickel Manganese Cobalt oxide, e.g. $\text{LiNi}_{0.33}\text{Mn}_{0.33}\text{Co}_{0.33}\text{O}_2$ (NMC 111), $\text{LiNi}_{0.6}\text{Mn}_{0.2}\text{Co}_{0.2}\text{O}_2$ (NMC 622).
OEM	Original equipment manufacturer.
Open circuit	The state when a battery or cell is disconnected from an external circuit.
Open Circuit Voltage (OCV)	The potential difference (voltage) across the terminals of a cell or battery when no current is allowed to flow. This can be correlated with the State of Charge (SoC).
PV	Photovoltaic (array): solar electric panels.
Reuse	Battery pack is re-used in its entirety in the same application as in first life.
Remanufacture	Selection of modules at end-of-first life and assembly into batteries or packs for second-life applications.
Repair	Battery pack is re-used in the same application as in first life, but faulty modules are replaced.
Risk	Risk = probability of hazard occurring x severity of hazard.
RUL	Remainder of Useful Life
Salt	The inorganic compound employed to produce ions in the cell. This is typically lithium hexafluorophosphate (LiPF_6) which dissociates in the organic solvent to produce lithium cations (positively charged ions, Li^+) and hexafluorophosphate anions (negatively charged ions, PF_6^-).
Separator	A plastic film permeable to lithium and hexafluorophosphate ions that prevents the anode and cathode from touching and causing a short circuit.
SLDLiBESS	Second-life domestic lithium-ion battery energy storage system.
Solid Electrolyte Interface (SEI)	The protective layer that forms on the anode during the first charge from reduction of the LiPF_6 and solvent which prevents further, explosive degradation of the electrolyte and thermal runaway.
Solvent	Mixture of organic carbonates, containing ethylene carbonate, as this is essential for the formation of the SEI. Ethylene carbonate is a solid at room temperature and other carbonates are essential to reduce viscosity.
Specific energy	The energy per kg of battery.

State of Charge (SoC)	The amount of charge stored compared to that equivalent to full charge, expressed as %.
State of Health (SoH)	The current capacity of a cell or battery compared to its capacity at its beginning of life, expressed as %.
ToU	Time of use billing.
Virtual Power Plant (VPP)	Grouping of DLiBESS to support the grid.
VOC	Volatile organic compounds.

Chapter 1 . Introduction

In broad terms, the work described in this thesis concerns the safety aspects of lithium-ion batteries, and particularly what happens when things go wrong.

Lithium-ion batteries (LiBs) have penetrated deeply into society, finding a wide range of applications in personal electronic devices since their discovery and development in the 1980's and 90's and, more recently, in larger energy systems including personal mobility devices (E-scooters, E-bikes, E-motorcycles etc.), electric vehicles (EVs) and battery energy storage systems (BESS). The plethora of applications is primarily due to the unique characteristics of LiB technology including: high energy densities, high voltage, good stability, low self-discharge rate, long-life cycle, and availability of a wide range of chemistries with diverse electrode designs [1, 2]. LiBs are incorporated into ever more applications and are to be found at scales as diverse as their applications: this is evidenced by the uptake of LiBs having increased eight-fold between 2010 and 2018 to 160 GWh [3] and the steady increase in annual sales of LiBs which are predicted to be c.a. 4 TWh by 2040 [4]. In the UK, it is forecast that the number of LiBs reaching end of their life in automotive applications (End-of-First-Life, EoFL) will be approximately 75,000 units, or 28,000 tonnes by 2025 [5]. The advent of lithium-ion technology and the paradigm shift in the energy and power density capabilities that it represents, are perceived as the enabling technology for an extremely broad range of energy storage applications [6]. Most particularly, LiBs are increasingly recognised as essential and integral to enable the storage of electrical energy from renewable energy sources.

1.1. Composition and structure of a lithium-ion battery

The smallest unit of a LiB is the cell [7]. Cells are connected in series and/or parallel to make a module [8] (sometimes called a string), modules are connected in series and/or parallel to make a battery or battery pack [8]. A cell is comprised of two electrodes physically separated by a porous polymer separator soaked in a liquid electrolyte made of organic solvents with a lithium salt dissolved into it along with chemical additives [9], Figure 1.1 shows a schematic of a lithium-ion cell as part of a stack of cells.

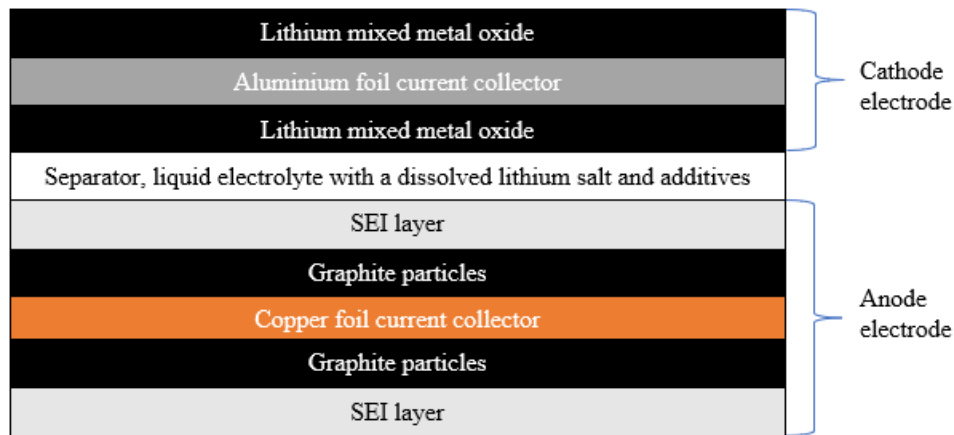


Figure 1.1. Schematic of a lithium-ion cell.

As can be seen from Figure 1.1, the electrodes comprise a number of components: thus, the cathode is made from an aluminium foil current collector coated with a lithium mixed metal oxide [10]; the anode is made from a copper foil current collector normally coated with graphite particles [10]. The electrodes are pressed tightly together either side of a porous polymer separator (typically polyethylene (PE), polypropylene (PP), or both [11]) with the pores filled with electrolyte during the manufacturing process. The most common electrolyte comprises a mixture of organic carbonates (always ethylene carbonate (EC), with e.g. dimethyl carbonate (DMC) and/or ethyl methyl carbonate (EMC), and/or diethyl carbonate (DEC) [12]), and lithium hexafluorophosphate (LiPF_6) as the lithium salt, see **Error! Reference source not found.** for chemical structures and formulae. Additives form up to 5% of the electrolyte either by weight or volume [13].

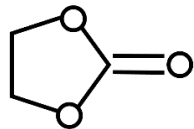
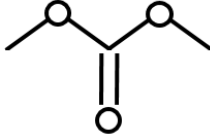
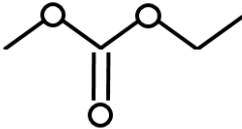
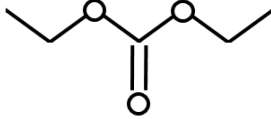
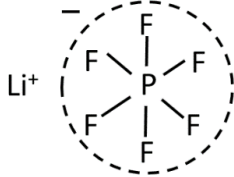
The foil current collectors are made as thin as possible to reduce the mass and volume of the cell, in turn making the energy densities as high as possible [14]. Improved manufacturing methods over the last decade have made thinner current collectors possible and cell designers have utilised these thinner materials to increase energy density in newer cells [15].

As most LiBs have graphite anodes, the mixed metal oxide layer of the cathode is used to name the cell [8, 15], for example: a LCO cell has a lithium cobalt oxide cathode, a LFP cell has a lithium iron (ferrous) phosphate cathode, a NCA cell a nickel cobalt aluminium oxide cathode, and a NMC cell has a nickel manganese cobalt oxide cathode.

Names can be made more descriptive by including the mole stoichiometry of each metal making the mixed metal oxide: lithium and oxygen are excluded from the name, as the proportion of lithium changes during charge and discharge cycles and the oxygen content

is constant: for example, a NMC 111 (sometimes NMC 333) cell has equal proportions of nickel, manganese, and cobalt ($\text{LiNi}_{1/3}\text{Mn}_{1/3}\text{Co}_{1/3}\text{O}_2$); and a NMC 811 cell has 80% nickel, 10% manganese and 10% cobalt ($\text{LiNi}_{0.8}\text{Mn}_{0.1}\text{Co}_{0.1}\text{O}_2$) [16].

Table 1.1. Chemical formulas and structures for common electrolyte components.

Name	Chemical Formula	Chemical Structure
Ethylene carbonate	$\text{C}_3\text{O}_3\text{H}_4$	
Dimethyl carbonate	$\text{C}_3\text{O}_3\text{H}_6$	
Ethyl methyl carbonate	$\text{C}_4\text{O}_3\text{H}_8$	
Diethyl carbonate	$\text{C}_5\text{O}_3\text{H}_{10}$	
Lithium hexafluorophosphate	LiPF_6	

At the time of writing, as stated above, the most common active anode material is graphite [17], coated on a copper foil current collector. The graphite particles are obtained from natural resources or synthesised, and refined in a process called spheroidization, producing particles between 8 and 30 μm [18]. The graphite is bound to the copper using polyvinylidene fluoride (PVDF) as a binding agent [18]. An alternative anode is lithium titanate oxide (LTO) [10, 19], which although deemed safer [10], can't be cycled through as wide a voltage range as graphite, and therefore makes the cell energy densities (energy per unit mass (J kg^{-1}) and energy per unit volume (J m^{-3})) lower [10, 19].

If the two electrodes physically touch each other when in the charged state, an internal short circuit is produced, any stored electrical energy will be released in an uncontrolled manner producing a large amount of heat [20], which is why the electrodes are physically

separated, with an electrically insulating material. The separator is porous to facilitate the transport of lithium ions dissolved in the electrolyte from one electrode to the other in charge and discharge cycles, with channels of c.a. $1\mu\text{m}$ in diameter [21]. The separator plays no part in the electrochemical reactions in the cell and is such ‘dead weight’, hence, it is made as light and therefore as thin as possible, typically between 20 and 25 μm for polypropylene and polyethylene separators [21, 22], which is about a fifth to a third the thickness of a standard sheet of A4 paper.

Cells can be made in different shapes and sizes (form factors): cylindrical, prismatic and pouch [23]. The cell components are housed in a casing, this can be a hard case which provides structural integrity, i.e. cylindrical and prismatic cells, or a soft case, as with pouch cells [24, 25]. All casings must prevent water ingress and electrolyte loss [25] and are shown in Figure 1.2 to 1.8.

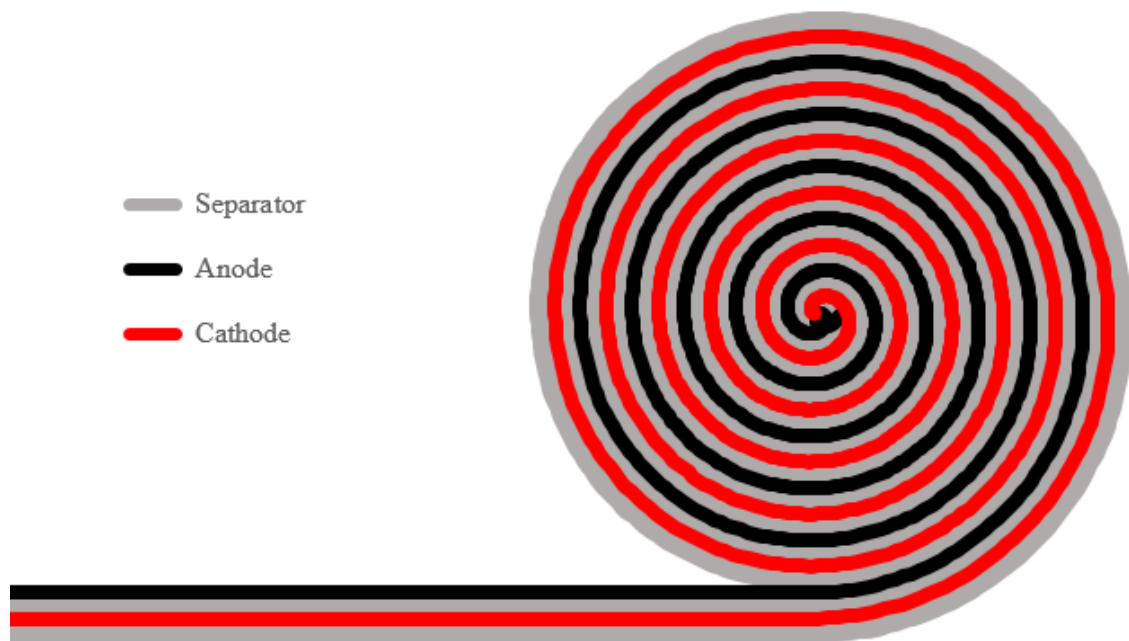


Figure 1.2. A schematic showing the components rolled in a cylindrical can.

A cylindrical cell has its components rolled, taped shut, and known as a jelly roll [26], as seen in Figure 1.2. The jelly roll is placed inside an aluminium or steel can which is welded closed [27], as can be seen in

Figure 1.3, its shape is like a standard UK AA (LR6) cell. The cathode in a cylindrical cell is connected to the lid of the can and the anode to the base [28, 29].

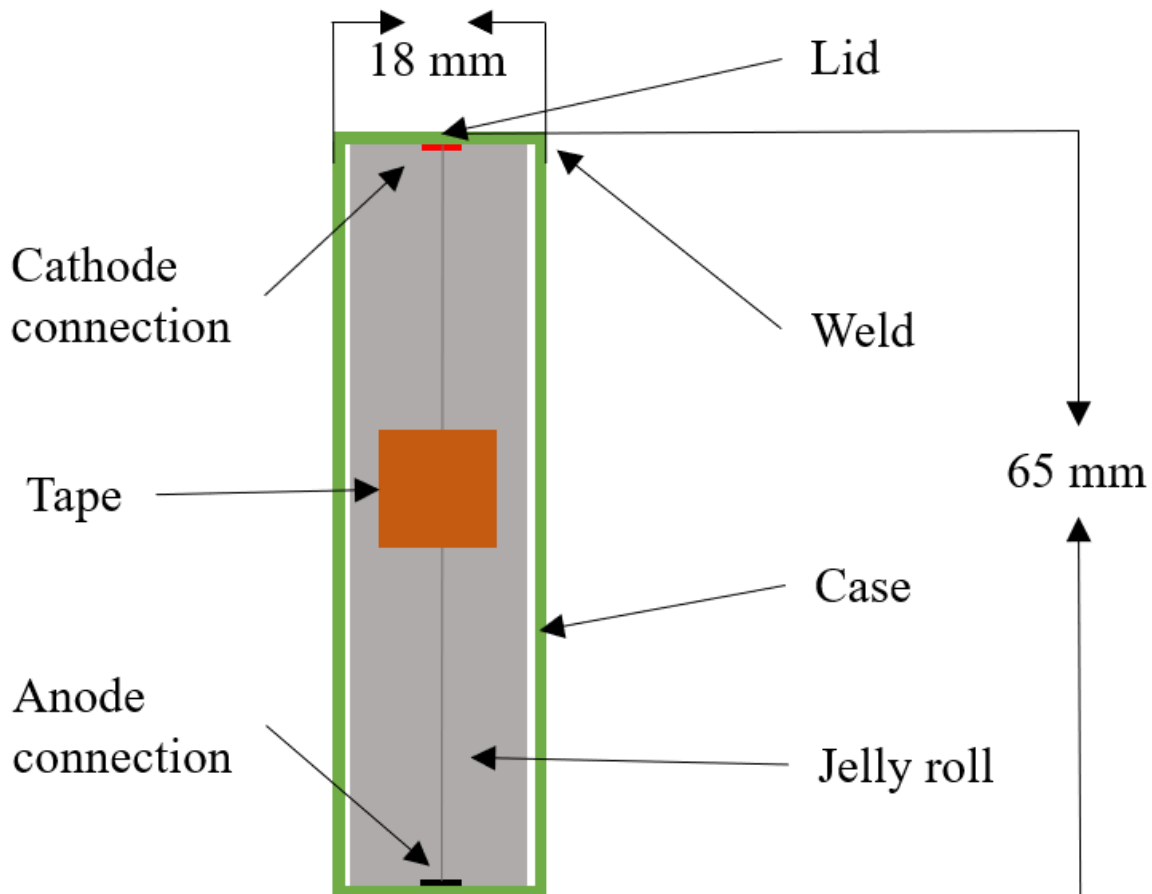


Figure 1.3. Schematic cross section of a typical 18650 cylindrical cell.

The size of the can used in a cylindrical cell is used to classify the cell, for example, an 18650 cell is 18 mm in diameter and 65 mm in length [30]: for comparison a UK AA cell is 14.5 mm in diameter and 50.5 mm in length [31]. The International Electrotechnical Commission (IEC) have further classifications and include details of the cathode chemistry and shape, with lithium-ion cells having a prefix 'I', followed by the cathode chemistry ('C' for cobalt) then the shape ('R' for cylindrical cells). A cylindrical LCO cell of the above dimensions is an ICR18650 cell [30]. Cylindrical cells are used in Tesla, Smart and Mini EV's and are made by manufacturers such as Panasonic [32, 33].

A prismatic cell has its components rolled in a similar fashion to a cylindrical cell except the jelly roll is flatter, i.e. an elliptic spiral [8], as can be seen in Figure 1.4. The jelly roll is inserted into aluminium or steel case [26] then the lid is welded on, as can be seen in Figure 1.5.

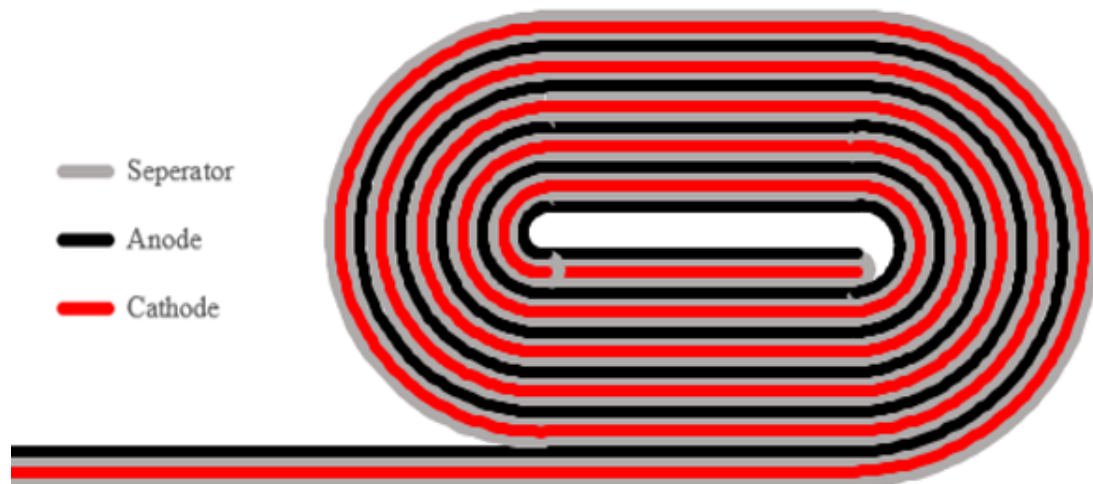


Figure 1.4. A schematic showing how the components are wound in a prismatic cell.

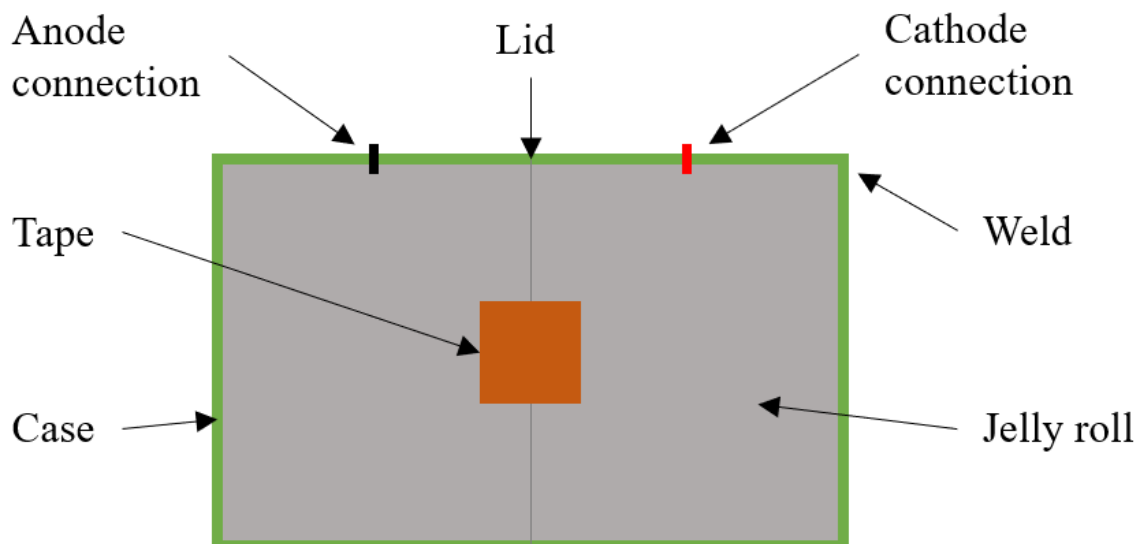


Figure 1.5. Schematic cross section of a prismatic cell.

The shape of a prismatic cell is like a UK 9V PP3 cell (47 mm high, 26 mm wide and 17 mm thick [31]). Prismatic cells are classified by the IEC with the letter ‘P’, if this cell uses a LCO cathode and the same size as a standard UK 9V PP3 cell, it would be an ICP264717 [30]. Prismatic cells are used in Toyota and Mitsubishi EV’s and are made by manufacturers such as PEVE and LEJ [33].

A pouch cell can have its electrodes either elliptically rolled as can be seen in Figure 1.4, stacked in an anode-separator-cathode-separator pattern, see Figure 1.6, or using a z-fold on the separator, see Figure 1.7 [34, 35], in this case the separator is one continuous piece, snaking around the individually cut electrodes. After stacking the electrodes using

any of the methods, the electrode stack is placed inside an aluminium/plastic laminate pouch and heat sealed [35], see Figure 1.8.



Figure 1.6. A schematic showing the stacking of the electrodes and separator of a pouch cell.

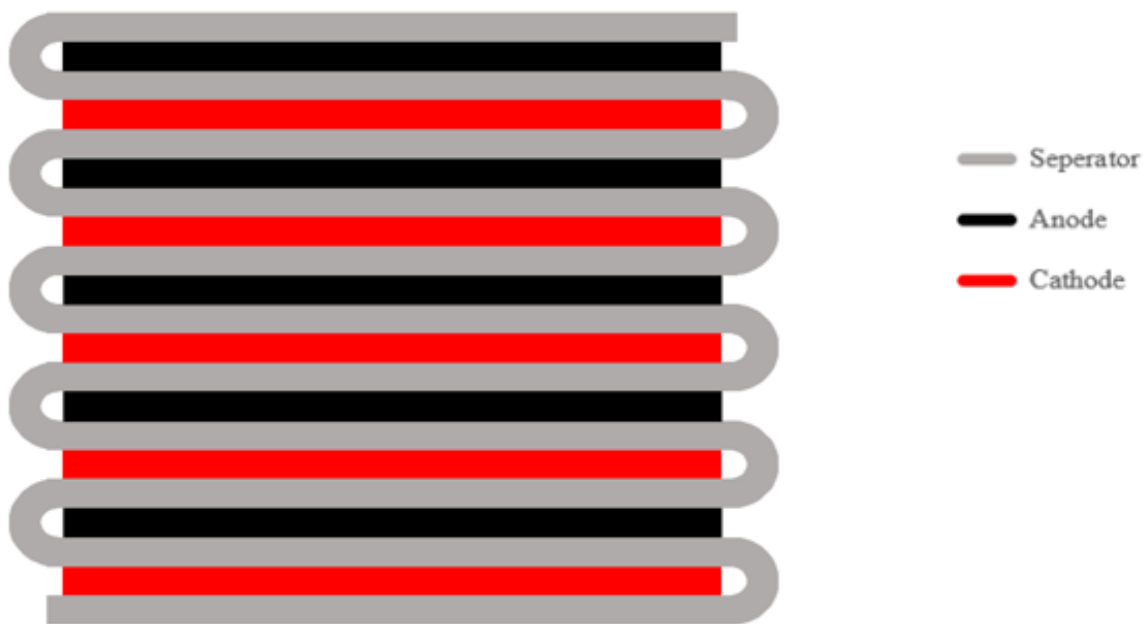


Figure 1.7. A schematic showing the 'Z' folding of the electrodes and separator of a pouch cell.

The laminate pouch is tri-layer with typically, polypropylene (melting point 165°C [36]) on the inside, aluminium (melting point 660°C [37]) in the middle and a polyamide (various melting points (220°C for polyamide 6, 190°C for polyamide 11 [38]) or polyethylene terephthalate (220 – 250°C [35]) on the outside [35]. The laminate is heat sealed at a temperature above the melting point of the inner polypropylene but less than the outer polyamide after the electrode stack is inserted [35]. Unlike cylindrical and prismatic cells, there is no classification system for size or cathode type. Pouch cells are

used in Nissan, Opel and Ford EV's and are made by manufacturers such as LG Chem and Envision-AESC [33].

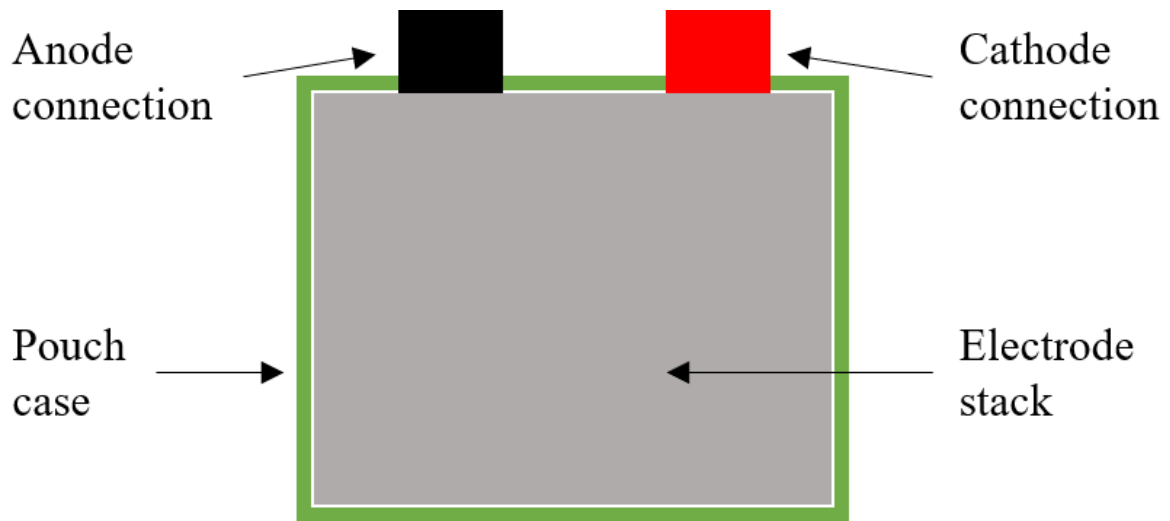


Figure 1.8. Schematic cross section of a pouch cell.

1.2. Charge and discharge

The electrochemistry that takes place during the charging and discharging of a lithium-ion cell is the simplest of all rechargeable cells. Lithium ions move from one electrode to the other by de-intercalating from one electrode and intercalating into the other electrode, as shown in Figure 1.9. Lithium intercalation in graphite is a process where lithium ions are inserted in between the graphene layers [39, 40] and lithium intercalation in a LCO cathode is a process where lithium ions are inserted in between the crystal structure layers [39]. De-intercalation is the removal of the lithium ions from the graphite or crystal structure layers.

As can be seen in Figure 1.9, when the cell is fully discharged, the anode is empty of lithium, it is carbon in the form of graphite with the empirical formula C_6 [41]. The cathode is full of intercalated lithium with the empirical formula $LiCoO_2$ [41]. As the cell charges the lithium content in the cathode reduces becoming $Li_{1-x}CoO_2$ and the anode lithium content increases to LiC_6 when fully charged [41, 42]. A maximum of half of the lithium ions that were originally intercalated in the cathode are intercalated in the anode, as once the lithium content (the 'x' in $Li_{1-x}CoO_2$) is above 0.55 the structure begins to collapse in a highly exothermic process [43]. As the cell discharges, the reverse happens, the lithium ions that were intercalated into the anode, de-intercalate and intercalate into

the cathode, reforming the cells original state [44]. A charge/discharge cycle is shown in Figure 1.10 showing the direction of movement of lithium ions (Li^+) and electrons (e^-).

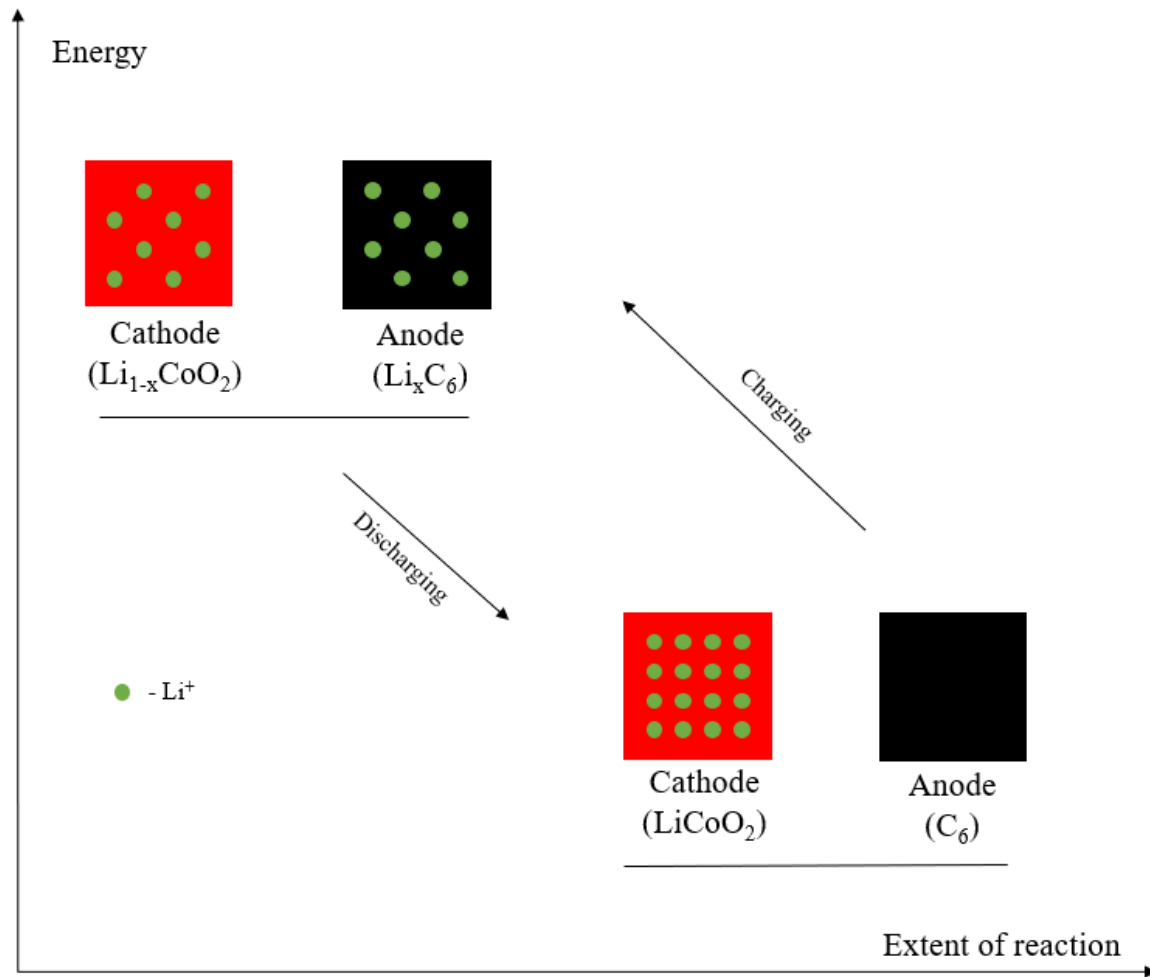


Figure 1.9. A simplified diagram of a charge/discharge cycle inside a LCO cell.

As can be seen in Figure 1.10 when discharging a cell, electrons move from the anode, around the external circuit, through an electrical appliance, providing energy for the appliance to function, then to the cathode, while lithium ions move through the electrolyte and separator from the anode to the cathode [45]. Charging a cell requires an external power source, provided a voltage difference between the electrodes, forcing negatively charged electrons around the external circuit from the cathode to anode, while lithium ions move through the electrolyte and separator from the cathode to the anode [46, 47].

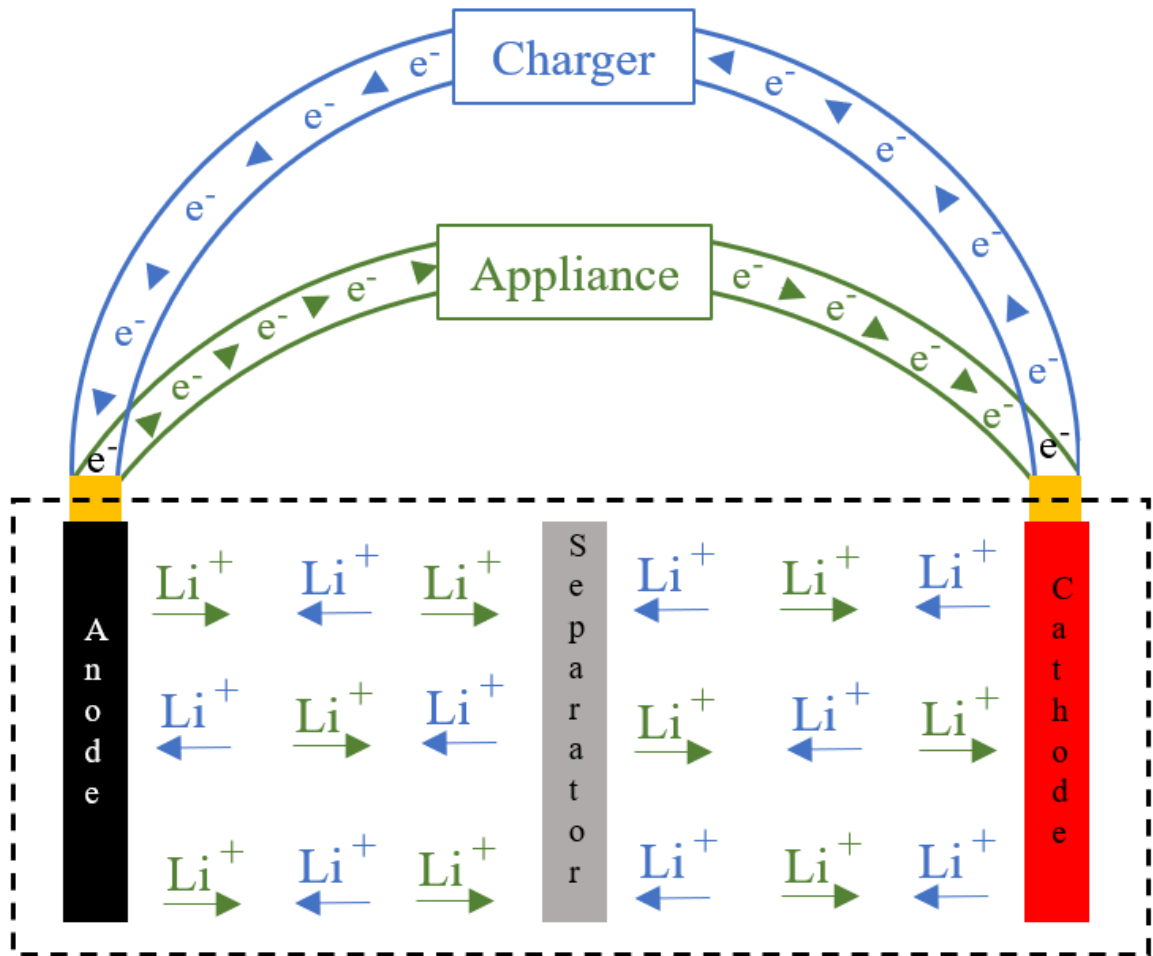
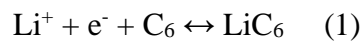


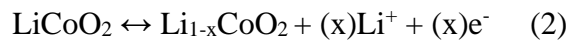
Figure 1.10. The charging and discharging of a lithium-ion cell.

By definition, oxidative processes, where a species loses an electron and becomes (more) positively charged, take place at the anode, and reductive processes, where species gain an electron and become (more) negatively charged, take place at the cathode [48].

However, the reactions in a LiB cell are reversible, at the anode the reaction is:



Going from left to right during charging. The reaction at a LiCoO_2 cathode is:



Going from left to right during charging. During discharge the reaction at the anode is oxidative and at the cathode the reaction is reductive, but during charging a reductive reaction occurs at the anode and an oxidative reaction occurs at the cathode, so the anode should be called the cathode and vice-versa [10, 41]. To avoid confusion, the names of the electrodes are given by the discharge reactions, i.e. the anode is the graphite coated

copper electrode, and the cathode is the mixed metal oxide coated aluminium electrode, and do not change for charging.

1.3. A summary of the history of lithium-ion batteries

The patent for the first prototype lithium-ion cell was registered in 1985 (U.S Patent number 4,668,595) [49], building on work by John. B. Goodenough and others earlier in the decade [50]. The first application of LiBs was in Sony camcorders in 1991 [51, 52], but this expanded rapidly into mobile phones and laptops [51, 52], using all three form factors. The next paradigm shift was the use of LiBs in EVs (again using all three form factors) heralded by the first production LiB EV, the Tesla Roadster in 2008 [53]. This also triggered very large scale production of LiBs in gigafactories. Plug in hybrid EVs (PHEV's), which can be charged by connecting to an external power source or using an onboard generator fuelled by the combustion engine, were followed by the all-electric Nissan Leaf in 2010 and a significant increase in the LiB market in 2015 due to the introduction of Chinese EV buses [54]. The first lithium-ion battery energy storage system (LiBESS) was installed in 2008 in Guadeloupe in a collaboration between SAFT, Tenesol, ADEME and EDF SEI and was several domestic LiBESS (DLiBESS), consisting of 15 SAFT 11 kWh units each connected to a 2 kW photovoltaic (PV) system. The first large scale (5MW) LiBESS was commissioned for Portland Electric in 2012.

1.4. Safety systems

1.4.1. The solid electrolyte interface (SEI)

The first major safety benefit of a LiB is the solid electrolyte interface (SEI), see Figure 1.1. When fully charged, LiBs are thermodynamically unstable, as the graphite anodes have essentially the same potential as metallic lithium, c.a. 0.1 V difference [55], and hence should immediately and exothermically reduce the organic carbonates employed in the electrolyte [56-58]. The reason that this does not occur is the serendipitous formation of the SEI during the first charge [59, 60]: thus, during manufacture, newly assembled cells are left at low SoC over a period of c.a. 2 weeks to ensure the formation of a compact SEI layer on the graphite particles.

Figure 1.11 shows the potentials of various cathode materials, for example lithium nickel manganese oxide ($\text{Li}_x\text{Ni}_{0.5}\text{Mn}_{1.5}\text{O}_4$ (LNMO)) cathodes are stable when cycled up to 4.6 V vs Li/Li^+ but will oxidise the electrolyte at potentials above this. Lithium titanate anodes

are stable when cycled above 1.55 V vs Li/Li⁺ but will reduce the electrolyte at potentials below this. Graphite can be cycled to c.a. 0.1 V vs Li/Li⁺, but this is outside the electrolyte stability window (shown in blue in Figure 1.11): however, the formation of the SEI layer on the anode expands the window to c.a. 0 – 4.8 V vs Li/Li⁺.

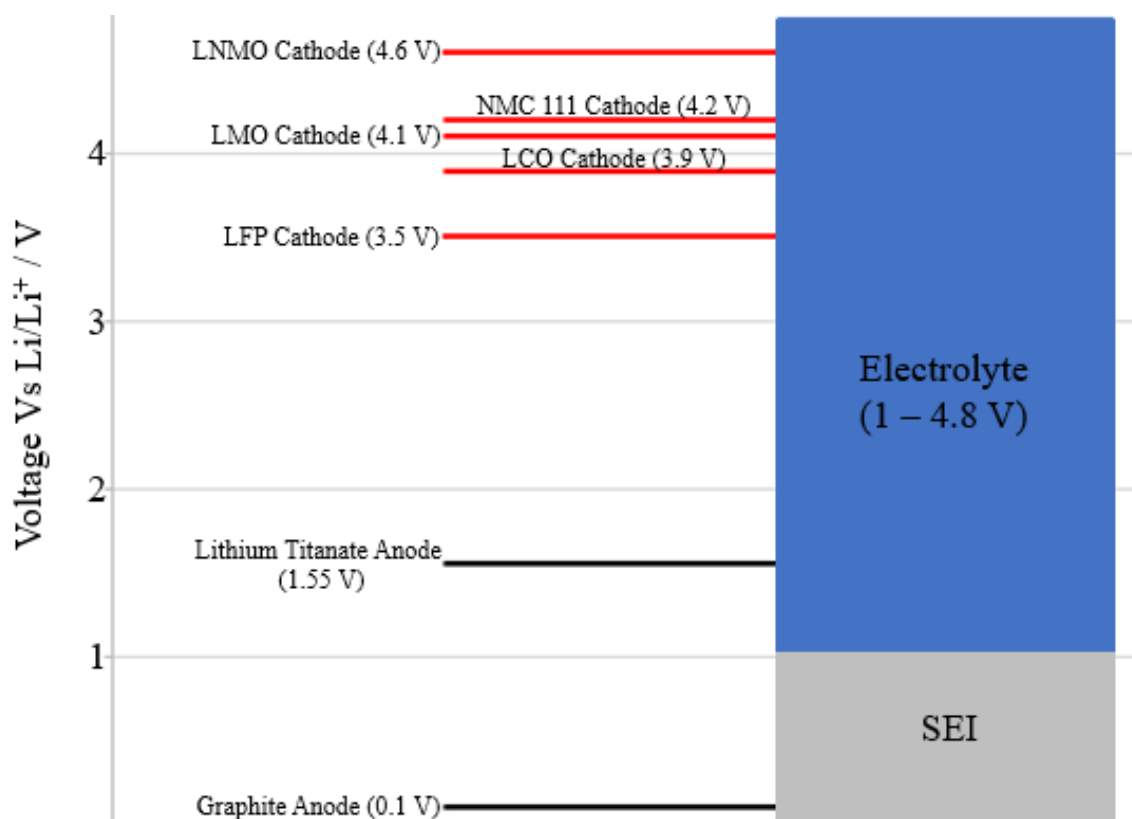


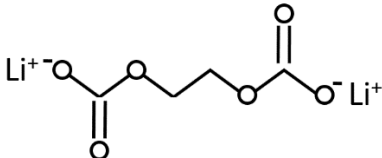
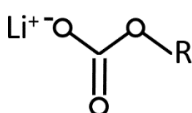
Figure 1.11. A schematic showing the electrochemical stability windows of the electrodes and electrolyte in lithium ion cells [10, 54].

Cycling a cell through a greater potential difference gives the cell a higher energy density, as the potential difference (measured in voltage) is energy (in joules) per coulomb of charge. A LNMO/graphite cell can be cycled with a maximum potential difference of 3.6 V (4.6 V - 1 V = 3.6 V), but with the SEI layer a maximum potential difference 25 % higher, 4.5 V (4.6 V - 0.1 V = 4.5 V) can be obtained.

The SEI layer allows the transport of lithium ions to and from the anode [10], through micro-pores in its structure [13], but is impervious to the solvent molecules [10]. The exact reactions responsible for the formation of the SEI are unknown [61], but it has been proposed that cyclic carbonates such as ethylene carbonate (which is always a component of the electrolyte), react with the lithium ions (from the lithium salt (LiPF₆ [62])) [61] to produce Li₂CO₃ or Li₂C₄O₆H₄ [13, 63], see Table 1.2 for chemical structures and formulas. The SEI layer has also been found to be composed of layers itself [64]: an

inorganic layer at the graphite surface [61, 65], consisting of compounds such as LiF and Li₂O [10], and an organic outer layer [61, 65] consisting of compounds such as Li₂CO₃ and lithium alkyl carbonates (ROCO₂Li)[62], where ‘R’ stands for the rest of the molecule. Damage to the SEI is one of the primary causes of thermal runaway, i.e. uncontrolled positive feedback, in lithium-ion cells that can result in fire or explosions.

Table 1.2. Chemical formulas and structures for SEI components.

Name	Chemical Formula	Chemical Structure
lithium carbonate	Li ₂ CO ₃	Ionic bonded crystal
dilithium ethylene dicarbonate	Li ₂ C ₄ O ₆ H ₄	
lithium fluoride	LiF	Ionic bonded crystal
lithium oxide	Li ₂ O	Ionic bonded crystal
lithium alkyl carbonates	ROCO ₂ Li	

1.4.2. The battery management system

The primary physical safety system is the battery management system (BMS). The purpose of the BMS is to ensure as far as possible (i.e. BMSs are known to fail, as may be seen, for example, from incidents involving the overcharge of EVs [66]) safe operation, to facilitate longevity, monitor state of function in the form of state of charge (SoC, the percentage of stored charge compared to the maximum charge [67, 68]) and state of health (SoH, the maximum capacity compared to that when the cell was new, also expressed as a percentage [69, 70]), provide alerts for causes of concern such as extremes of temperature, cell imbalance, and the remaining useful life [70, 71]. The BMS should prevent overcharge (e.g. when charging a smart phone, the BMS disconnects the battery from the charger at 100 % SoC) and over discharge, both of which can lead to hazardous incidents [72]. When cells are connected in series, to reach the required voltage for an application [73], they must be actively balanced. Cells have different capacities due to manufacturing tolerances, testing equipment precision and environmental conditions [65, 73]. The cell with the lowest capacity reaches 100 % SoC first and if charging is not terminated it will overcharge before the other cells are fully charged [74]. This becomes a hazardous event and is described in more detail in Section 1.6.2.

The most common definition of SoH is the ratio of the current maximum capacity of a cell, module or battery, Q_c , to the maximum capacity when new, i.e. at beginning of life (BoL), Q_{BoL} , expressed as a percentage [69], and shown in Figure 1.12:

$$SoH = \left(\frac{Q_c}{Q_{BoL}} \right) \times 100\% \quad (3)$$

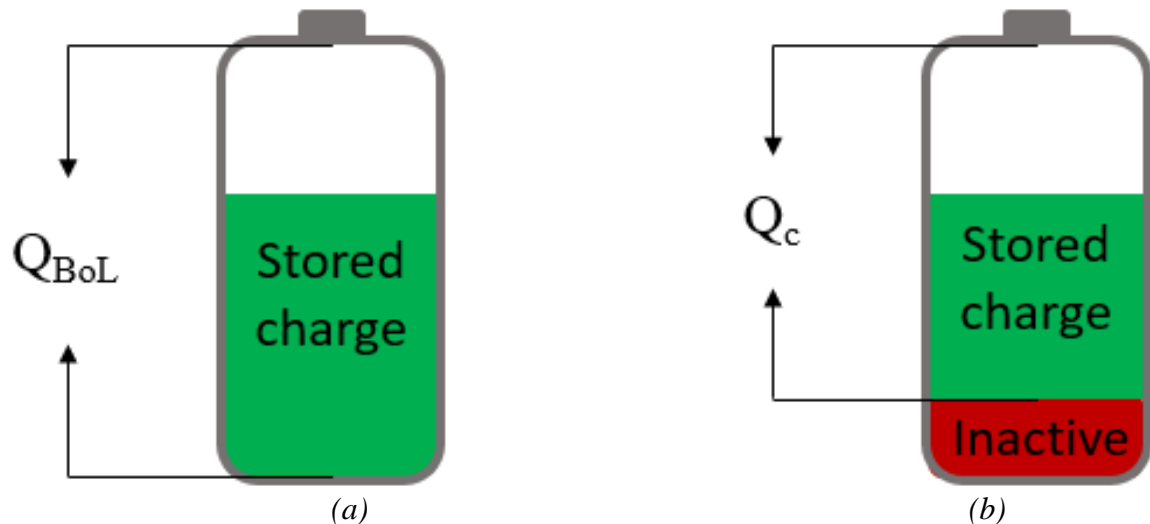


Figure 1.12. Representation of a lithium-ion battery at (a) Beginning of Life, BoL, and (b) after ageing.

The charge contained in a cell is known as capacity, in Ah: 1Ah = 3600 Coulombs (C) [75] and as can be seen in Figure 1.12, in (a) at BoL, the charge that can be stored in the cell (Q_{BoL}) is at a maximum. As the cell ages, through cycling and/or calendar ageing (i.e. while sitting idle) [60], a portion of the cell becomes inactive (red section in Figure 1.12(b)), Q_c , the capacity of the cell is thus reduced compared to Q_{BoL} [76].

Typically, the SoC of a new cell is determined from a calibration curve of open cell voltage (OCV) vs SoC [67, 77]. Determining the SoC of an aged cell is extremely challenging [67] as the charge corresponding to 100 % SoC cannot be determined accurately [67], and each cell has its own unique calibration curve, i.e. LCO calibration curves are different for each manufacturer [78] are temperature, age, hysteresis and history dependent [79], and cells need time to relax to reach thermodynamic equilibrium before reliable voltage readings can be made [67, 80, 81] (see Figure 1.13). A further complication in LFP cells is they have significantly flatter voltage vs charge curves than other chemistries [81-83], as shown in Figure 1.14, meaning voltage readings must be both accurate and precise to avoid large inaccuracies in SoC estimations [67, 68].

The blue and orange lines in Figure 1.13 show the difference in the OCV-SoC relationship depending on the time a cell is relaxed before measurements are taken. The blue line is for readings taken 24 hours after discharging a cell and the orange line is for readings taken 1 hour after discharging a cell. As the cell relaxes the OCV increases (after discharge, decreases after charging [80]) until all the components are in thermodynamic equilibrium. In this example, if a voltage measurement is taken at the dotted black line, it will read as a 20% SoC for a cell given a 24 hour rest period, but 40% SoC for a cell given a 1 hour rest period.

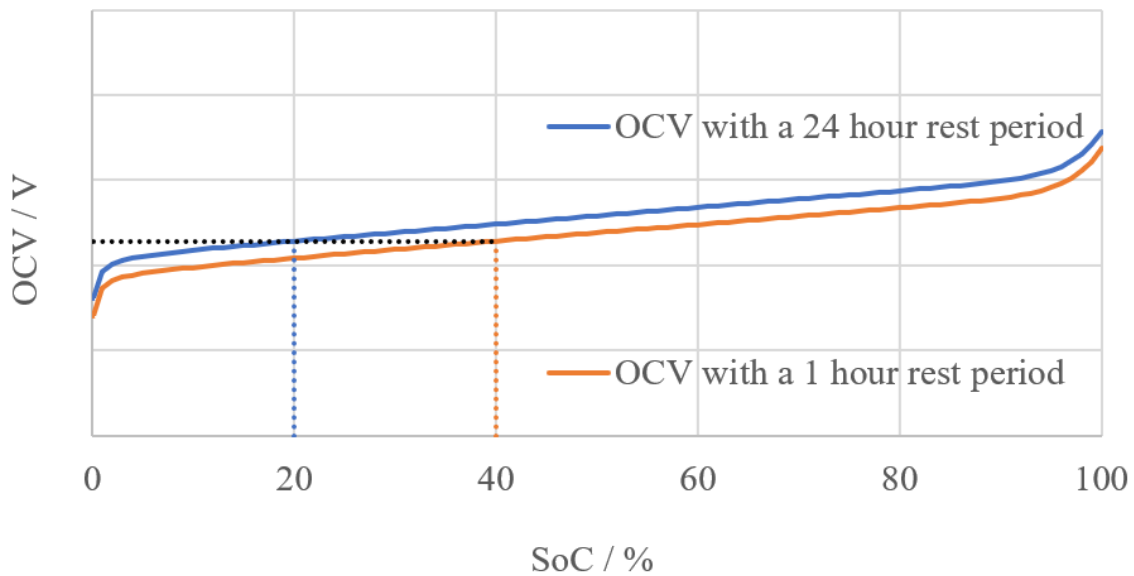


Figure 1.13. An example of an OCV-SoC calibration curve, showing a difference in rest periods before measurements are made [79].

The blue line (NMC cathode) and red line (LFP cathode) in Figure 1.14 are both for a graphite anode, the cyan line uses a LTO anode and an NMC cathode. Comparing the LFP curve to the others, it is much flatter and therefore more difficult to determine an accurate SoC from a voltage measurement, any errors in measurement will lead to a greater error in SoC estimation for this chemistry.

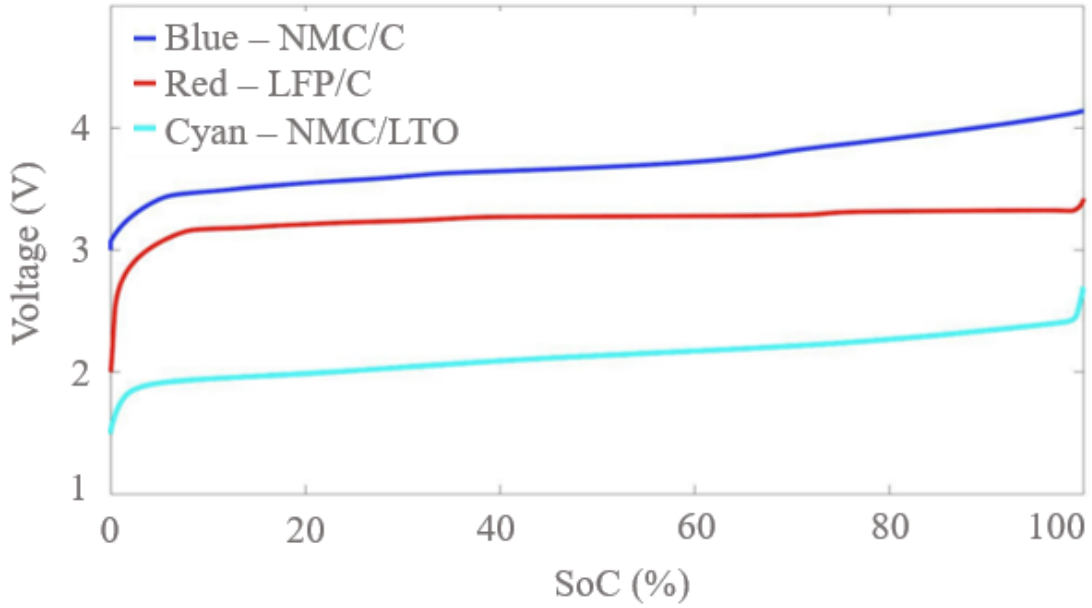


Figure 1.14. A comparison of different OCV-SoC curves for different cell chemistries, reproduced from ‘Cell state-of-charge inconsistency estimation for LiFePO₄ battery pack in hybrid electric vehicles using mean-difference model, Zheng Y, et al.’ [83].

An alternative numeric definition of SoH is in terms of the internal resistance, or impedance [68] which can be measured for both new and used cells [84]. In alternating current (AC) theory, the impedance, Z , is given by Ohm’s Law [85]:

$$Z = \frac{V}{I} \quad (4)$$

Where V is the voltage, and I is the current. The resistance R , is the specific case of (4) when applying a direct current (DC) [85]:

$$R = \frac{V}{I} \quad (5)$$

The internal resistance or impedance of a cell is that of all the components of the cell, current collectors, electrodes, separator, SEI, electrolyte, and wires [85]. When measured by DC techniques it is the internal resistance and when measured by AC techniques it is referred to as the internal impedance [86]. As the cell ages and the SoH decreases the internal resistance increases, and hence the BMS can be programmed to use this relationship to determine the cell SoH [87].

1.4.3. Physical safety systems

The physical safety systems employed at cell level in LiBs are essentially designed to cut one of the two circuits in the battery: the internal ionic circuit (movement of lithium ions) and the external, electronic circuit (movement of electrons). Physical safety systems

include shutdown separators, positive temperature coefficient thermistors (PTC), thermal fuses, safety vents, and current interrupting devices (CID).

The separator can be made of a tri-layer construction, PP-PE-PP [70]. As PE has a lower melting point than PP (135 °C, compared to 165 °C) [87, 88], it melts first as the cell increases in temperature, blocking the pores of the PP layers [89] and hence stopping the flow of ions [89] in an irreversible process [88, 90]. However, not all the PE layer melts simultaneously [91], so the cell may not completely shut down. If the temperature of the cell exceeds the higher melting point and the polymer structure collapses, this can result in internal short circuit (anode and cathode touch) which generates large quantities of heat and potentially leading to thermal runaway [92].

A PTC has a temperature dependent electrical resistance [70]. A PTC is made from conducting particles in a polymer and, as the PTC increases in temperature, it expands and the conducting particles move apart, increasing the electrical resistance [89]. For example, a Panasonic cylindrical cell was shown to have a low resistance, c.a. 1-10 m Ω [89] at the normal operating temperature of a cell. In this temperature range the PTC consumes a small amount of energy and therefore only heats up a small amount due to Joule heating [71]. As the PTC increases in temperature the resistance increased by 29.49 m Ω between 22.15 and 89.98 °C [89]. However, at higher temperatures, a phase change in the PTC occurs which increases the resistance from 11.29 Ω at 100.2 °C to 139.3 Ω at 100.6 °C, effectively shutting down the electronic circuit [89]. Once the temperature drops, the PTC returns to its original state and the cell can be cycled again [71, 89], but not indefinitely and it will ultimately fail in the high resistance state [90].

Thermal fuses can be incorporated in cells which break when either a large current passes or when the temperature of the cell rises above a set level [89]. Such fuses are typically made from an alloy of tin, bismuth, indium, and zinc to achieve the desired operating temperature [89]. A fuse is irreversibly destroyed once it breaks the circuit [88].

Safety vents are built into cells to relieve pressure if undesired internal reactions produce gas [92], preventing an explosion [89]. A weak point can be made in the casing, for example, by scoring the cap of a cylindrical cell [89]: if excess pressure builds inside the cell, the cap breaks at this point releasing the pressure [93] in a controlled way [91]. Such “blast caps” are typically made from an aluminium-ferrous alloy [71]. By attaching the vent to the cathode with a current interrupting device (CID), when the cell vents it also

breaks the connection to the cathode [71] breaking the electrical circuit. Safety vents are irreversibly destroyed once activated [94].

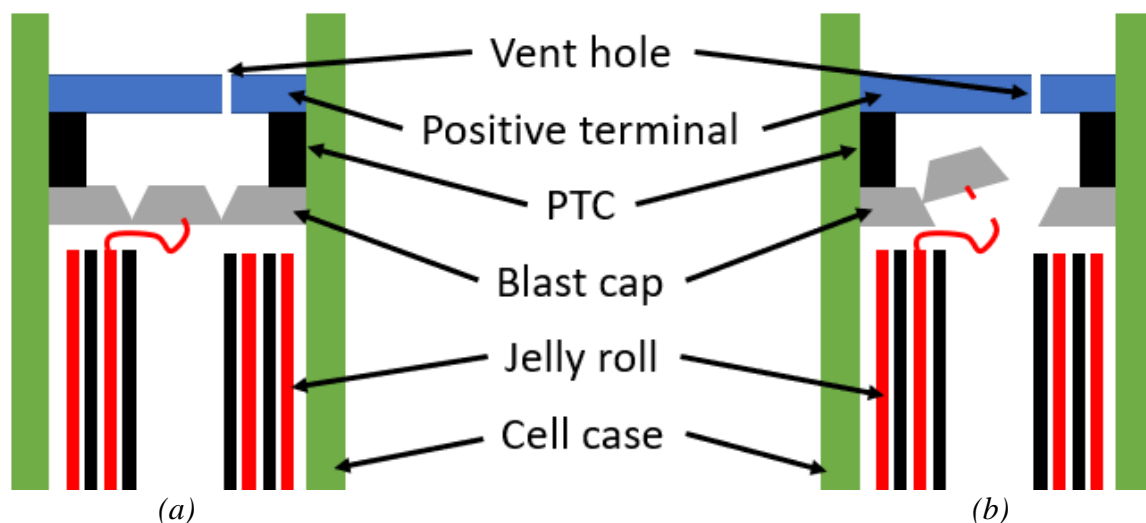
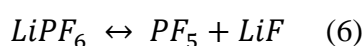


Figure 1.15. A cross section of a cylindrical cell; (a) with the blast cap in-tact; and (b) once the blast cap has operated and the electrical connection is broken.

1.4.4. Chemical additives

Chemical additives form up to 5% of the solvent, by weight or volume [13], are commercially secret [17] and are critically important to the safe function of LiBs. They have several functions: facilitating compact SEI formation [13], and/or improving the SEI structure [13], enhancing the thermal stability of LiPF_6 [13], improving the conductivity, viscosity and wettability of the solvent [13], protecting the aluminium current collector from corrosion [95], reducing the organic electrolyte solvent flammability [13], providing overcharge protection/toleration [13] and terminating cell operation under abuse conditions [13]. Some specific examples of additives are presented below.

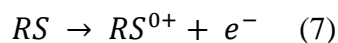
The electrolyte salt, LiPF_6 , exists in thermal equilibrium with PF_5^- [95, 96]



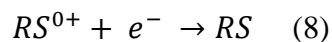
The PF_5 so produced can attack both the organic solvent [97-99] and the SEI, reducing the stability of the SEI [98, 100], producing gaseous products, such as carbon dioxide, hydrogen, oxygen, ethylene, fluoromethane and fluoroethane [96]. A simple solution to this problem exploits Le Chatelier's Principle by adding a low concentration of LiF to the electrolyte (e.g. 0.05 % wt%) to force the equilibrium (6), to the left, inhibiting the decomposition of LiPF_6 [101].

The alkyl carbonate solvents employed in lithium-ion cells are the main thermal components of these devices, and their reaction with exposed lithiated anodes and/or with the oxygen produced as the cathode structure collapse are responsible for heat and gas generation [102]. Gases such as carbon dioxide, carbon monoxide, water and heat can be produced by the exothermic oxidation of the organic electrolyte solvents [103]. The flashpoints of the typical solvents DMC, EMC and EC are 15, 22 and 33 °C respectively [70], and flame-retardant additives can be employed to lower the flammability of the electrolyte [99]. Both halogenated and non-halogenated organic phosphorous compounds have been used as flame retardant additives [70], but toxicity and environmental concerns have led to more focus on the latter [70]. The organophosphorus compounds generate radical scavenging species in fire [70, 104], which remove the hydrogen and hydroxyl radicals [70, 104] essential to maintain combustion [70, 99]. They can also act to form a char, which acts as a barrier between the liquid and gas phases to inhibit combustion [99].

The use of overcharge protection additives inherently acknowledges that BMS are fallible, and the protection is achieved using redox shuttles (RS) [102]. If the BMS malfunctions, RS can provide additional protection against overcharge [102]. These species are reversibly oxidised and reduced [102] (i.e. the shuttle is rapidly oxidised to the cation radical RS^{0+} , which in turn can be rapidly reduced back to the neutral species RS) at the cathode and anode, respectively, during charging, providing a safe ionic short circuit which converts the current supplied, to heat [105]. Once the potential of the cathode surpasses the reduction potential of the shuttle, the shuttle is oxidised [106]:

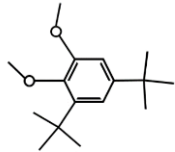
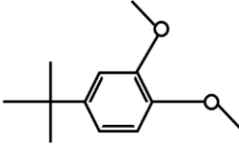
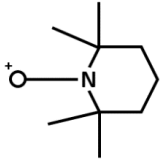
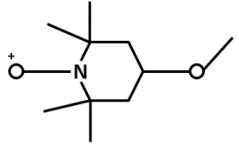
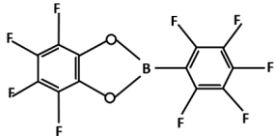


The radical cation then diffuses to the anode where it is reduced back to RS:



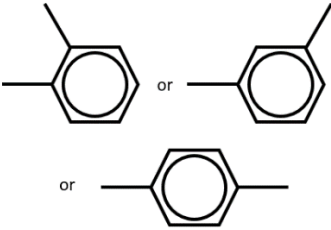
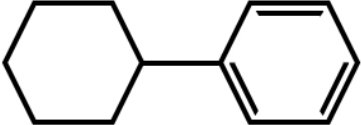
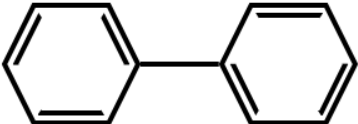
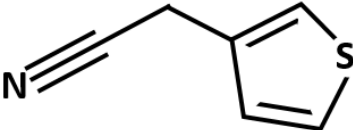
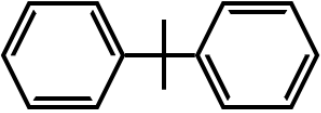
The potential of the cathode is pinned at that of the shuttle: at lower potentials, the RS is inactive [106]. Examples of redox shuttles are 3,5-di-tert-butyl-1,2-dimethoxybenzene (DBDB), 4-tert-butyl-1,2-dimethoxybenzene (TBD), 2,2,6,6-tetramethylpiperidinyloxiide (TEMPO), 4-methoxy-TEMPO, and 2-(pentafluorophenyl)-tetrafluoro-1,3,2-benzodioxaborole (PFPTFBB) [107], chemical formulas and structures are shown in **Error! Reference source not found.** Thermal runaway due to overcharge typically occurs at SoC > 140 % and hence potentials for overcharge protection can be significantly higher than the nominal voltage of the cell and range from 3.52 to 4.90 V [70].

Table 1.3. Chemical names, abbreviations, formulae, and structures for selected redox shuttles.

Name	Chemical Formula	Chemical Structure
3,5-di-tert-butyl-1,2-dimethoxybenzene (DBDB)	$C_{16}H_{26}O_2$	
4-tert-butyl-1,2-dimethoxybenzene (TBD)	$C_{12}H_{18}O_2$	
2,2,6,6-tetramethylpiperidinyloxiide (TEMPO)	$C_9H_{18}NO$	
4-methoxy-TEMPO	$C_{10}H_{20}NO_2$	
2-(pentafluorophenyl)-tetrafluoro-1,3,2-benzodioxaborole (PFPTFBB)	$C_{12}BF_9O_2$	

Shutdown additives are oxidised at high potentials to release a gas [90] (typically CO_2) which triggers a CID [70] [90] or a safety vent: they may also polymerize on the cathode surface [70] to prevent further overcharge [70]. Examples of these species include xylene, cyclohexylbenzene, biphenyl, 3-thiopheneacetonitrile, and 2-2-diphenylpropane [70], chemical formulas and structures are shown in **Error! Reference source not found.**

Table 1.4. Chemical names, abbreviations, formulas, and structures for selected shutdown additives.

Name	Chemical Formula	Chemical Structure
xylene	C_8H_{10}	
cyclohexylbenzene	$C_{12}H_{16}$	
biphenyl	$C_{12}H_{10}$	
3-thiopheneacetonitrile	C_6H_5NS	
2-2-diphenylpropane	$C_{15}H_{16}$	

1.5. Thermal runaway of cells

Thermal runaway has been quoted in the literature as: “A process of uncontrolled heat release and rapid temperature rise.” [108], “The cell condition where the internal cell reactions generate more thermal heat than the cell can dissipate. The condition causes cell venting and premature failure”[108], “.... in some cases, the temperature rises to very high levels at which the structure of the battery fails. This phenomenon is called Thermal-runaway” [109], and “Thermal runaway refers to the situation in which the battery temperature rises uncontrollably due to the heat generated by the mutual reactions of battery components.” [110].

The first two quotes are from different chapters in the same book, the first only mentions the rapid temperature rise but the second only mentions the production of more heat than

can be dissipated, which could be a slow temperature rise. Also, there is no definition of ‘rapid’ in the first quote. The third quote mentions a high temperature, again without any numerical value, but does not state if this must be rapid or a slow temperature rise can commence thermal runaway. The fourth quote gives a better definition of what temperature rise is necessary and a reason, although, it may be difficult to ascertain if the temperature rise is indeed uncontrollable and due to the reactions of the components when the cell is in use. The four quotes show that a clear definition of thermal runaway is not yet agreed in the academic literature: further, most academic papers do not include a definition of thermal runaway [111] when discussing it. Hence comparisons of thermal runaway between different research groups becomes challenging.

The problem with defining the onset of thermal runaway is the balance between the most accurate definition and what can be measured with the required precision. The simplest definition is when a clear rise in temperature can be measured, which occurs once the heat generated by thermal runaway is produced faster than it can be dissipated: this is usually expressed as a rate of temperature rise, with values from 1 °C s⁻¹ [112, 113] to 1 °C min⁻¹ [114] often quoted, but can be as low as 10 °C min⁻¹ for lower energy density LFP cells [113]. Such a definition is not very useful in real life applications, as the cell will be undergoing thermal runaway before the onset is measured, due to the time lag of the heat energy conducting from the inside of the cell to the external surface. In addition, the minimum detectable rate of temperature increase will be dependent on the equipment employed. A more accurate definition of thermal runaway is when the exothermic reactions in the cell become self-sustaining, but this is far more difficult to detect and measure.

The rate constant for the reaction responsible for the heat generated in a chemical process increases exponentially with temperature as represented by the Arrhenius Law:

$$k_{generation} = A_{generation} e^{\frac{-E_a}{RT}} \quad (9)$$

Where $k_{generation}$ is the reaction rate constant, $A_{generation}$ is the pre-exponential factor, E_a is the activation energy (J mol⁻¹), R is the universal gas constant (8.314 J mol⁻¹ K⁻¹) and T is the temperature (K). As the reaction rate increases, the heat generation rate (Q (J s⁻¹)) increases. However, heat dissipation (q) does not grow as quickly as the temperature of the cell increases. A plot of heat generation rate and heat dissipation rate as a function of temperature is shown in Figure 1.16 to illustrate this.

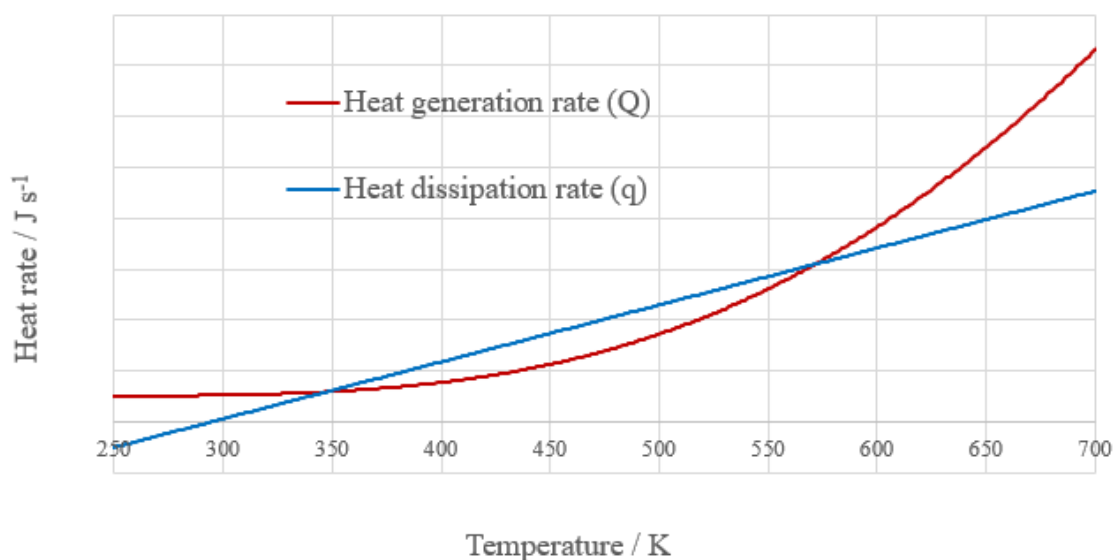


Figure 1.16. Heat generation and heat dissipation (for illustration purposes).

There are four sections in Figure 1.16, the first is for temperatures below 295 K (set as the ambient temperature), here the heat dissipation rate is negative, meaning that heat will flow from the surroundings to the cell. The second region is for temperatures between 295 and 347 K, here the heat generation rate is greater than the heat dissipation rate, meaning the cell will increase in temperature. The third region is for temperatures between 347 and 572 K, here the heat dissipation rate is greater than the generation rate, meaning that if the cell is at any temperature in this region it will cool under normal operating conditions. The fourth region is for temperatures above 572 K, here the heat generation rate is greater than the dissipation rate, meaning the cell will rise in temperature, causing a greater increase in heat generation than heat dissipation, which causes another temperature increase. When this cycle is self-sustaining, thermal runaway has commenced.

1.6. Abuse and malfunction of cells causing thermal runaway

The malfunction of a safety system or the abuse of a lithium-ion cell can cause thermal runaway and these malfunctions/abuses are generally categorised into three types: thermal, electrical, and mechanical.

1.6.1. Thermal abuse

If a cell is thermally abused by an external heating source, thermal runaway commences, as the SEI starts to decompose c.a. 80 °C [102], although it can regenerate, with SEI regeneration and decomposition rates equal up to c.a. 250 °C [102], albeit with a less

compact layer [113]. The solvent components of the electrolyte vaporise at temperatures from 77 to 248 °C, see **Error! Reference source not found.**

Table 1.5. The boiling points for common electrolyte solvents [115].

Solvent	Molecular Formula	Boiling Point / °C
Ethyl Acetate (EA)	C ₄ H ₈ O ₂	77
DiMethyl Carbonate (DMC)	C ₃ H ₆ O ₃	91
Ethyl Methyl Carbonate (EMC)	C ₄ H ₈ O ₃	110
DiEthyl Carbonate (DEC)	C ₅ H ₁₀ O ₃	126
Propylene Carbonate (PC)	C ₄ H ₆ O ₃	242
Ethylene Carbonate (EC)	C ₃ H ₄ O ₃	248

The vaporisation of the solvent will cause either vent caps to blow (prismatic and cylindrical cells) or cell rupture (pouch cells) to relieve the pressure, releasing electrolyte vapour and liquid electrolyte droplets [116], which can ignite in the presence of an ignition source. At 130 °C the PE separator melts and clogs the pores of the PP separator (stopping the movement of lithium ions): the PP melts at 165 °C and both processes involve an endothermic phase change, which temporarily slows down the temperature rise. With no separator separating the electrodes a massive internal short circuit occurs, the electrodes begin to decompose, and solid particles are ejected from the cell [116], these can be a source of ignition [117]. The solid particles are mainly comprised of carbon (68.0 - 69.0 % by weight), small organic molecular chemicals, carbonate, metal and metal oxide, c.a. 8.49 - 300.00 µm [118].

1.6.2. Electrical abuse

Electrical abuse can be in three forms: overcharging, an internal short circuit and over discharging, all leading to thermal runaway.

A cell can be overcharged (charging the cell to greater than 100 % SoC [119]) by a malfunctioning charger, an incorrect SoC estimation by the BMS [119], or by incorrect cell balancing [120]. During overcharging the internal resistance of the cell increases by a multiple between 5 and 7 [121] which produces heat by Joule's first law: $Q = I^2Rt$ where Q is the heat generated (J), I is the electrical current (amps), R is the electrical resistance (Ohms) [119], and t is time (seconds). As overcharging continues, the lithium in the cathode de-intercalates below the lower safe limit, using LCO as an example, the lower safe limit of lithium is 0.45 (Li_{0.45}CoO₂) as mentioned in SChapter 1744125919ection 1.2, and the structure begins to exothermically collapse [119], oxygen

from the cathode is released and exothermically oxidises the organic electrolyte solvents [122], producing carbon dioxide, carbon monoxide, water and heat [101, 103], as mentioned in Section 1.4.4. The remaining oxygen can react with the lithiated anode, heating the cell to c.a. 700 °C [122]. When the temperature of the cell is sufficiently high, the electrolyte will vaporise and can combust in the presence oxygen [120], producing carbon dioxide and water vapour (complete combustion). Before the amount of gas generated is enough to burst a safety vent or rupture the cell, the excess lithium de-intercalated from the cathode, migrates to the anode, which is at its stoichiometric limit (LiC_6) and is reduced to metallic lithium on the surface of the anode [119]. The lithium metal then reacts exothermically with the organic electrolyte at elevated temperatures generating heat and gases [119] such as POF_3 and organophosphates [123]. The exothermic reactions increase in rate as described in Section 1.5. The gas produced builds up inside the cell until the pressure is sufficient to either burst a safety vent or rupture the cell [119, 124, 125], any unreacted lithium metal deposited on the anode will now be exposed to the air, and moisture in the air reacts with the metallic lithium, producing more heat [119]. When the cell bursts, droplets of the flammable electrolyte and hydrocarbons are released [124] which can subsequently ignite in the presence of an ignition source [126]. The ignition source can be hot ejected particles from the cell, such as fragments of electrodes [125] or an electric arc [126].

A cell can develop an internal short circuit from an internal manufacturing defect, such as a fragment of metal on the cut edge of an electrode, a particle in the electrolyte, or a defect in the separator [20]. An abuse event can introduce an internal short circuit to a cell, for example, in a high-speed electric vehicle accident, an electrically conductive object can pierce the cell and short circuit the electrodes [20]. When the electrodes are in a low resistance electrical connection, Joule heating occurs due to the large current, and electrical resistance of metals increases with temperature [127], generating more heat per Coulomb of charge, reaching a maximum heat generation rate when the internal short circuit resistance matches the resistance of the cell [128]. The heat produced causes the rate of exothermic reactions to increase, generating more heat as described in Section 1.5 and thermal runaway occurs.

A cell can be over discharged, by being the weakest cell in a string of series connected cells and the BMS fails to monitor it properly [102], or a failure of the BMS [20]. The lithium content of the anode reduces to zero (C_6) and the SEI layer begins to breakdown,

releasing heat and gases [20], such as, carbon dioxide and carbon monoxide [102]. Then, as the over discharging continues, the copper current collector of the anode begins to dissolve into the electrolyte and deposit on the surface of the cathode [102], which grows into dendrites as more copper gets deposited [20], until a dendrite breaches the separator and creates an internal short circuit [20]. When the cell is next charged, thermal runaway can occur [103], due to the presence of an internal short circuit.

1.6.3. Mechanical abuse

Mechanical abuse is, for example, the crushing of a cell. When a cell is crushed, the separator can develop a fault (tear or crack [128]), creating a place where the electrodes can touch, and thermal runaway can commence as described in Section 1.6.2.

1.7. Accidents and scope (BEIS)

There have been many recorded incidents of thermal runaway of lithium ion batteries to date, a selection is listed in Tables 1.6 to 1.10.

Table 1.6. A brief list of some notable portable equipment lithium-ion safety incidents.

Line	Date	Location	Application	Damages / Injuries / Deaths / Costs	Ref
1	2009 - 2016	USA	Electronic cigarettes	133 injuries 38 seriously injured	[129, 130]
2	31/10/2014	At sea	10" pipeline corrosion monitor	4 people injured	[131]
3	2016	Worldwide	Samsung Galaxy Note 7	\$4 Billion (direct) \$20 Billion (reputational)	[132, 133]

In Table 1.6, line 1, a Michigan, USA, law firm reported “*The U.S. Fire Administration reported at least 195 incidents of e-cigarette devices exploding or starting fires between 2009 and 2016. These incidents produced 133 injuries, and 38 cases involved severe injuries.*”. This shows that not only are the authorities in the U.S. monitoring and recording lithium-ion portable electronic fires, but lawyers are also looking to file lawsuits against manufacturers for damages. In line 2, International Marine Contractors Association reported that one of their members suffered an explosion of a pipeline corrosion monitor, photographs of the event are available in the reference, some flying debris managed to puncture a safety helmet, injuring the worker and 3 others. In line 3, Samsung recalled 2.5 million Galaxy Note 7 smartphones on the 2nd of September 2016,

as they determined there was a fire and explosion risk with the installed lithium-ion batteries, the U.S authorities were involved by the 8th of September 2016 telling people not to turn on or charge these phones on planes, the next day they told people to stop using the phones completely. After a costly recall, on the 11th of October 2016, Samsung told people to turn off the phones and stop using them, later Samsung had to send an update to phones that were not returned which limited or prevented their charging.

Table 1.7. A brief list of some notable electric vehicle lithium-ion safety incidents.

Line	Date	Location	Application	Damages / Injuries / Deaths / Costs	Ref
1	17/11/2010	Pearl of Scandinavia Ferry enroute from Oslo to Copenhagen	Nissan Qashqai (converted by owner)	No injuries or deaths, 2 cars and 3 trailers burnt, ships car deck damaged,	[134]
2	06/06/2011	MGA Research, Wisconsin, USA	GM Chevrolet Volt	No injuries or deaths	[135]
3	29/10/2012	New Jersey, USA	3 Toyota Prius's and 16 Fisker Karma's	No injuries or deaths, more than a million dollars of damage	[136]
4	08/05/2018	Fort Lauderdale, Florida, USA	Tesla Model S	2 deaths, 1 injury	[137]
5	01/06/2019	Antwerp, Belgium	Tesla Model S	No injuries or deaths	[138]

In Table 1.7, line 1, the Division for Investigation of Maritime Accidents, now the Danish Maritime Authority, investigated a fire on the Pearl of Scandinavia. A car converted by the owner, was charging on the car deck of the ferry, using a cable that the owner converted for the Norwegian electrical system, and ignited. The fire spread due to red-hot metal fragments flying to other compartments of the ferry. Four firefighting teams took over 3 hours to extinguish the fire. In line 2, a Chevrolet Volt that was deliberately crashed in a safety test spontaneously ignited 3 weeks later, while at a storage facility. In line 3, storm Sandy flooded a parking lot with salt water, although this incident is due to an extreme weather event, it does highlight the susceptibility of electric vehicles to fire, with one electric vehicle causing a cascade of fires, 19 vehicles in total. In line 4, an electric vehicle driven at a reported 116 mph in a 25 mph zone, crashed and caught fire, killing the driver and a passenger, the fire was extinguished but re-ignited as it was being removed from the scene and again whilst at a storage yard. In line 5, a Tesla electric

vehicle caught fire while being charged with a supercharger, what is of note is that the fire service, worried about re-ignition, put the car in a water tank overnight.

Table 1.8. A brief list of some notable aviation lithium-ion safety incidents.

Line	Date	Location	Application	Damages / Injuries / Deaths / Costs	Ref
1	07/01/2013	Worldwide	Boeing Dreamliner	No injuries or deaths	[139]
2	14/08/2019	Norway	Alpha Electro G2	No injuries or deaths	[140]
3	2006 - 2022	USA	All aircraft	354 incidents	[141]

In Table 1.8, line 1, Boeing’s new Dreamliner aeroplane fleet was grounded by the FAA, after two incidents with the on-board lithium-ion batteries, one at Boston Logan Airport and one on a plane shortly after take-off. In line 2, an electric Pipistrel plane lost power and crash landed into a lake. In line 3, up to the 25th of February 2022 the FAA has recorded 354 incidents involving lithium-ion batteries, noting that the FAA is not aware of all incidents.

Table 1.9 A brief list of some notable recycling facility lithium-ion safety incidents.

Line	Date	Location	Application	Damages / Injuries / Deaths / Costs	Ref
1	14/08/2002	Clarence, New York, USA	Recycling	No injuries or deaths, no costs reported	[142]
2	23/04/2017	Houston, Texas, USA	Batteries being transported	No injuries or deaths, house damaged	[139]
3	2017	USA & UK	Recycling	8 injuries, 3 deaths	[143]

In Table 1.9, line 1, a 68 gallon drum filled with lithium-ion batteries caught fire, believed to be due to short circuits between batteries. In line 2, a container on a train filled with lithium-ion batteries ignited and exploded, a house 350 feet away suffered damage from the explosion. In line 3, a recycling magazine summarised that there have been 289 reported incidents in 2017 of lithium-ion battery fires in USA recycling facilities, but they believe the true figure to be above 1,500, they also state that there were an average of 332 fires at UK facilities per year between 2001 and 2014.

Table 1.10. A brief list of some notable Battery Energy Storage Systems (BESS) lithium-ion safety.

Line	Date	Location	Application	Damages / Injuries / Deaths / Costs	Ref
1	03/08/2012	Kahuku, Hawaii, USA	30 MW BESS, 15 MW battery	No injuries or deaths reported	[144]
2	10/08/2016	Franklin, Wisconsin, USA	BESS	No injuries or deaths reported	[139]
3	03/03/2019	Seoul, South Korea	23 BESS installations	No injuries or deaths reported	[145]
4	19/04/2019	Surprise, Arizona, USA	BESS	Several injuries to first responders	[146]

In Table 1.10, line 1, firefighters had previous experience at this BESS, allowing a fire to burn out in April 2011 and attending another in May 2012, their experience gave them caution to the toxicity of the fire. Line 2, a fire started and spread to the batteries, producing large amounts of smoke, and taking several hours to control the fire, it is of note that the batteries were fuel for the fire and present a hazard even when not in use. Line 3, the government in South Korea suspended operations at 522 of the nation's 1490 BESS after 23 fires at BESS's in the country. Line 4, after a smoke alarm is triggered and an inbuilt fire suppression system is activated, firefighters wait c.a. 3 hours before opening the door to the BESS, when it exploded, blowing the firefighters away and one through a chain link fence, traces of contaminants, such as, HCN were found on an officers clothing.

1.8. Summary of Chapter

This Chapter began with the fundamentals of how LiBs are constructed and operated. It then introduced safety systems and benefits that are inherent to LiBs and utilised by manufactures. A discussion of thermal runaway was followed by its general causes, and finally notable safety incidents that have occurred.

1.9. Outline of Thesis

Chapter 2 describes the four sets of experiments undertaken and equipment employed during this PhD. The final set of experiments at Durham and Darlington Fire and Rescue Services (DDFRS) are not discussed in detail due to space limitations.

Chapter 3 begins with the first set of thermal and mechanical abuse experiments at DNV GL (DNV 1). The effect of different nail positions when penetrating a module on thermal runaway was assessed. Valuable experience was gained from these with respect to operating procedures and test equipment placement. These led to an investigation into the effect of SoC on thermal runaway, and the second set of experiments at Fire Services College generated the realisation of the importance of the emitted white vapour at low SoC.

Chapter 4 begins with the first set of electronic abuse experiments at DNV 1 then builds on Chapter 3 with experiments that attempted to ignite the emitted white vapour from a mechanically abused lithium-ion module in an enclosed environment.

Chapter 5 introduces a novel method for determining the Heat Release Rate (HRR) from a lithium-ion fire. It builds on the measurements made by optical videos in Chapter 3, providing a more accurate analysis of the flames by use of a calibration box and constantly re-calibrated images.

Chapter 6 is the report that was commissioned by the Office of Product Safety and Standards of the Department of Business Energy & Industrial Strategy (BEIS) on The Safety of Second-life Batteries in Battery Energy Storage Systems.

Chapter 7 sets future work which will be complimentary to this Thesis.

1.10. References

1. Wu, W., et al., Experimental investigation on the thermal performance of heat pipe-assisted phase change material based battery thermal management system. *Energy Conversion and Management*, 2017. 138: p. 486-492.
2. Kim, T., et al., Lithium-ion batteries: outlook on present, future, and hybridized technologies. *Journal of materials chemistry A*, 2019. 7(7): p. 2942-2964.
3. Pillot, C. The rechargeable battery market and main trends 2018-2030. in 36th annual international battery seminar & exhibit. avicenne energy. 2019.
4. Lebedeva, N., Li-ion batteries for mobility and stationary storage applications. Publications Office of the European Union, 2018.
5. Skeete, J.-P., et al., Beyond the Event horizon: Battery waste, recycling, and sustainability in the United Kingdom electric vehicle transition. *Energy Research & Social Science*, 2020. 69: p. 101581.

6. Diouf, B. and R. Pode, Potential of lithium-ion batteries in renewable energy. *Renewable Energy*, 2015. 76: p. 375-380.
7. Shin, D., et al., A statistical model-based cell-to-cell variability management of lithium-ion battery pack. *IEEE Transactions on Computer-Aided Design of Integrated Circuits and Systems*, 2014. 34(2): p. 252-265.
8. Saw, L.H., Y. Ye, and A.A. Tay, Integration issues of lithium-ion battery into electric vehicles battery pack. *Journal of Cleaner Production*, 2016. 113: p. 1032-1045.
9. Manthiram, A., An outlook on lithium ion battery technology. *ACS central science*, 2017. 3(10): p. 1063-1069.
10. Vuorilehto, K., *Lithium-ion batteries: basics and applications*, ed. R. Korthauer. 2018: Springer.
11. Roth, C.J.W.M., *Lithium-ion batteries: basics and applications*, ed. R. Korthauer. 2018: Springer.
12. Zhang, S., et al., LiPF₆-EC-EMC electrolyte for Li-ion battery. *Journal of Power Sources*, 2002. 107(1): p. 18-23.
13. Zhang, S.S., A review on electrolyte additives for lithium-ion batteries. *Journal of Power Sources*, 2006. 162(2): p. 1379-1394.
14. Zhu, P., et al., A review of current collectors for lithium-ion batteries. *Journal of Power Sources*, 2021. 485: p. 229321.
15. Lain, M.J., J. Brandon, and E. Kendrick, Design strategies for high power vs. high energy lithium ion cells. *Batteries*, 2019. 5(4): p. 64.
16. Johnson, C.S., Charging Up lithium-ion battery cathodes. *Joule*, 2018. 2(3): p. 373-375.
17. Asenbauer, J., et al., The success story of graphite as a lithium-ion anode material—fundamentals, remaining challenges, and recent developments including silicon (oxide) composites. *Sustainable Energy & Fuels*, 2020. 4(11): p. 5387-5416.
18. Roth, E., D. Doughty, and J. Franklin, DSC investigation of exothermic reactions occurring at elevated temperatures in lithium-ion anodes containing PVDF-based binders. *Journal of power sources*, 2004. 134(2): p. 222-234.
19. Zhang, W.-J., A review of the electrochemical performance of alloy anodes for lithium-ion batteries. *Journal of Power Sources*, 2011. 196(1): p. 13-24.

20. Zhang, G., et al., Internal short circuit mechanisms, experimental approaches and detection methods of lithium-ion batteries for electric vehicles: A review. *Renewable and Sustainable Energy Reviews*, 2021. 141: p. 110790.
21. Jang, J., et al., A review of functional separators for lithium metal battery applications. *Materials*, 2020. 13(20): p. 4625.
22. Zhong, S., et al., Recent progress in thin separators for upgraded lithium ion batteries. *Energy Storage Materials*, 2021. 41: p. 805-841.
23. Schröder, R., M. Aydemir, and G. Seliger, Comparatively assessing different shapes of lithium-ion battery cells. *Procedia Manufacturing*, 2017. 8: p. 104-111.
24. Kisters, T., E. Sahraei, and T. Wierzbicki, Dynamic impact tests on lithium-ion cells. *International Journal of Impact Engineering*, 2017. 108: p. 205-216.
25. Woehrle, T., *Lithium-ion batteries: basics and applications*, ed. R. Korthauer. 2018: Springer.
26. Liu, B., et al., Safety issues and mechanisms of lithium-ion battery cell upon mechanical abusive loading: A review. *Energy Storage Materials*, 2020. 24: p. 85-112.
27. Gerlitz, E., et al., Analysis of the variety of lithium-ion battery modules and the challenges for an agile automated disassembly system. *Procedia CIRP*, 2021. 96: p. 175-180.
28. Li, S., et al., Optimal cell tab design and cooling strategy for cylindrical lithium-ion batteries. *Journal of Power Sources*, 2021. 492: p. 229594.
29. Yao, X.-Y. and M.G. Pecht, Tab design and failures in cylindrical Li-ion batteries. *IEEE Access*, 2019. 7: p. 24082-24095.
30. Tagawa, K. and R.J. Brodd, Production processes for fabrication of lithium-ion batteries. *Lithium-ion batteries: Science and technologies*, 2009: p. 181-194.
31. Dell, R. and D.A.J. Rand, *Understanding batteries*. 2001: Royal society of chemistry.
32. Halimah, P.N., S. Rahardian, and B.A. Budiman, Battery cells for electric vehicles. *International Journal of Sustainable Transportation Technology*, 2019. 2(2): p. 54-57.
33. Casals, L.C. and B.A. García. A review of the complexities of applying second life electric car batteries on energy businesses. in *Energy Syst. Conf.* 2014.
34. G. Reinhart, T.Z., J. Kurfer, M. Westermeier, C. Thiemann, M. Glonegger et al, *Future Trends in Production Engineering*. Proceedings of the First Conference of

- the German Academic Society for Production Engineering (WGP), Berlin, Germany, 8th-9th June 2011, ed. G. Schuh, Neugebauer, R. and Uhlmann, E. 2011: Springer Science & Business Media.
35. Sumol V. Gopinadh, V.A., Md. Jamal Nawaz Ansari, Deepak Srivastava, Arjun Raj M., Bibin John , Aiswarya Samridh, P. S. Vijayakumar, and T. D. Mercy, Lithium-Ion Pouch Cells: An Overview. Energy Harvesting and Storage Fundamentals and Materials, ed. M.K. Jayaraj, A. Antony, and P.P. Subha. 2022: Springer Nature Singapore Pte Ltd.
 36. Liu, Z., et al., Safer Lithium-Ion Batteries from the Separator Aspect: Development and Future Perspectives. ENERGY & ENVIRONMENTAL MATERIALS, 2021. 4: p. 336-362.
 37. Jones, F.O. and K.O. Wood, The melting point of thin aluminium films. British Journal of Applied Physics, 1964. 15(2): p. 185.
 38. Pepin, J., V. Miri, and J.-M. Lefebvre, New insights into the Brill transition in polyamide 11 and polyamide 6. Macromolecules, 2016. 49(2): p. 564-573.
 39. Ceder, G., A. Van der Ven, and M.K. Aydinol, Lithium-intercalation oxides for rechargeable batteries. JOM, 1998. 50(9): p. 35-40.
 40. Aurbach, D., et al., A short review of failure mechanisms of lithium metal and lithiated graphite anodes in liquid electrolyte solutions. Solid state ionics, 2002. 148(3-4): p. 405-416.
 41. Julien, C., et al., Lithium batteries. 2016: Springer.
 42. Jeon, Y., H.K. Noh, and H.-K. Song, A lithium-ion battery using partially lithiated graphite anode and amphi-redox LiMn₂O₄ cathode. Scientific reports, 2017. 7(1): p. 14879.
 43. Lyu, Y., et al., An overview on the advances of LiCoO₂ cathodes for lithium-ion batteries. Advanced Energy Materials, 2021. 11(2): p. 2000982.
 44. Blum, A.F. and R.T. Long, Fire Hazard Assessment of Lithium Ion Battery Energy Storage Systems. 2016, SpringerBriefs in Fire: Springer.
 45. Richardson, G., G. Denuault, and C. Please, Multiscale modelling and analysis of lithium-ion battery charge and discharge. Journal of Engineering Mathematics, 2012. 72: p. 41-72.
 46. Zhang, Z., et al., A Review on Electrode Materials of Fast-Charging Lithium-Ion Batteries. The Chemical Record, 2022. 22(10): p. e202200127.

47. Ceder, G., Opportunities and challenges for first-principles materials design and applications to Li battery materials. *MRS bulletin*, 2010. 35(9): p. 693-701.
48. Burrows, A., et al., *Chemistry3: Introducing inorganic, organic and physical chemistry*. 2021: Oxford university press, p735.
49. Yoshino, A., K. Sanechika, and T. Nakajima, SECONDARY BATTERY, U.S. Patent, Editor. 1987, Asahi Kasei Kogyo Kabushiki Kaisha: United States. p. 25.
50. Bredas, J.-L., et al., An electrifying choice for the 2019 chemistry Nobel Prize: Goodenough, Whittingham, and Yoshino. 2019, ACS Publications. p. 8577-8581.
51. Jow, T.R., et al., *Electrolytes for lithium and lithium-ion batteries*. Vol. 58. 2014: Springer.
52. Scrosati, B., History of lithium batteries. *Journal of solid state electrochemistry*, 2011. 15(7-8): p. 1623-1630.
53. Hardman, S., E. Shiu, and R. Steinberger-Wilckens, Changing the fate of Fuel Cell Vehicles: Can lessons be learnt from Tesla Motors? *international journal of hydrogen energy*, 2015. 40(4): p. 1625-1638.
54. Sanders, M. Lithium-ion battery raw material supply and demand 2016–2025. in Document presentado en the “Advanced Automotive Battery Conference”, San Francisco. 2017.
55. Yang, C., et al., 4.0 V aqueous Li-ion batteries. *Joule*, 2017. 1(1): p. 122-132.
56. Li, N.W., et al., An artificial solid electrolyte interphase layer for stable lithium metal anodes. *Advanced materials*, 2016. 28(9): p. 1853-1858.
57. Flandrois, S. and B. Simon, Carbon materials for lithium-ion rechargeable batteries. *Carbon*, 1999. 37(2): p. 165-180.
58. Gachot, G., et al., Thermal behaviour of the lithiated-graphite/electrolyte interface through GC/MS analysis. *Electrochimica acta*, 2012. 83: p. 402-409.
59. Takenaka, N., et al., Frontiers in theoretical analysis of solid electrolyte interphase formation mechanism. *Advanced Materials*, 2021. 33(37): p. 2100574.
60. Barcellona, S. and L. Piegari, Effect of current on cycle aging of lithium ion batteries. *Journal of Energy Storage*, 2020. 29: p. 101310.
61. Collins, J., et al., Carbon surface functionalities and SEI formation during Li intercalation. *Carbon*, 2015. 92: p. 193-244.
62. An, S.J., et al., The state of understanding of the lithium-ion-battery graphite solid electrolyte interphase (SEI) and its relationship to formation cycling. *Carbon*, 2016. 105: p. 52-76.

63. Okuno, Y., et al., Decomposition of the fluoroethylene carbonate additive and the glue effect of lithium fluoride products for the solid electrolyte interphase: an ab initio study. *Physical Chemistry Chemical Physics*, 2016. 18(12): p. 8643-8653.
64. Kranz, S., et al., Is the solid electrolyte interphase in lithium-ion batteries really a solid electrolyte? Transport experiments on lithium bis (oxalato) borate-based model interphases. *Journal of Power Sources*, 2019. 418: p. 138-146.
65. Verma, P., P. Maire, and P. Novák, A review of the features and analyses of the solid electrolyte interphase in Li-ion batteries. *Electrochimica Acta*, 2010. 55(22): p. 6332-6341.
66. Sun, P., et al., A review of battery fires in electric vehicles. *Fire technology*, 2020. 56: p. 1361-1410.
67. Li, Z., et al., On state-of-charge determination for lithium-ion batteries. *Journal of Power Sources*, 2017. 348: p. 281-301.
68. Huria, T., G. Ludovici, and G. Lutzemberger, State of charge estimation of high power lithium iron phosphate cells. *Journal of Power Sources*, 2014. 249: p. 92-102.
69. Yang, S., et al., Review on state-of-health of lithium-ion batteries: Characterizations, estimations and applications. *Journal of Cleaner Production*, 2021. 314: p. 128015.
70. Chombo, P.V. and Y. Laonual, A review of safety strategies of a Li-ion battery. *Journal of Power Sources*, 2020. 478: p. 228649.
71. Venkatapathy, K., E. Tazelaar, and B. Veenhuizen. A systematic identification of first to second life shift-point of lithium-ion batteries. in *2015 IEEE Vehicle Power and Propulsion Conference (Vppc)*. 2015. IEEE.
72. Fathi, M., *Integrated systems: Innovations and applications*. 2015: Springer.
73. Qi, J. and D.D.-C. Lu. Review of battery cell balancing techniques. in *2014 Australasian Universities Power Engineering Conference (AUPEC)*. 2014. IEEE.
74. Hannan, M.A., et al., A review of lithium-ion battery state of charge estimation and management system in electric vehicle applications: Challenges and recommendations. *Renewable and Sustainable Energy Reviews*, 2017. 78: p. 834-854.
75. Tekkök, S.Ç., et al. The Application of Kalman Filter for Lead-Acid Battery State of Charge Estimation. in *2021 8th International Conference on Electrical and Electronics Engineering (ICEEE)*. 2021. IEEE.

76. Sepasi, S., R. Ghorbani, and B.Y. Liaw, Inline state of health estimation of lithium-ion batteries using state of charge calculation. *Journal of Power Sources*, 2015. 299: p. 246-254.
77. Huang, S.-C., et al., An online SOC and SOH estimation model for lithium-ion batteries. *Energies*, 2017. 10(4): p. 512.
78. Awadallah, M.A. and B. Venkatesh, Accuracy improvement of SOC estimation in lithium-ion batteries. *Journal of Energy Storage*, 2016. 6: p. 95-104.
79. Farmann, A. and D.U. Sauer, A study on the dependency of the open-circuit voltage on temperature and actual aging state of lithium-ion batteries. *Journal of Power Sources*, 2017. 347: p. 1-13.
80. Li, A., et al., Fast characterization method for modeling battery relaxation voltage. *Batteries*, 2016. 2(2): p. 7.
81. Lin, C., Q. Yu, and R. Xiong, A study on the impact of open circuit voltage tests on state of charge estimation for lithium-ion batteries. *Applied Energy*, 2017. 205: p. 892-902.
82. Xiong, R., Q. Yu, and C. Lin, A novel method to obtain the open circuit voltage for the state of charge of lithium ion batteries in electric vehicles by using H infinity filter. *Applied energy*, 2017. 207: p. 346-353.
83. Zheng, Y., et al., Cell state-of-charge inconsistency estimation for LiFePO₄ battery pack in hybrid electric vehicles using mean-difference model. *Applied energy*, 2013. 111: p. 571-580.
84. Waag, W., S. Käbitz, and D.U. Sauer, Experimental investigation of the lithium-ion battery impedance characteristic at various conditions and aging states and its influence on the application. *Applied energy*, 2013. 102: p. 885-897.
85. Choi, W., et al., Modeling and applications of electrochemical impedance spectroscopy (EIS) for lithium-ion batteries. *Journal of Electrochemical Science and Technology*, 2020. 11(1): p. 1-13.
86. Schweiger, H.-G., et al., Comparison of several methods for determining the internal resistance of lithium ion cells. *Sensors*, 2010. 10(6): p. 5604-5625.
87. Haifeng, D., W. Xuezhe, and S. Zechang. A new SOH prediction concept for the power lithium-ion battery used on HEVs. in 2009 IEEE vehicle power and propulsion conference. 2009. IEEE.
88. Venugopal, G., Characterization of thermal cut-off mechanisms in prismatic lithium-ion batteries. *Journal of Power Sources*, 2001. 101(2): p. 231-237.

89. Xu, B., et al., Mitigation strategies for Li-ion battery thermal runaway: A review. *Renewable and Sustainable Energy Reviews*, 2021. 150: p. 111437.
90. Balakrishnan, P., R. Ramesh, and T.P. Kumar, Safety mechanisms in lithium-ion batteries. *Journal of power sources*, 2006. 155(2): p. 401-414.
91. Kong, L., et al., Li-ion battery fire hazards and safety strategies. *Energies*, 2018. 11(9): p. 2191.
92. Li, W., et al., Fire boundaries of lithium-ion cell eruption gases caused by thermal runaway. *Iscience*, 2021. 24(5): p. 102401.
93. Li, W., et al., Comparison of current interrupt device and vent design for 18650 format lithium-ion battery caps. *Journal of Energy Storage*, 2020. 32: p. 101890.
94. Ould Ely, T., D. Kamzabek, and D. Chakraborty, Batteries safety: recent progress and current challenges. *Frontiers in Energy Research*, 2019. 7: p. 71.
95. Gabryelczyk, A., et al., Corrosion of aluminium current collector in lithium-ion batteries: A review. *Journal of Energy Storage*, 2021. 43: p. 103226.
96. Wang, Q., et al., Effect of LiPF₆ on the thermal behaviors of four organic solvents for lithium ion batteries. *Journal of thermal analysis and calorimetry*, 2007. 89(1): p. 245-250.
97. Yamaki, J.-i., Thermally stable fluoro-organic solvents for lithium ion battery, in *Fluorinated Materials for Energy Conversion*. 2005, Elsevier. p. 267-284.
98. Lee, H.-H., et al., The function of vinylene carbonate as a thermal additive to electrolyte in lithium batteries. *Journal of Applied Electrochemistry*, 2005. 35(6).
99. Roth, E.P. and C.J. Orendorff, How electrolytes influence battery safety. *The Electrochemical Society Interface*, 2012. 21(2): p. 45.
100. Kim, J., et al., Thermal degradation of solid electrolyte interphase (SEI) layers by phosphorus pentafluoride (PF₅) attack. *Journal of The Electrochemical Society*, 2017. 164(12): p. A2418.
101. Chen, L., et al., Toward wide-temperature electrolyte for lithium-ion batteries. *Battery Energy*, 2022. 1(2): p. 20210006.
102. Feng, X., et al., Thermal runaway mechanism of lithium ion battery for electric vehicles: A review. *Energy Storage Materials*, 2018. 10: p. 246-267.
103. Rinkel, B.L., et al., Electrolyte oxidation pathways in lithium-ion batteries. *Journal of the American Chemical Society*, 2020. 142(35): p. 15058-15074.

104. Guo, F., et al., Experimental study on flammability limits of electrolyte solvents in lithium-ion batteries using a wick combustion method. *Experimental thermal and fluid science*, 2019. 109: p. 109858.
105. Adachi, M., K. Tanaka, and K. Sekai, Aromatic compounds as redox shuttle additives for 4 V class secondary lithium batteries. *Journal of the electrochemical society*, 1999. 146(4): p. 1256.
106. Chen, Z., Y. Qin, and K. Amine, Redox shuttles for safer lithium-ion batteries. *Electrochimica Acta*, 2009. 54(24): p. 5605-5613.
107. Chen, Z., et al., Abuse-tolerant electrolytes for lithium-ion batteries. *Advanced Science*, 2021. 8(11): p. 2003694.
108. Brodd, R.J., *Batteries for sustainability: selected entries from the encyclopedia of sustainability science and technology*. 2012: Springer Science & Business Media.
109. Torabi, F. and V. Esfahanian, Study of thermal–runaway in batteries I. Theoretical study and formulation. *Journal of The Electrochemical Society*, 2011. 158(8): p. A850.
110. Song, L., et al., Review on thermal runaway of lithium-ion batteries for electric vehicles. *Journal of Electronic Materials*, 2022. 51(1): p. 30-46.
111. Börger, A., J. Mertens, and H. Wenzl, Thermal runaway and thermal runaway propagation in batteries: What do we talk about? *Journal of Energy Storage*, 2019. 24: p. 100649.
112. Xu, C., et al., Internal temperature detection of thermal runaway in lithium-ion cells tested by extended-volume accelerating rate calorimetry. *Journal of Energy Storage*, 2020. 31: p. 101670.
113. Feng, X., et al., Investigating the thermal runaway mechanisms of lithium-ion batteries based on thermal analysis database. *Applied Energy*, 2019. 246: p. 53-64.
114. Huang, L., et al., Uncovering LiH triggered thermal runaway mechanism of a high-energy LiNi_{0.5}Co_{0.2}Mn_{0.3}O₂/graphite pouch cell. *Advanced Science*, 2021. 8(14): p. 2100676.
115. Eshetu, G.G., et al., In-depth safety-focused analysis of solvents used in electrolytes for large scale lithium ion batteries. *Physical chemistry chemical physics*, 2013. 15(23): p. 9145-9155.
116. Ostanek, J.K., et al., Simulating onset and evolution of thermal runaway in Li-ion cells using a coupled thermal and venting model. *Applied energy*, 2020. 268: p. 114972.

117. Zhang, Y., et al., Quantitative identification of emissions from abused prismatic Ni-rich lithium-ion batteries. *ETransportation*, 2019. 2: p. 100031.
118. Chen, S., Z. Wang, and W. Yan, Identification and characteristic analysis of powder ejected from a lithium ion battery during thermal runaway at elevated temperatures. *Journal of hazardous materials*, 2020. 400: p. 123169.
119. Ren, D., et al., Overcharge behaviors and failure mechanism of lithium-ion batteries under different test conditions. *Applied Energy*, 2019. 250: p. 323-332.
120. Bandhauer, T.M., S. Garimella, and T.F. Fuller, A critical review of thermal issues in lithium-ion batteries. *Journal of the Electrochemical Society*, 2011. 158(3): p. R1.
121. Ouyang, D., et al., Investigation of a commercial lithium-ion battery under overcharge/over-discharge failure conditions. *RSC advances*, 2018. 8(58): p. 33414-33424.
122. Zhang, H., L. Wang, and X. He, Trends in a study on thermal runaway mechanism of lithium-ion battery with $\text{LiNi}_x\text{MnyCo}_{1-x-y}\text{O}_2$ cathode materials. *Battery Energy*, 2022. 1(1): p. 20210011.
123. Kang, Y., et al., Overcharge investigations of LiCoO_2 /graphite lithium ion batteries with different electrolytes. *ACS Applied Energy Materials*, 2019. 2(12): p. 8615-8624.
124. Liu, P., et al., Thermal Runaway and Fire Behaviors of Lithium Iron Phosphate Battery Induced by Overheating and Overcharging. *Fire Technology*, 2022: p. 1-22.
125. Zhu, Y.-l., et al., Rupture and combustion characteristics of lithium-ion battery under overcharge. *Journal of Energy Storage*, 2021. 38: p. 102571.
126. Bloch, D., et al., Li-ion batteries, in *Li-ion batteries*. 2022, EDP Sciences.
127. Potter, H., The electrical resistance of ferromagnetics. *Proceedings of the Physical Society*, 1937. 49(6): p. 671.
128. Liu, L., et al., Internal short circuit evaluation and corresponding failure mode analysis for lithium-ion batteries. *Journal of Energy Chemistry*, 2021. 61: p. 269-280.
129. wolf-mueller, O.B.o. Explosions of e-cigarette batteries cause fires and injuries. 2019 January 3, 2019 [cited 2023 09/01/2023]; Available from: <https://www.wolfmuellerlaw.com/explosions-of-e-cigarette-batteries-cause-fires-and-injuries/>.

130. Administration, U.S.F., Electronic Cigarette Fires and Explosions in the United States, 2009-2016. 2017: United States Fire Administration.
131. IMCA. Lithium battery pack explosion. 2014 31 October 2014 [cited 2023 17/02/2023]; Available from: <https://www.imca-int.com/safety-events/lithium-battery-pack-explosion/>.
132. Hesler, P. and A. Kenneth A. Travers. Lithium-ion Battery Energy Storage Systems - The risks and how to manage them. 2019 17/07/2019 [cited 2023 09/01/2023]; Available from: <https://www.hazardexonthenet.net/article/171930/Lithium-ion-Battery-Energy-Storage-Systems-The-risks-and-how-to-manage-them.aspx#>.
133. Samsung confirms battery faults as cause of Note 7 fires. 2017 23 January 2017 [cited 2023 09/01/2023]; Available from: <https://www.bbc.co.uk/news/business-38714461>.
134. Authority, D.M. and D.M.A.I. Board. Marine Accident Report Division for Investigation of Maritime Accidents Pearl of Scandinavia fire 17th November 2010. 2011 02 August 2011 [cited 2023 09/01/2023]; Available from: <https://dmaib.dk/media/8371/pearl-of-scandinavia-fire-on-17-november-2010.pdf>.
135. Herron, D. Chevy Volt fire: What did NHTSA know and when did they know it? 2012 23/01/2012 [cited 2023 09/01/2023]; Available from: <https://www.torquenews.com/1075/chevy-volt-fire-what-did-nhtsa-know-and-when-did-they-know-it#:~:text=Between%20April%2020%20and%20May%2012%2C%202011%2C%200Chevy,the%20Volt%20was%20moved%20to%20a%20storage%20lot>.
136. Undercoffler, D. Fisker and Toyota feel the wrath of super storm Sandy. 2012 01/11/2012 [cited 2023 09/01/2023]; Available from: <https://www.latimes.com/business/la-xpm-2012-nov-01-la-fi-mo-autos-sandy-hurts-fisker-toyota-20121101-story.html>.
137. Levin, A. Tesla That Caught Fire in Florida Crash Reached 116 MPH. 2018 26/06/2018 [cited 2023 09/01/2023]; Available from: <https://www.bloomberg.com/news/articles/2018-06-26/tesla-model-s-that-caught-fire-in-florida-hit-speed-of-116-mph?leadSource=uverify%20wall>.
138. Heisler, Y. Tesla Model S catches fire at a Supercharger station in Belgium. 2019 03/06/2019 [cited 2023 09/01/2023]; Available from: <https://bgr.com/tech/tesla-fire-model-s-supercharger-station-belgium/>.

139. Hutchison, V., LI-ION BATTERY ENERGY STORAGE SYSTEMS. 2017, Worcester Polytechnic Institute.
140. Nikel, D. All-Electric Plane Crash Lands In Blow To Norway's Aviation Strategy. 2019 15/08/2019 [cited 2023 09/01/2023]; Available from:
<https://www.forbes.com/sites/davidnikel/2019/08/15/all-electric-plane-crash-lands-in-lake-in-blow-to-norways-aviation-strategy/?sh=ae4833e557d5>.
141. FAA. Battery incident chart. 2022 25/02/2022 [cited 2023 09/01/2023]; Available from:
https://www.faa.gov/hazmat/resources/lithium_batteries/media/Battery_incident_chart.pdf.
142. Lisbona, D. and T. Snee, A review of hazards associated with primary lithium and lithium-ion batteries. *Process safety and environmental protection*, 2011. 89(6): p. 434-442.
143. Fogelman, R. Is the recycling industry facing a fire epidemic? 2018 05/01/2018 [cited 2023 09/01/2023]; Available from:
<https://www.recyclingproductnews.com/article/27240/is-the-recycling-industry-facing-a-fire-epidemic>.
144. Wesoff, E. Battery Room Fire at Kahuku Wind-Energy Storage Farm. 2012 03/08/2012 [cited 2023 09/01/2023]; Available from:
<https://www.greentechmedia.com/articles/read/Battery-Room-Fire-at-Kahuku-Wind-Energy-Storage-Farm>.
145. Hering, G. As fire investigation concludes, South Korea battery makers eye market relaunch. 2019 14/06/2019 [cited 2023 09/01/2023]; Available from:
<https://www.spglobal.com/marketintelligence/en/news-insights/trending/bVy2KGU3Opsle5Vv8QG0-Q2>.
146. Hill, D., McMicken Battery Energy Storage System Event: Technical Analysis and Recommendations. 2020: DNV GL Energy Insights USA, Incorporated.

Chapter 2 . Experimental

2.1. The Envision-AESC cells and modules.

The Envision AESC modules used in the Nissan Leaf 2 electric vehicle were employed in these experiments. They have 8 cells connected in a 2 submodule, 2 parallel, 2 series configuration, i.e. 2 cells are connected in parallel to make a pair, 2 pairs are connected in series to make a submodule, and 2 submodules make a module as shown in Figure 2.1. The electronic configuration of an Envision AESC module for the Nissan Leaf 2 electric vehicle (a), the stacking of the cells inside the module (b) and the electrical connections on the front face of the module (c), not to scale. The cells are stacked on top of each other as shown on Figure 2.1(b) and have electrical connections on the outside front face of the module as shown in Figure 2.1(c). The specifications of the Nissan Leaf cell and modules are summarised in Table 2.1.

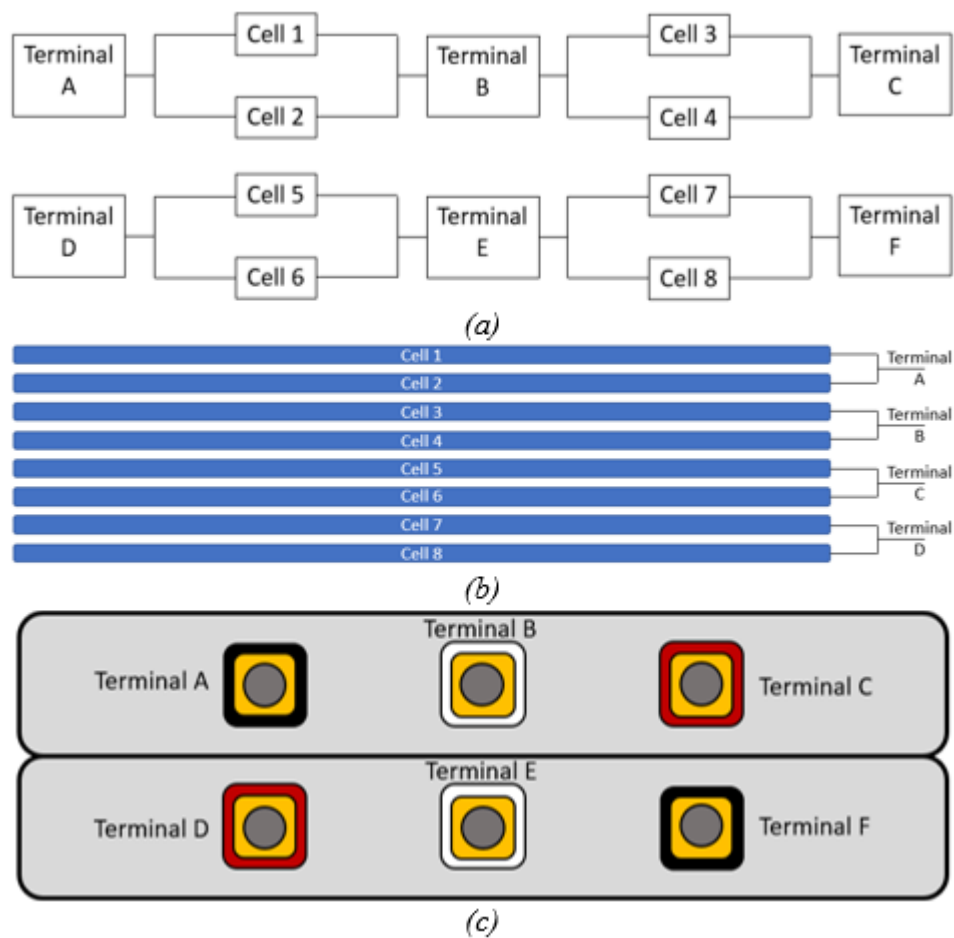


Figure 2.1. The electronic configuration of an Envision AESC module for the Nissan Leaf 2 electric vehicle (a), the stacking of the cells inside the module (b) and the electrical connections on the front face of the module (c), not to scale.

Table 2.1. The cells and modules employed in the work presented in this thesis.

<i>Cell / module</i>	<i>Dimensions (length x width x height) / mm</i>	<i>Mass / kg</i>	<i>Voltage / V</i>	<i>Energy capacity / Wh</i>	<i>Volumetric energy density / Wh L⁻¹</i>	<i>Energy density / Wh kg⁻¹</i>
<i>Cell</i>	<i>261 x 216 x 7.9</i>	<i>0.914</i>	<i>3.65</i>	<i>209</i>	<i>469</i>	<i>229</i>
<i>Module</i>	<i>300 x 222 x 68</i>	<i>8.5</i>	<i>14.6</i>	<i>1670</i>	<i>369</i>	<i>196</i>

The Nissan Leaf 2 modules used in these experiments had been rejected by AESC Envision’s rigorous quality control system. Details of the reasons why they failed were not passed on at delivery in August 2019. However, all of the modules used were able to undergo charge and discharge cycles, and the modules were tested at their specific SoCs.

In Figure 2.1 the potential difference measurement (Volts, V) across terminals A and B can be represented by V_{ab} , and as cells 1 and 2 are connected in parallel, the voltage differences across each of these are identical. The voltage across terminals A and C (V_{ac}) satisfies the equation:

$$V_{ac} = V_{ab} + V_{bc} \quad (1)$$

When the SoC of V_{ab} and V_{bc} are identical and under static conditions, a further relationship is made:

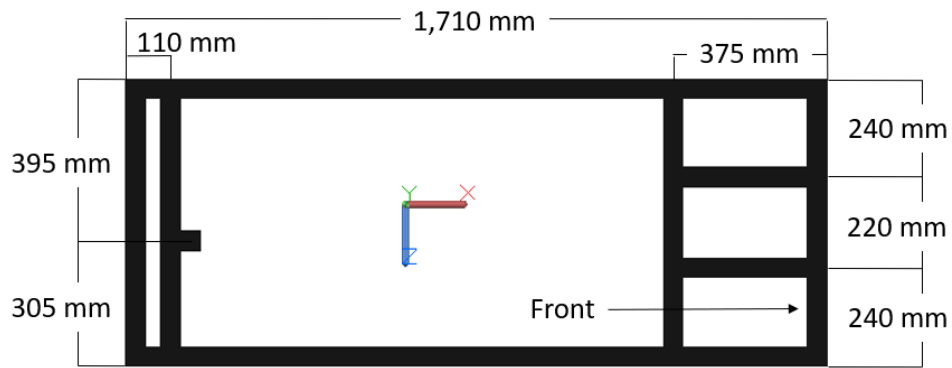
$$V_{ab} = V_{bc} = \frac{V_{ac}}{2} \quad (2)$$

2.2. The battery and camera rigs

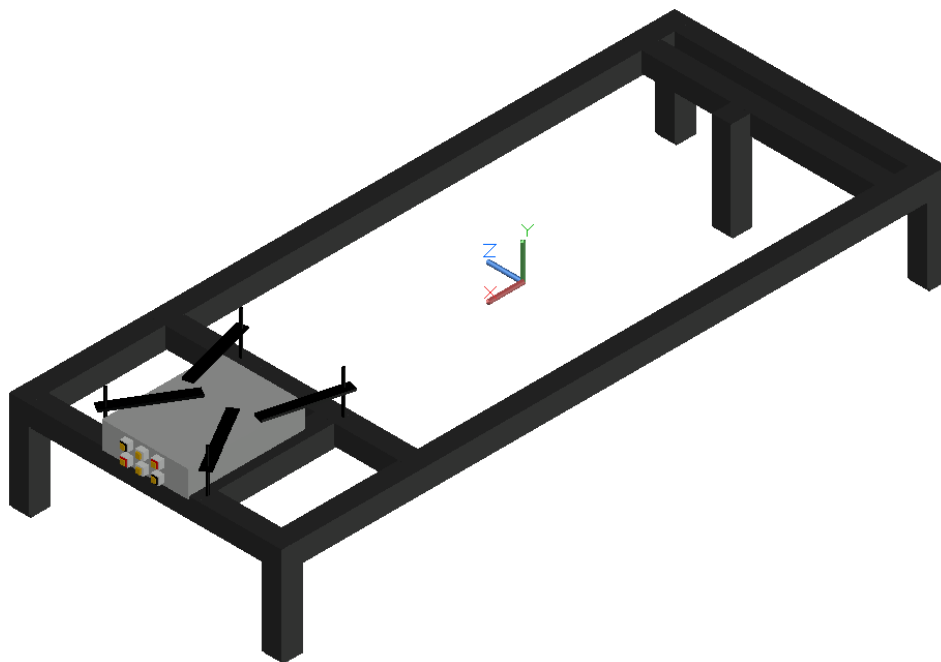
A bespoke battery rig was designed and built in-house by Mr. Neville Dickman in the mechanical workshops to secure the test cells and modules, see (b)

Figure 2.2.

The battery rig was constructed from 50 mm mild box steel, 3 mm thick. The box sections were welded together at each join. The rig was 1710 mm long, 700 mm wide and 250 mm high. A 3D view of the battery rig with a single module attached is shown in Figure 2.2(b). The module was mounted on the rig using M8 bolts and 150 mm long, 25 mm wide, 6 mm thick mild steel plates.



(a)



(b)

Figure 2.2. The battery rig designed and built for the experiments: (a) plan view and (b) 3D view with a module attached.

For the nail penetration experiments, the battery rig was modified to include a hammer and nail, see Figure 2.3. The hammer was a 75 mm long, 100 mm diameter mild steel cylinder, with a 12 mm diameter hole, 25 mm deep, hole drilled into the exposed face, into which a 100 mm long, 12 mm diameter mild steel nail, sharpened at a 30 degree angle, was fixed with a M6 socket head bolt, leaving 75 mm protruding (enough to completely pierce a 68 mm module). The hammer was mounted at the end of a 1500 mm long arm which was made by joining two 40 mm wide, 6 mm thick steel plates to make a ‘T’ section. The bottom end of the arm was pivoted on a 25 mm diameter shaft and bearing, 110 mm above the rig. In order to hold the arm upright, and allow remote activation, a 1000 mm long, 3 mm thick, 40 mm mild box steel support was mounted to

the rig. This had an 11 mm diameter hole drilled through it 945 mm from the bottom, to allow a 10 mm diameter pin through, which was retracted using a cord.

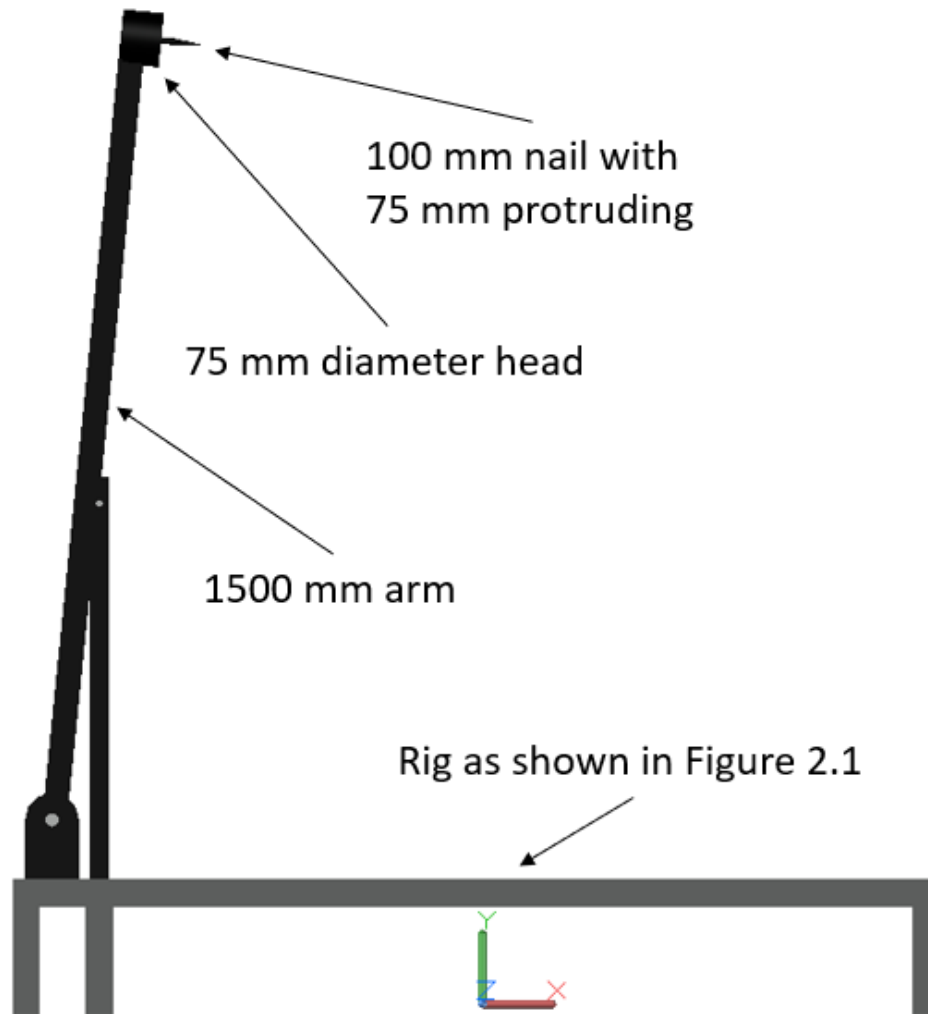


Figure 2.3. The rig with the hammer and arm attached (left side view).

In order to allow safe retraction of the battery rig, skids and a chain were added, as shown in Figure 2.4. The skids were made from a piece of 1900 mm long, 50 mm wide, 6 mm thick mild steel, and a piece of 2000 mm long, 50 mm wide, 6 mm thick mild steel, welded together along their lengths, to create an 'L' shaped section, with the 2000mm length under the rig and the 1900 mm length welded to the legs. The 50 mm overhang at each end of the longer piece was bent 12.5 degrees towards the upright, reducing the horizontal length to 49 mm. The bending of the bottom piece of the skid stopped the battery rig from getting caught and snagging on the floor when being pulled or pushed into position.

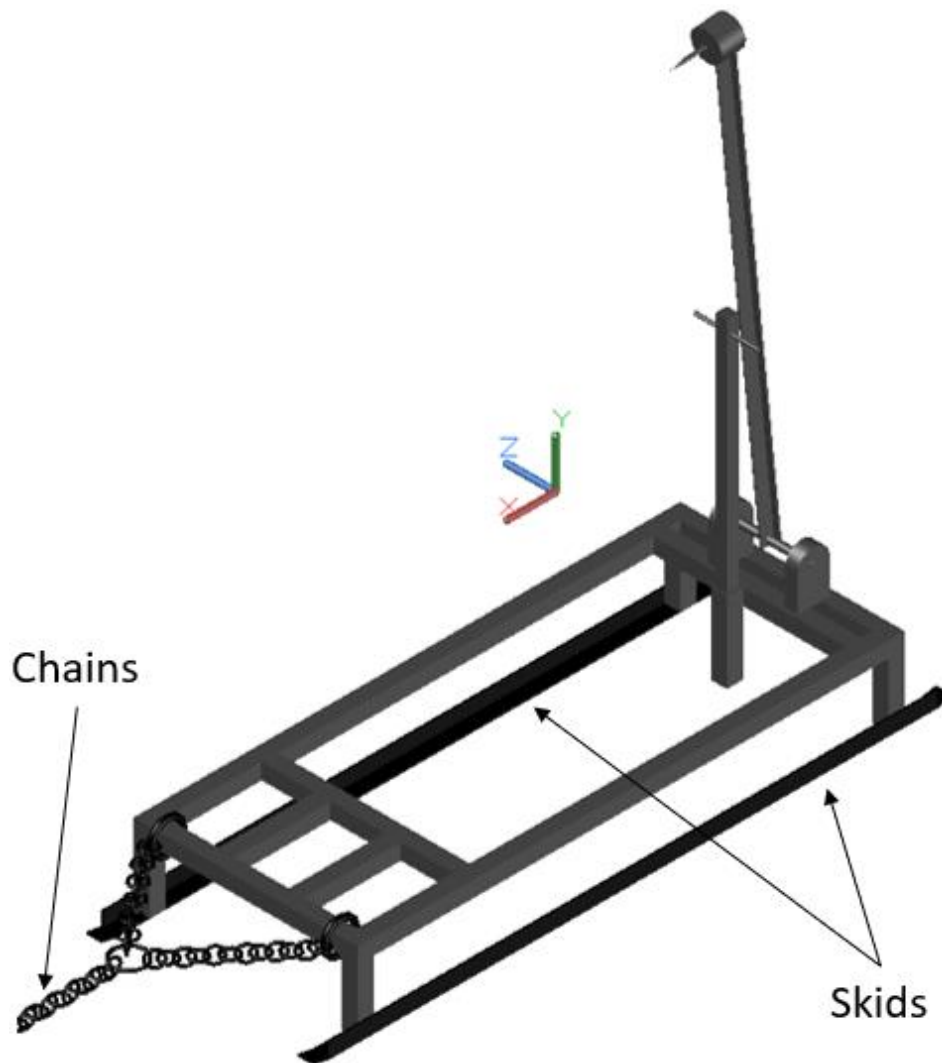


Figure 2.4. The rig with hammer, arm, chain, and skids attached.

One experiment involved the simultaneous nail penetration of two modules, and the double hammer required is shown in Figure 2.5. The double nail head in Figure 2.5 was fabricated from a plate of mild steel 500 mm long, 50 mm wide and 25 mm thick. Three holes were drilled, one at the centre of the largest face, 13mm in diameter, and on the same face two holes, 12mm in diameter were drilled and tapped 100mm from the ends and 25mm from the top and bottom edges. The plate was fixed to the cylinder at the top of the arm by removing the original nail and bolting in place. Two nails of the same dimensions as for the single penetration were then screwed into the tapped holes.

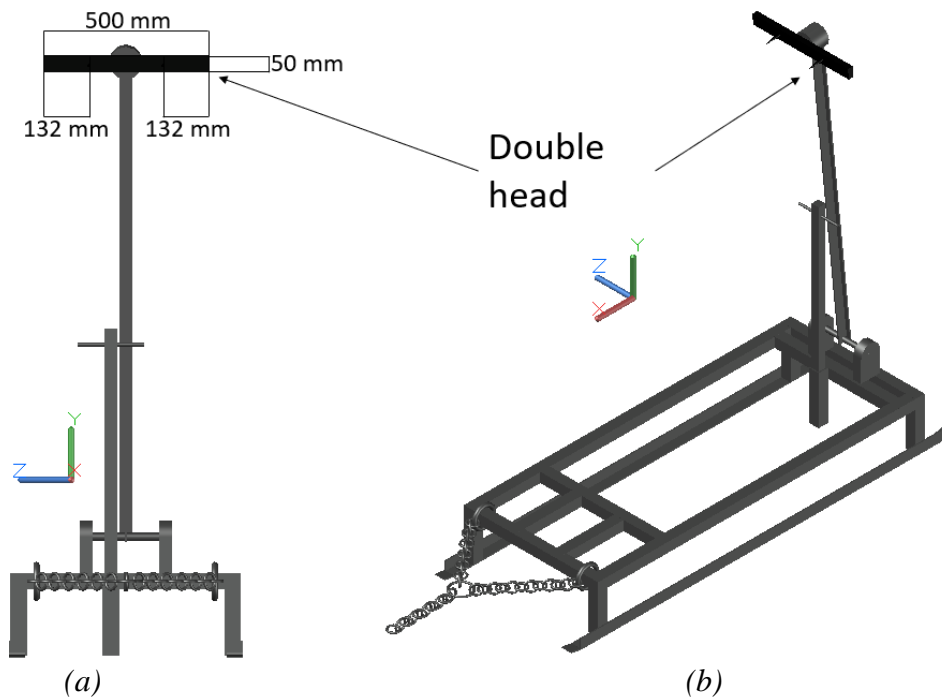


Figure 2.5. The rig with arm, chain, skids, and a double hammer head, (a) front view and (b) 3D view.

A bespoke camera rig was designed and built in-house; views are shown in Figure 2.6. This was to allow a camera to be mounted directly in front of the battery rig and pulled out of the container with the rig when a test was completed.

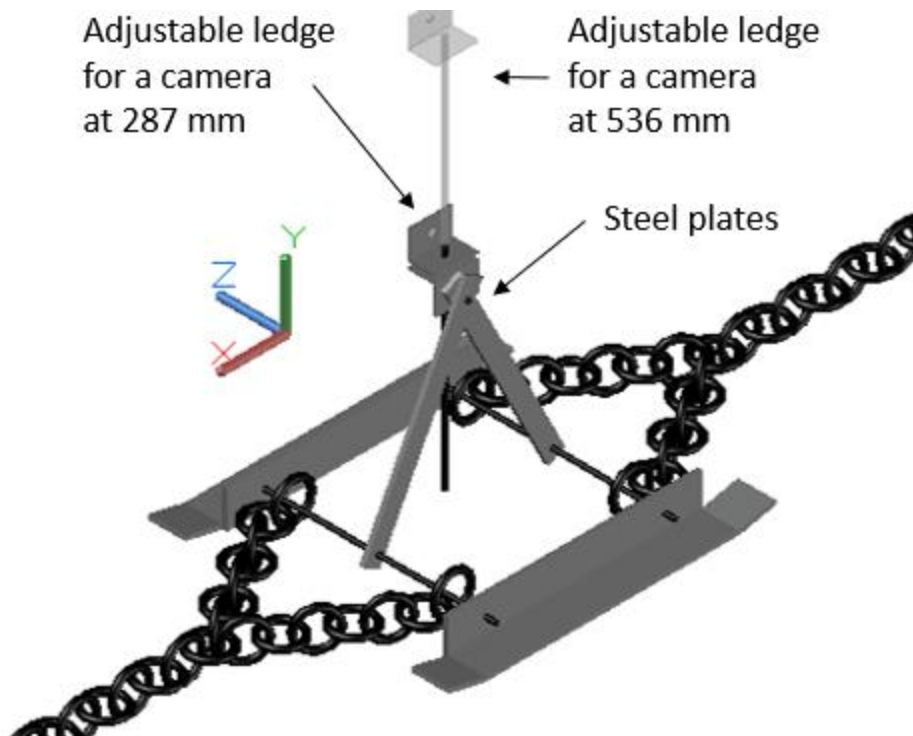


Figure 2.6. A 3D view of the camera rig.

The camera rig was fabricated from two skids, four M8 bolts, two mild steel plates and two aluminium 'L' shaped section. The skids were made of the same materials and methods as the battery rig skids, but with an overall length of 437 mm (438 mm before bending). The skids were drilled 50 mm from the ends in the vertical section, 25 mm up with 8 mm diameter holes. Two mild steel plates 300 mm long, 25 mm wide, 6 mm thick had an 8 mm diameter holes drilled 25 mm from the top edge and 15 mm from the bottom edge, on the 300 mm x 25 mm face. Two M8 bolts 330 mm in length were used to join the skids and plates, with a 25 mm long M8 bolt used to join the top edges of the two mild steel plates. An aluminium 'L' section of 37 mm height, 37 mm width was cut into two 57 mm length pieces, 8mm diameter holes were drilled through the centre of the 37 mm by 57 mm faces. The M8 bolt that was used to join the two steel plates at the top was also used to join one of the aluminium 'L' sections (fixed ledge) to the top of the steel plates. A 280 mm long M8 bolt was then bolted to the last aluminium 'L' section (adjustable ledge), and then lowered through the hole of the fixed ledge. By adjusting the nuts in between the aluminium sections, the height of the adjustable ledge could be adjusted between 287 mm and 536 mm. The chains on the battery rig were attached to the camera rig, enabling both rigs to be pulled out of the container simultaneously.

2.3. The optical cameras

Five optical cameras were employed to record the experiments: GoPro Hero 7 Black, GoPro Hero 9 Black, VMotal GSV8560, Crosstour CT7000 and Apexcam M80 Air. Details of these cameras are summarised in

Table 2.2 to 2.6. Two CCTV kits, Sansco and Maisi, were also employed for the safety of personnel during the experiments, these had only one setting 1920p x 1080p at 30 FPS. A DJI Phantom Pro 3 drone with camera was employed for aerial videos, with a resolution of 1920p x 1080p at 30 FPS.

Table 2.2. The setup options for the GoPro Hero 7 Black optical cameras.

Aspect ratio	Resolution / Pixels	Maximum frame rate / FPS
4:3	4096 x 3072	30
	2704 x 2028	60
	1920 x 1440	120
	1280 x 960	240
16:9	3840 x 2160	60
	2704 x 1520	120

	1920 x 1080	240
	1280 x 720	240

Table 2.3. The setup options for the GoPro Hero 9 Black optical cameras.

Aspect ratio	Resolution / Pixels	Maximum frame rate / FPS
4:3	4096 x 3072	30
	2704 x 2028	60
	1920 x 1440	120
16:9	5120 x 2880	30
	3840 x 2160	60
	2704 x 1520	120
	1920 x 1080	240

Table 2.4. The setup options for the Vmotal GSV8560 optical cameras.

Aspect ratio	Resolution / Pixels	Maximum frame rate / FPS
16:9	3840 x 2160	25
	2688 x 1520	30
	1920 x 1080	60
	1280 x 720	90

Table 2.5. The setup options for the Crosstour CT7000 optical cameras.

Aspect ratio	Resolution / Pixels	Maximum frame rate / FPS
16:9	1920 x 1080	30
	1280 x 720	30

Table 2.6. The setup options for the Apexcam M80 Air optical cameras.

Aspect ratio	Resolution / Pixels	Maximum frame rate / FPS
16:9	3840 x 2160	30
	2560 x 1440	30
	1920 x 1080	60
	1280 x 720	120

2.4. The thermal cameras

Two thermal cameras were employed, a FLIR A655sc 25° and an Infrasy ISGX380. The FLIR camera was set to record with a resolution of 640p x 480p, at 1 FPS with a range of -40 to 650 °C. The ISGX camera was set to record with a resolution of 384p x 288p, at 50 FPS with a range of -40 to 1000 °C. When the thermal cameras were employed, the surface of the battery module was coated in a black matt spray paint, with an emissivity of 0.9.

2.5. The thermocouples, voltage cables and DAQ

Type 'K' thermocouples with 10m leads were employed. These can measure temperatures in the range of 0 to 700 °C. When these were situated on a cell/module, they were cemented in place using Omega CC high temperature cement. Voltage cables were made from 1.5 mm² copper wire, insulated with 0.8 mm thick PVC, with a maximum working voltage of 600V and a maximum working temperature of 105 °C. The temperature and voltage measurements were logged by an Agilent 34970A Data Acquisition unit (DAQ).

2.6. The gas sensors

Details of the Draeger gas sensors are shown in

Table 2.7.

Table 2.7. The Draeger gas sensors.

Device + (Part number) + [Serial numbers]	Sensor + (Part number)	Max. conc. / ppm
XAM5000 (8,320,000) [0379,0065,0111]	XXS CO (6,810,882)	2000
	XXS NO ₂ (6,810,884)	50
	XXS SO ₂ (6,810,885)	100
XAM5100 (8,322,750) [0006,0007,0133]	XXS HCL (6,809,140)	30

The XXS NO₂ sensor was also sensitive to HCN: as a guide, 60 ppm of HCN would give a reading of $\leq \pm 10$ ppm of NO₂ on the device. The XXS HCl sensor employed is reactive to HCl and HF, along with other gases. The device used in these experiments was setup and calibrated for the detection of HCl and as such there was cross sensitivity to HF. As a guide, HF will give a reading reduced by a factor of 0.66 when shown on a

HCl-calibrated device. For example, 10 ppm of HF will result in a displayed value of 6.6 ppm HCl.

2.7. The GC-MS

The analyses using the GC-MS were carried out by Dr. Wojciech Mrozik, School of Engineering, Newcastle University. Gas samples were collected into 3 dm³ SKC FlexiFoil PP bags by a Casella Solutions Apex2 Plus pump. An Inficon HAPSITE ER GCMS was employed on site, the gas chromatography utilises a 15 m long, 1.0 µm internal diameter analytical column and Non Evaporable Getter (NEG) pump, with a Tri-Bed micro-concentration trap. The GC-MS employed nitrogen as the carrier gas. After the gas chromatography the sample enters an electron ionisation quadrupole mass spectrometer. An in-built library allows the identification of many common compounds.

2.8. The potentiostats

Cells and modules were charged using the Constant Current Constant Voltage (CCCV) protocol, where the cell/module was first charged at a constant current before switching to constant voltage at the preset State-of-Charge (SoC). Charging was terminated when the current dropped below preset value. For the experiments at DNV 1, a HCP-1005 Bio-Logic potentiostat was employed, at FSC an Electronic Test & Power Systems LAB/SM310 DC was employed and at DNV 2 and DDFRS an Electronic Test & Power Systems LAB-DSP 012.5-120 was employed to charge the cells/modules.

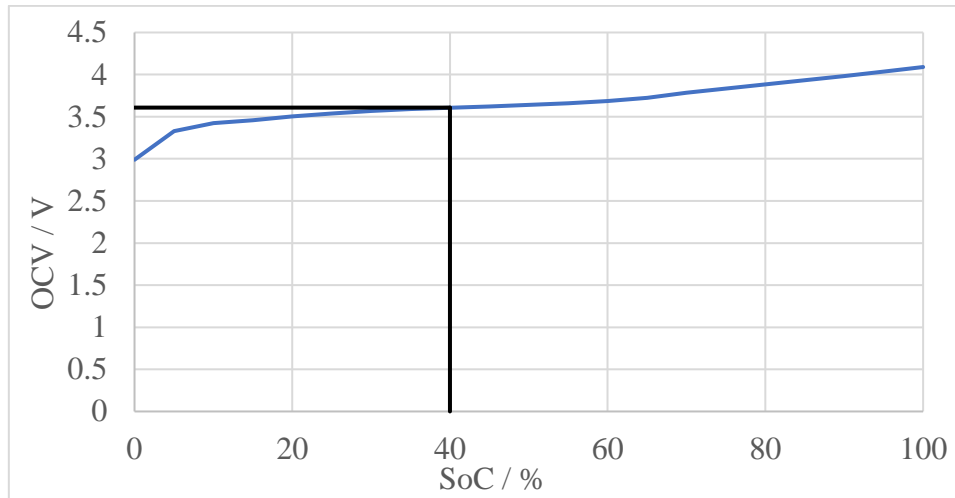
2.9. The experimental methods

Four methods to instigate thermal runaway were employed: thermal abuse, nail penetration, blunt impact, and overcharge. All cells in a module were charged prior to the experiments to the desired SoC using the constant charge constant current (CCCV) method. The necessary OCV for a particular SoC can be found from the plot in figure 2.6, and as shown the OCV for a 40 % SoC is 3.608 V.

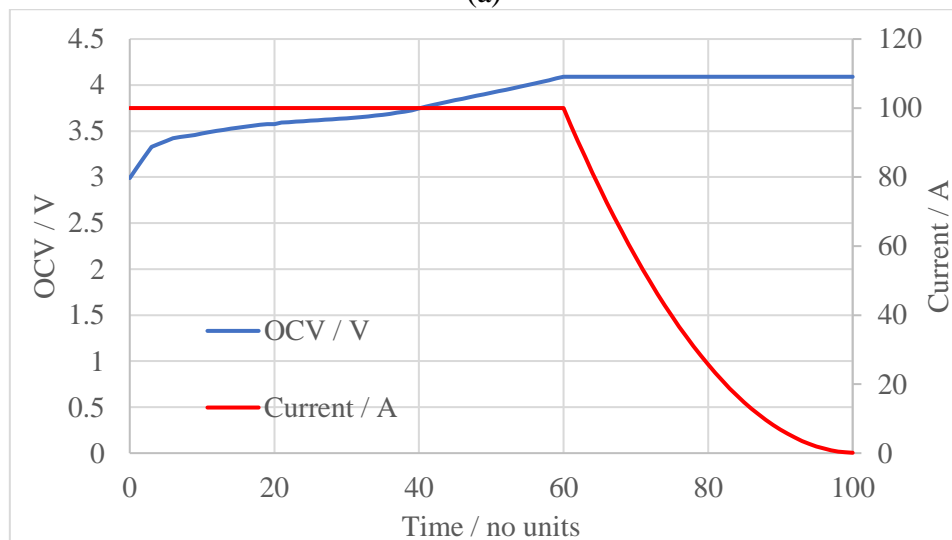
2.9.1. Charging a cell

When charging a cell to 40 % SoC, it is first charged at 100 A to 3.608 V, then the potentiostat holds the voltage of the cell at 3.608 V until the current drops to a set limit, 0.1 amps was used in these experiments. Figure 2.7(a) shows the OCV / SoC curve for the Nissan Leaf cells used in these experiments (marked at 40 % SoC) and (b) shows the

current and voltage curves for charging a cell to 100 % SoC using the CCCV method in these experiments.



(a)



(b)

Figure 2.7. (a) The OCV SoC curve for an AESC Envision cell, marked at 40 % SoC and (b) the CCCV charging curve for an AESC Envision cell, with current when charging to 100 % SoC.

In Figure 2.7, at time zero, the potentiostat is turned on, the OCV is at 3 V and the current is at 100 A, as time increases, charge accumulates in the cell and the OCV rises. Once an OCV of 4.09 is achieved, at a time of 60 units, the current begins to drop, as the voltage is held constant, until the cut off current is reached, 0.1 A at a time of 100 units.

2.9.2. Thermal abuse experimental method

The procedure for a thermal abuse experiment was to secure a module to the battery rig in the desired position, so the gas burner could be slid directly underneath. Then voltage cables and thermocouples were attached to the DAQ and module, the cameras and gas sensors placed in position, personnel retreated to a safe distance, and finally the propane gas heater was ignited and slid it into position underneath the module. (b)

Figure 2.2 shows the module attached to the rig for this experimental method and **Error! Reference source not found.** shows the experimental set up. Once thermal runaway had commenced then the propane gas burner was retracted by pulling on an attached rope.

2.9.3. Nail penetration experimental method

The procedure for nail penetration experiments was to position and secure the module(s) on the rig, so when the hammer and nail were released, the nail would penetrate the module(s) in the desired position, see Figure 2.8. The hammer arm was then laid behind the rig, so it could not accidentally fall and penetrate the module(s), the voltage cables and thermocouples were attached to the module(s) and DAQ, cameras and gas sensors placed in position and the arm was raised into its primed position, resting on a retractable pin, as shown in Figure 2.3 to 2.5. Once all personnel were at a safe distance, the retractable pin could be pulled with the aid of a rope or pneumatic control, causing the arm, hammer, and nail to fall by the force of gravity and the nail penetrated the module(s).

The procedure for a blunt impact experiment was the same as for a nail penetration experiment with the only difference being that the nail had been removed from the cylinder at the top of the arm in Figure 2.3.

The procedure for an overcharge experiment was to position and secure the cell/module(s) to the battery rig, attach any voltage cables and thermocouples, place any cameras and gas sensors in position, attach the overcharge cables to the module DAQ, and power supply, retreat to a safe distance and turn on the power supply. The rig designs used are shown in (b)

Figure 2.2.

2.10. The experiments

Seven experiments were conducted at RAF Spadeadam in January 2020 (DNV 1), these are listed in Table 2.8, three experiments were conducted at Fire Services College (FSC), these are listed in

Table 2.9, ten experiments were conducted at RAF Spadeadam in April and May 2021 (DNV 2), these are listed in

Table 2.10 and eight experiments were conducted at Durham and Darlington Fire and Rescue Services in February and March 2022 (DDFRS), these are listed in

Table 2.11. The experiments at DNV 1 and FSC used the rig design as shown in Figure 2.3, DNV 2 used multiple designs and the figure numbers for each experiment are listed in Table 2.12, DDFRS used a rig design as shown in Figure 2.4, with the arm and hammer removed. The column ‘experimental set up’ in Table 2.8 to 2.11 gives the figure number corresponding to the figure which shows the experimental setup. The results of the DDFRS tests are not included in this thesis for reasons of space.

The nail penetration experiments had different penetration points in the module and are shown in Figure 2.8.

Table 2.8. A list of experiments conducted at DNV 1.

Experiment number	Type of test	SoC / %	Number of modules	Experimental set up
A1	Thermal abuse	100	1	2.9 to 2.11
A2	Nail penetration	100	1	2.9 to 2.11
A3	Nail penetration	100	1	2.9 to 2.11
A4	Nail penetration	100	1	2.9 to 2.11
A5	Blunt impact	100	1	2.9 to 2.11
A6	Overcharge	>100	1	2.9 to 2.11
A7	Overcharge	>100	3	2.9 to 2.11

Table 2.9. A list of experiments conducted at FSC 1.

Experiment number	Type of test	SoC / %	Number of modules	Experimental set up
B1	Nail penetration	75	1	2.12 to 2.14

B2	Nail penetration	50	1	2.12 to 2.14
B3	Overcharge	>100	5	2.12 to 2.14

Table 2.10. A list of experiments conducted at DNV 2.

Experiment number	Type of test	SoC / %	Number of cells/modules	Experimental set up
C1	Nail penetration	10	1 module	2.15 to 2.17
C2	Overcharge	>100	1 cell	2.15 to 2.17
C3	Overcharge	>100	1 module	2.15 to 2.17
C4	Nail penetration	40	1 module	2.15 to 2.17
C5	Nail penetration	40	1 module	2.15 to 2.17
C6	Twin nail penetration	35	2 modules	2.15 to 2.17
C7	Nail penetration	40	1 module	2.15 to 2.17
C8	Overcharge	>100	8 modules	2.19 to 2.21
C9	Nail penetration	100	1 module	2.22 to 2.24
C10	Overcharge	>100	3 modules	2.22 to 2.25

Table 2.11. A list of experiments conducted at DDFRS, all at >100 % SoC.

Experiment number	Type of test	Number of modules	Set up	Extinguisher
D1	Overcharge	5	2.26 to 2.29	-
D2	Overcharge	1	2.26 to 2.29	-
D3	Overcharge	5	2.26 to 2.29	Cold Cut Cobra
D4	Overcharge	5	2.26 to 2.29	F500 EA
D5	Overcharge	5	2.26 to 2.29	Liquid nitrogen
D6	Overcharge	5	2.26 to 2.29	AVD
D7	Overcharge	5	2.26 to 2.29	AVD

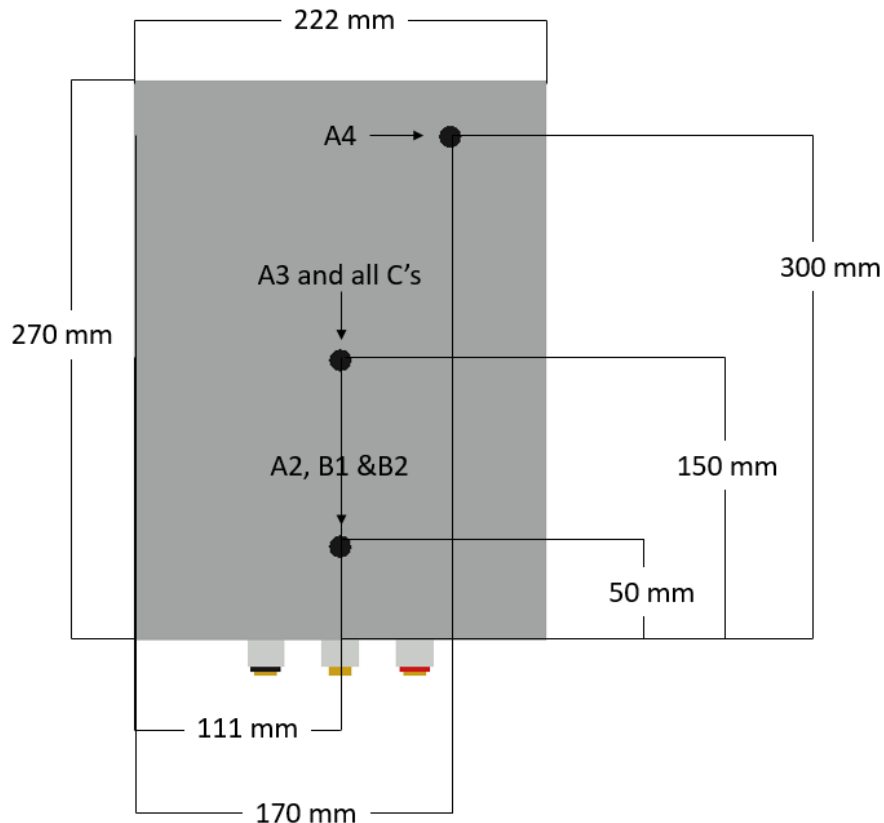


Figure 2.8. Positions of the nail penetration in the experiments.

The experimental setup shown in **Error! Reference source not found.** and 2.10 was employed during the DNV 1 experiments and a photograph from optical camera 1 of the setup is shown in Figure 2.11. These were performed in the open air using the rig as shown in Figure 2.3 with either a single module attached to the front, or three modules stacked on top of each other. Thermal and optical cameras were placed 3m from the centre of the module, 180 degrees apart and 45 degrees from the x and z axis. The charger (potentiostat) and DAQ were positioned 10 m in front of the module(s), connected to the module(s) with electronic and thermostat cables. In experiment DNV 1, the flexible gas pipe to the propane burner was protected by a steel pipe within 2 m of the module. The burner was slid into position along guides directly beneath the rig.

Additionally, Draegar gas sensors were employed at DNV 1, in various locations depending on the prevailing wind direction. But the wind pattern and speed were unpredictable, which made the recorded data of less scientific value than anticipated. They did however serve very well as a guide for future experiments as they did function when the wind blew in their direction, recording different chemical species and their concentrations.

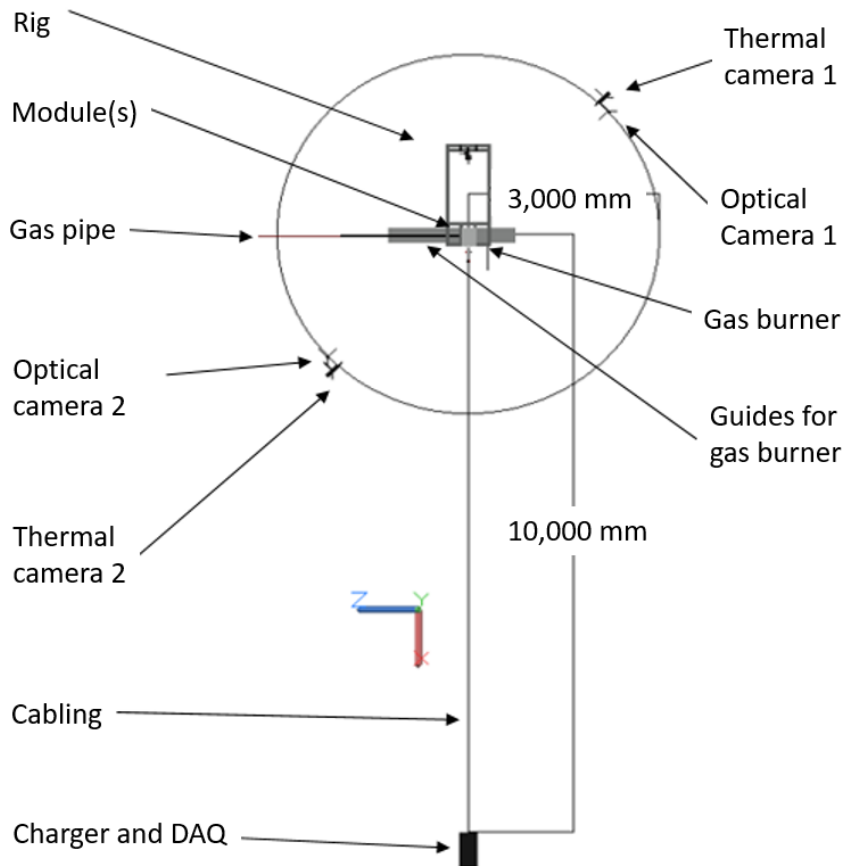


Figure 2.9. Plan view of the experimental setup at DNV 1.

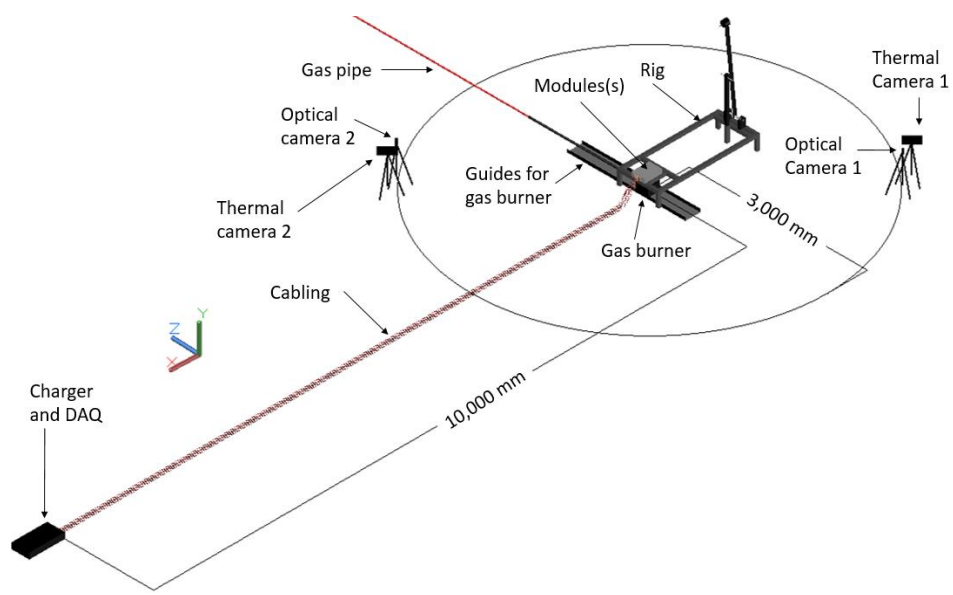


Figure 2.10. 3D view of the experimental setup at DNV 1.

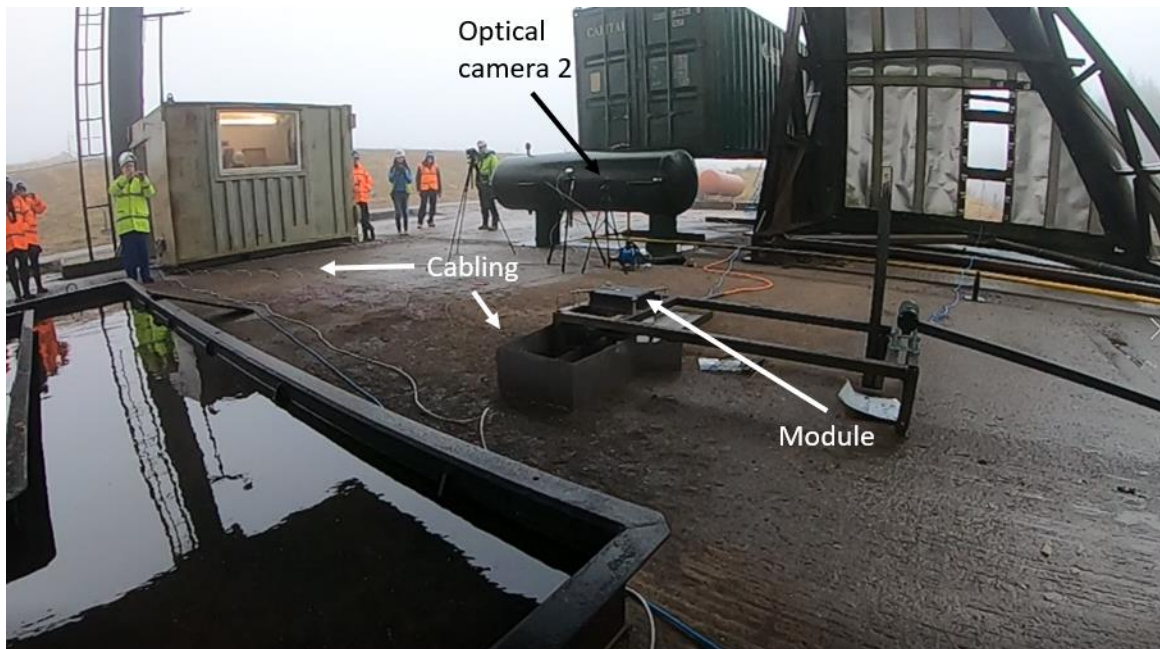


Figure 2.11. A photograph of the experimental setup at DNV 1 (taken from Optical camera 1).

The experimental setup shown in Figures 2.12 and 2.13 was employed during the FSC experiments: these were carried out inside a 66 m³ container using the rig as shown in Figure 2.3 with either a single module (B1 & B2) attached to the front of the rig, or a five-module stack (B3) attached to the front of the rig. A photograph of the setup is shown in Figure 2.14.

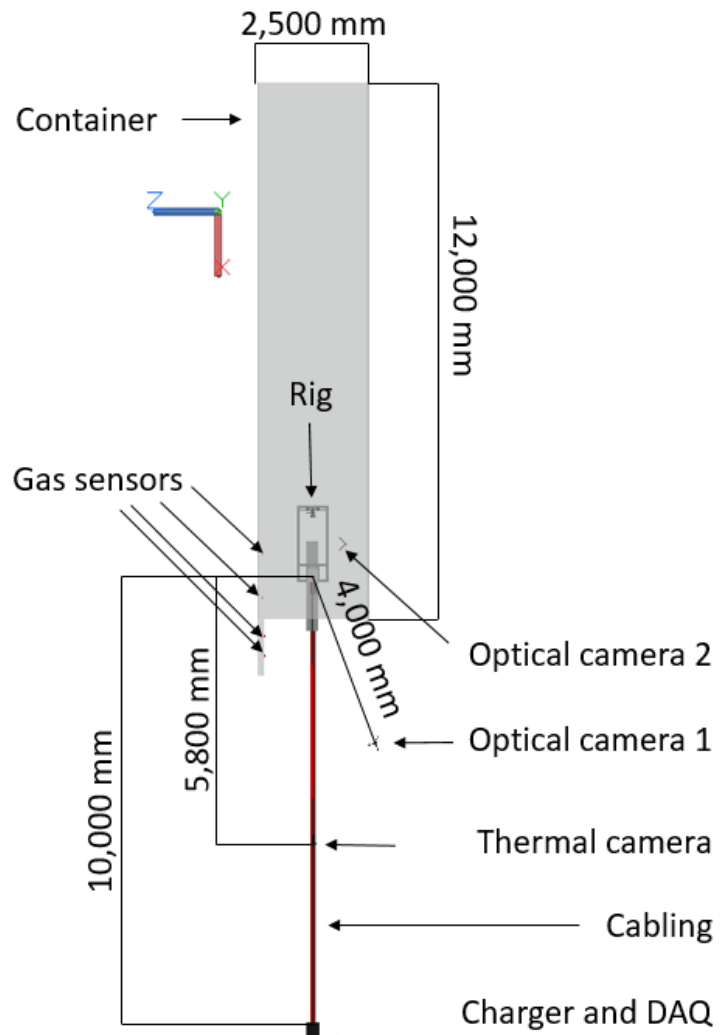
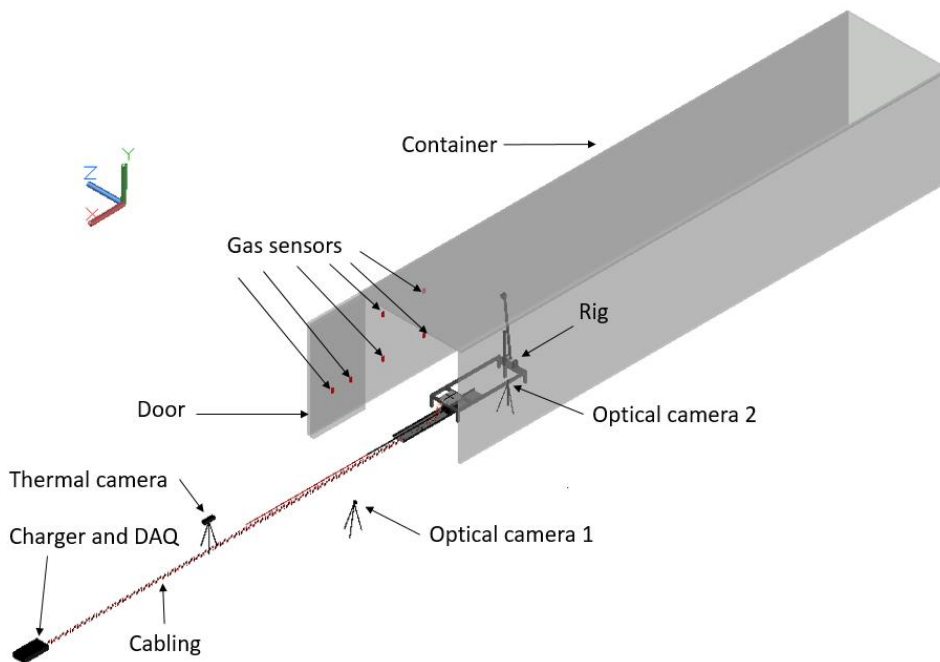


Figure 2.12. Plan view of the experimental setup at FSC.



(b)

Figure 2.13. 3D view of the experimental setup at FSC.

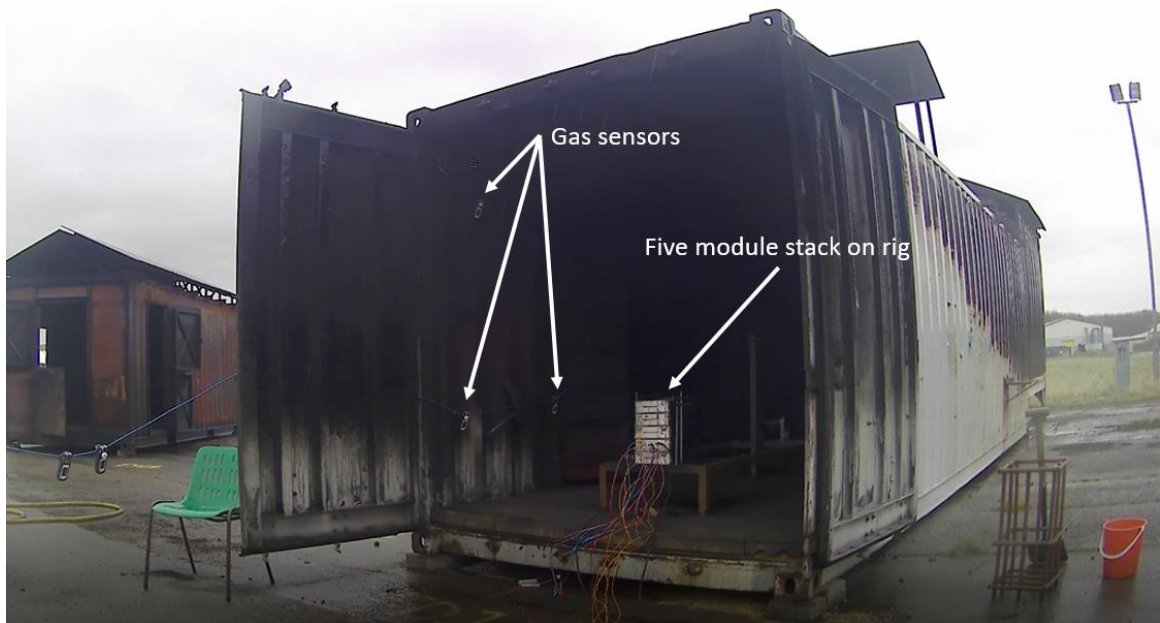


Figure 2.14, A photograph of the experimental setup at FSC.

The rig and module(s) were placed inside the container, as shown in 2, which measured 2.5 x 12 m, with the left side door of the front opened at 90°, and the right side door folded flat against the side wall (not shown). Optical camera 1 was placed 4 m from the centre of the module(s) 20° to the x axis, and optical camera 2 was placed inside the container, 1 m from the centre of the module(s) 45° to the x and z axis. A thermal camera was placed 5.8 m from the module(s), directly in front, on the x axis. The charger (potentiostat) and DAQ were positioned 10 m in front of the module(s), connected to the module(s) with electronic and thermostat cables. Gas sensors were placed on the left side door, which was opened at 90° and on the container wall, shown in red in Figure 2.13.

The experimental setup shown in Figures 2.15 and 2.16 was used for some of the DNV 2 experiments: these were carried out inside a 66 m³ shipping container with internal dimensions of about 12 m x 2.35 m x 2.35 m. The rig, camera rig, and polythene blast wall were at various positions during the different experiments, as shown in **Error!**

Reference source not found..

The moveable polythene wall was used to trap any vented gases from the module(s) after penetration inside the container but also to provide a safe release should a deflagration occur. The gases were allowed to accumulate before various squibs and other devices were employed to try and cause deflagration.

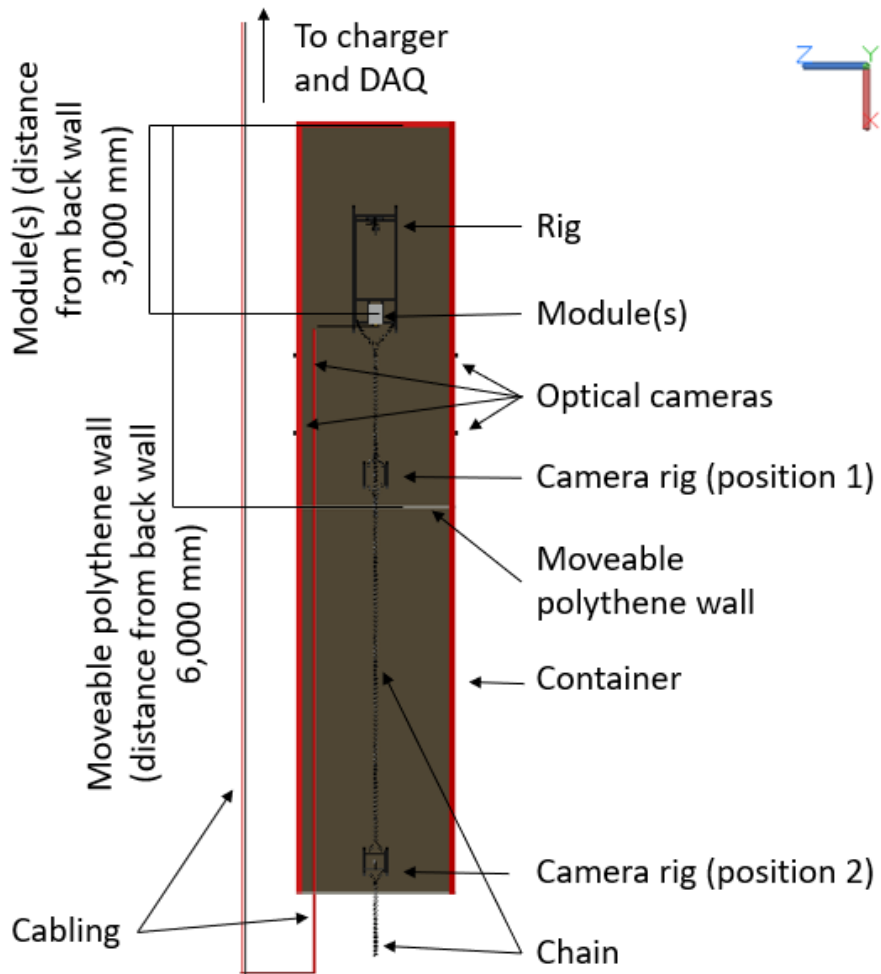


Figure 2.15. Plan view of the experimental setup at FSC.

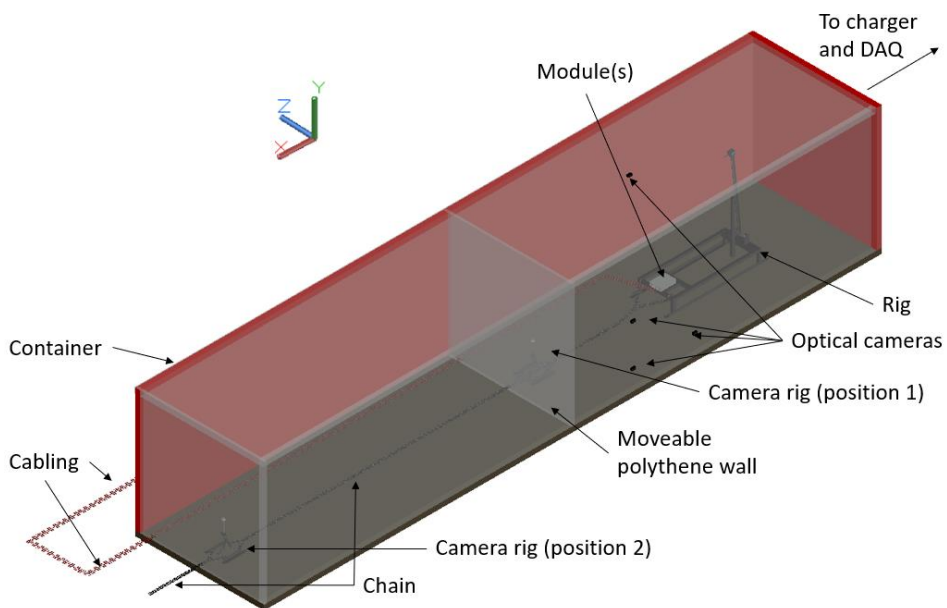


Figure 2.16. 3D view of the experimental setups at DNV 2.

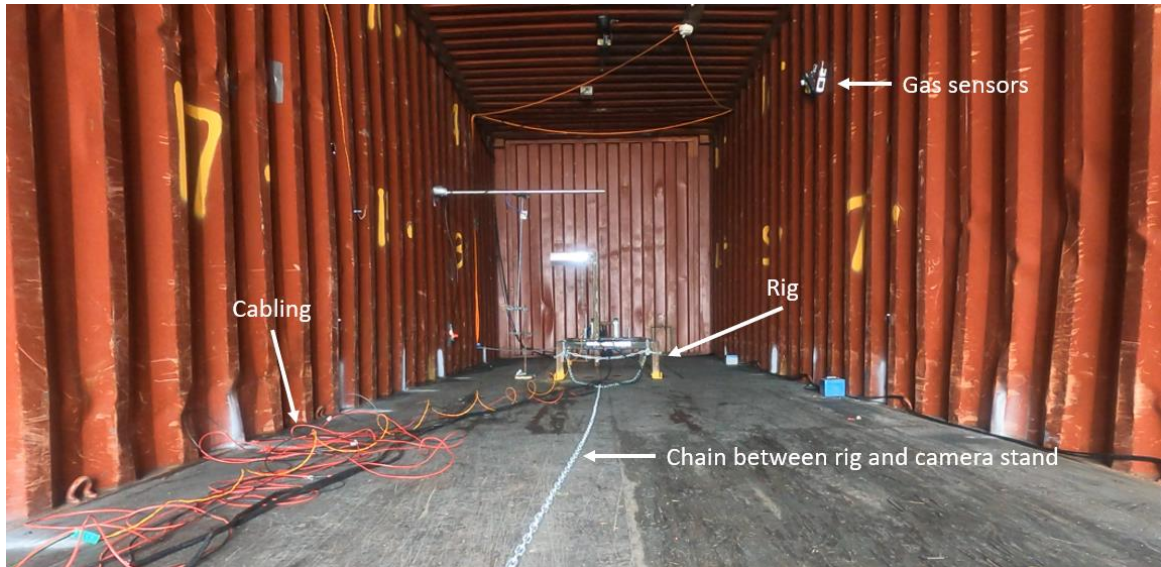


Figure 2.17. A photograph of the experimental setup at DNV 2.

Table 2.12. The nail penetration rig and polyethylene blast wall positions in the DNV 2 experiments using the arrangement in figure 2.11.

Experiment number	Rig Position / mm	Blast Wall Position / mm	Rig Design Figure Number
C1	3,000	12,000	2.3
C2	3,000	12,000	2.3
C3	3,000	12,000	2.3
C4	3,000	12,000	2.3
C5	3,000	6,000	2.3
C6	0	3,000	2.4
C7	3,000	6,000	2.3

The dimensions given in Table 2.12 are for the rig measuring from the inside edge of the back wall of the container to its back edge. In Figure 2.165 and 2.16 the rig and polythene wall were set 3 m and 6 m from the back container wall respectively. The camera rig was positioned just in front of the polythene wall, (camera rig position 1 in Figure 2.16), camera rig position 2 was employed when the full container was used, i.e. the polythene wall was positioned 12 m from the back container wall. The camera rig was attached to the battery rig with a chain, allowing both pieces of equipment to be removed without the need for personnel to enter the container following an experiment. The cells were charged and monitored from a blast resistant box c.a. 15 m from the container and connected by cabling. For experiment C6, two modules were laid side by side and penetrated simultaneously with the double penetration head: both cells were charged to 35 % SoC.

The experimental configuration is shown in Figure 2.20 and 2.19 for experiment C8, 8 modules were lined up horizontally, with the 68 x 300 mm face as the top and bottom, the terminals were facing towards the front, as shown in Figure 2.20. They were held together with two 10 mm thick, 25 x 300 mm mild steel plates at each end, four in total, each bolted at the top and bottom to the plates on the other side of the 8 module stack with M8 nuts and bolts. These were placed on top of a concrete block which served as a stand. 500 mm thick concrete blocks were erected around the perimeter to form a U shape, 4 m long by 3.5 m wide. An optical camera was placed 6 m away from the modules, directly in front. The modules were charged and measured from c.a. 50 m away in a blast resistant cabin, connected by cabling.

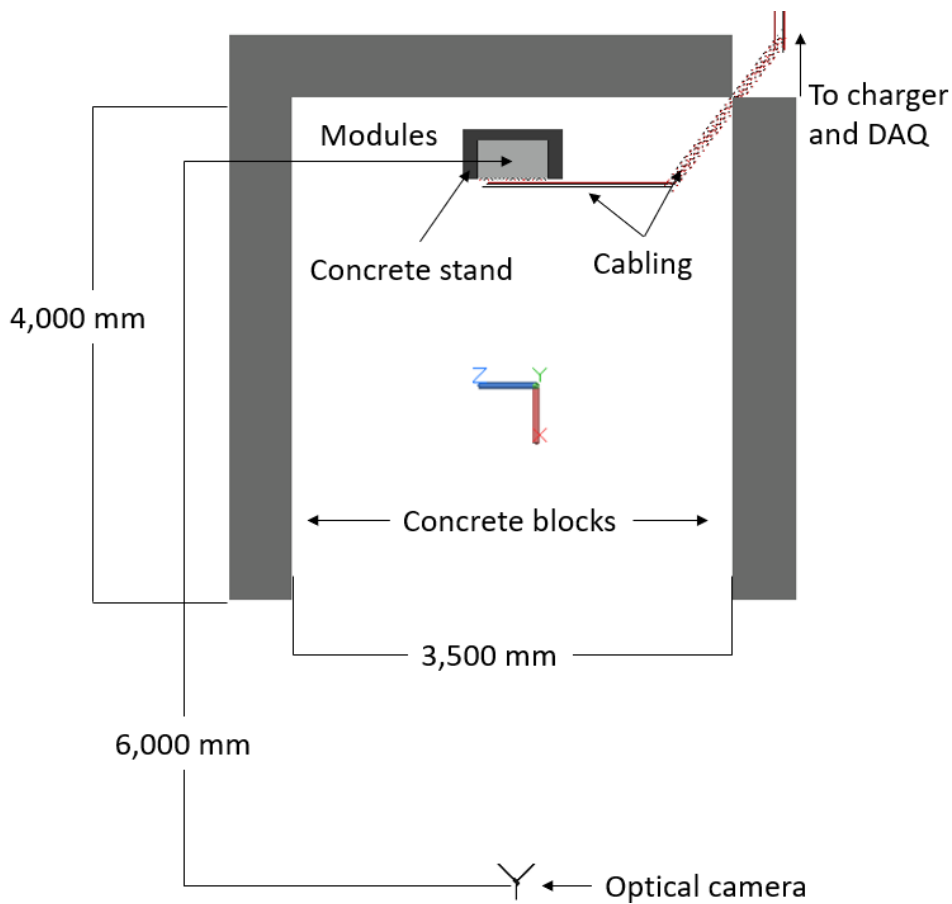


Figure 2.18. Plan view of the experimental setup at DNV 2 for experiment C8.

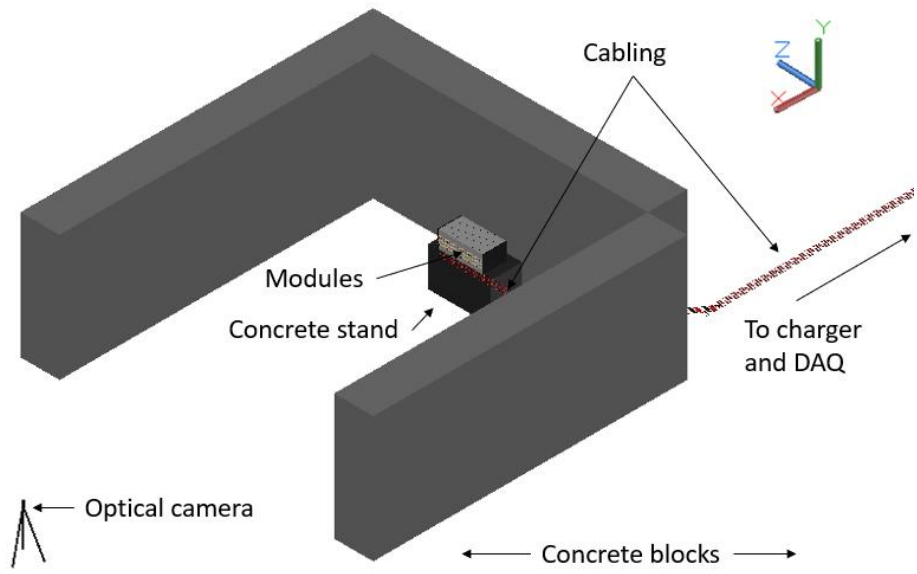


Figure 2.19. 3D view of the experimental setup at DNV 2 for experiment C8.

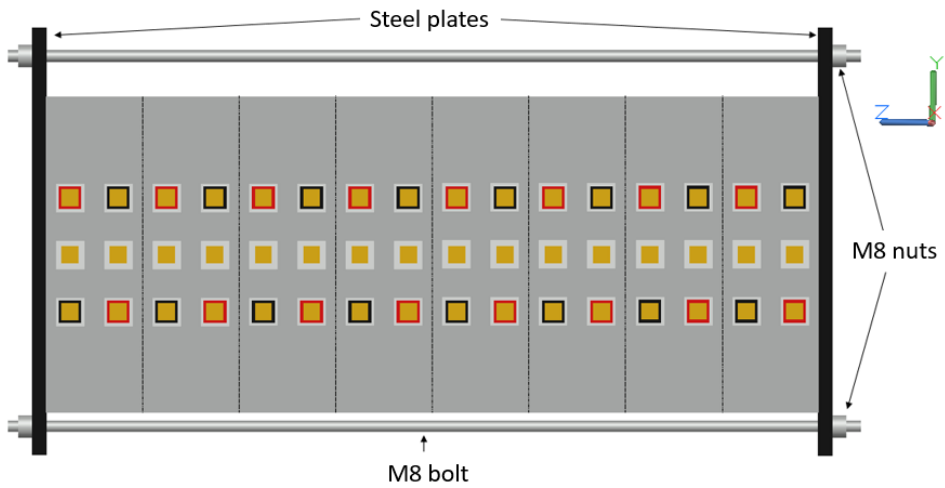


Figure 2.20. Front view of the 8 module stack, encased in steel plates, for experiment C8.

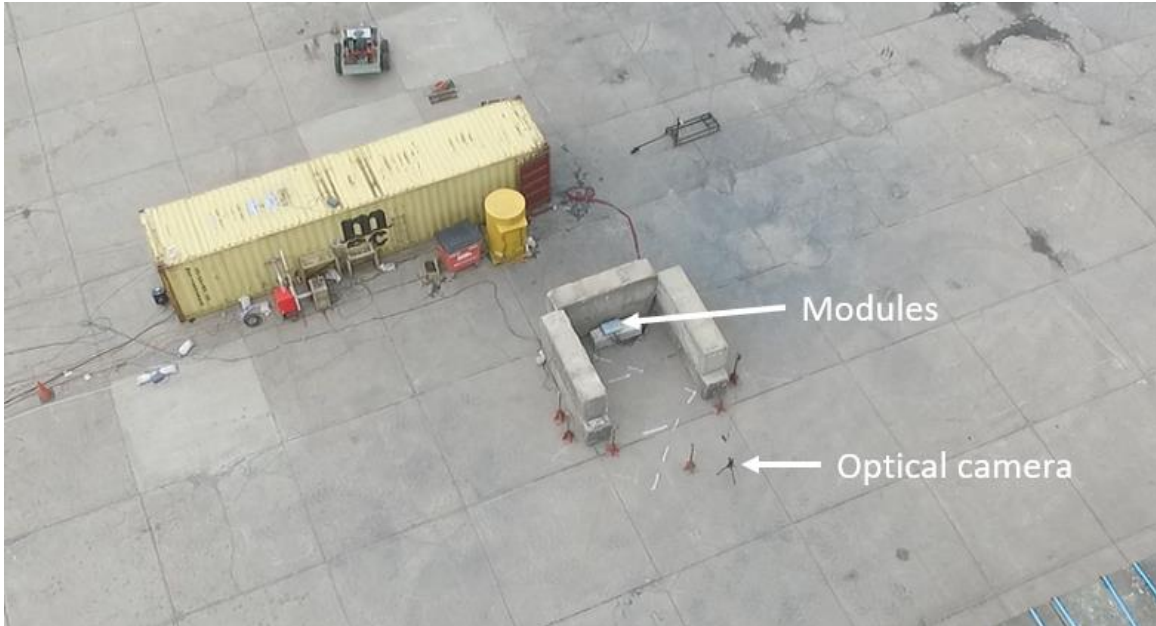


Figure 2.21. A photograph of the experimental setup at DNV 2, for experiment C8.

The experimental configurations shown in Figure 2.23 and 2.23 were for experiments C9 and C10 at DNV 2, they were performed outside using the rig as shown in Figure 2.3 with the arm laid flat for overcharge experiment (C10). Figure 2.24 is a photograph of the setup taken by a drone.

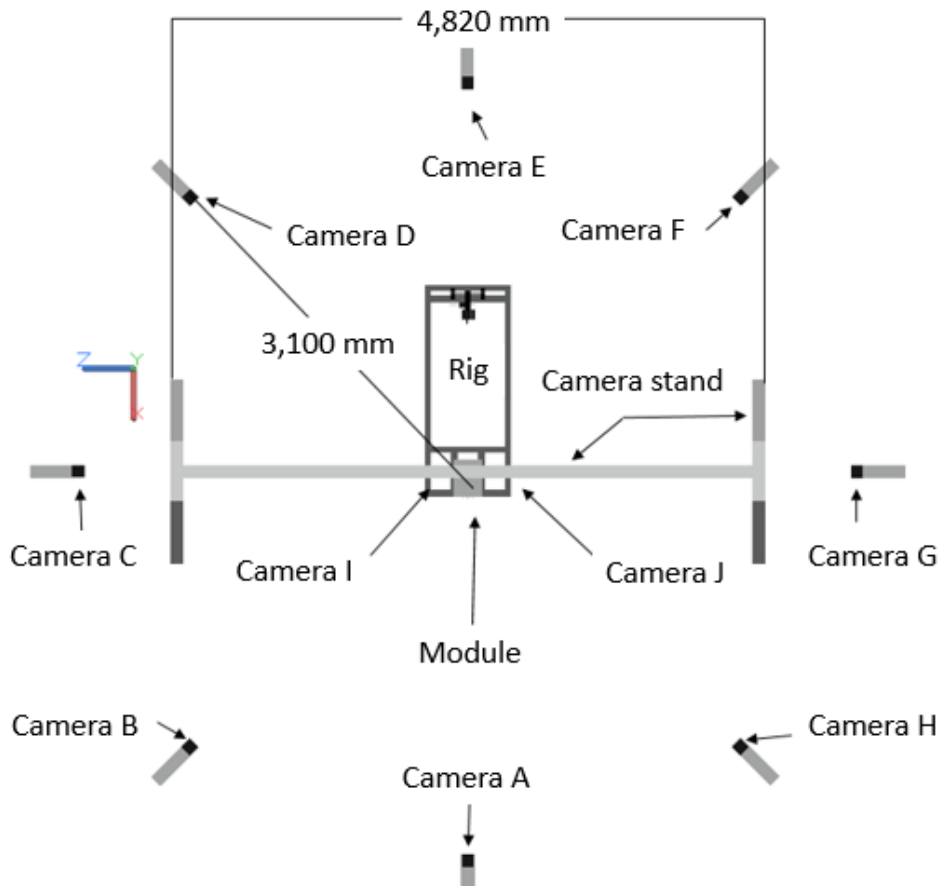


Figure 2.22. Plan view of the experimental setup at DNV 2, for experiments C9 and 10.

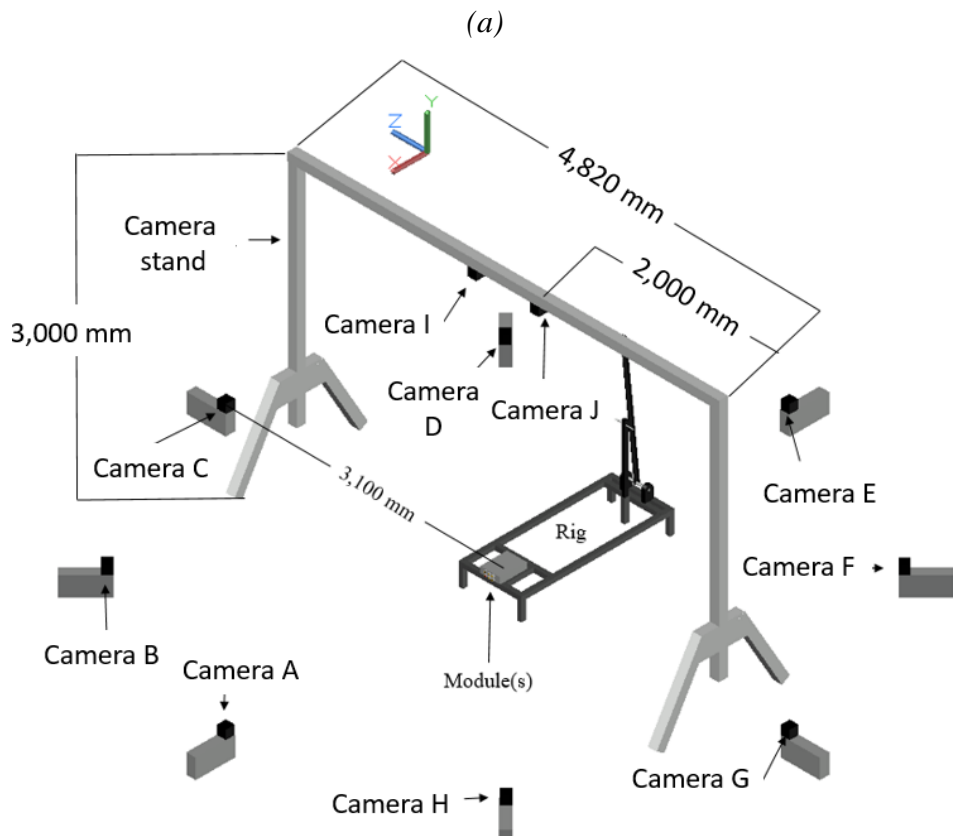


Figure 2.23. 3D view of the experimental setup at DNV 2, for experiments C9 and 10.

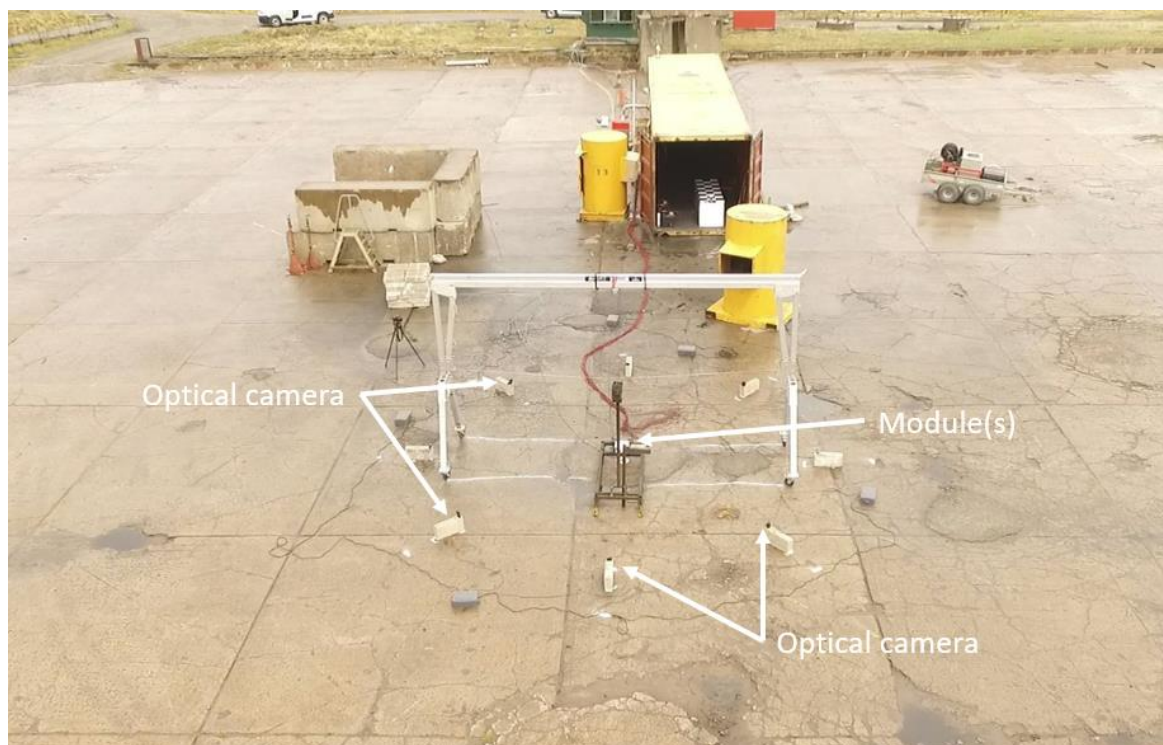


Figure 2.24. A photograph of the experimental setup at DNV 2, for experiments C9 and 10.

Figure 2.25 shows how 3 modules were stacked and bolted together for experiment C10.

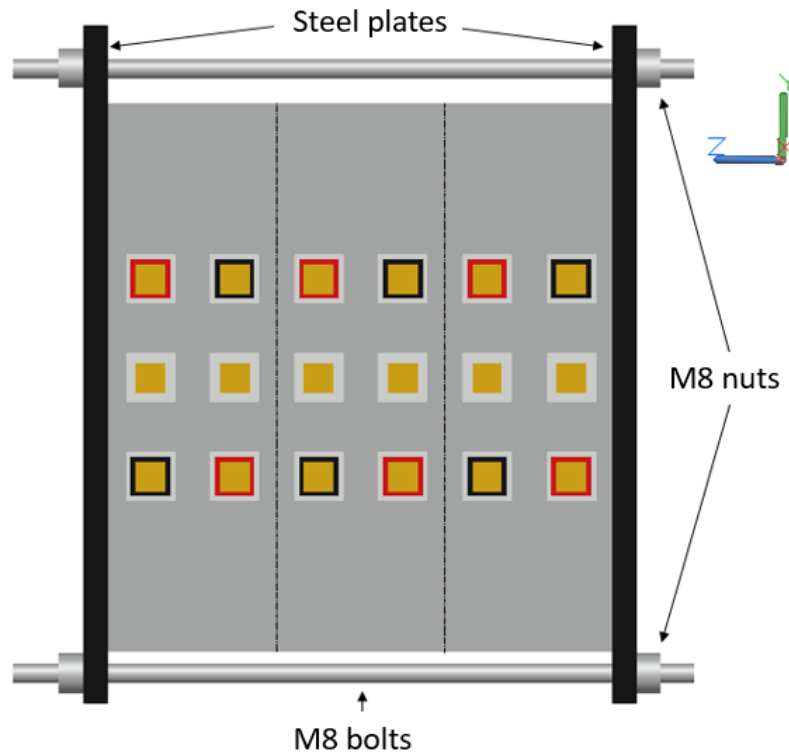


Figure 2.25. Front view of the 3 module stack used in experiment C10.

In Figures 2.22 and 2.23, 8 optical cameras were positioned around the module(s), 3.1 m from the centre and placed on concrete blocks, 440 mm long, 215 mm high and 107 mm wide which made the camera lenses approximately the same height as the module(s). Two further cameras were attached to a 3 m high, 4.82 m long frame, made from 100 mm by 100 mm aluminium box section, obtaining a birds' eye view of the experiments. For experiment C10, the modules were held together by a 400 x 275 mm, 10 mm thick mild steel plate, each side, bolted together with M8 nuts and bolts, as shown in Figure 2.25. As with the DDFRS experiments, experiment C10 is not reported further due to space considerations.

The experimental configuration shown in Figures 2.26 and 2.27 was employed during the experiments at DDFRS, they were performed inside a container using the rig as shown in Figure 2.3. Figure 2.28 shows how 5 modules were stacked in a steel box with space on top to administer fire extinguishing agents.

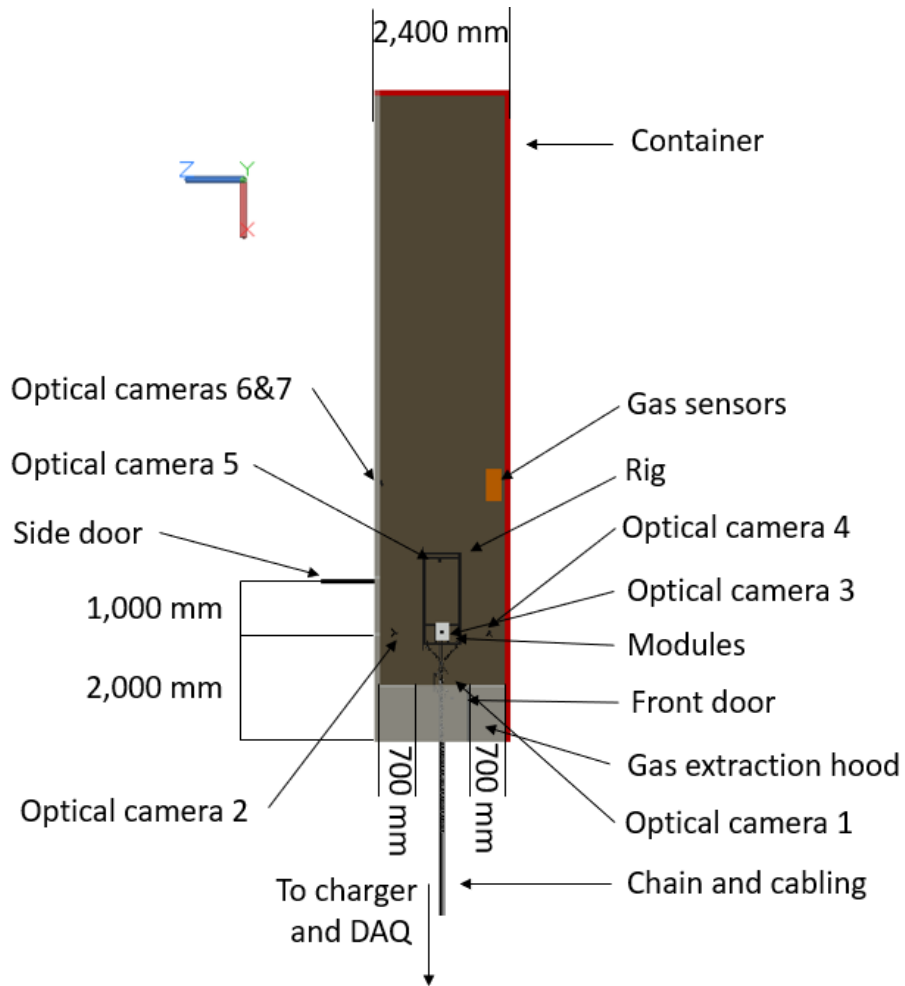


Figure 2.26. Plan view of the experimental setup at DDFRS.

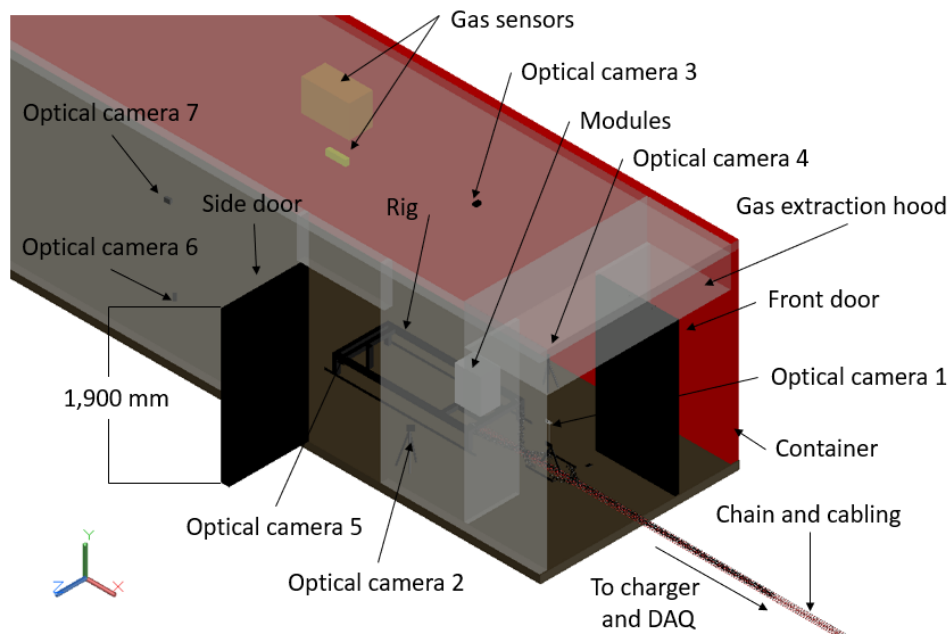


Figure 2.27. 3D view of the experimental setup at DDFRS.

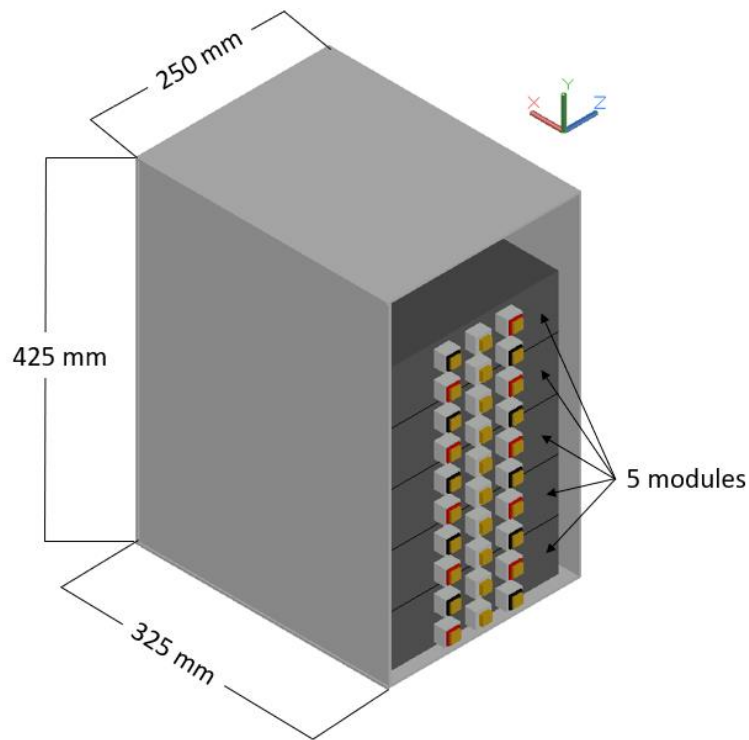


Figure 2.28. 3D view of the 5 module stack used in experiments at DDFRS.

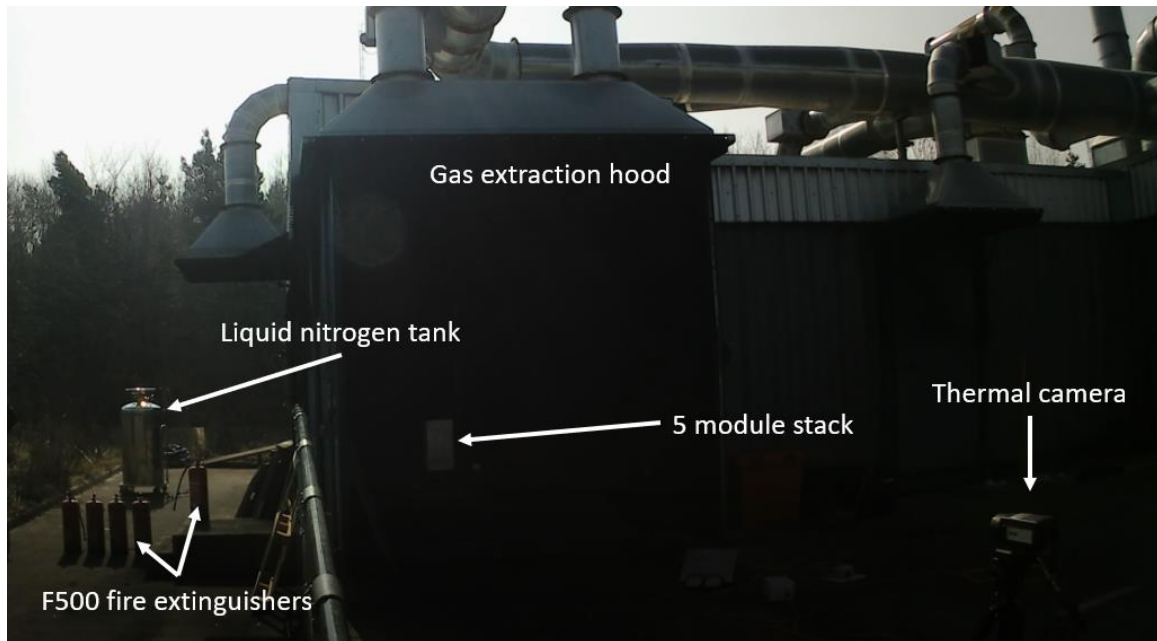


Figure 2.29. A photograph of the experimental setup at DDFRS.

The experiments at DDFRS were conducted in a 66 m³ shipping container, with two steel doors and a gas extraction hood fitted. The steel doors were 1m in width and 1.9 m in height, positioned as shown in Figure 2.27. The gas extraction hood spanned the width of the container and was positioned above the front steel door as shown in Figure 2.27 and 2.27. 6 optical cameras were used to record the modules during the experiments and one

optical camera (optical camera 7) was used to record the gas sensors and their positions are shown in Figure 2.27 and 2.27. The DAQ and charger were placed c.a. 15 m from the module(s) connected by cabling. All the experiments involved overcharging two of the cells in the second bottom module: loss of this and the lowest module was expected: the aim of the tests was to assess if thermal propagation to the top 3 modules could be prevented. Unless otherwise stated, suppression was deployed 1 minute after fire was initiated. A report on the DDFRS experiments can be found in [1].

2.11. References

1. Palmer, A. *Fire extinguisher tests NU for UK-FA*. 2023; Available from: <https://www.youtube.com/watch?v=VL1HGWbJc6s>. Lst accessed 18th January 2024.

Chapter 3 . Mechanical Abuse

3.1. Introduction

This Chapter describes the mechanical abuse experiments, A1 - 5, B1 & 2, as listed in Chapter 2. Although experiments C1, 4 - 7 & 9 are mechanical abuse experiments, C1 & 4 - 7 are covered in Chapter 4, and C9 is covered in Chapter 5.

The first set of experiments were carried out at the DNV GL testing facilities at RAF Spadeadam, Cumbria, in January 2020 (DNV 1) and were largely intended to explore the effect of different abuse methods. They were performed in an open air environment as the quantity and toxicity of any gases that could be released were not known. Observers were positioned upwind and gas sensors downwind, but on the experimental days the wind was gusty and changed direction, hence the readings from the gas sensors could only be used as a guide to what chemical species were present.

The first experiment (A1) was the thermal abuse of 1 module at 100 % SoC, the method and setup are described in Chapter 2. At that time, heating was considered to be the most reliable way to initiate thermal runaway, and it was important to know that if a later abuse experiment failed, the module(s) could be ignited by the burner, rather than leave the module(s) in an unsafe condition. Experiments A2 to 4 were nail penetrations, with the different nail position, see Figure 2.8, to assess the impact of nail position.

Experiments B1 & 2 were held at Fire Services College, Moreton-in-the Marsh, in March 2020, both were nail penetrations in between the tabs of the modules, the same as experiment A2, but this time the effect of SoC was investigated. The experiments were conducted in an open container, approximately the size of a standard 40-foot shipping container, see Figure 2.13. Importantly, this offered greater protection from the weather than the first set of experiments allowing the gas sensors to be positioned closer to the modules and in a more protected environment, but again, the open container was not ideal for gas analysis.

3.2. Results

3.2.1. Experiment A1.

Frames from the optical video camera located to the front of the module are shown in Figure 3.1. The burner was moved under the module 27 s into the experiment. Smoke and small flames was observed 46 s after the burner was introduced (Figure 3.1(a)). After 106 s the burner was removed, and 24 s later, flare-like flames were observed to issue from the modules (Figure 3.1(b)), as expected, as the pouch cells are designed to vent from the bottom of the cell (i.e. furthest away from the tabs) on ignition.



(a) Small flames are first observed 46 s after the introduction of the burner.



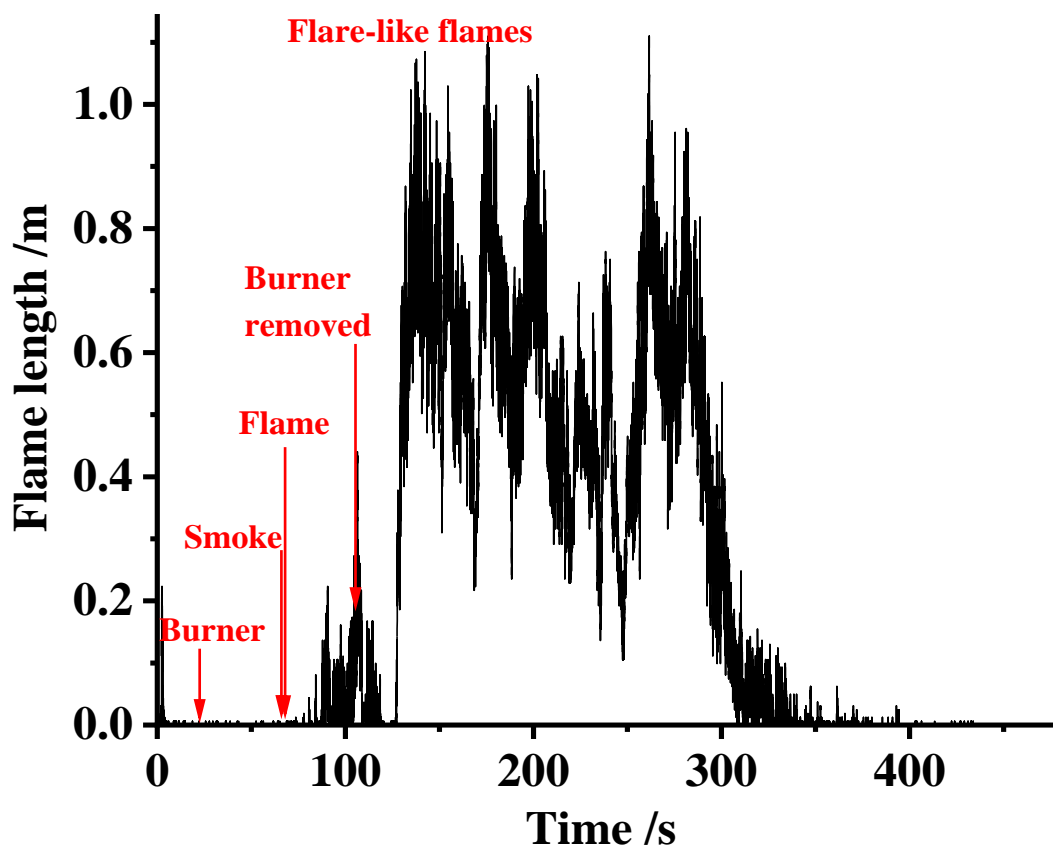
(b) Flare-like flames are observed 130 ss after the introduction of the burner.

Figure 3.1. Frames from the optical videos taken during experiment A1.

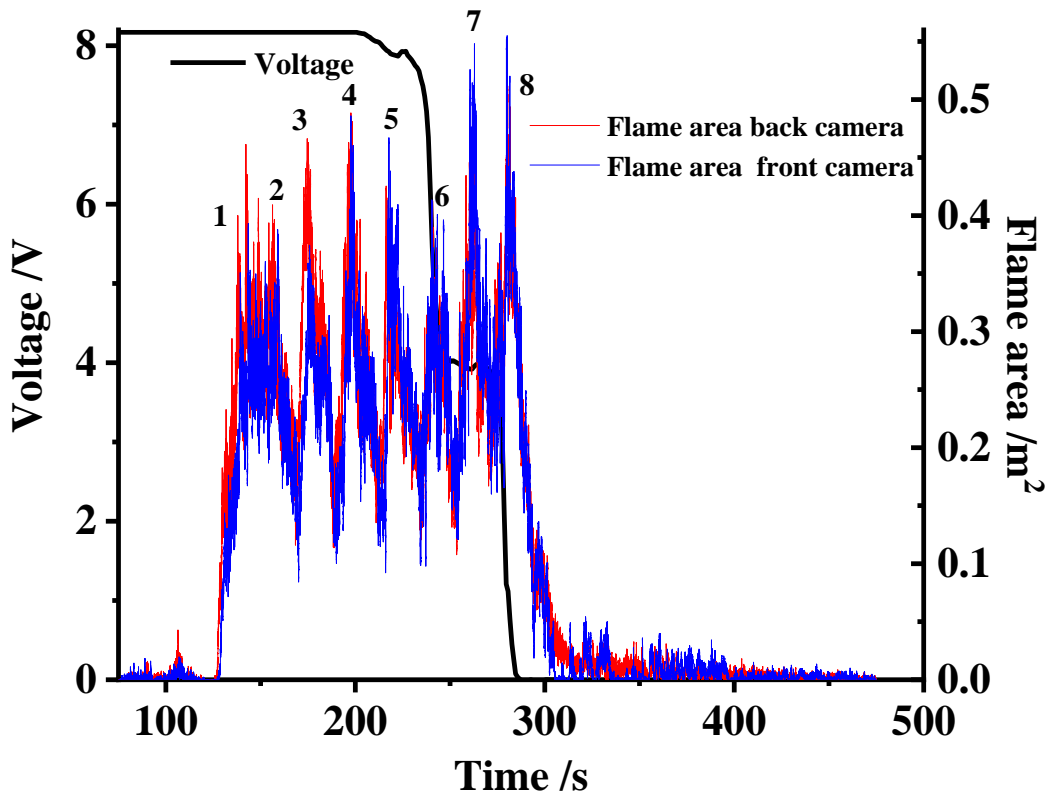
The optical images were accessed for pixels that represented flames. These were summed to find flame areas, and the furthest flame representing pixel was used to measure lengths.

The sequential loss of the cells can be seen in the plots of flame lengths calculated using the images from the two GoPro optical cameras, see Figure 3.2(a) and more clearly in the plots of flame areas in Figure 3.2(b) where seven separate peaks were observed in a span of 3 minutes, suggesting distinct thermal propagation between the cells at each peak.

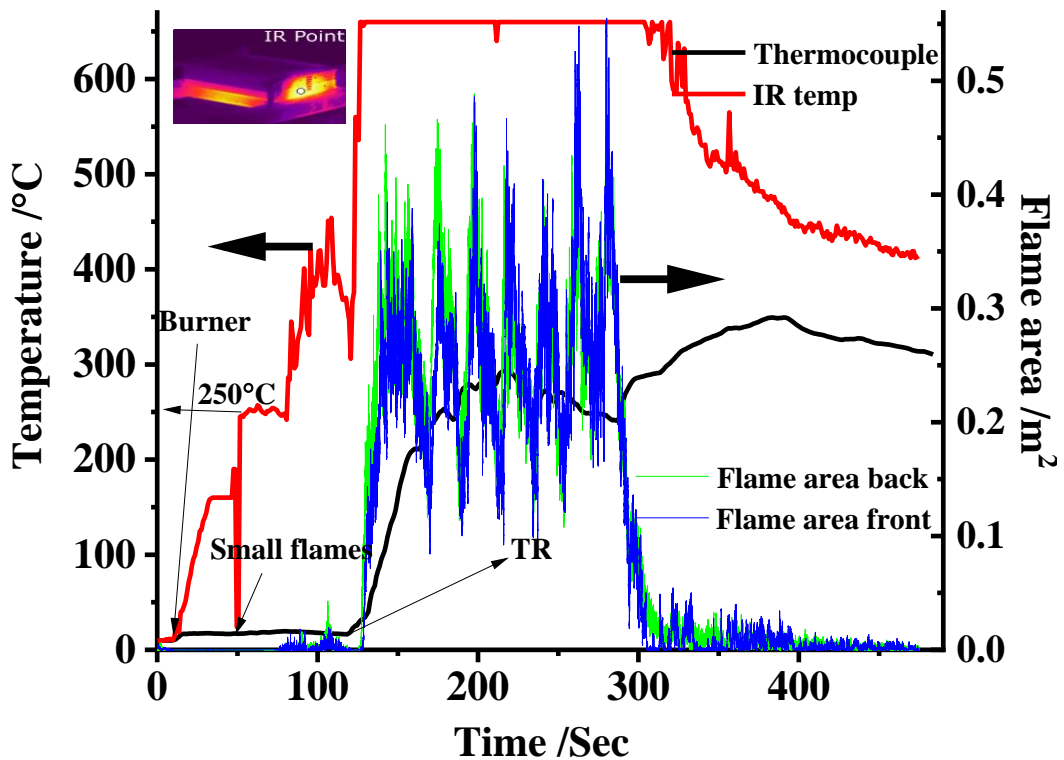
Figure 3.2(c) show plots of the thermocouple data, on the top face of the module, recorded during experiment A1 as well as the temperature of the module at the location shown in the insert obtained from the thermal imaging camera (“IR Temp”).



(a) A plot of flame lengths with significant events labelled.



(b) A plot of the module voltage and flame areas.



(c) A plot of temperatures measured by the InfraRed camera, a thermocouple on the module, and flame areas.

Figure 3.2. Data from experiment A1, (a) flame lengths, (b) voltage and flame areas, and (c) flame areas, thermocouple, and IR temperature.

The flames visible in Figure 3.1(a) were external to the module and were due to the burner. In Figure 3.1(b), flames began to be generated from the module in addition to the burner. In Figure 3.1(c), with the burner completely removed, all flames were being generated from the module itself and flare-like flames were observed from the module, with flame lengths as shown in Figure 3.2(a): the latter shows six spikes due to flares: i.e. less clearly defined than the flame areas in Figure 3.2(b). As can be seen in Figure 3.2(c), the IR temperature increased immediately as the burner was moved beneath the module, rising steadily until c.a. 2 min after which it increases very rapidly (at c.a. $98\text{ }^{\circ}\text{C s}^{-1}$) signalling thermal runaway.

In this Thesis thermal runaway is defined as a rate of temperature rise of $1\text{ }^{\circ}\text{C min}^{-1}$, as discussed in Chapter 1 the onset of thermal runaway is most commonly defined in terms of the rate of temperature rise (observed when heat dissipation lags behind heat generation), but the definition varies widely: e.g. from $1\text{ }^{\circ}\text{C s}^{-1}$ [1] to $1\text{ }^{\circ}\text{C min}^{-1}$ [2].

The camera was calibrated to operate over the ranges -40 to $150\text{ }^{\circ}\text{C}$ and 100 to $650\text{ }^{\circ}\text{C}$, and hence flatlined when the temperature reached the top of its range: subsequently, the temperature recorded by the thermal camera decreased after c.a. 6 min to c.a. $400\text{ }^{\circ}\text{C}$, and this coincided with a lack of flames around the region monitored. The thermocouple temperature lagged that of the IR by c.a. 2 min, showing little or no increase until ignition occurred and the production of the flare-like flame, after which it increased to c.a. $275\text{ }^{\circ}\text{C}$ for c.a. 1 min before increasing again to $300\text{--}350\text{ }^{\circ}\text{C}$: the unstable nature of the response reflecting the influence of the flames.

From Figure 3.2(b), it can be seen that the voltage of the top two parallel pairs of cells in the module, collapse in two clear steps once the temperature on the top face of the module reached c.a. $275\text{ }^{\circ}\text{C}$ (unfortunately, the monitoring of the output voltage from the lower quartet of cells failed): these steps are clear in Figure 3.3 which shows the first derivative of the voltage: the voltage collapsed rapidly (c.a. 42 and 55 V min^{-1}) in both steps. The temperature registered by the thermal camera rose and then remained at c.a. $250\text{ }^{\circ}\text{C}$ before increasing rapidly as thermal runaway and ignition took place: this may be due to the collapse of the ceramic-coated separators between the cells [3-5].

As can be seen from Figure 3.2(b), the voltage of the top quartet of cells was maintained for a significant time whilst the module was venting flare-like flames: it does not seem unreasonable to postulate that the flares between 125 s and 233 s were due to the lower

quartet of cells sequentially igniting (the 8 cell module was ignited from underneath, the voltage measurements were of the upper 4 cells, and the voltage was stable as the first 4 cells ignited). After which one cell of one of the remaining parallel pairs ignited with a minor loss of voltage followed by the second of the same pair, causing the voltage to decrease by 50 %: this process was then repeated. The maintenance of the cell voltage well after the ignition of the module suggests that, in contrast to reports in the literature, a drop in cell voltage cannot reliably be employed as an early warning of thermal runaway [5].

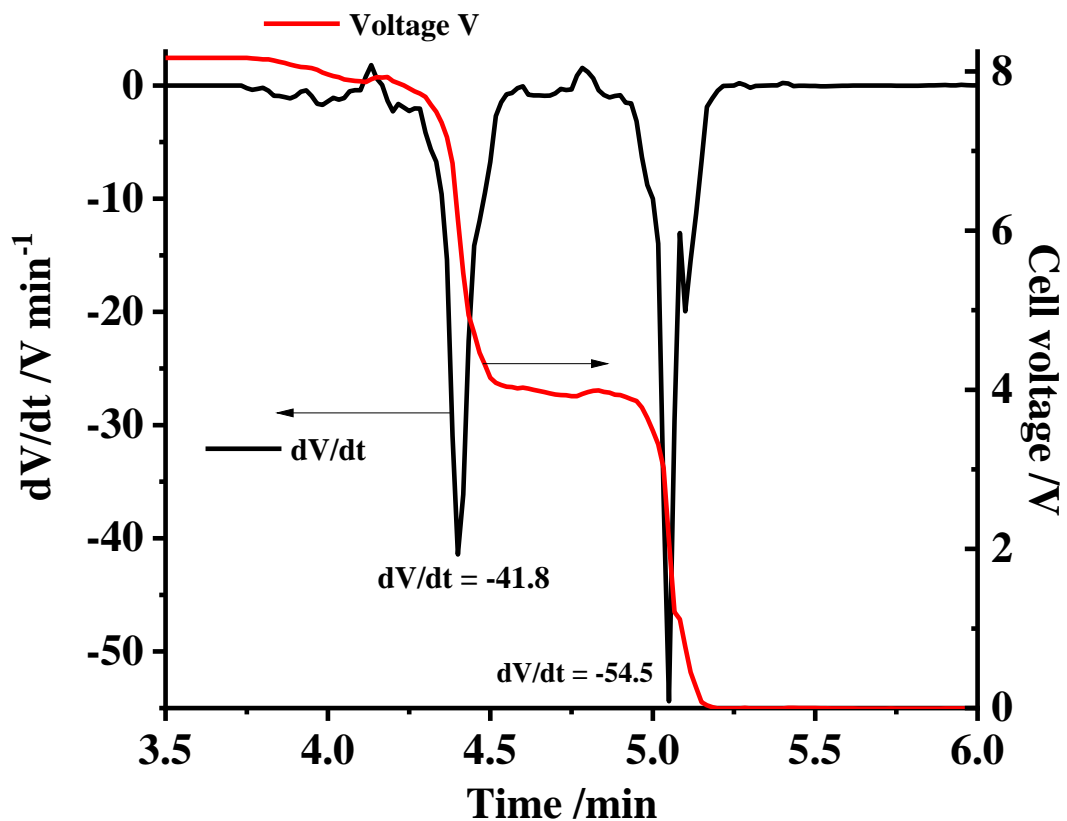


Figure 3.3. The voltage of the cells of the top quartet of the module, in Figure 3.2(b) and the first derivative from experiment A1.

As can be seen from Figure 3.2(c), the module remained hot after the last cell ignition and it was generally observed that the module carcasses remained at temperatures significantly above 300 °C for over 40 min after the fires had ceased, and hence were still potential ignition sources.

3.2.2. Experiments A2, A3 & A4.

Experiment A2 involved nail penetration in the middle of the side of the module nearest the module terminals and hence essentially between the connecting tabs of the pouch cells and is shown in Figure 2.8.

Figure 3.4 shows frames from the optical videos taken,



(a) *The nail has just touched the module case commencing the experiment (time = 0 s).*



(b) *The nail has fully penetrated the module (time = 4.17 ms).*



(c) The nail has bounced up, partially out of the module (time = 16.68 ms).



(d) The nail re-enters the module, the head of the arm now rests ontop of the module case without deforming the case further (time = 66.72 ms).



(e) A white vapour begins to be emitted from the module from about where the nail penetrated (time = 0.233 s).



(f) The white vapour is now being emitted at greater rate (time = 0.54 s).



(g) Ignition of the white vapour occurs (time = 9.5 s).



(h) The ignition of the white vapour spreads and a thinner fume from the module is observed (time = 13.4 s).



(i) Flare-like flames are now observed coming from the module (time = 18 s).

Figure 3.4. Frames from the optical videos taken during experiment A2.

In Figure 3.4, in (a) the nail is just touching the module case whereas c.a. 4.17 ms later, in (b), it had penetrated sufficiently deeply into the module to significantly deform the case before it bounced up again, see (c), albeit without the nail coming free: it then moved down into the module again such that the hammer touched the casing, (d), this time without deformation. As the nail protruded 75 mm from the hammer and the modules are 68 mm deep, the deformation of the module is clear in (b) and there was no apparent bulging of the module, these all suggest that all cells were penetrated in the first 4.17 ms. This supposition was supported by visual inspection of the module carcass which showed a clear exit hole on the underside of the module, see Figure 3.5. When the hammer bounced back and the nail partially retraced, it may not have then penetrated again fully.

The subsequent images in Figure 3.4 highlight the stages generally observed during all the abuse experiments performed on the Envision AESC modules, as well as reflecting the literature of LiB abuse experiments in general. Thus: (e) & (f), the initial evolution of dense, white vapour starting with a wisp immediately after penetration, then (g) & (h), ignition of the vapour to produce much thinner fumes, followed by (i), flare-like flames. Once all the electrical energy was expended, the fire resembled that from burning plastic with smoky flames and thin black smoke.



Figure 3.5. A photograph of the underside of the module employed in experiment A2, showing the exit hole (arrowed) of the nail.

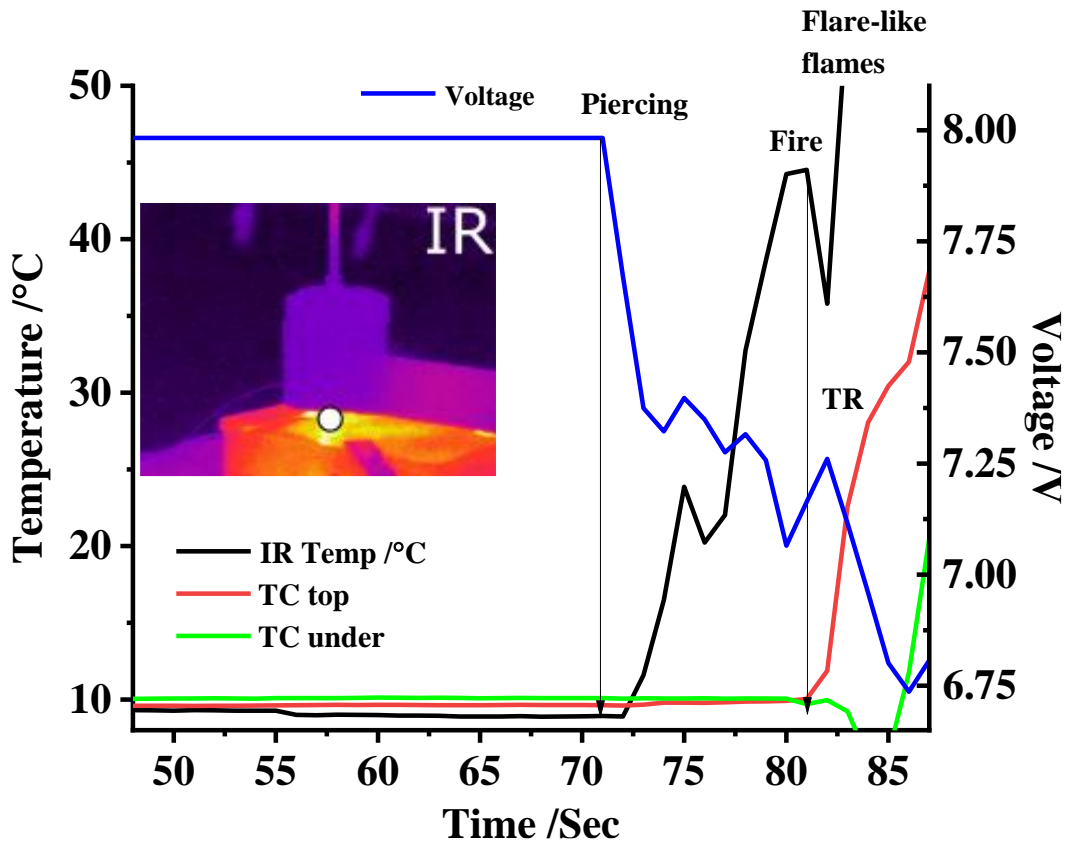
The evolution of white “smoke” or vapour has been observed previously [6] but its significance has been overlooked. From a first responder perspective, it could be mistakenly, and dangerously, attributed to smoke or steam especially as it re-appears if a burning cell is extinguished with water. In fact, the white vapour has flammable and toxic components (see below), and includes vaporised solvent [6, 7] which will condense on contact with cooler air: such a mixture could result in a vapour cloud explosion [8] if ignited in a confined space with the required concentration of oxygen. The explosion of the McMicken LiBESS in Surprise, Arizona has been reported [9, 10] to have taken place when a pair of cells in a single module (28 64 Ah NMC pouch cells arranged as 14 parallel pairs in series per module, 14 modules per vertical rack [9, 10]) were forced into thermal runaway either by lithium dendrites penetrating the separator [9] or arc heating [10]. This produced a gaseous mixture which included H_2 , CO, and CO_2 [9], likely to be mainly products of electrolyte degradation and plastic components. The mixture is also believed to contain a range of small chain alkanes, HCN, HF, NO_x and droplets of solvent [6, 7, 11-13] (and see Section 3.3. below), in other words a vapour cloud. H_2 has lower and upper flammability limits of 4 and 75 % and an auto-ignition temperature of 574 °C;

these are 2.75 %, 28.6 %, and 450 °C for C₂H₄; 5 %, 15 %, and 540 °C for CH₄; and 12.5 %, 75 %, and 609 °C for CO. However, a combination of these gases can result in not only lower flammability limits than that of the individual gases, but also a lower auto ignition temperature.

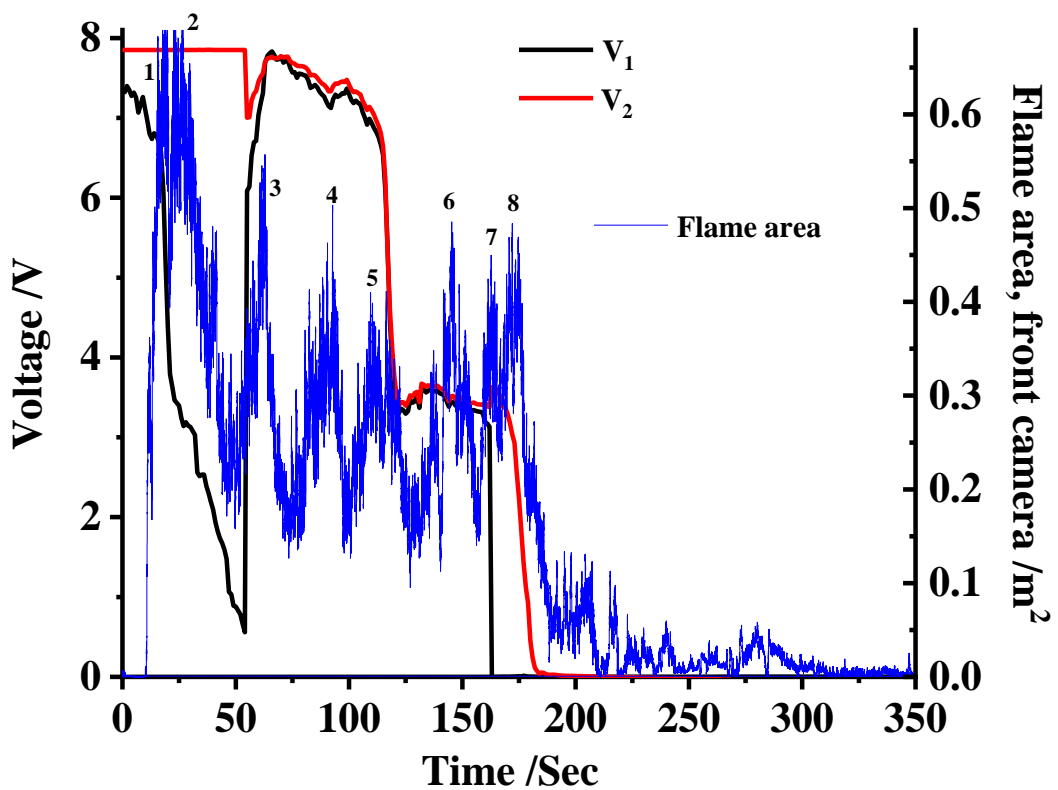
The Novec 1230 fire suppressant which was released 30 s after the laser smoke detection system triggered displaced oxygen from the container and hence prevented ignition: the gases continued to be produced as adjacent cells and modules went into thermal runaway, without any fire. When the fire department arrived on the scene, “low lying white clouds of gas/vapour mixture were observed issuing from the structure” [9]: see Figure 3.8(c) of the vapour cloud generated in experiment B2. On opening the door of the container some 3 h after the smoke alarm, it has been postulated [10] that the hot gases near the ceiling of the container billowed and touched a hot module, triggering the violent vapour cloud explosion.

As with experiment A1 above, swelling of the pouch cells was not observed in experiment A2: however, in contrast to experiment A1 above, flare-like flames were ejected from the front of the module, which was the strongest point of the casing.

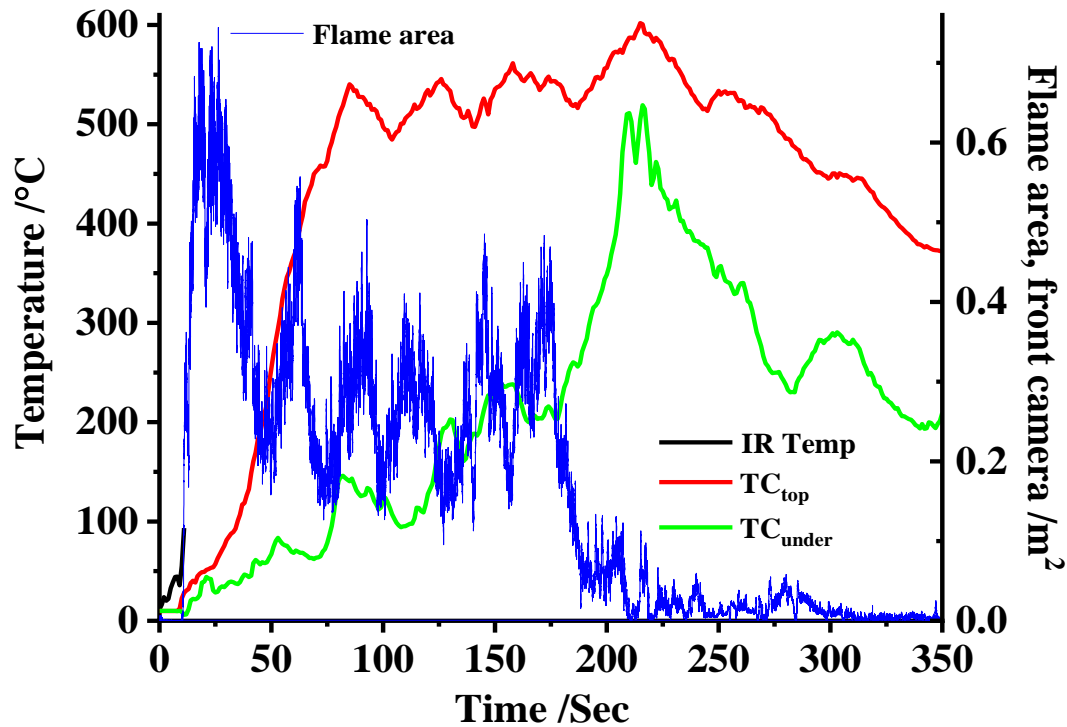
Figure 3.6(a) shows plots of the thermocouple temperatures along with the temperature of the module at the point of impact obtained from the thermal images up to thermal runaway, and the voltage V_2 of the top quartet of cells. Figure 3.6(b) and (c) show all the DAQ data (voltage and thermocouple) for the experiment.



(a) Voltage, thermal imaging, and thermocouple data from experiment A2.



(b) Voltage and the flame area data from experiment A2.



(c) Thermal camera, thermocouple, and the flame area data from experiment A2.

Figure 3.6. Data from experiment A2, (a) voltage, thermal imaging, and thermocouple, (b) voltage and the flame areas, and (c) thermal camera, thermocouple, and the flame areas.

As may be expected, the responses of the thermocouples lag significantly behind that of the thermal camera, see Figure 3.6, as the data from the latter were taken from an area immediately adjacent to the point of impact, as can be seen in the insert to (a). In addition, the temperature of the underside of the module increased more slowly than that of the module on the top face, again as may be expected.

The voltage of the top quartet of cells collapsed immediately, see Figure 3.6, and in a single step after penetration at c.a. 50 V min^{-1} from 8 V to c.a. 0.6 V as the temperature of the top face of the module reached c.a. $324 \text{ }^\circ\text{C}$. However, and very surprisingly, the voltage then recovered to c.a. 6.3 V at 168 V min^{-1} before increasing more slowly to 7.8 V before decreasing again as the temperature on the top face of the module reached $420 \text{ }^\circ\text{C}$: this collapse was in two stages, again reflecting the sequential failure of the parallel pairs of cells. The first step tracked that of the lower quartet of cells and occurred at c.a. 50 V min^{-1} . The remaining two parallel cells of the top quartet then decreased faster (100 V min^{-1} c.f.f. 24 V min^{-1}) and 36 s earlier than the remaining parallel cells in the lower quartet. The varying thermocouple responses reflect the effect of the flames licking around them.

Figure 3.6(a) & (b) show the flame areas calculated from the front video camera data (the rear camera failed to record): as can be seen, the ignition of the various cells is shown by the various flame area peaks, where the flame areas drop after the initial peaks from the ignition of a new cell, and then spike to a peak again when the next cell ignites. From the figures, it is clear that the magnitude of the maximum flame areas varied between c.a. 0.4–0.7 m², at each cell ignition. After the last cell ignited, the flame area quickly reduced as the remaining flames were simply due to the remaining burning plastic. In terms of the failure of individual cells, Figure 3.6(b) suggests that the cells fail as in the order shown in Figure 3.7.

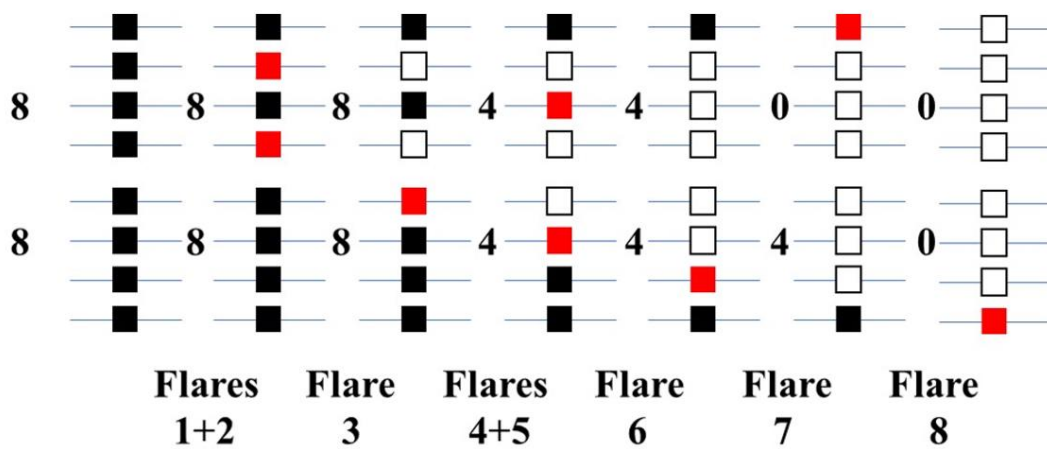


Figure 3.7. The failure of the individual cells of the module during experiment A2 based on the voltage and flame area data in Figure 3.6(b), black represents undamaged cells, red represents failed cells from previous flare, and white represents dead cells.

In Figure 3.7, the black cells are undamaged, the red cells have failed as a result of the previous flare, and the white cells are dead. The numbers refer to the measured voltages. Abaza et al. [14] and Zhao and co-workers [15] postulate that a high rate of voltage collapse during nail penetration indicates a low short circuit resistance, and that this determines the short circuit current and hence the heating rate and temperature rise. The short-circuit resistance R_s is given by:

$$R_s = R_{\text{nail}} + R_{\text{cnt}} \quad (1)$$

where R_{nail} is the resistance of the nail and R_{cnt} the contact resistance. However, the variability across nominally identical experiments [14] suggests that this may be a somewhat over-simplistic model, and the data in Figure 3.6 definitely support this critique as, despite having all been penetrated, all eight cells are sustaining significant voltages some 2 minutes after thermal runaway was marked by the appearance of the flare-like flames and with temperature of the top surface of the module at over c.a. 500 °C.

Yokoshima and co-workers [16] have suggested a more sophisticated circuit model of nail penetration involving multiple cells. The authors employed X-Ray imaging to study the nail penetration of LiCoO₂ pouch cells in-situ: they observed increases in cell voltage after penetration as well as the melting of the nail and the boiling of the organic solvent of the electrolyte (ethylene carbonate, diethylene carbonate and lithium hexafluorophosphate) due to the high short circuit current densities and consequent Joule heating. The increase in cell voltage was ascribed to the breaking of the internal short circuit through the nail due to the melting of the nail and the boiling away of the electrolyte. They also observed a white gas which they linked to the boiling electrolyte. Thus the initial collapse of the cell voltages of the top quartet of cells in Figure 3.6 must be due to the initial short circuiting of the four cells by the nail: the recovery logically must then be due to the loss of the short circuit, which may be due to the boiling away of the electrolyte around the nail and/or melting of the aluminium current collectors: given that the melting points of aluminium and copper are 660 and 1083 °C, respectively, it is most likely the former that melts away from the nail and breaks the circuit. Recent studies by Feng and co-workers [17, 18] provide a complementary explanation of the data in Figure 3.6, involving the vapourisation of the electrolyte and this is covered in Section 3.3. below.

Again, the data in Figure 3.6 strongly suggest that, at least for this chemistry and form factor, voltage drop cannot be employed as an early warning of thermal runaway.

Abaza and co-workers [14] investigated the nail penetration of 15 Ah NMC + LMO pouch cells and stated that such abuse should not result in the swelling of the cells as the gases produce could escape past the nail: however, they did observe swelling. Two further nail penetration experiments were carried out at the DNV GL site, differing from experiment A2 only in the location of the penetration (middle of the casing and in the lower corner, see Figure 2.8, and in both cases, the cells swelled before popping and ejecting dense white vapour before the vapour ignited. In experiment A3, the cells expanded for 6 s after nail penetration before popping after which they ejected dense white vapour for 2 s which then ignited. In experiment A4, the cells expanded for 4 s before popping, ejecting both thick black smoke and white vapour, igniting 10 s after a significantly audible popping: black smoke has been attributed to the ejection of cathode particles [18, 19]. Flare-like flames were seen in both experiments, emerging from the rear and side of the module in both cases, in contrast to experiment A2. In both cases, the

cell voltages of the top quartet of cells collapsed in a single step after which the voltage of the lower quartet collapsed, 96 s and 48 s for experiments A3 and A4, respectively, after nail penetration as was observed in experiment A2.

3.2.3. Experiments B1 & B2.

The first experiment at the Fire Services College was a nail penetration between the tabs, identical to experiment A2 except the module was charged to c.a. 4.03 V, i.e. 75 % SOC. The same sequence of events were observed as in the A2 experiment, see Figure 3.8: a wisp of white vapour as soon as the nail penetrated 0.532 s (a) and 0.538 s (b), then the evolution of thick white vapour followed by (in this case) the almost immediate ignition of the vapour 3.794 s (c) and 3.858 s (d), then flare-like flames from the front, side and rear of the module 10.567 s (e) and 82.6 s (f) after penetration.



(a) A photograph taken 0.532 s into experiment B1.



(b) A photograph taken 0.538 into experiment B1.



(c) A photograph taken 3.794 s into experiment B1.



(d) A photograph taken 3.858 s into experiment B1.



(e) A photograph taken 10.567 s into experiment B1.



(f) A photograph taken 82.6 s into experiment B1.

Figure 3.8. Frames from the optical videos taken during experiment B1.

Following on from experiment B1, and experiment A2, the aim of experiment B2 at the FSC was to assess the validity of the generally held perception that higher SoCs represent more of a hazard [7, 20], particularly in terms of toxic and flammable gas release [13] and involved a repeat of the 75 % SoC experiment at 50 % SoC (B2).

Figure 3.9 shows frames from the optical videos taken during experiment B2: (a) was 26.47 s after the nail penetrated the module; (b) was 35.47 s after penetration and (c) was 52.13 s after penetration. The white vapour did not ignite during the experiment, as can be seen from Figure 3.9(c), was clearly heavier than air, rolling across the ground, pushed by the slight breeze running from right to left in the images.

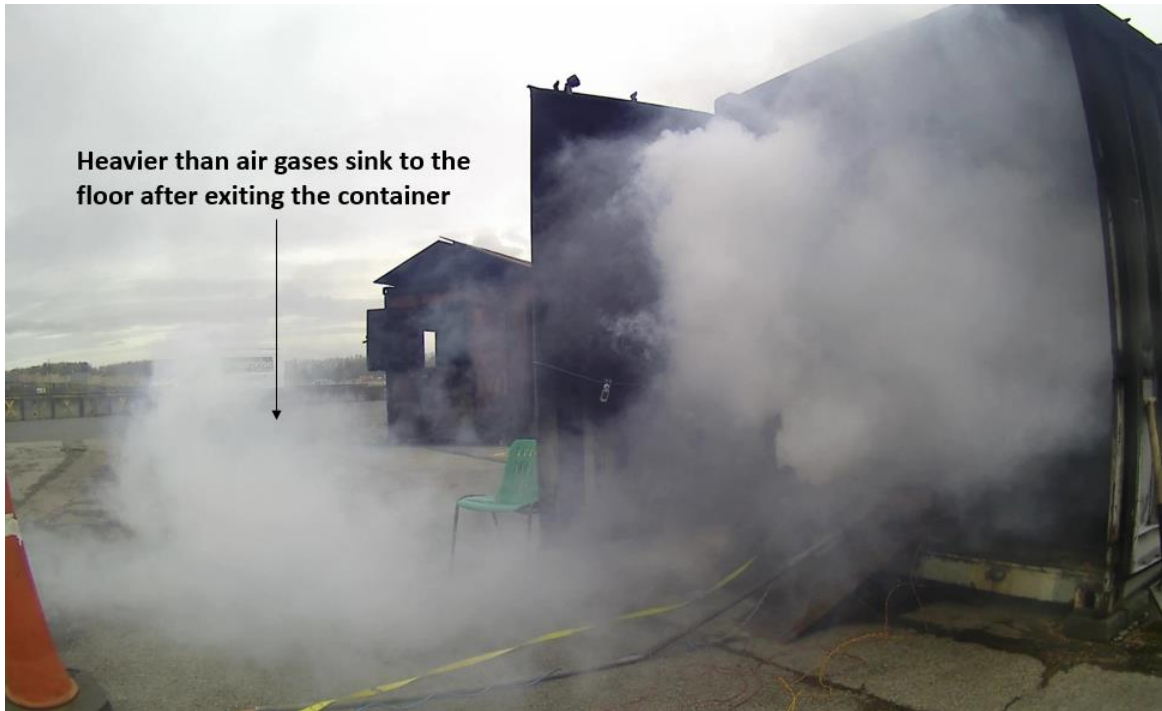
Figure 3.10 shows plots of the gas sensor, thermocouple and thermal readings taken during the experiment.



(a) A photograph taken 82.6 s into experiment B1.

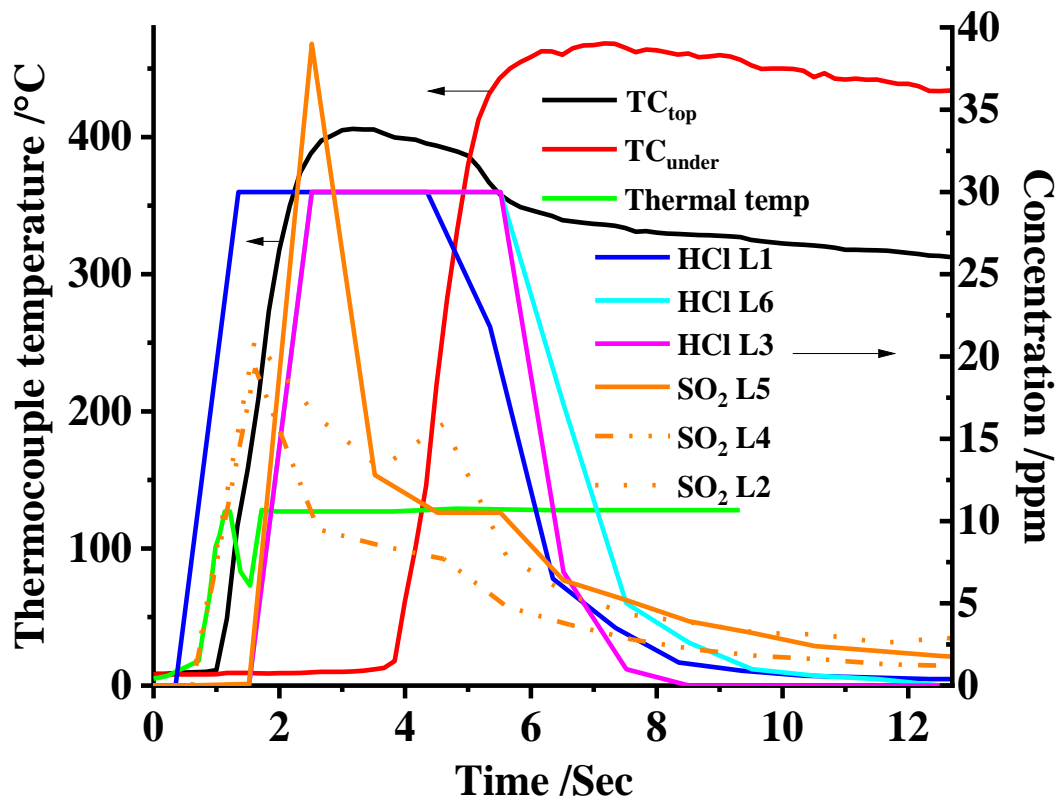


(b) A photograph taken 82.6 s into experiment B1.

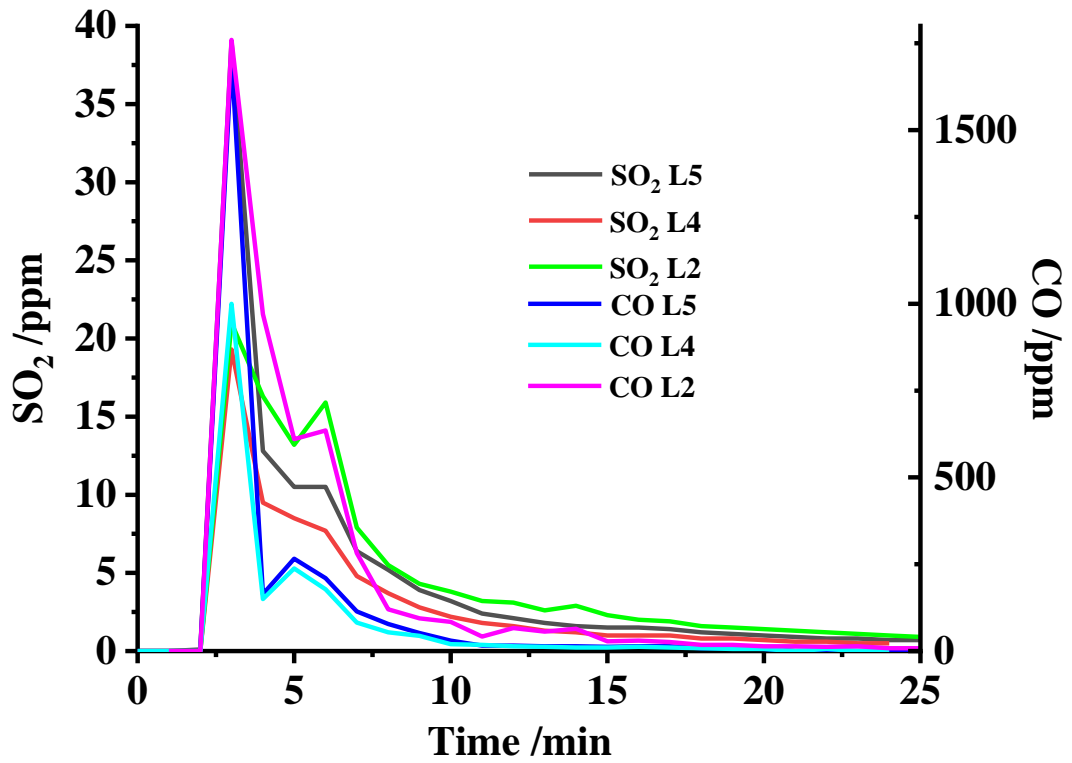


(c) A photograph taken 82.6 s into experiment B1.

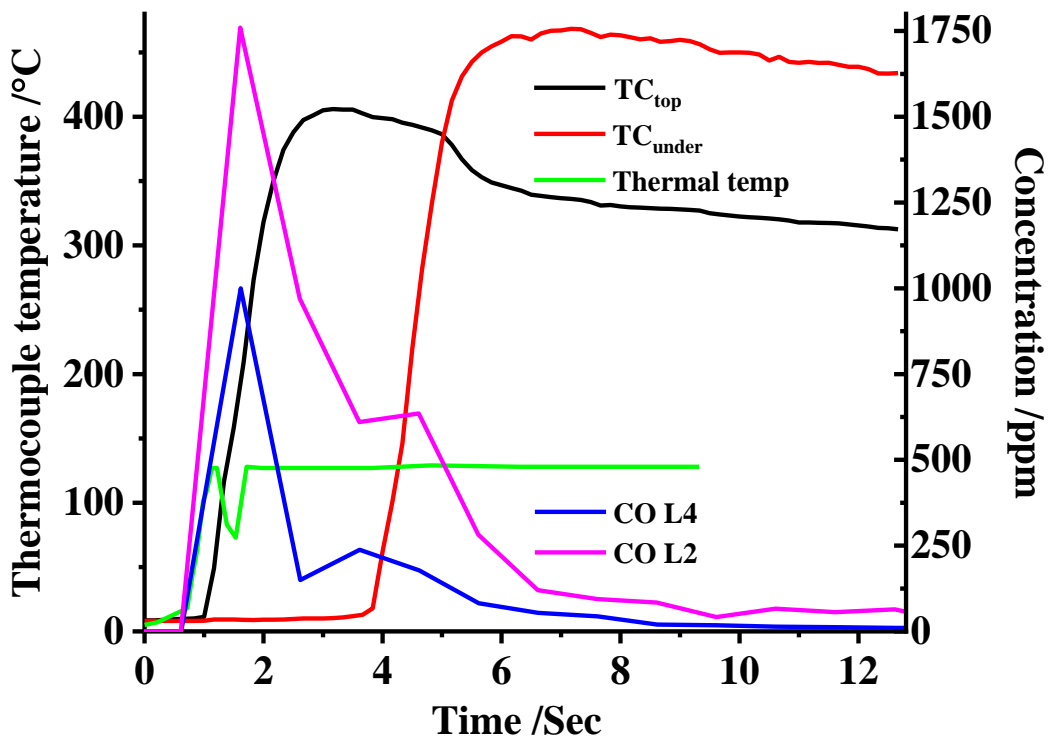
Figure 3.9. Frames from the optical videos taken during experiment B2, they were collected at the times specified in the text.



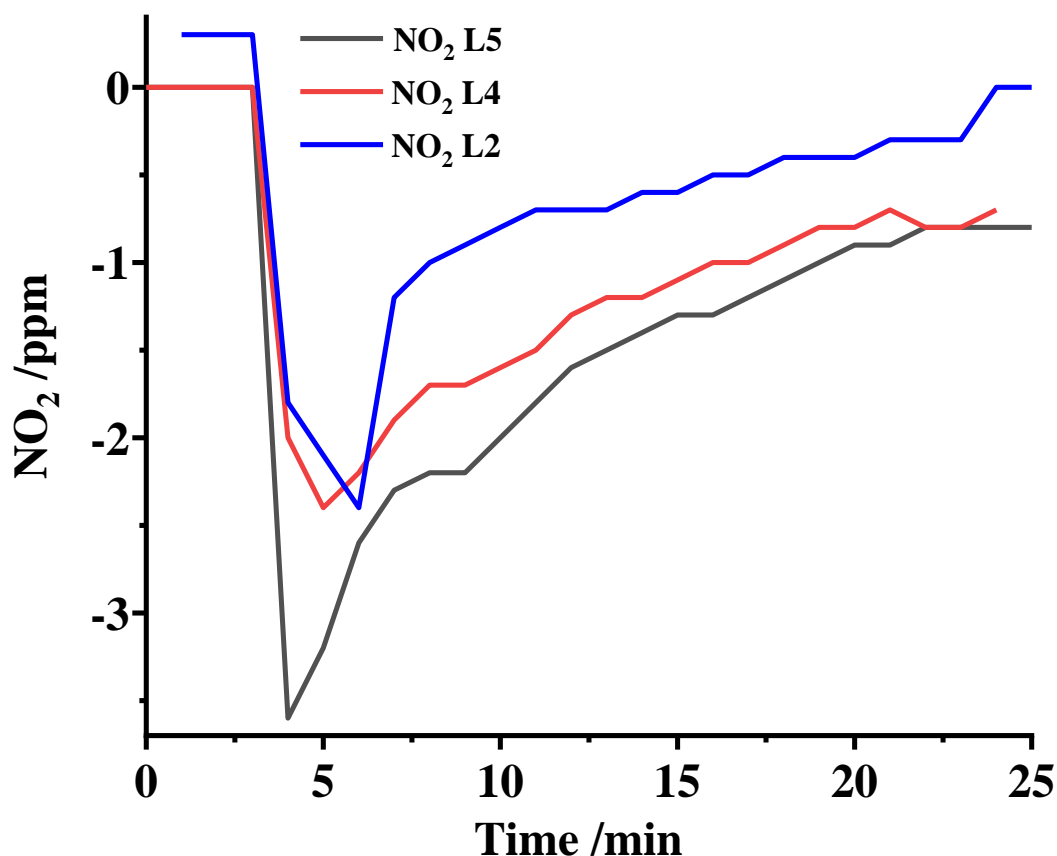
(a) Thermocouple thermal camera, HCL, and SO₂ data from experiment B2.



(b) SO₂ and CO data from experiment B2.



(c) Thermocouple and CO data from experiment B2.



(d) NO₂ data from experiment B2.

Figure 3.10. Thermocouple, thermal camera, and concentrations of gases detected during experiment B2.

As can be seen from Figure 3.10(d), the HCl/HF sensors went over their maximum range of 30 ppm: the locations L1–L6 correspond to those on Figure 3.11 and a full scale diagram is shown in Figure 2.13. In addition, **Error! Reference source not found.** summarizes the maximum sensor readings observed during the experiment and the times that they occurred after nail penetration.

During thermal runaway of LiBs and prior to ignition, a variety of gases are produced within the cells and vented to the atmosphere, including HF, CO₂, CO, H₂, a wide range of small chain alkanes and alkenes [6, 7, 11-13, 21] and the solvents comprising the electrolyte such as ethylene carbonate and dimethyl carbonate [6, 7]. The response of the NO₂ sensor suggests that HCN was also produced, and this compound has been reported previously [20, 22-24], and, as was stated above, the personal protective equipment of the first responders attending the explosion of the LiBESS at Surprise were contaminated with HCN [25].

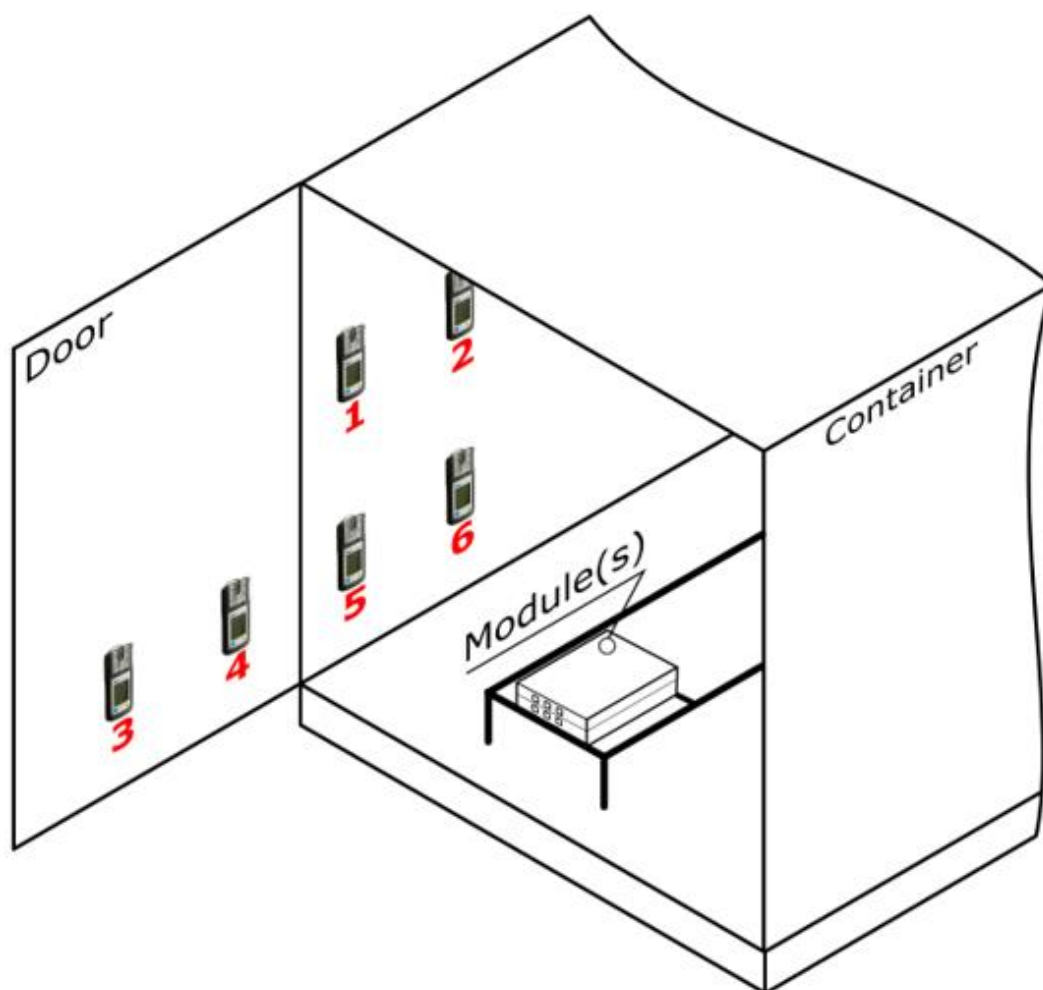


Figure 3.11. Schematic showing the locations of the gas sensors in the FSC experiments.

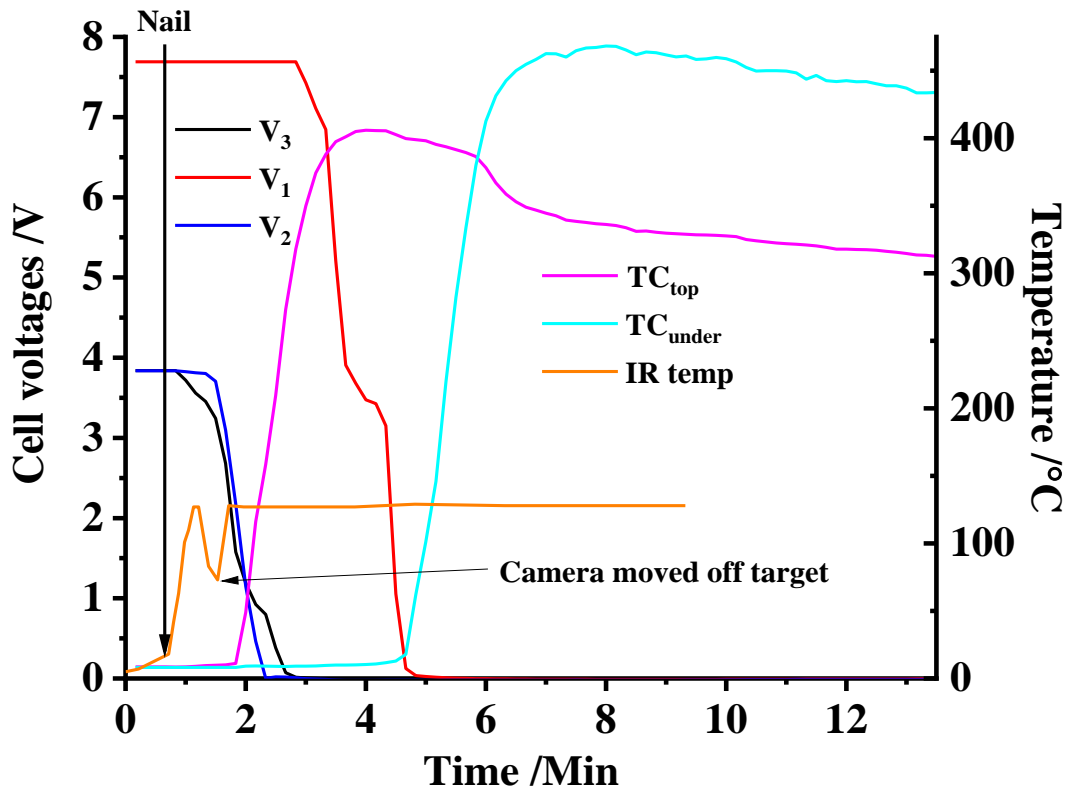
Table 3.1. Maximum sensor readings and times observed during experiment B2.

Gas	Location	Time / min	Maximum concentration / ppm	Comments
CO	2	3	1760	
	4	3	1000	
	5	3	1710	
SO ₂	2	3	21	
	4	3	19.3	
	5	3	39	
NO ₂	2	6	-2.4	Interference by HCN
	4	5	-2.4	
	5	4	-3.6	
HCl	1	1-5	30	Over range
	3	2-6	30	
	6	2-6	30	

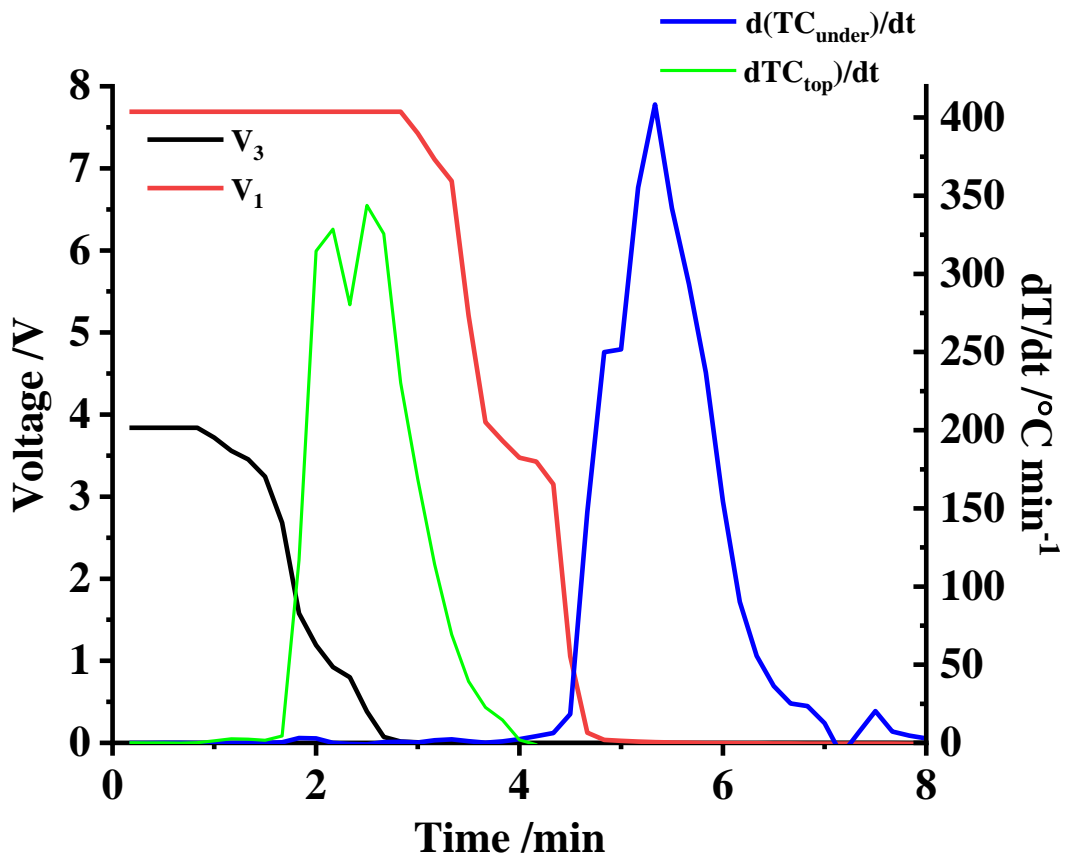
The data in Table 3.1 suggest that the heavier-than-air SO₂ filled the lower part of the container and drifted with the wind past the door. Interestingly, the time dependence of its concentration matched exactly that of CO, see Figure 3.10, and all sensors showed the CO and SO₂ reaching their maximum concentrations 3 min after nail penetration. This was confirmed during the other two experiments at the College (nail penetration at 75 % SoC and overcharge of two of the cells in one of the modules of a 5-module stack), suggesting the two gases had a common origin. Reductive additives to aid SEI formation typically contain sulphur [26] including SO₂, CS₂, polysulfide, cyclic alkyl sulfites such as ethylene sulfite and propylene sulfite, and aryl sulfites. Sulphur may also come from alternative lithium salts such as LiFSI [27]. However, ethylene sulphite is commonly employed in LiBs [28-31] and hence it is highly likely that this additive is the source of the SO₂ and at least some of the CO.

The amount of vapour released within the container, unlike the other experiments where the vapour ignited almost immediately after release, allowed a much larger volume of the container to be saturated by a flammable mixture. If this mixture were to ignite, there could be a possibility of a flash fire, fire balls developing, or in extreme cases even a vapour cloud explosion. The severity of the deflagration event would depend on the amount of overpressure generated as the flame accelerates at significant speed in the vapour cloud. Any of these scenarios would be extremely dangerous [32].

Figure 3.12 shows plots of the thermocouple temperatures and cell voltages observed during the experiment. In contrast to the experiments where the vapour ignited causing the thermocouple readings to fluctuate due to the flames, the first derivatives of the thermocouple readings from experiment B2 at the College showed a homologous response, see Figure 3.12(b) with a single, well-defined maximum for each thermocouple. As can be seen in the figures, even though the nail penetrated all the cells, whilst the voltages of the top four cells collapsed fairly soon after penetration, the lower four cells retained their charge for c.a. 2 min.



(a) Voltage, thermocouple, and thermal camera data from experiment B2.



(b) Voltage and the first derivatives of thermocouple data from experiment B2.

Figure 3.12. Voltage, thermocouple, and thermocouple data recorded during experiment B2, and the first derivatives of thermocouple data.

Figure 3.13 shows frames taken from the thermal camera video at 60 and 143 s, respectively, after nail penetration. Throughout the experiment, solid objects were ejected from the module and bounced as they hit the ground; these objects appeared to be at temperatures \leq c.a. 100 °C, i.e. showing white in Figure 3.13(a), circled. These events were not visible to the naked eye and did not appear in the optical video due to the dense vapour. Also, clearly visible in Figure 3.13(a) is a jet of vapour being ejected horizontally. In Figure 3.13(b), liquid can be seen dropping from the module, circled, which also registered at \leq c.a. 100 °C, the temperature in the target sights did not rise above c.a. 129 °C throughout the experiment, despite the thermocouples on the module registering temperatures as high as 450 °C. Interestingly, the potentially adverse effect of the vapour cloud on thermal imaging cameras was confirmed during an incident involving a domestic lithium-ion battery energy storage system (LiBESS) in Campbelltown, Australia in summer 2022 [33]. The LiBESS went into thermal runaway without ignition, generating the vapour cloud. The LiBESS was located on a wall in a side room c.a. 8 m x 6 m and 2.4 m high, and the room was full of the vapour cloud when the fire service arrived, with zero visibility. The first sweep of the room with a thermal imaging camera gave no reading and the fire officers then left the room, at which point a roof panel dislodged and the natural ventilation reduced the vapour cloud by c.a. 30%. A second sweep using the camera then showed the heat signature of the LiBESS at c.a. 300 °C and increasing by c.a. 25 °C in the next 10 s. This effect of the vapour cloud on thermal imaging had not been observed previously.



(a) A frame taken by the thermal camera in experiment B2 at 60 s.



(b) A frame taken by the thermal camera in experiment B2 at 143 s.

Figure 3.13. Frames from the thermal camera taken during experiment B2.

3.3. Discussion

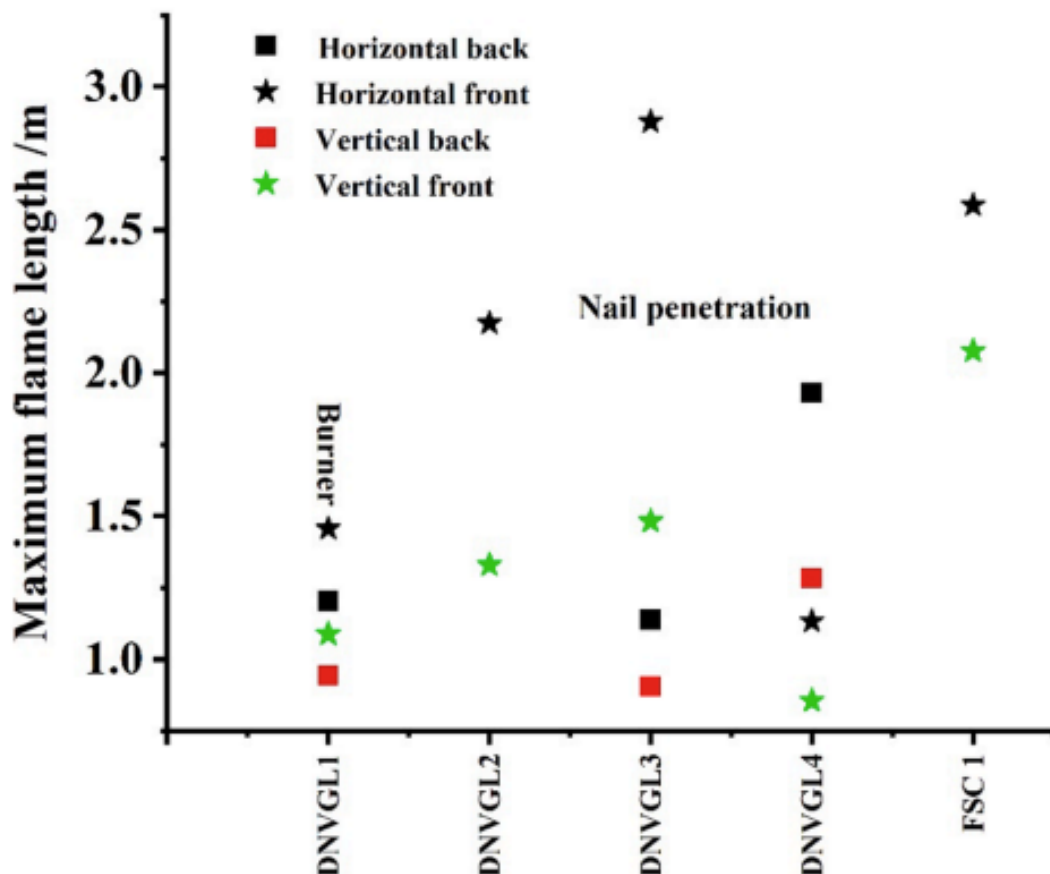
As the DNV 1 experiments were conducted in an entirely open environment, and the FSC experiments were in the partially contained environment of an open container, the boundary conditions constraining the escaping gases and the local environmental temperature during the battery fires were different, hence affecting the flame lengths. The maximum vertical and horizontal flame lengths measured via image processing in each experiment are shown in Figure 3.14(a). Experiments A2, A3 and A4, all nail penetration experiments but with penetration at different points on the modules, showed different maximum flame lengths, with a maximum flare of 217 cm observed. It can be seen from Figure 3.14(a) that the maximum flare length was observed in experiment B1 at the FSC (75 % SoC, nail penetration). The maximum flame length measured was 275 cm, which is c.a. 9 times the length of the module itself. Hence, careful consideration must be made in safety designs to account for safety distance, as from these observations any flammable material or mixture up to 275 cm from the pack could receive intense and rapid heating rates from these flares in the case of a module failure. It is worth noting that there are few studies reporting SO₂ and hence, ideally, the mechanism by which this is produced requires further attention. In this case, the yield of SO₂ was significantly higher in the 50 % SoC experiment (19–39 ppm) than in the 75 % SoC test (5.1 ppm – see Figure 3.14(b)). This agrees with the work of Lecocq et al. [27], who found that more SO₂ was released at lower SoC's, but contrary to other studies [13, 20, 34] reporting higher amounts of SO₂ at the higher SoC's (albeit for different chemistries).

Carbon monoxide has been identified as one of the main constituents of the gas released during thermal runaway [33-37]. Ribiere et al. [20] found that the amount of CO produced increased with SoC, and this has been confirmed by other studies [13, 22, 38]. However, it appears the cathode chemistry of the LiB has a major influence on the gases produced: thus Said et al. [39] found comparable levels of CO for LCO and NMC, but an order of magnitude less for LFP; Golubkov et al. [40] found much higher amounts of CO released from LFP compared to NCA. Sun et al. [13] found that the amount of CO released was in the order: LMO > LFP > LCO > NMC, with LMO producing almost as twice as much CO as NMC. The authors concluded that a 10 Ah pouch cell could produce > 10,000 ppm CO, which exceed levels that that can cause serious sickness, and even death (1000–2000 ppm in 1–2 min). During these experiments, the CO reached concentrations of 1000–1760 ppm in 3 min. This suggests a potentially serious threat to

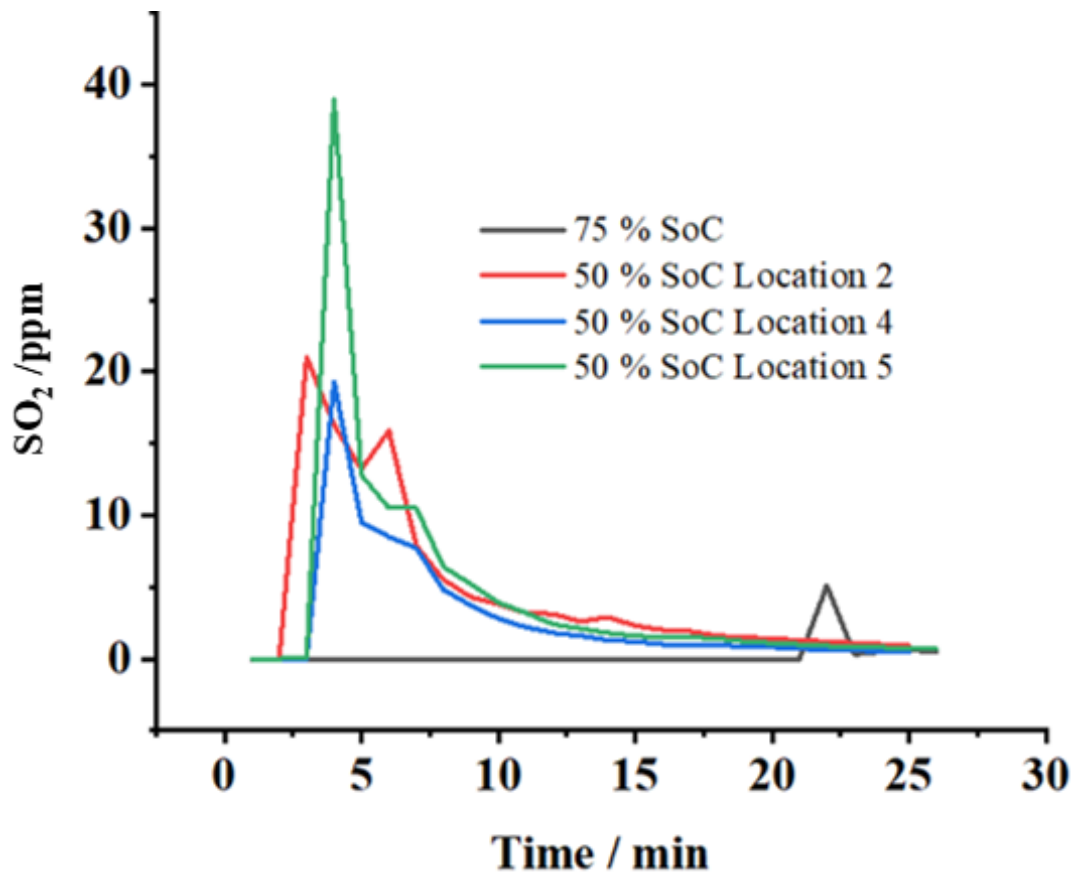
health and life just from this component of the white vapour. Ribiere and co-workers [20] have evaluated the toxicity levels of the fumes from burning LiBs, based on their work on LMO cells which has allowed the estimation of the battery energy in Wh that could lead to exposure above the Immediate Effects Threshold (IET) and the First Lethal Effects Threshold (FLET) caused by 60 mins exposure to a LiB fire in a 50 m³ room, and typical data are shown in Table 3.2. Thus, a single burning 236 Wh pouch cell in a 50 m³ unventilated room would take 2.8 min and 5.1 min to reach the IET and FLET of HF, respectively. The same times would be required for a burning 8 cell, 53.8 Ah module in a 400 m³ room.

<i>Threshold</i>	<i>HF/ppm</i>	<i>CO/ppm</i>	<i>NO/ppm</i>	<i>SO₂/ppm</i>	<i>HCl/ppm</i>
<i>IET</i>	60	290	280	530	1320
<i>FLET</i>	110	1140	2080	4710	7880

Table 3.2. Immediate effects thresholds and first lethal effects thresholds for various gases produced by lithium ion cells during the thermal runaway.



(a) Maximum vertical and horizontal flame lengths measured in DNV 1 experiments A1–4 and FSC experiment B1.



(b) A comparison of SO₂ concentrations for experiment B1 (75 % SoC) and experiment B2 (50 % SoC).

Figure 3.14. Comparisons of flame measurements and SO₂ concentrations from experiments A1-4, B1 and B2.

The thermal runaway of LiBs has been studied in depth of late [3, 17, 18, 41, 42], and the steps involved in thermal runaway are broadly accepted as [3]:

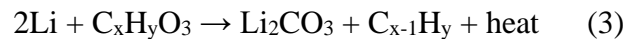
1. The breakdown of the Solid Electrolyte Interface (SEI). The Solid Electrolyte Interface (SEI) is the other front-line safety system: LIBs are unique in battery technology in that the fully-lithiated graphite anodes typically employed have c.a. the same redox potential as that of metallic lithium [43] and hence should immediately reduce the organic carbonates employed in the electrolyte to hydrogen, various flammable gaseous hydrocarbons and heat [44]. The reason that this does not occur is the serendipitous formation of a protective barrier, the SEI, which is permeable to lithium ions, between the anode and solvent during the first charge. The SEI continuously varies in thickness during the life of the battery, but overall increasing in thickness and incorporating lithium ions as it does so [45]. The exact composition of the SEI is unknown, although it is known to incorporate lithium ions and is likely dynamic: it is generally represented as

lithium salts of carbonate fragments, and the breakdown of the SEI may be represented as [3]:



This commences around 60–70 °C, but the SEI can self-heal up to 80 – 120 °C [17, 46], albeit to form a less-effective barrier to the solvent. Feng and co-workers [46] suggest that there are three stages: (i) initial SEI decomposition 80 – 120 °C; (ii) the balanced region between 120 and 250 °C where the self-healing rate is equal to the rate of decomposition and (iii) thermal runaway above 250 °C due to separator collapse, major internal short circuit and hence rapid increase in temperature. Wang et al. [47] have reported that the activation energy barrier for the decomposition of the SEI, and the onset temperature, both decrease with increasing SoC.

2. The reduction of the organic carbonate solvent by exposed lithiated graphite. Once holes form in the SEI, direct reduction of the solvent can take place which can be represented in general terms as:



where $\text{C}_x\text{H}_y\text{O}_3$ is an organic carbonate (e.g. $\text{C}_3\text{H}_4\text{O}_3$, ethylene carbonate (EC); $\text{C}_3\text{H}_6\text{O}_3$, dimethyl carbonate (DMC); $\text{C}_4\text{H}_8\text{O}_3$ ethyl methyl carbonate (EMC), $\text{C}_5\text{H}_{10}\text{O}_3$ diethyl carbonate (DEC) and $\text{C}_4\text{H}_6\text{O}_3$ propylene carbonate (PC)), C_{x-1}H_y represents a number of short chain alkanes and alkenes and Li represents the lithium in the graphite. CO is also generated by reaction with the solvent, e.g.:



Hydrogen is produced via reduction of the binders employed in the cells (e.g. PVDF [3]). This becomes significant at temperatures where the SEI does not self-heal.

3. Melting and collapse of the separator. The temperature at which collapse of the separator is initiated depends upon composition: e.g. the melting point of polyethylene is 130 °C, polypropylene 170 °C and ceramic-coated polymer/mixed polymer separators c.a. 200 °C [3, 46]. However, melting may not result in the immediate collapse of the separator structure. Once the integrity of the separator is lost, significant internal short circuits can occur and, until the work of Feng and co-workers [17, 18, 48], this was considered to be the trigger and main driving force behind thermal runaway [5, 7, 46].

4. The exothermic collapse of the cathode structure to generate oxygen as well as (in certain cases) highly oxidising oxides [46]: the onset temperature at which this occurs is highly dependent upon the oxide, e.g. from 150 °C to 310 °C [3, 46]. The oxygen then exothermically oxidizes the organic solvents in the electrolyte [36].

The mechanism of thermal runaway following overcharge involves the same steps as discussed above but is initiated by the over-lithiation of the anode to form lithium metal at the surface [49] and the exothermic delithiation and collapse of the cathode structure [3] resulting in increased resistance and hence Joule heating. The lithium metal will exothermically reduce the solvent as detailed above and can form dendrites which grow through the separator to cause an internal short circuit. When the temperature exceeds that of the melting point of lithium, 180 °C [50] this will also result in an internal short circuit. Lithium plating is increased with increasing temperature [51] suggesting that cells retaining their charge but under thermal abuse from adjacent cells could show enhanced lithium plating. The model discussed above has become increasingly challenged: thus, there remains no clear and quantitative definition of thermal runaway [5, 18], there is disagreement as to whether gases are vented before or during thermal runaway from prismatic or cylindrical cells and the exact nature of the gases produced [6, 18, 19]. In addition, there are new theories of thermal runaway and refinements of the current, rather generalised “model”. Thus, Liu and co-workers [52] have shown that the oxygen produced as the cathode structure collapses is consumed at the anode (“chemical crosstalk”) in a highly exothermic process (c.a. 7x more heat produced than from cathode collapse alone) which can commence at 150 °C (e.g. for NMC cathodes), significantly below the temperature for the collapse of the more stable separators (e.g. PET nanofibers, 257 °C) and hence thermal runaway can be initiated without the need for separator collapse and concomitant significant ISC. There is also increasing evidence that thermal runaway may not simply be defined as a temperature rise of 1 °C s⁻¹ if thermal runaway is more generally defined as a self-sustaining heating process, i.e. once the temperature of a cell passes a point of no return, the exothermic reactions continue to generate heat and the cell will progress inevitably to an exponential increase in temperature [53]. It has been stated that [6] if the electrolyte boils away from a cell, thermal runaway cannot happen: a simple search of the literature proves this is not the case, with venting of electrolyte succeeded by thermal runaway [53]. Moreover, recently, Feng and co-workers [17, 18] have shown that lithiated graphite anode and NMC cathode powders can undergo a direct

and highly exothermic solid state redox reaction at temperatures \geq c.a. 250 °C (presumably the via the transfer of lithium ions) and have proposed that internal short circuit initiates thermal runaway but is not responsible for its propagation. Instead, the internal short circuit generates sufficient Joule heating for significant vaporisation of the solvent to take place this, coupled with the collapse of the separator allows direct electrochemical reaction between anode and cathode which generates sufficient heat to raise the temperature above 800 °C and perpetuate thermal runaway.

Temperature is often quoted as a potential early signal of thermal runaway: however, overcharging can result in little or no temperature change; i.e. a few degrees during the overcharge process [53], whilst there can be a wide variation in temperature across the can of a lithium ion cell subjected to thermal abuse [6].

There is a major dearth of system-level research as opposed to cell or module level: such studies are becoming increasingly critical as it is becoming apparent that self-ignition may occur at lower temperatures in larger assemblies of cells/modules [45].

Finally, the composition, ubiquitous nature and hazards of the white vapour have not been recognised. It can be viewed that the white vapour is produced by the pyrolysis of the electrolyte by the heat generated in thermal runaway. This gas cannot ignite within the cells as the oxygen produced during thermal runaway is insufficient to sustain combustion [3], which thus takes place once the gases produced exit the cell and if there is an ignition source present or via friction between gas and the exit point, and the cell SoC is $>50\%$.

The latter point is interesting as, for example at 50 % SoC, there should still be a sufficient stored electrical energy for arcing to occur and provide an ignition source.

Feng et al. [18] suggest that the “white smoke” is primarily due to solvent vaporised prior to thermal runaway, and that such venting happens at successively higher temperatures as the various components vaporise. We disagree with two key facts: venting from the pouch cells studied takes place during thermal runaway, and the white vapour not only contains condensed solvent droplets but also pyrolysis products, as can be seen from the gas sensor data obtained during the experiments at the FSC: further, evidence for pyrolysis comes from the observation of the tied evolution of SO₂ and CO. The black “smoke” observed in DNV 1 experiment A4 may be attributed to the melting of the aluminium current collectors and concomitant ejection of the cathode active material [15]: this experiment of all the nail penetration tests was the only one where the

thermocouple temperatures were comparable to the melting point of aluminium (600 °C [20]). White hot metal was ejected from both the overcharge experiments at the DNV 1 site, suggesting molten aluminium, although Feng and co-workers have reported the melting of copper (m.p. 1083 °C [20]) during abuse experiments employing LCO cells [18].

The data from experiment A2 at the DNV 1 site supports the solid-state short circuit theory postulated by Feng et al. [17, 18, 42]: from Figure 3.6(b) and (c) it can be seen that the revival of the cell voltage V_1 occurs when the temperature of the top of the module reaches 280 °C. The recent paper by He and co-workers [53] also supports the solid-state short circuit theory: the authors reported that the voltages of the cylindrical LCO cells employed in their experiments (1880 mAh) suddenly decreased during heating but, once all the electrolyte had been lost from the cells, the voltages were re-established. The authors made no comment on the phenomenon but it is clear that the behaviour is the same as that observed in experiment A2 at the DNV 1 site. Thus, in this experiment, the initial nail penetration and attendant Joule heating causes the voltage of only four of the cells in the module to collapse, despite all eight having been penetrated. Presumably, the short circuit between the other four is removed due to the aluminium current collectors melting away from the nail (as observed by Yokoshima et al. [16]) with attendant vaporisation of the solvent around the nail. This then also happens with the remaining four cells, such that their voltage increases. The latter occurs during the production of flare-like flames as two of the cells fail, see Figure 3.6(c): the internal short circuit generates sufficient Joule heat to vaporize the solvent (producing white vapour, as observed in-situ by SEM [8], which ignites some seconds after exiting the cell) and cause the collapse of the separator. The latter is followed at temperatures greater than c.a. 250 °C by direct contact of the (essentially dry) anodes and cathodes and a solid state redox reaction in which lithium ions are injected into the cathode and, perhaps, oxygen abstracted to form Li_2O , the reaction resulting in the production of significant amounts of heat and the thermal runaway and collapse of the remaining cells. The temperature of the top face of the module was c.a. 250 °C at the start of the recovery of the cell voltage, see Figure 3.6(b) and (c).

3.4. Conclusion

The experiments in this Chapter were focused on the extremely important phenomenon of thermal process in runaway in lithium ion batteries, a key consideration with respect to the safe operation of these devices. In the experiments carried out in this Chapter, the behaviour of cells in thermal runaway was shown to depend strongly upon factors such as the nature of the abuse and the SoC.

The first visible indication of thermal runaway is the evolution of a thick, white vapour via the pyrolysis of the electrolyte: it is believed that this is common across LiB cathode chemistries, form factors and manufacturers. This vapour is comprised of: H₂, SO₂, NO₂, HF, HCl, CO, CO₂, droplets of organic solvent and a large range of small chain alkanes and alkenes. If sufficient air is present, at high SOC, >50%, this vapour inevitably ignites in less than 1 min. However, at low SOC, ≤50%, the vapour may not ignite: and it will not ignite if insufficient air is present. As a result, in a confined space, there could be the possibility of a flash fire, fire balls developing, or in extreme cases, even a vapour cloud explosion. This explosion hazard, along with the toxicity of the white vapour, could be faced by first responders wherever lithium ion batteries are present in an enclosed space and one or more cells are in thermal runaway. Thus, as well as EV road traffic and LiBESS incidents, this includes incidents in storage warehouses, battery manufacturing plants, electric vehicle assembly plants, road, rail and sea transportation of EVs/battery packs, hybrid electric ships and ferries. Smaller lithium-ion batteries are also causing concern, due to the large amount of white vapour produced during thermal runaway, mobility scooters in e.g. lifts, and e-bike/scooters in the home, can quickly fill an enclosed space with the vapour cloud. As an additional problem, the white vapour could be mistaken for steam, especially following the extinguishing of fire.

Maximum flame flare lengths during the failure of the modules also reached up to 275 cm, which highlights that any flammable material or mixture up to 275 cm from the pack could receive intense and rapid heating rates in the case of a module failure, something that needs to be considered for safety distance design.

Throughout these abuse experiments, the voltages of cells in modules engulfed in flames were maintained for many minutes: in addition, cell voltages have been observed to collapse during abuse, but then re-establish, negating their use as an early warning of thermal runaway. This finding is first analysed in this Thesis, and the latter phenomenon supports a wholly novel and recent theory in which thermal runaway is perpetuated

following solvent venting via direct, solid-state electrochemical reaction between anode and cathode: this theory could have significant implications with respect to the design of safe, all-solid state lithium batteries.

Finally, the vapour cloud can mask the heat produced during thermal runaway and hence appear to cause the malfunction of thermal imaging cameras.

References

1. Ren, D., et al., Investigating the relationship between internal short circuit and thermal runaway of lithium-ion batteries under thermal abuse condition. *Energy Storage Materials*, 2021. 34: p. 563-573.
2. Ren, D., et al., A comparative investigation of aging effects on thermal runaway behavior of lithium-ion batteries. *ETransportation*, 2019. 2: p. 100034.
3. Wang, Q., et al., A review of lithium ion battery failure mechanisms and fire prevention strategies. *Progress in Energy and Combustion Science*, 2019. 73: p. 95-131.
4. Orendorff, C.J., The role of separators in lithium-ion cell safety. *The Electrochemical society interface*, 2012. 21(2): p. 61.
5. Feng, X., et al., Thermal runaway features of large format prismatic lithium ion battery using extended volume accelerating rate calorimetry. *Journal of power sources*, 2014. 255: p. 294-301.
6. Larsson, F., et al., Gas explosions and thermal runaways during external heating abuse of commercial lithium-ion graphite-LiCoO₂ cells at different levels of ageing. *Journal of power sources*, 2018. 373: p. 220-231.
7. Sun, P., et al., A review of battery fires in electric vehicles. *Fire technology*, 2020. 56: p. 1361-1410.
8. Atkinson, G., J. Hall, and A. McGillivray, Review of Vapour Cloud Explosion Incidents 2017, HSE.
9. Hill, D. and A.P.S. Company, McMicken Battery Energy Storage System Event: Technical Analysis and Recommendations. 2020: DNV GL Energy Insights USA, Incorporated.
10. Swart, J., K. White, and M. Cundy, APS McMicken Progress Report. 2020, Exponent, Inc.

11. Sturk, D., L. Hoffmann, and A. Ahlberg Tidblad, Fire tests on e-vehicle battery cells and packs. *Traffic injury prevention*, 2015. 16(sup1): p. S159-S164.
12. Chen, S., et al., Lower explosion limit of the vented gases from Li-ion batteries thermal runaway in high temperature condition. *Journal of Loss Prevention in the Process Industries*, 2020. 63: p. 103992.
13. Sun, J., et al., Toxicity, a serious concern of thermal runaway from commercial Li-ion battery. *Nano Energy*, 2016. 27: p. 313-319.
14. Abaza, A., et al., Experimental study of internal and external short circuits of commercial automotive pouch lithium-ion cells. *Journal of Energy Storage*, 2018. 16: p. 211-217.
15. Zhao, W., G. Luo, and C.-Y. Wang, Modeling nail penetration process in large-format Li-ion cells. *Journal of The Electrochemical Society*, 2014. 162(1): p. A207.
16. Yokoshima, T., et al., Direct observation of internal state of thermal runaway in lithium ion battery during nail-penetration test. *Journal of Power Sources*, 2018. 393: p. 67-74.
17. Feng, X., et al., Investigating the thermal runaway mechanisms of lithium-ion batteries based on thermal analysis database. *Applied Energy*, 2019. 246: p. 53-64.
18. Feng, X., et al., Additive manufactured closed-cell aluminum alloy foams via laser melting deposition process. *Materials Letters*, 2018. 233: p. 126-129.
19. Liao, Z., et al., Hazard analysis of thermally abused lithium-ion batteries at different state of charges. *Journal of Energy Storage*, 2020. 27: p. 101065.
20. Ribière, P., et al., Investigation on the fire-induced hazards of Li-ion battery cells by fire calorimetry. *Energy & Environmental Science*, 2012. 5(1): p. 5271-5280.
21. Larsson, F., et al., Toxic fluoride gas emissions from lithium-ion battery fires. *Scientific reports*, 2017. 7(1): p. 1-13.
22. Diaz, F., et al., Gas generation measurement and evaluation during mechanical processing and thermal treatment of spent Li-ion batteries. *Waste Management*, 2019. 84: p. 102-111.
23. Warner, N., Overview of a year of battery fire overview of a year of battery fire testing by DNV GL for Con Ed, NYSERDA and FDNY 34. DNV GL, NFPA 855 Committee Meeting. 2018.
24. Gully, B., et al., Technical Reference for Li-ion Battery Explosion Risk and Fire Suppression. DNV GL, 2019. 1025.

25. Abbot, T., Fire Chief of Surprise, Arizona, P. Christensen, Editor. 2019.
26. Zhang, S.S., A review on electrolyte additives for lithium-ion batteries. *Journal of Power Sources*, 2006. 162(2): p. 1379-1394.
27. Lecocq, A., et al., Scenario-based prediction of Li-ion batteries fire-induced toxicity. *Journal of Power Sources*, 2016. 316: p. 197-206.
28. Ren, F., et al., Comprehensive understanding of reduction mechanisms of ethylene sulfite in EC-based lithium-ion batteries. *The Journal of Physical Chemistry C*, 2019. 123(10): p. 5871-5880.
29. Jankowski, P., et al., Impact of sulfur-containing additives on lithium-ion battery performance: from computational predictions to full-cell assessments. *ACS Applied Energy Materials*, 2018. 1(6): p. 2582-2591.
30. Wrodnigg, G.H., J.O. Besenhard, and M. Winter, Cyclic and acyclic sulfites: new solvents and electrolyte additives for lithium ion batteries with graphitic anodes? *Journal of power sources*, 2001. 97: p. 592-594.
31. Wu, Z., et al., The roles of sulfur-containing additives and their working mechanism on the temperature-dependent performances of li-ion batteries. *Journal of The Electrochemical Society*, 2018. 165(11): p. A2792.
32. Babrauskas, V., *Ignition handbook: principles and applications to fire safety engineering, fire investigation, risk management and forensic science*. 2003.
33. Abraham, D., et al., Diagnostic examination of thermally abused high-power lithium-ion cells. *Journal of Power Sources*, 2006. 161(1): p. 648-657.
34. Nedjalkov, A., et al., Toxic gas emissions from damaged lithium ion batteries—analysis and safety enhancement solution. *Batteries*, 2016. 2(1): p. 5.
35. Chen, Y., et al., Toxicity identification and evolution mechanism of thermolysis-driven gas emissions from cathodes of spent lithium-ion batteries. *ACS Sustainable Chemistry & Engineering*, 2019. 7(22): p. 18228-18235.
36. Ohsaki, T., et al., Overcharge reaction of lithium-ion batteries. *Journal of power sources*, 2005. 146(1-2): p. 97-100.
37. Onuki, M., et al., Identification of the source of evolved gas in Li-ion batteries using ²H₂ 1-labeled solvents. *Journal of The Electrochemical Society*, 2008. 155(11): p. A794.
38. Essl, C., et al., Comprehensive hazard analysis of failing automotive Lithium-ion batteries in overtemperature experiments. *Batteries*, 2020. 6(2): p. 30.

39. Said, A.O., C. Lee, and S.I. Stoliarov, Experimental investigation of cascading failure in 18650 lithium ion cell arrays: impact of cathode chemistry. *Journal of Power Sources*, 2020. 446: p. 227347.
40. Golubkov, A.W., et al., Thermal runaway of commercial 18650 Li-ion batteries with LFP and NCA cathodes–impact of state of charge and overcharge. *Rsc Advances*, 2015. 5(70): p. 57171-57186.
41. Bugryniec, P.J., et al., Pursuing safer batteries: thermal abuse of LiFePO₄ cells. *Journal of Power Sources*, 2019. 414: p. 557-568.
42. Zhu, X., et al., Internal short circuit and failure mechanisms of lithium-ion pouch cells under mechanical indentation abuse conditions: An experimental study. *Journal of Power Sources*, 2020. 455: p. 227939.
43. Balakrishnan, P., R. Ramesh, and T.P. Kumar, Safety mechanisms in lithium-ion batteries. *Journal of power sources*, 2006. 155(2): p. 401-414.
44. Wang, A., et al., Review on modeling of the anode solid electrolyte interphase (SEI) for lithium-ion batteries. *npj Computational Materials*, 2018. 4(1): p. 15.
45. Mao, Z., et al., Calendar aging and gas generation in commercial graphite/NMC-LMO lithium-ion pouch cell. *Journal of The Electrochemical Society*, 2017. 164(14): p. A3469.
46. Feng, X., et al., Thermal runaway mechanism of lithium ion battery for electric vehicles: A review. *Energy Storage Materials*, 2018. 10: p. 246-267.
47. Wang, Q., et al., Thermal behavior of lithiated graphite with electrolyte in lithium-ion batteries. *Journal of The Electrochemical Society*, 2005. 153(2): p. A329.
48. Feng, X., et al., Mitigating thermal runaway of lithium-ion batteries. *Joule*, 2020. 4(4): p. 743-770.
49. Yuan, Q., et al., Overcharge failure investigation of lithium-ion batteries. *Electrochimica Acta*, 2015. 178: p. 682-688.
50. Periodic Table: Lithium. 28/02/2023]; Available from: <https://www.rsc.org/periodic-table/element/3/lithium>.
51. Zhu, Y., et al., Fast lithium growth and short circuit induced by localized-temperature hotspots in lithium batteries. *Nature communications*, 2019. 10(1): p. 2067.
52. Liu, X., et al., Thermal runaway of lithium-ion batteries without internal short circuit. *Joule*, 2018. 2(10): p. 2047-2064.

53. He, X., et al., Experimental study of self-heating ignition of lithium-ion batteries during storage: effect of the number of cells. *Fire technology*, 2020. 56: p. 2649-2669.

Chapter 4 . The January 2020 (DNV 1) experiments (continued) and Spring 2021 (DNV 2)

4.1 Introduction

As well as thermal and mechanical abuse, electronic abuse experiments were carried out at the DNV site in January 2020 (DNV 1) where Envision-AESC modules were overcharged. Nail penetration experiments were again carried out at the site in Spring 2021 (DNV 2), as the 50 % SoC experiment at the FSC (B2) had clearly shown the importance of the vapour cloud explosion hazard, and the subsequent realisation that statements in the literature referring to gas, smoke and steam all represented the production of the vapour cloud, it was realised that vapour cloud explosion hazard was underrated.

4.1 Overcharge experiments at DNV January 2020

4.1.1 Experiment A6 (*overcharge of a single module*)

Figure 4.1 shows frames from the two optical cameras (“front” and “rear”) taken at c.a. the same instants during the overcharge experiment. Thus, (a)(front) and (b)(rear) show the gassing of the pouch cells and expansion of the aluminium module case, (c) and (d) were taken 45.8 ms later: whilst the front camera (c) clearly shows flames at the front of the module, the back camera (d) shows the module has been forced open via the break tabs on the case. 41.7 ms later, the flame front had detached from the module, (e) whilst the back camera (f) frame shows the gaping of the module without any observable flames, (g) and (h) were taken 8.3 ms after (e) and (f), the detached flame seen by the front camera has almost disappeared (g), whilst the first spark from the rear camera can be seen in the image (h). Figure 4.1(i) and (j) taken 29.2 ms after (g) and (h) show ignition of the cells at the front and to one side. The initial small flames appear to be molten material detaching from the module before a significant amount of flammable vapour is produced which causes the large diffusion flame to develop. The frames in Figure 4.1(k) and (l) were taken 10s after the frames in (a) and (b) and show the typical flare-like flames which develop.



(a) A photograph of the front of the module when the pouch cells gassed, and the aluminium module case expanded (time = 0 s).



(b) A photograph of the rear of the module when the pouch cells gassed, and the aluminium module case expanded (time = 0 s).



(c) A photograph of the front of the module when the module had been forced open (time = 45.8 ms).



(d) A photograph of the rear of the module when the module had been forced open (time = 45.8 ms).



(e) A photograph of the front of the module when the flame front detaches (time = 57.5 ms).



(f) A photograph of the rear of the module when the flame front of the front of the module detaches (time = 87.5 ms).



(g) A photograph of the front of the module when the first spark of the rear of the module can be seen (time = 95.8 ms).



(h) A photograph of the rear of the module when the first spark of the rear of the module can be seen (time = 95.8 ms).



(i) A photograph of the front of the modules during ignition (time = 125 ms).



(j) A photograph of the rear of the module during ignition (time = 125 ms).



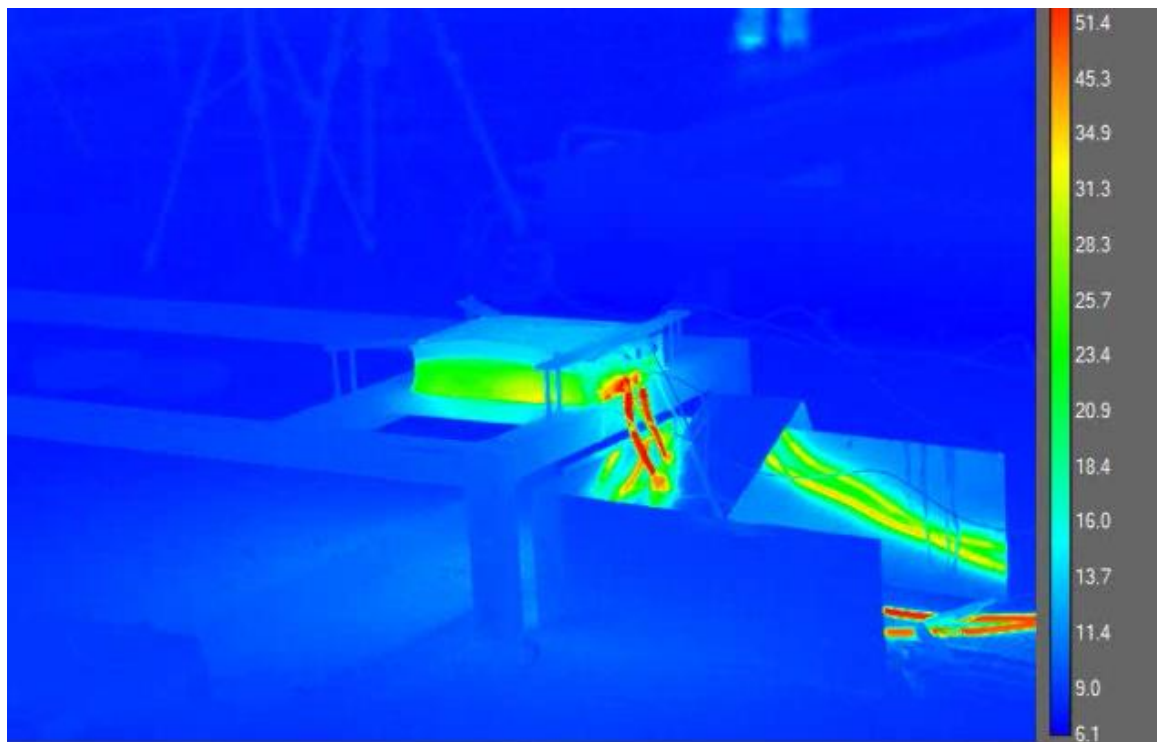
(k) A photograph of the front of the module once flare-like flames had developed (time = 10 s).



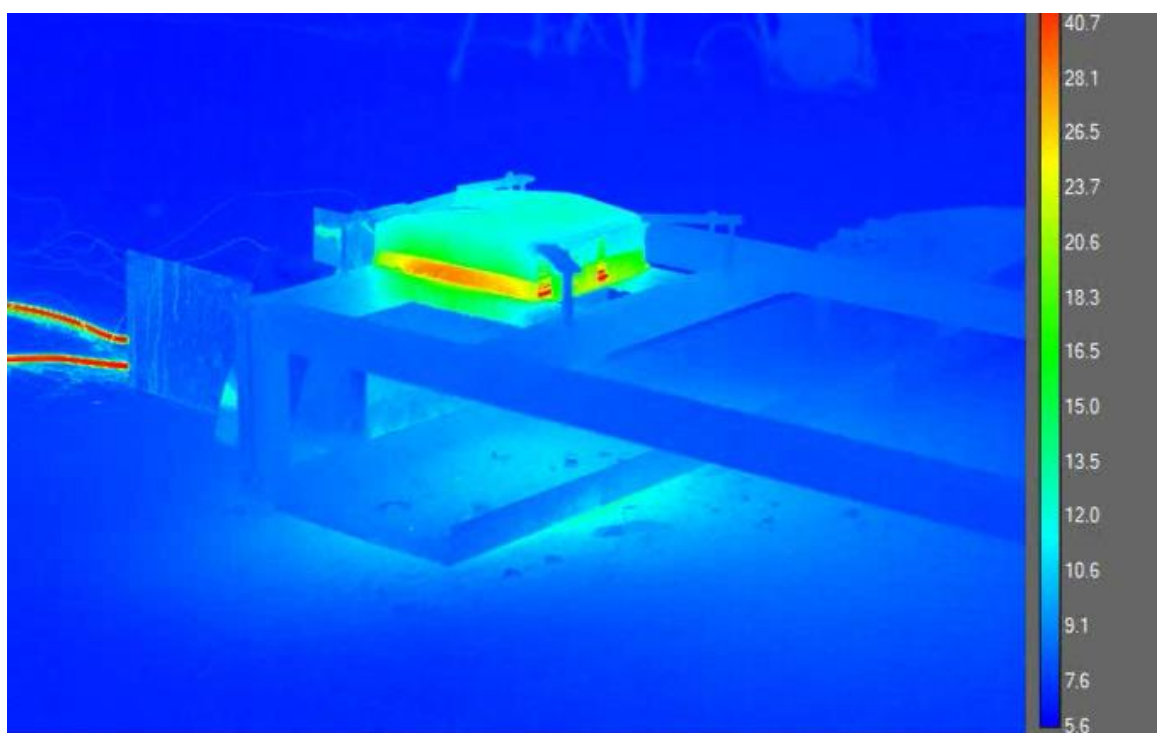
(l) A photograph of the rear of the module once flare-like flames had developed (time = 10 s).

Figure 4.1. Frames from the (a), (c), (e), (g), (i) and (k) front optical camera and (b), (d), (f), (h), (j) and (l) back optical camera, for experiment A6. They were collected at the times specified in the captions.

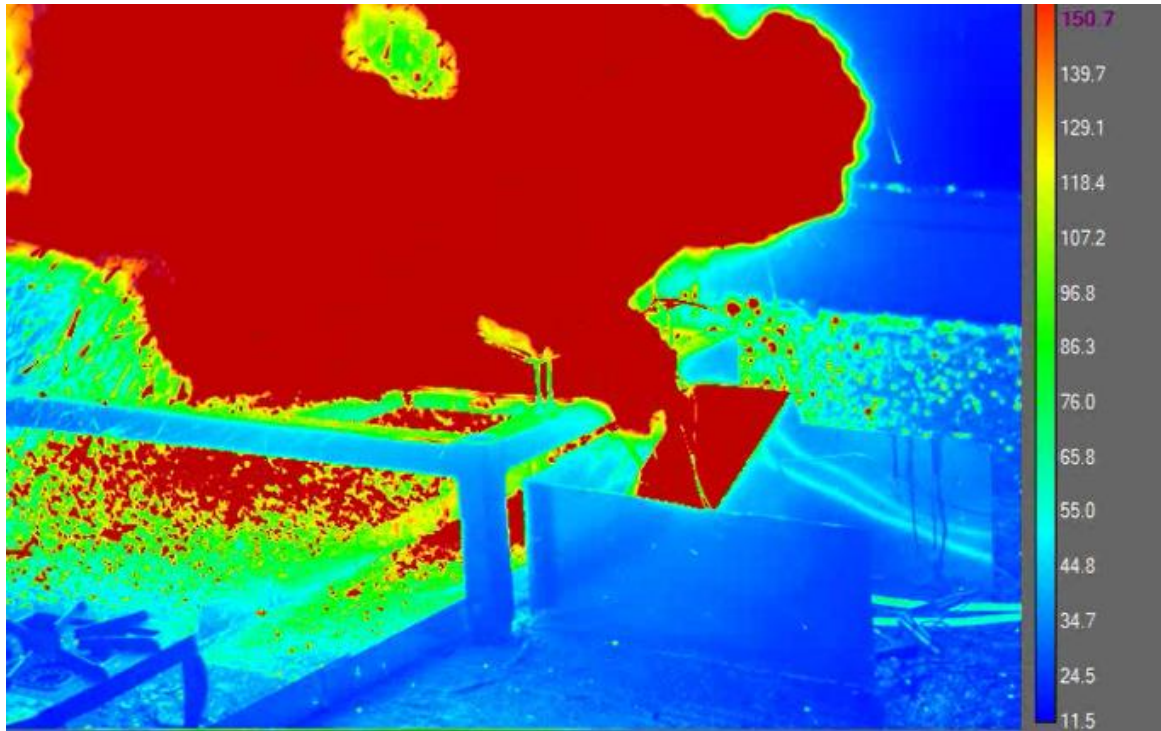
Figure 4.2 shows frames from the thermal camera videos during experiment A6, (a) from the front thermal camera, (b) from the rear thermal camera, both were taken around the same time that the images in Figure 4.1(a) & (b). 1 s later (i.e. after the image in figure 4.2(i)), (c) from the front thermal camera and (d) from the rear thermal camera.



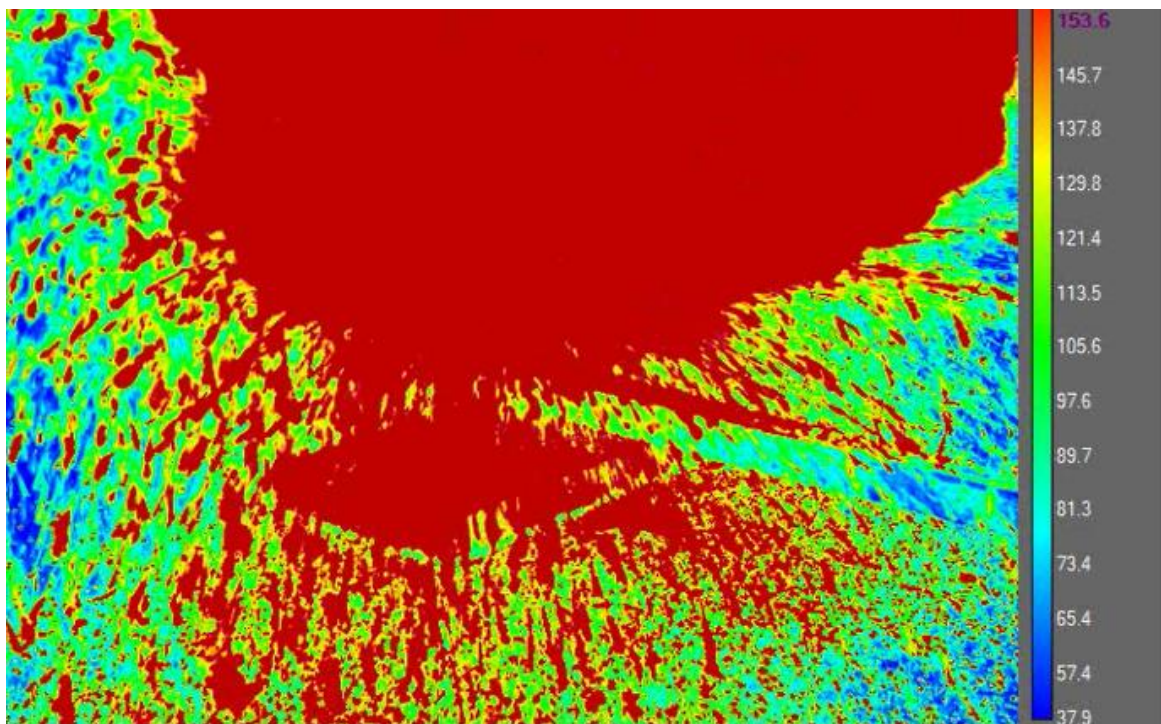
(a) A frame from the thermal camera of the front of the module (time = 0 s).



(b) A frame from the thermal camera of the rear of the module (time = 0 s).



(c) A frame from the thermal camera of the front of the module (time = 1 s).



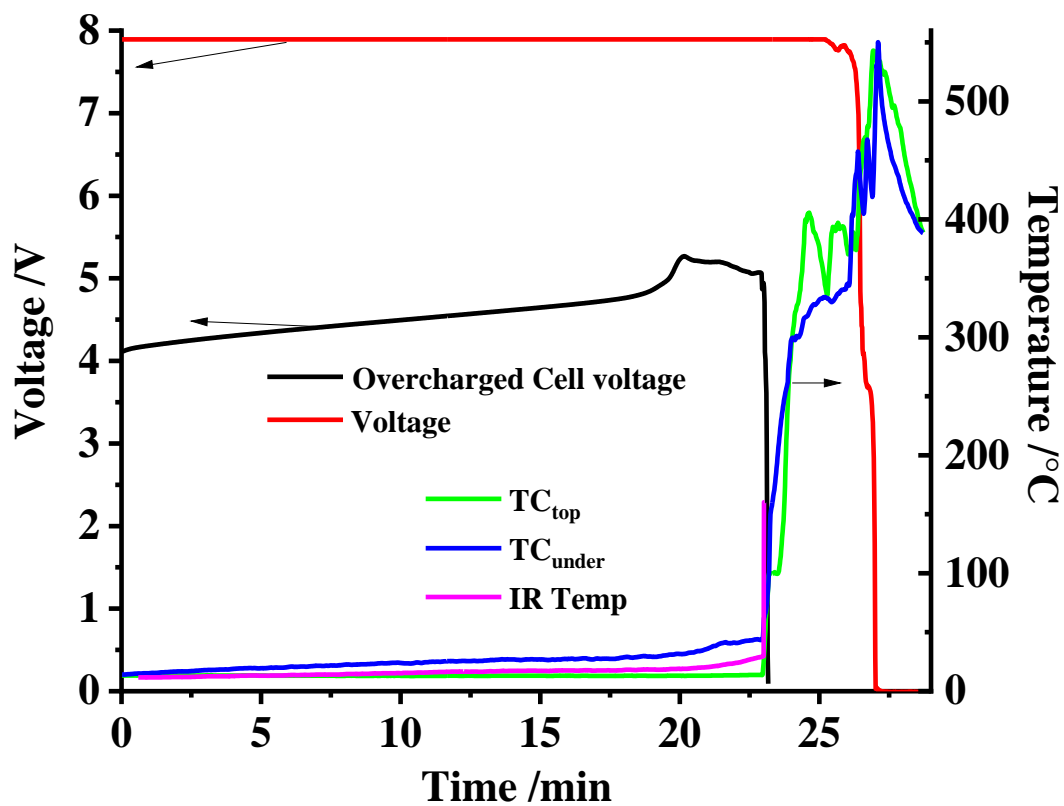
(d) A frame from the thermal camera of the rear of the module (time = 1 s).

Figure 4.2 Thermal images taken (a) & (c) using the front thermal camera and (b) & (d) the rear thermal camera. (a) and (c) are 1 s apart, as are (b) and (d). All vertical axis are temperature in degrees Centigrade.

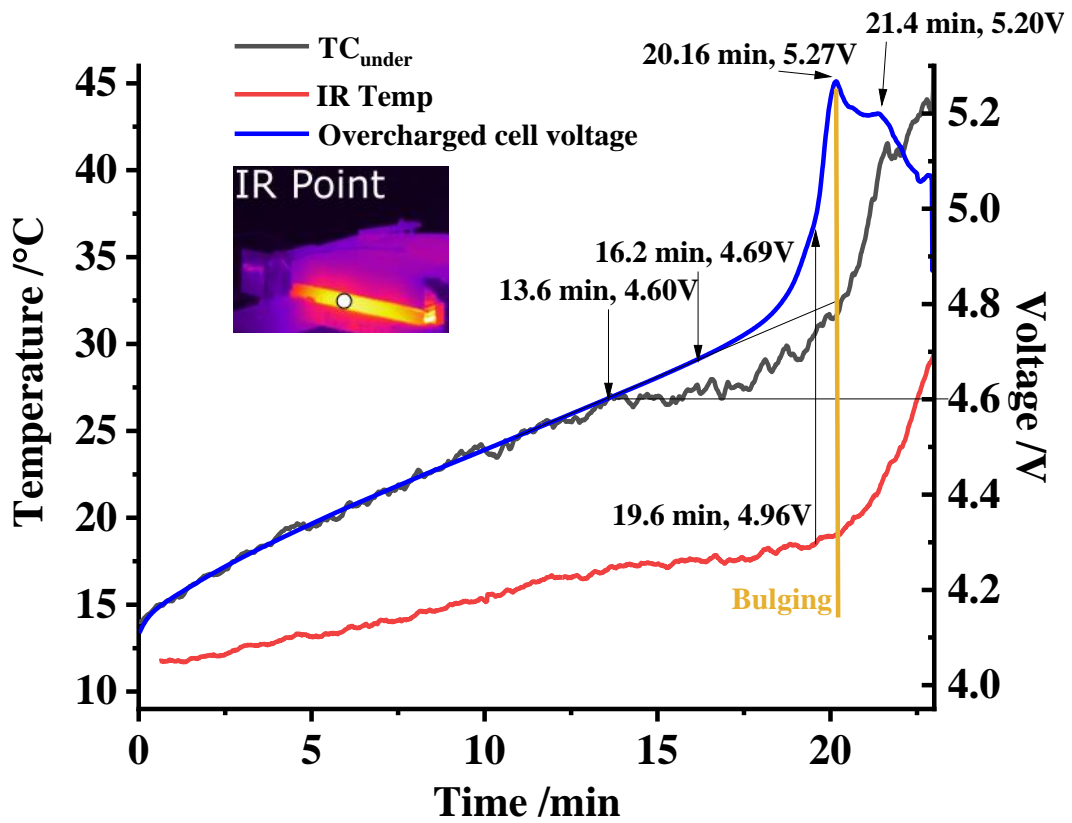
As can be seen in Figure 4.2(b) & (c), the temperature of the thermocouple on the top face of module (TC_{top}) remained unchanged at c.a. 13 °C prior to thermal runaway, whilst

the temperature of the thermocouple on the underside of the module (TC_{under}) increased to c.a. 44°C and the pouch cells facing the thermal camera reached c.a. 30°C . The variation in temperature between the two surfaces of the module is not unexpected as the overcharged pair of cells were located in the lower half of the module.

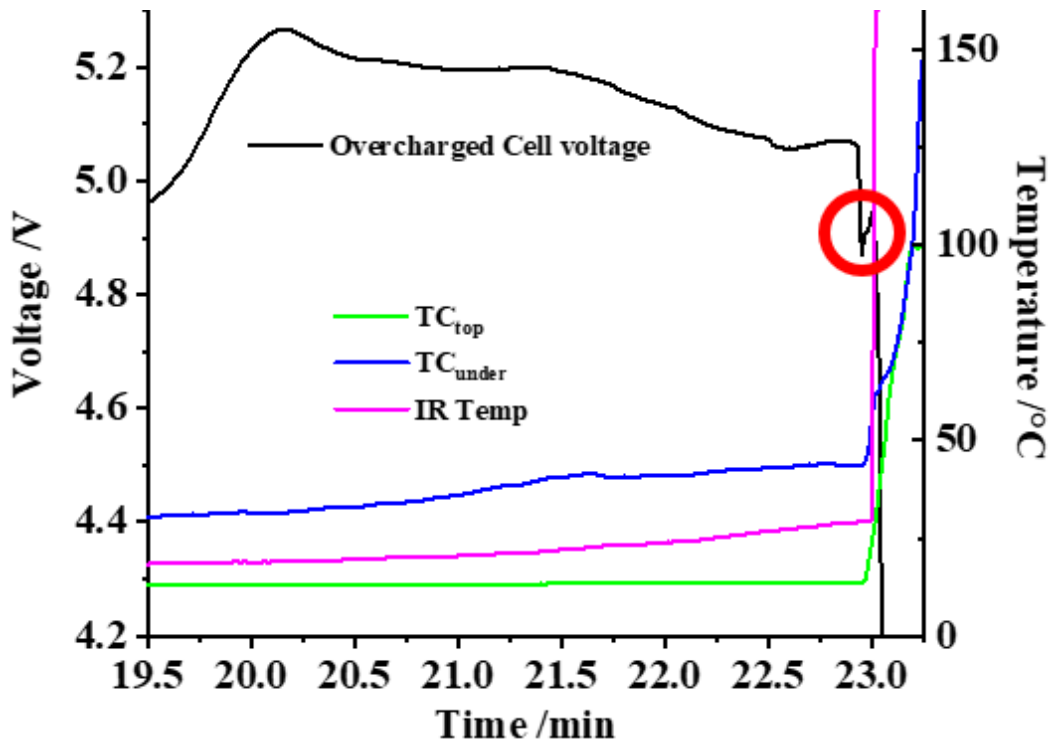
Figure 4.3 shows plots of the DAQ and thermal camera data (the point employed to determine the latter is shown in (b)) during (a) the overcharging and thermal runaway of the module, (b) up to thermal runaway, (c) 3.5 minutes prior to thermal runaway to thermal runaway, (d) temperatures and flame areas from thermal runaway, and (e) voltages and flame areas from thermal runaway.



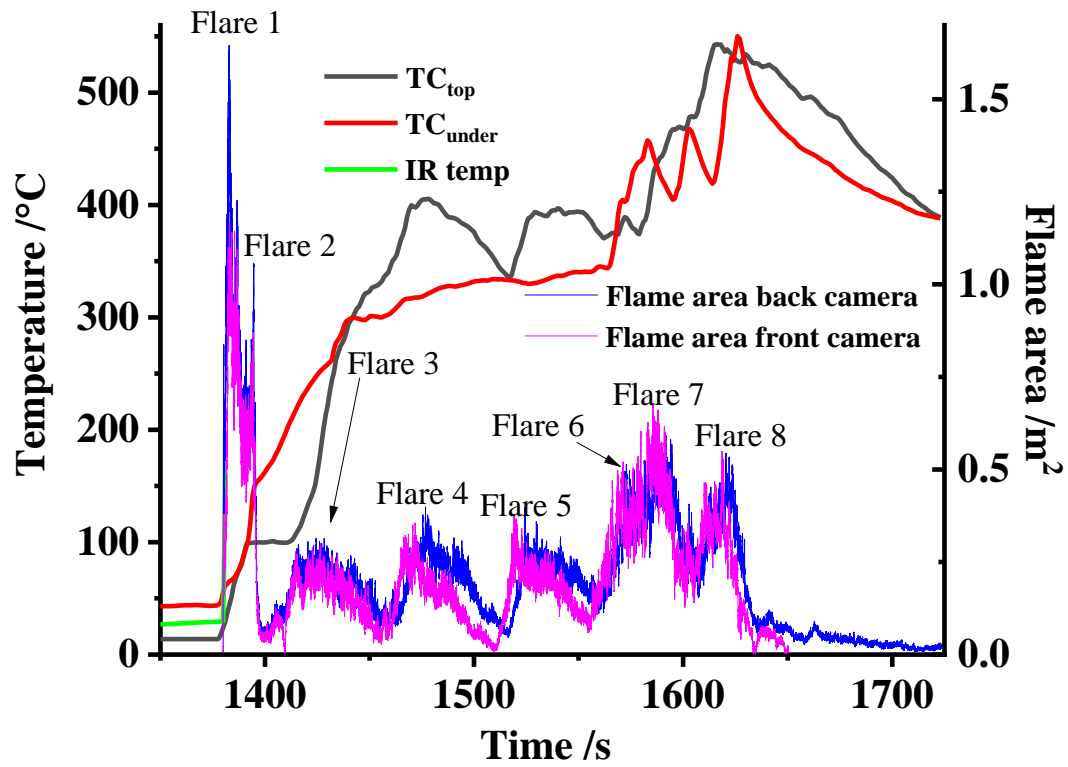
(a) Voltage, thermocouple, and thermal camera data from experiment A6.



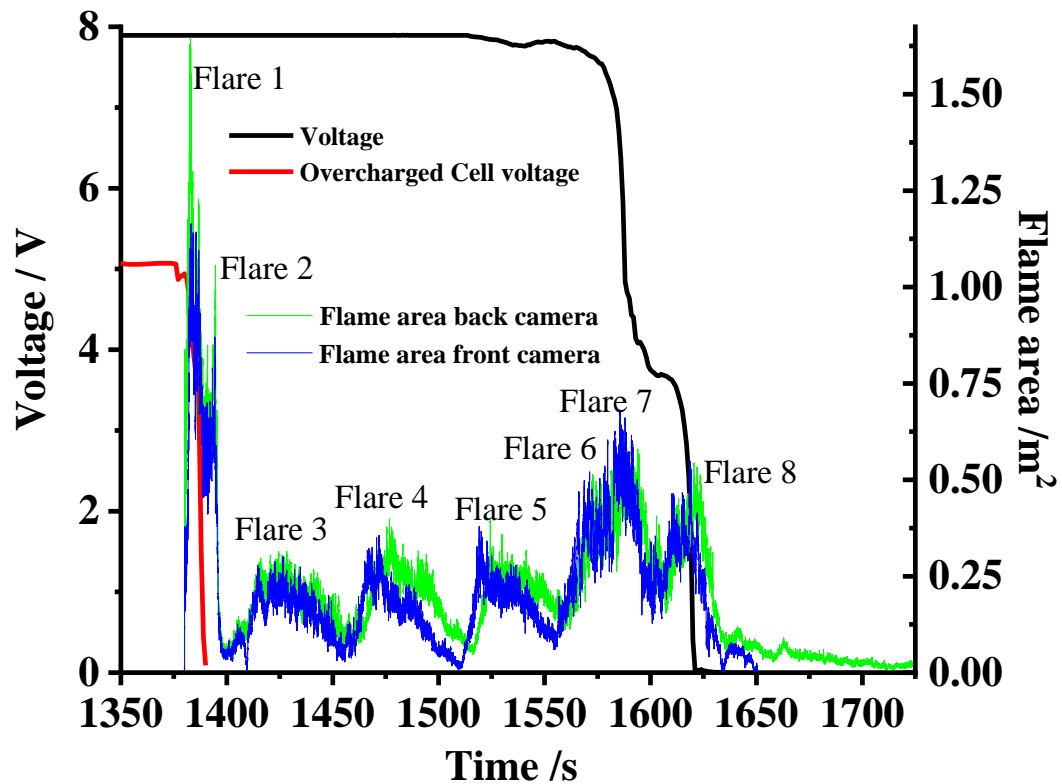
(b) Thermocouple, thermal camera, and voltage data from experiment A6.



(c) Voltage, thermocouple, and thermal camera data from experiment A6.



(d) Thermocouple, thermal camera, and flame area data from experiment A6.



(e) Voltage and flame area data from experiment A6.

Figure 4.3. Plots of the DAQ, thermal camera (the point employed to determine the latter is shown in the inset to (d)), and flame area data from experiment A6.

The variation in the voltage of the overcharged cells prior to thermal runaway showed a distinct pattern which was essentially seen in all three overcharge experiments: of note is the small decrease and recovery in the cell voltage immediately prior to the collapse of the overcharged cells' voltage (circled in Figure 4.3(c)) which will be discussed further below. The start of the bulging of the cells within the module, which coincided with the maximum in the voltage of the overcharged cells, see Figure 4.3(b), was ascertained from a careful analysis of the thermal videos of the module during overcharge. The fact that surface emissivity depends on the viewing angle was utilised to identify the start of the module case bulging. Any surface deformation will change the local surface emissivity, and this will be reflected in the thermal images: such a change was detected around the edges of the top surface of the top module case and the time at which this occurred was identified as the beginning of bulging.

The optical (see Figures 4.1(i) & (j)) and thermal videos (see Figure 4.2(c) & (d)) clearly showed an explosion as the module descended into thermal runaway, and this is reflected in the plots of flame area in Figure 4.3(d) and (e), as the flame area of the first flare is c.a. three times that of subsequent flares. As can be seen from the images, and most clearly from thermal images Figure 4.2(c) & (d), at ignition a large number of hot particles were emitted from the module explosively away from the experimental setup. These ejected hot particles, along with the gas flares, are an additional source of hazard recorded in these experiments. The explosion was caused by the two overcharged cells venting and the vent gases igniting, causing flares 1 & 2 on Figure 4.3(d) & (e). The remaining cells in the top quartet then ignited sequentially, flares 3 & 4, before the lower quartet started to fail. Flare 5 was due to one of the cells in the two parallel pairs failing and venting, followed rapidly by a cell in the other parallel pair, flare 6, such that the cell voltage remained at c.a. 8V. Flare 7 marked the venting of the second cell of a pair having a failed cell, causing the voltage to fall to c.a. 4V, followed by the failure of the final cell, flare 8, and complete loss of voltage. The cell voltage of the lower quartet was maintained for c.a. 3 minutes with intense flames around the module, this delay was also seen in experiments A3 and A4 and may be due to the time it takes for heat to propagate to these cells and initiate thermal runaway. From Figure 4.3(d), plotting the temperature of the two thermocouples as well as the flame area peaks of the overcharge experiment, the temperature profile follows a similar behaviour to the cell failure from thermal propagation seen in the voltage (Figure 4.3(e)): After the first two cells ignited there was

a sharp increase in temperature from the thermal runaway, followed by steady increase in temperature as the cells individually ignited, with local peaks of temperatures seen as the flame areas spike, and is therefore likely linked to thermal propagation of thermal runaway between the individual cells in the module.

4.1.2 Experiment A7 (single module overcharge in stack of three).

Figure 4.4 shows frames from the optical videos taken during the overcharge experiment A7 at the DNV GL site. After c.a. 25 minutes of charging the parallel pair of cells at 100 A that were originally at 96.5% SOC, the module expanded, see (a)(front) and (b)(rear), and the first wisps of white vapour appeared. 8.3 ms later in (c) and (d) ignition occurred, and projectiles were ejected almost immediately after, this can be seen in (e) and (f) taken c.a. 87.5 ms after the images in (a) and (b). The module then erupted into flames, see (g) and (h) taken 154 ms after the first images, which then became the flare-like flames in (i) and (j) taken 46.2 s after the image in (a). The flames were then extinguished using a 6 litre AFFF extinguisher Foam Spray 13A 113B Model FS EX 6, which required 18 s and resulted in the production of the dense white vapour again, see (k) and (l) taken 119 s after the image in (a). Again, it is worth noting that the vapour is due to the gases emitted by the cells and is replaced by much thinner fumes when these gases ignited, and the vapour could easily be mistaken for steam. The modules re-ignited 112 seconds after being extinguished, initially without the flare-like flames (m) and (n) taken 238 s after (a) and (b), but these re-appeared, see the images in (o) and (p) taken 257 s after the images in (a) and (b).

Figure 4.5 shows plots of the DAQ inputs recorded during the overcharge experiment A7. TC_{top} and TC_{under} are the temperature of the thermocouples located on the top surface and underside of the middle module (and hence sandwiched between the modules and isolated from any flames). Figure 4.5(a) shows the full experimental period, (b) leading up to thermal runaway and (c) – (e) post thermal runaway. From the figures it can be seen that the four cells in the top half of the overcharged module retained their full charge until after the second set of flare-like flames from the re-ignition finished, and it appears such electrical energy is essential to the production of such violent fire, see also discussion of 50 % SoC nail penetration experiment (B2) at FSC in Chapter 3.

Figure 4.6 shows a generic voltage plot of an overcharge experiment labelled with regions and events that occur in overcharge experiments.

Table 4.1 lists the SoC's and voltages where these regions and events have occurred in experiments A6 and A7.



(a) A photograph of the front of the modules when the first wisps of white vapour were noticed (time = 0 s).



(b) A photograph of the rear of the modules when the first wisps of white vapour were noticed (time = 0 s).



(c) A photograph of the front of the modules when ignition first occurred (time = 8.3 ms).



(d) A photograph of the rear of the modules when ignition first occurred (time = 8.3ms).



(e) A photograph of the front of the modules when projectiles were first noticed to be emitted (time = 87.5 ms).



(f) A photograph of the rear of the modules when projectiles were first noticed to be emitted (time = 87.5 ms).



(g) A photograph of the front of the modules when flames were first noticed (time = 154 ms).



(h) A photograph of the rear of the modules when flames were first noticed (time = 154 ms).



(i) A photograph of the front of the modules when flare-like flames were observed (time = 46.2 s).



(j) A photograph of the rear of the modules when flare-like flames were observed (time = 46.2 s).



(k) A photograph of the front of the modules once the flames had been extinguished and a dense white vapour cloud had been produced (time = 119 s).



(l) A photograph of the rear of the modules once the flames had been extinguished and a dense white vapour cloud had been produced (time = 119 s).



(m) A photograph of the front of the modules as it re-ignited (time = 238 s).



(n) A photograph of the rear of the modules as it re-ignited (time = 238 s).

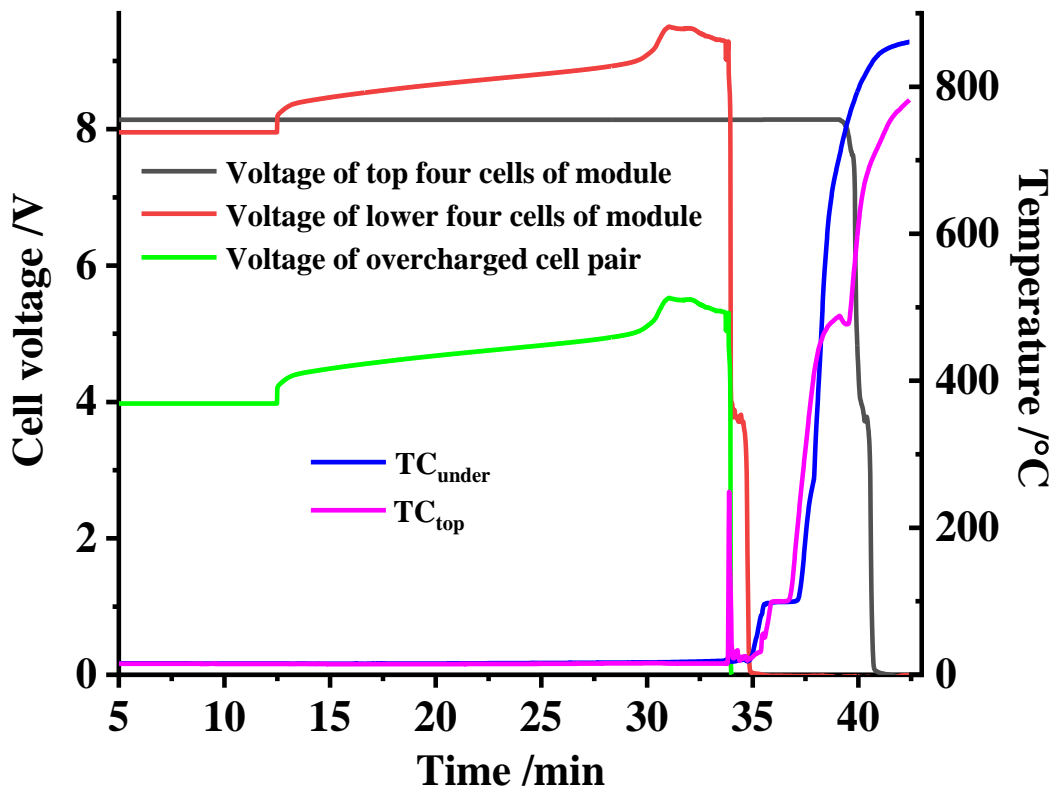


(o) A photograph of the front of the modules as flare-like flames were re-produced after extinguishments (time = 257 s).

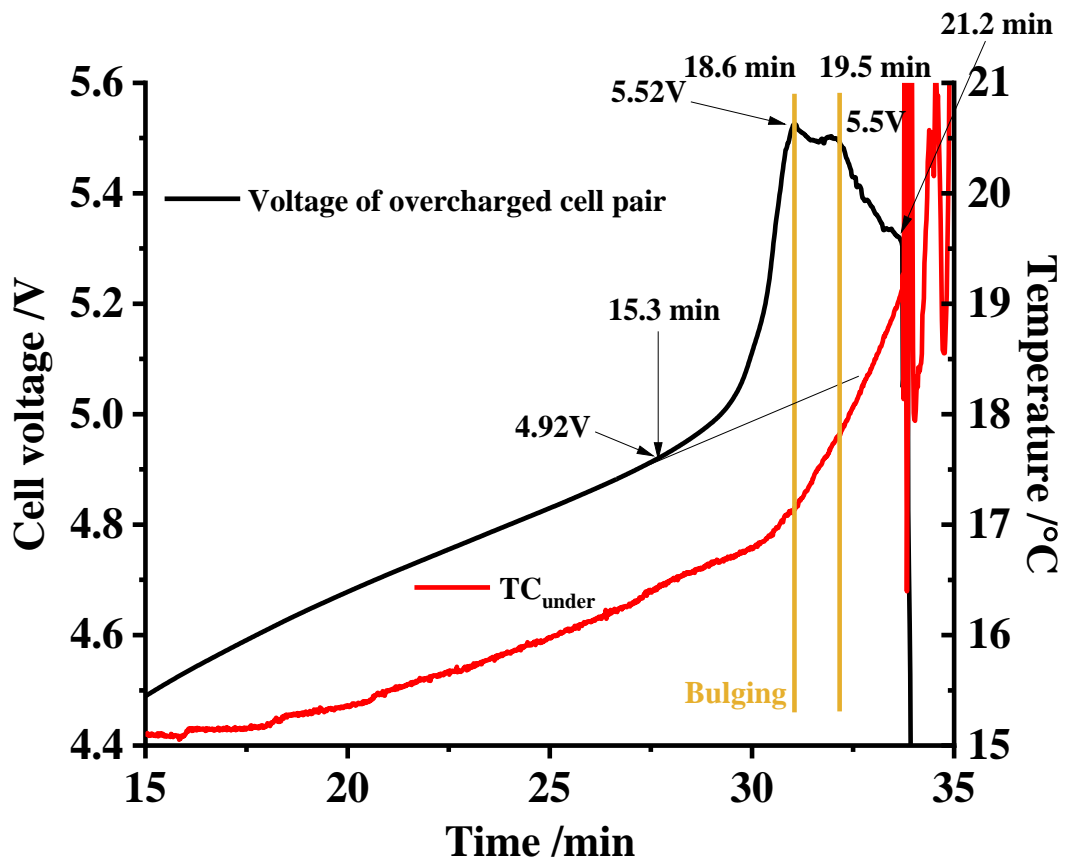


(p) A photograph of the rear of the modules as flare-like flames were re-produced after extinguishments (time = 257 s).

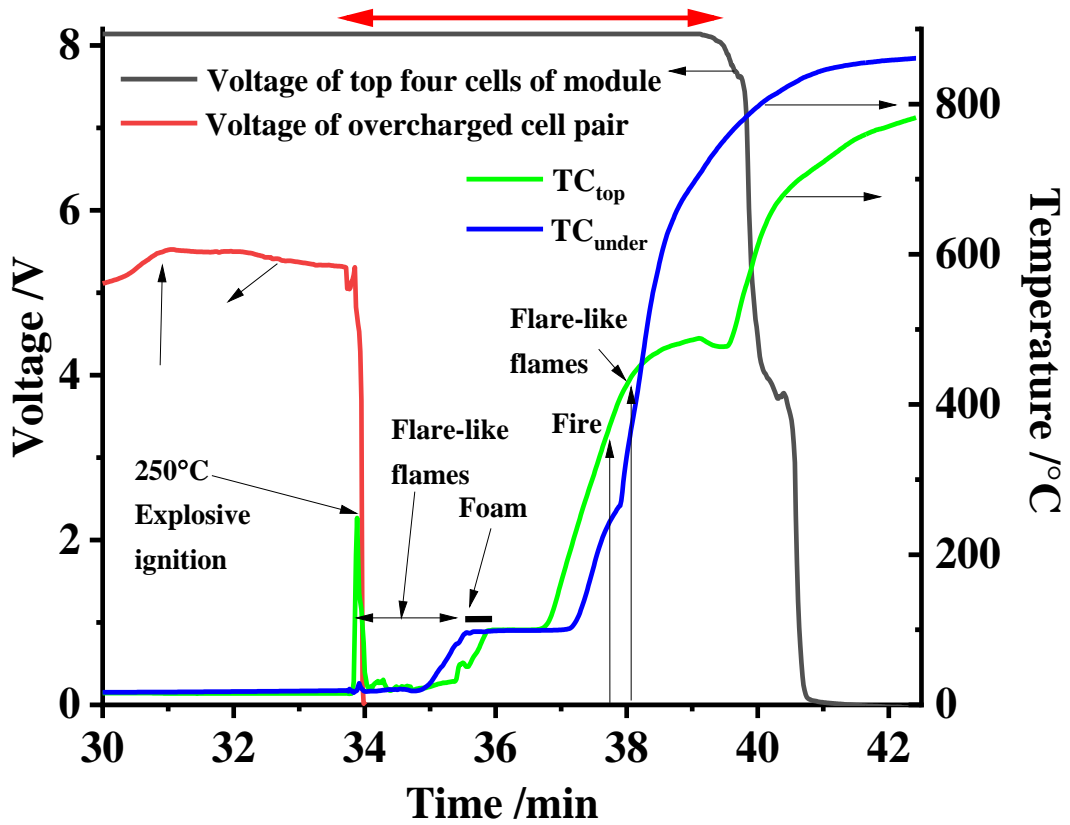
Figure 4.4. Frames from the videos taken during the overcharge of a single module in a stack of three at the DNV GL site (experiment A7).



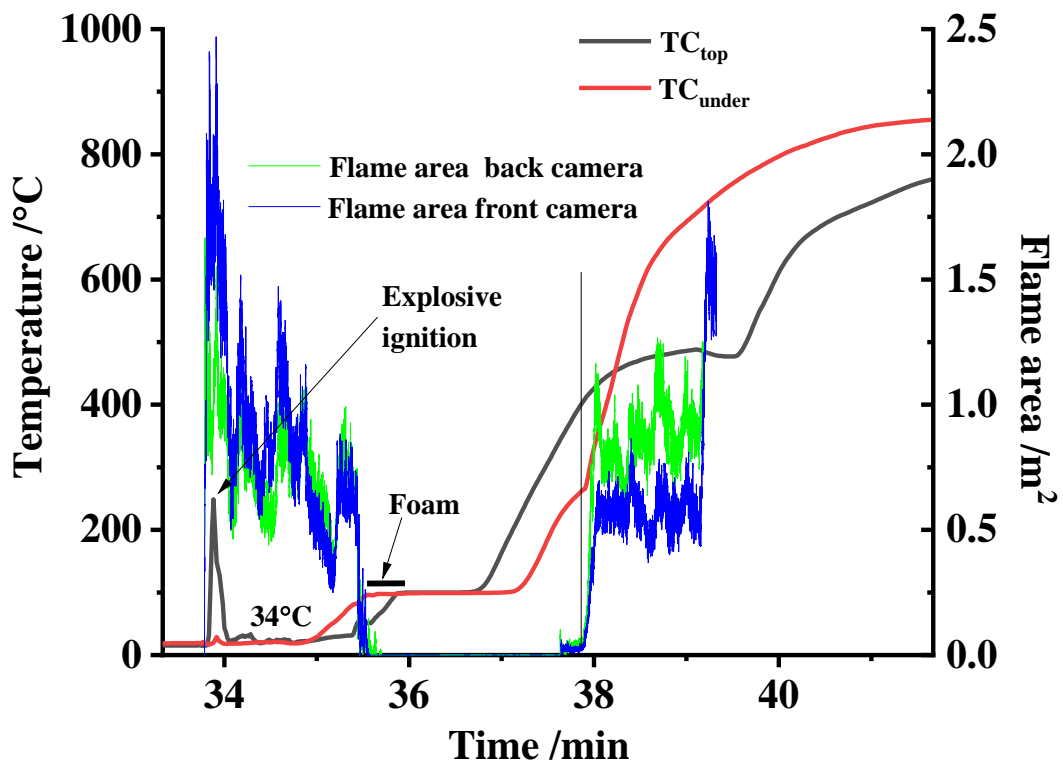
(a) Voltage and thermocouple data from experiment A7.



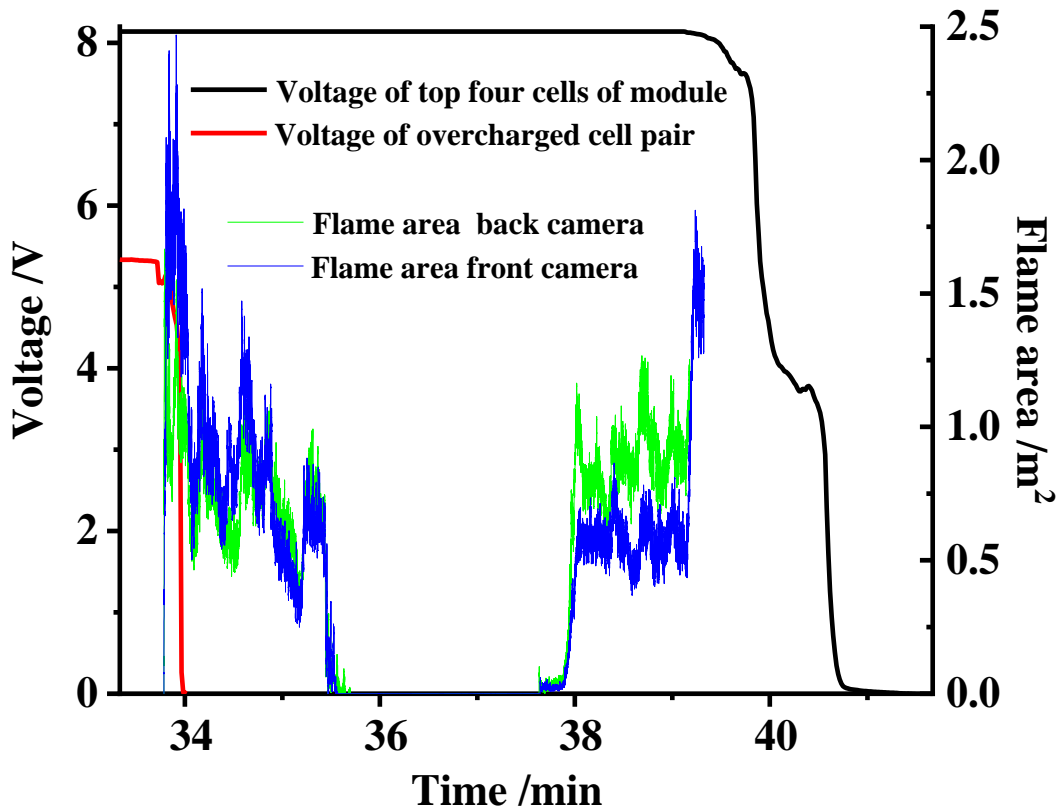
(b) Voltage and thermocouple data from experiment A7.



(c) Voltage and thermocouple data from experiment A7.



(d) Thermocouple and flame area data from experiment A7.



(e) Voltage and flame area data from experiment A7

Figure 4.5. The DAQ data and flame measurements for experiment A7, (a) all data, (b) the data leading up to thermal runaway and (c) – (e) after thermal runaway.

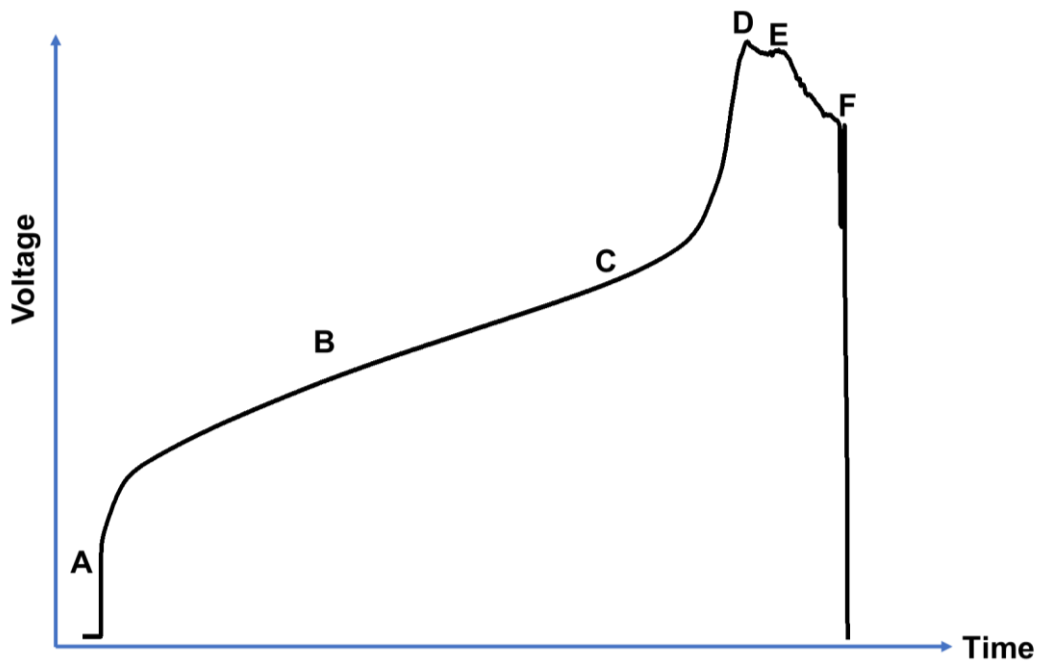


Figure 4.6. Generic representation of the voltage/time plot during overcharge.

The voltage of the overcharged cells in **Figure 4.5(a)–(c)** shows a very similar response to that observed in the previous experiment, see **Figure 4.3(a)–(c)**, with an initial rapid increase (region A in **Figure 4.6**) followed by: a slower but steady increase (region B), an inflexion at point C, a rapid increase in voltage to what is generally referred to in the literature as a “plateau” (region D–E), a relatively slow decrease then catastrophic collapse at point F. The SoCs and voltages at which these occur are summarised in

Table 4.1. In broad terms these characteristics have also been observed by other authors during the overcharge of NMC cells [1-5].

The significant rise in voltage in region A in **Figure 4.6** is due to the IR drop as soon as current flows through the resistance of the cells. The steady rise in voltage and slow increase in temperature in region B is due to the de-intercalation of Li^+ out of the NMC cathode and intercalation into the graphite particles of the anode: no side reactions take place in this region due to the overcapacities of anode and cathode [3], the voltage rises due to increased resistance, and the concomitant Joule heating causes the slow temperature rise. According to Zhu et al. [3], Ni(II) ions in the cathode are also oxidised to Ni(IV), but this does not result in its structural collapse or the oxidation of the solvent. In contrast, whilst Yuan et al. [1] also postulate the oxidation of Ni ions in this region, they suggest that the irreversible removal of Li_2O from the cathode takes place along with the extraction of Li^+ ions from octahedral and tetrahedral sites in the NMC cathode.

In general, the inflexion point C is taken as the onset of lithium metal plating on the anode, this reacts exothermically with the solvent to form an insulating SEI layer, both of which cause Joule heating, giving the rise in temperature [3]. Jiang and co-workers [4] also postulate that the onset of the exothermic collapse of the cathode occurs between C and D with the production of oxygen: the collapsed cathode and oxygen both then react exothermically with the solvent [6], although in experiment A7 the temperature does not increase at a greater rate in this section. Very significant structural collapse then takes place between E and F, when most of the lithium ions are removed from the cathode [3, 6, 7], according to [3]:



Zhu et al. [3] postulate that lithium dendrite formation also commences at C as does the leaching of Mn ions [8]. Lithium metal plating takes place when the flux of lithium ions

to the anode cannot satisfy the demand from the charging current [9]: however, dendrite formation is the last stage, the lithium first plates as islands which then transform into mossy growth followed by the formation of dendrites [9].

Zhu and co-workers [3] and Shan et al. [5] postulate that the “plateau” region D → E is due to a disproportionation reaction in the cathode that results in two co-existing phases, and that Li plating and Mn dissolution also take place in this region. In contrast, Jiang et al. [4] suggest that the plateau is due to a balance between the increased voltage associated with charging and the creation of multiple small internal short circuits (and hence voltage drop) due to dendrite formation. Dendrites are generally believed to grow from anode to cathode through the separator and touch the cathode, causing catastrophic internal short circuit, Joule heating and fire and/or explosion [10]. However, such dendrites are thin and expected to melt as soon as current flows, i.e. act as fuses, hence catastrophic short circuit would not be expected to occur [9] and could provide the balancing process against the voltage rise due to charging on the plateau. In any case, dendrites would not be expected to penetrate any ceramic coating on the separator [11], and the Envision-AESC separators are coated in this way.

Separators melt according to their composition, i.e.: polyethylene (PE) 130 °C, polypropylene (PP) and PP/PE/PP 165 °C whilst ceramic coated polymer separators collapse at temperatures > 200 °C [2]. The lithium metal on the anode will melt at 180 °C [1, 3] which will cause very significant and catastrophic internal short circuit and separator collapse and lithium metal melting is likely to occur at F: note the explosion at point F in Figure 4.5(d) and the temperature on the top of the module reaching a maximum of 250 °C.

Table 4.1 shows that thermal runaway (F) occurs at SoC = 131 – 134 %, which is significantly lower than reported in the literature [1-5]. However, a number of authors state that the outcome of overcharge tests are highly dependent upon the test parameters (including: form factor, C-rate [4], the stoichiometric ratio of anode to cathode [5]) and suggest therefore that the resulting irreproducibility of these tests render them unsuitable as a test method [2]. Further, comparisons between cells of the same chemistries etc but from different manufacturers is questionable due to the possible use of e.g. overcharge protection additives such as redox shuttles, the presence of which in a cell is a commercial secret [2].

Table 4.1. The SoCs and voltages at which the various regions and points in figure 4.6 occur for the overcharge experiments along with the maximum temperature changes recorded by the thermocouple under the overcharged module.

Experiment	SoC / %				Max change in TC_{under} / °C
A6	124 (C)	130 (D)	132 (E)	134 (F)	12
A7	123 (C)	128 (D)	129 (E)	131 (F)	30
	Voltage / V				
A6	4.7 (C)	5.27 (D)	5.20 (E)	5.06 (F)	
A7	4.92 (C)	5.53 (D)	5.50 (E)	5.32 (F)	

The thermocouple on the top face of the overcharged module (TC_{top}) showed a spike to c.a. 250 °C, see Figure 4.5(c) & (d), with an estimated temperature rate of increase of c.a. 5000 °C min⁻¹, which decreased back to a steady c.a. 34 °C for c.a. 1 min. The spike coincided with the explosive ejection of flare-like flames, see Figure 4.4(e-h), with the largest flame area and the collapse of the overcharged module as the gases were released: the collapse then protected the thermocouple. The temperatures of thermocouples on top and on the underside (TC_{under}) of the overcharged module then remained around 34 °C for c.a. 1 minute during the ejection of the vigorous flames. As the thermocouples were located between the modules, the latter suggest that there was little heat transfer through the overcharged module during this period, and most of the heat released was carried away by the flames. During the period between extinguishing the flames and re-ignition, both thermocouples registered a temperature of 100 °C, suggesting that cooling by the foam was reasonably efficient. As can be seen from Figure 4.5(d), prior to re-ignition and the reappearance of the flare-like flames around 38 minutes from the start of data collection (charging started after 12.5 minutes), the temperatures registered by both thermocouples started to increase, showing the existence of exothermic reactions in one or more modules. The rate of the increase in temperature between the bottom two modules (TC_{under}) starts to slow before exhibiting an inflexion at 37.9 minutes, corresponding to the first of the flare-like flames on re-ignition, and rising again rapidly, levelling out at c.a. 855 °C around 41.5 minutes. The onset of the rise in the temperature of the thermocouple between the top and middle modules (TC_{top}) was somewhat earlier than that of TC_{under} and levelled out at c.a. 482 °C during the re-ignition before increasing again. The somewhat curtailed flame analysis was due to the optical cameras overheating and ceasing to record before the final flares due to the ignition of the cells in the two other modules which were responsible for increasing thermocouple temperatures at times > 39.3 minutes.

The data in Figure 4.5 are consistent with the overcharge and explosion of two cells from the middle module, along with, in all likelihood, the other parallel pair of cells of the same quartet. However, the remaining quartet of cells do not fail until after the re-ignition, causing the increase in the temperature registered by TC_{top} to c.a. 750 °C. This suggests some of the initial flares observed between 33.8 and 35.5 minutes were due to cells in other modules, and none of the flares observed between re-ignition and the overheating of the cameras were due to the remaining quartet of cells in the middle module. The optical video footage shows flare-like flames emerging from the lower module at times corresponding to the flares following re-ignition in Figure 4.5(d) suggesting the increasing temperature between middle and bottom modules was due to the lower module undergoing thermal runaway, as the thermocouple between the top and middle modules does not mirror this increase despite the increase in flame area at the same time.

4.2 Nail penetration experiments at DNV April/May 2021

The 3 module overcharge experiment at the DNV 1 site in January 2020, discussed above (experiment A7), and particularly the 50 % SoC experiment at the FSC (experiment B2) triggered the realisation that statements in the academic literature and the media referring to “smoke”, “gas”, and “steam” simply referred to stages during a common timeline when LiBs are abused: the abuse triggers chemical processes that supersede the usual electrochemical reactions in the cell. The chemical processes generate gases and heat, the latter increasing the rate of the chemical reactions and hence generating more gases and heat. When the rate at which the heat is generated exceeds that at which the heat is dissipated, the temperature of the battery increases and uncontrolled positive feedback leads to thermal runaway: eventually, the blast caps on cylindrical and prismatic cells rupture, and pouch cells burst, venting the gases which take with them fine droplets of the solvents. Most often, the vapour cloud so produced is mistaken for smoke [12]. If the vapour cloud ignites immediately, long flare-like flames are produced with a thin fume: if ignition is delayed, a vapour cloud deflagration can result [13, 14]. LiBs can also explode on being abused due to the build up of gas inside the cells. Defects and contamination during the manufacturing process can also lead to thermal runaway and “spontaneous” combustion or failure [15].

Thermal runaway has been observed at low SoC (even 0 %) [16, 17], and has also not taken place at all. Experiment B2 suggested that, at low SoC, ignition of the vapour cloud could be delayed or postponed indefinitely, and the subsequent ignition of the vapour cloud so produced could cause an explosion. Thus, three nail penetration experiments were performed, C4 - C7, with the intention of (i) delaying or preventing ignition and so (ii) initiating a vapour cloud explosion, and (iii) investigating the composition of the vapour cloud. Experiments C4, C5 and C7 employed a single Envision-AESC module at 40 %, with the plastic blast wall at the end of the container for C4 and halfway into the container for C5 and C7. Experiment C6 utilised two modules at 35 % SoC with the blast wall $\frac{3}{4}$ of the way into the container, to maximise the concentrations of any gases and solvent droplets. Gas sensors and GCMS were deployed as detailed in Chapter 2.

4.2.1 Experiment C4

The previous sets of experiments undertaken (DNV 1 and FSC) had shown that after a nail had penetrated a module, white vapor was emitted, and this ignited for higher SoC modules. It was assumed that the higher SoC LiBs contained enough electrical energy to produce an arc which ignited the vapour cloud. For experiment C4, squibs were employed as an ignition source, and although this was the first attempt to ignite the vapour cloud, it was expected to be successful, hence no gas sensors were employed, as it was considered that the ignition would destroy them.

Figure 4.7 shows frames from the experiment: as can be seen at nail penetration (a), 1.33 s after nail penetration a white vapour cloud was vented from the righthand side of the module (b), the nail and hammer rose 10.2 seconds after penetration (c), followed by the explosive release of the black nanoparticles of cathode material (d), 27.2 seconds after nail penetration the white vapour cloud accumulated at the ceiling (d). A heavier than air vapour cloud was vented 64.9 seconds after penetration that collected on the floor of the container (e), reaching the end of the container after 85.4 seconds (f), followed by the ignition of the module 96.1 seconds after penetration (g), and an attempt to ignite the vapour at 120 seconds after penetration (h).



(a) A photograph taken during experiment C4 when the nail first penetrates the module (time = 0 s).



(b) A photograph taken during experiment C4 when a white vapour cloud began to be vented from the right hand side of the module (time = 1.33 s).



(c) A photograph taken during experiment C4 when the nail rose out of the module (time = 10.2 s).



(d) A photograph taken during experiment C4 when there was an explosive release of black material, presumably nanoparticles from the cathode, and the white vapour accumulates on the ceiling of the container (time = 27.2 s).



(e) A photograph taken during experiment C4 when a second type of vapour is emitted from the module, this sinks to the floor of the container suggesting it is heavier than air (time = 64.9 s).



(f) A photograph taken during experiment C4 when the heavier than air type vapour cloud accumulates on the floor of the container (time = 85.4 s).



(g) A photograph taken during experiment C4 when the module ignites (time = 96.1 s)



(h) A photograph taken during experiment C4 when the squibs are activated in an attempt to ignite the remaining vapour cloud (time = 120 s).

Figure 4.7. Frames collected from the optical video in experiment C4 (a), (b), (c), (d), (e), (f), (g) and (h). The images were collected at the times specified in the text.

Various squibs were ignited throughout the experiment, one is shown in Figure 4.7(h) but failed to cause the vapour cloud to explode, presumably because the flammable gas concentration was below the LEL, which is generally believed to be 5 – 11 %, (this was estimated on-site and included the input of Dr Rob Crewe who has significant experience in hydrocarbon ignitions and explosions, and the flammable gas was presumed to contain droplets of hydrocarbon solvent and hydrogen), depending upon conditions, chemistry etc. Thus, Wang and co-workers [18] report that the explosion risk is higher for LFP batteries than NMC due to a higher proportion of hydrogen and lower concentrations of CO and CO₂ (albeit with lower over volume of vapour cloud than NMC) hence the LEL for LFP was determined to be 5.4 %, and that for NMC 9.0 – 9.5 %. Rosewater and Williams [19] have proposed the following expression for the vapour cloud LEL:

$$E_{LEL} = V_{room} \times LEL \times \frac{E_{cell}}{V_{runaway}} \quad (4)$$

where E_{LEL} is the cell energy needed to reach specified LEL (Wh), the LEL is expressed as a decimal, V_{room} is the volume of the room, E_{cell} is the cell or battery energy (Wh) and $V_{runaway}$ is the volume of gas produced in thermal runaway.

In complete contrast, Jin et al. [20] have postulated that it is the small droplets of solvent that are responsible for the explosion of the vapour cloud: the team overcharged an 8.8 kWh battery in a BESS container and ignited the vapour cloud so produced with a heater. The explosion occurred with the concentrations of hydrogen and CO very significantly below their LELs.

A significant challenge is in researching the volume and composition of the vapour cloud produced by LiBs in thermal runaway, and the factors that affect these is the lack of scientific data: whilst there is a plethora of studies in the literature on cells, studies on larger assemblies of cells (modules, packs) are extremely rare: moreover, by far the majority of all studies focus on LiBs on fire and the smoke that is produced, rather than on LiBs in thermal runaway without ignition and hence producing the vapour cloud. In general, studies on the vapour cloud rather than smoke have involved sending LiBs into thermal runaway in oxygen-free environments [18, 21-23], with a fixed volume of air [24, 25] or at low SoC [26]. The latter study was serendipitous as the authors expected the LiB to ignite. Matters are further complicated by the fact that a range of analytic techniques are required if all the components of the vapour cloud are to be detected and

quantified, and this is generally not the case, and the amount of solvent vented is not determined.

From the limited data available, NMC cells produce c.a. 500 to 5300 L kWh⁻¹ of the vapour cloud, whilst LFP cells some 10x lower volumes: Koch et al. [24] and Hoelle et al. [25] have reported a linear relationship between the volume of vapour cloud produced (excluding droplets of solvent) and LiB capacity of c.a. 2 L Ah⁻¹. Assuming 4.2V at 100% SoC for NMC cells, this is equivalent to c.a. 480 L kWh⁻¹: however, the volumes and composition of the vapour cloud depend on SoC and exact NMC chemistry. With respect to composition: in general, the major components of the cloud are H₂, CO and CO₂, along with a range of gases that include: HCl, HCN, HF as well as hydrocarbons [13, 22, 23, 27]. The collapse of the separator then causes significant internal short circuit and consequent Joule heating leading to TR, the gases are expelled along with an aerosol of the cathode material and droplets of the organic solvent [13].

It is clear from the optical images in Figure 4.7 and the limited academic literature that very large volumes of vapour cloud can be produced by even small LiBs, hence the increasing number of reports in the media of explosions involving micro mobility devices such as e-scooters, e-bikes etc (see, for example [28, 29]).

4.2.1 Experiments C5 – C7

During experiments C5 – C7, the collapse of the various voltages followed the same pattern, with the two top cells pairs collapsing first, then the lower cell pairs, see Figure 4.8 & 4.9. In experiments C5 & C6, ignition of the module occurred, 60 s and 66 s after nail penetration, respectively: ignition did not occur in experiment C7.

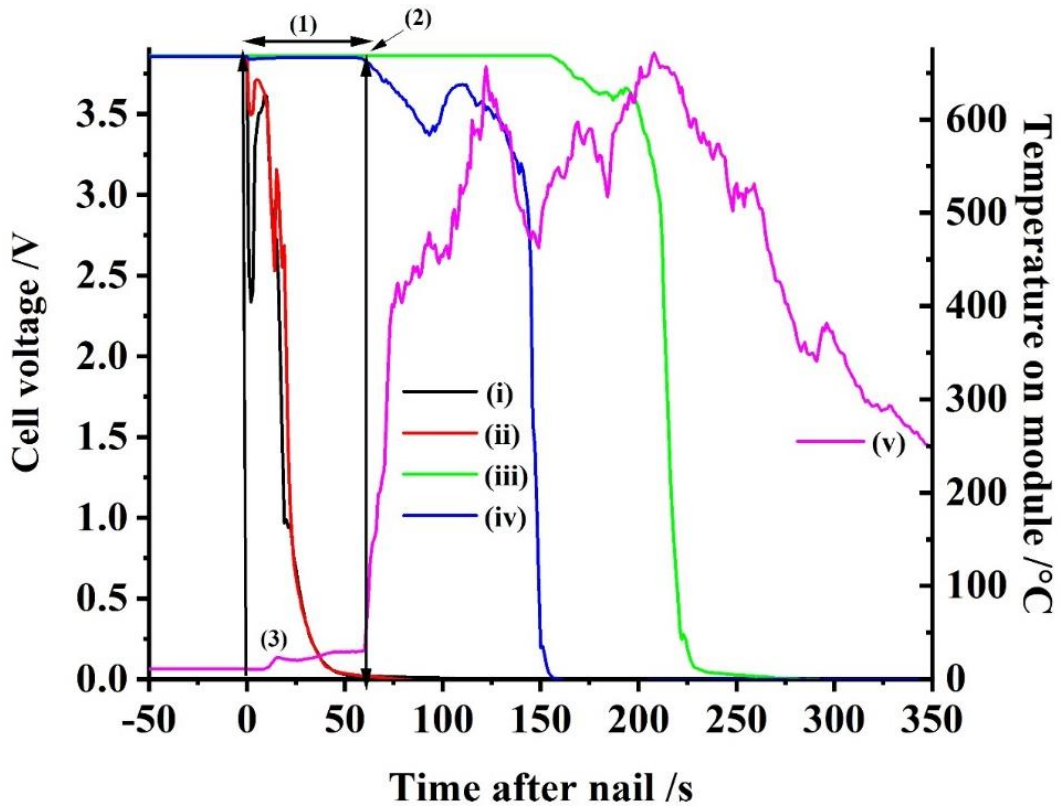


Figure 4.8. Plots of: (i) – (iv) the voltages of cell pairs 1 – 4, respectively, during experiment C5 in which one module at 40% SoC was penetrated with a nail, (v) the temperature of the thermocouple affixed to top of module. (1) Vapour cloud produced; (2) module ignites 60 s after penetration; and (3) blue/purple emission “flame” observed.

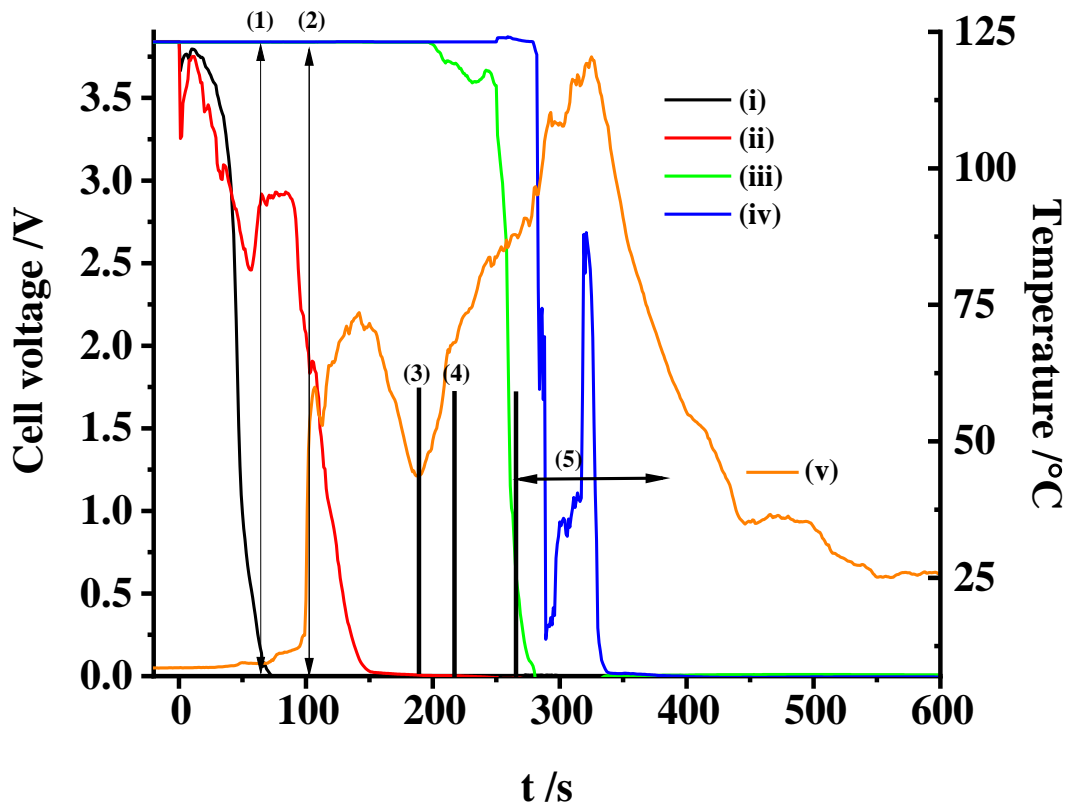


Figure 4.9. Plots of: (i) – (iv) the voltages of cell pairs 1 – 4, respectively, on one module during experiment C6 in which two modules each at 35b % SoC were penetrated, and (v) the thermocouple above the module.

Figure 4.10 shows a frame taken during experiment C5, nail penetration of a single module at 40 % SoC, 16.2s after nail penetration.



Figure 4.10. A frame taken during experiment C5 from an optical camera on the nail penetration rig, 16.2s after nail penetration.

Figure 4.11 shows frames from the video taken by the optical camera mounted on the floor behind the module and under the frame of the nail penetration rig during experiment C6: (a) 8.47s, (b) 11.4s, (c) 32.0s, (d) 67.0s, (e) 100.0s and (f) 103.0s after nail penetration.



(a)



(b)



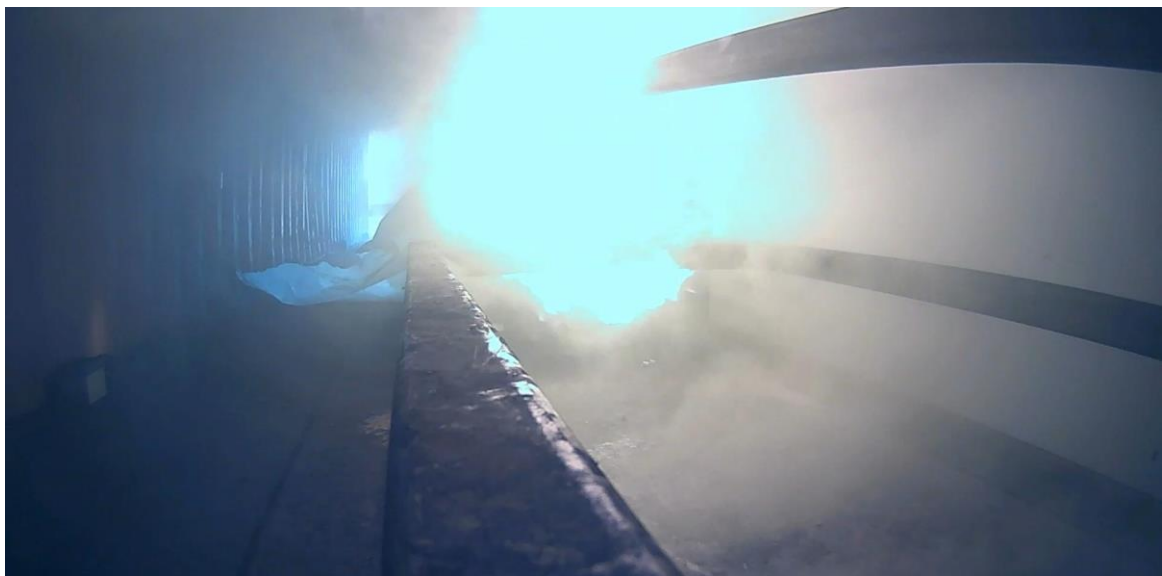
(c)



(d)



(e)



(f)

Figure 4.11. Frames from the video taken by the GoPro camera mounted on the floor behind the module and under the frame of the nail penetration rig during experiment C6: (a), (b), (c), (d), (e) and (f). The images were collected at the times specified in the text.

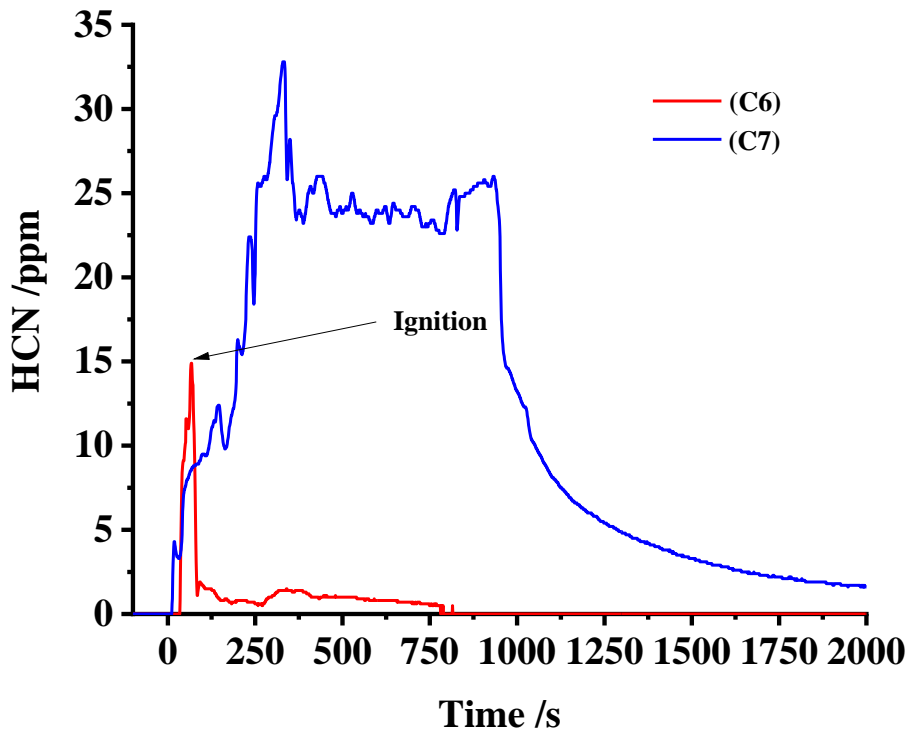
In experiment C6, as can be seen from Figure 4.9, the voltages of the topmost cell pairs 1 and 2 collapse together first, followed by 3 and finally 4. As stated above, the module ignited c.a. 66 s after penetration (the time taken for the voltages of cell pairs 1 & 2 to collapse), with the temperature in the air above the modules reflecting this ignition and subsequent flares. Unfortunately, the thermocouple mounted on the top surface of one of the modules failed: however, the time at which ignition occurred is clear from the vertical

response of the thermocouple located above the module, which increased at a rate of $13.8\text{ }^{\circ}\text{C s}^{-1}$.

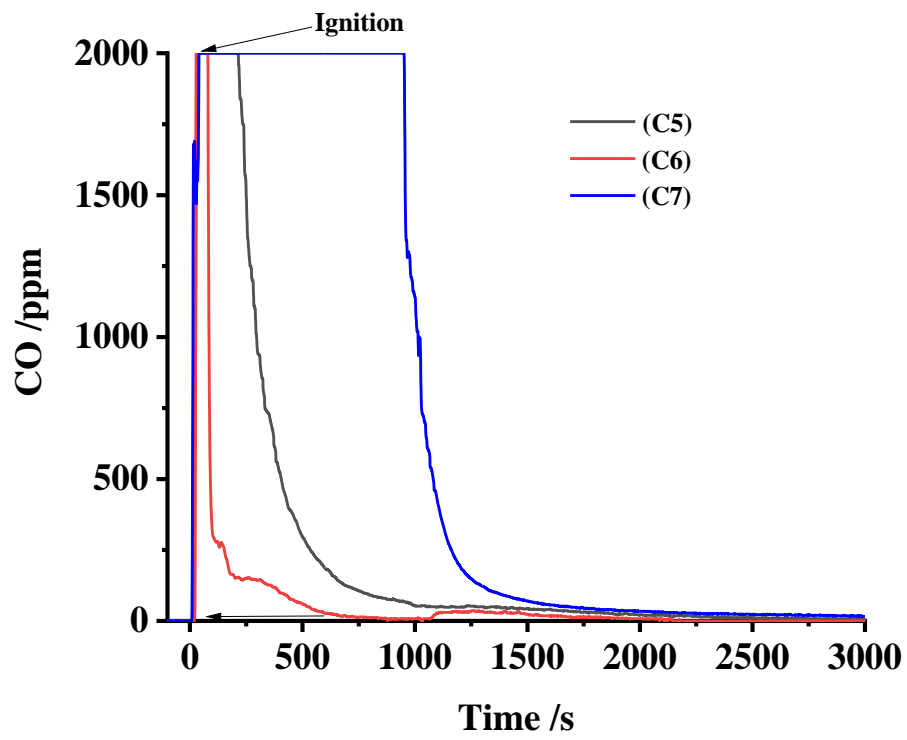
As can be seen from Figure 4.11(a), 8.47 seconds after nail penetration in experiment C6, the pouch cells swell due to the severe internal short circuit causing the generating of large volumes of gas: this breaks the contact with cell pairs 3 & 4, delaying their descent into thermal runaway (see Figure 4.9). The same sequence of events occurred in experiment C5 (see Figure 4.8). A purple/blue emission can be seen in Figure 4.11(b) 11.4 s after penetration, along with the emission of the vapour cloud from the same location and this is apparent in (c), 32 s after penetration. Figure 4.11(d), 67 s after penetration shows a frame taken after the module ignites into flames: 33 seconds later the module flared, see (e), 3 s later the vapour cloud was completely consumed, see (f). In all the experiments ignition of the modules (where ignition took place) was preceded by the purple/blue emission which was the source of the vapour cloud. This can be seen more clearly in Figure 4.10, taken during experiment C5, 16.2 s after nail penetration: there is a flame-like blue emission (ringed) behind the retort stand with vapour produced around the flame and from the tip, where the vapour is being ejected with high velocity.

Unfortunately, no cameras were placed on the nail penetration rig for experiment C7 as the video data from the previous experiments had not been processed and the blue/purple emission had thus not been observed. The module employed in experiment C7 did not ignite, and hence provides a useful comparison for the gases evolved during the various experiments, see Figure 4.12. Gas sensors were positioned at the back wall, and by the blast wall, at three heights, by the roof, floor and in halfway up, and at the same three heights in between the blast and back wall, moving as the blast wall changed positions. These are not shown in the 3D drawings in Chapter 2, as the small size of the sensors do not show against the container.

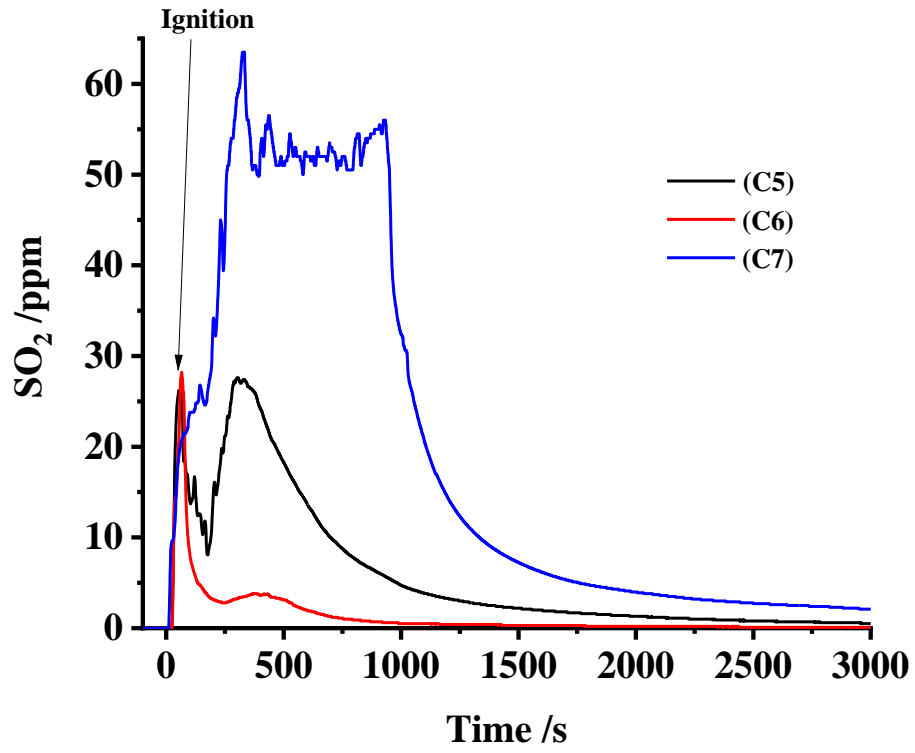
Figure 4.12 shows plots of the concentrations of (a) HCN, (b) CO, (c) SO₂, (d) H₂, for experiments C5, C6 and C7, and (e) HCN, SO₂, and CO for experiment C7.



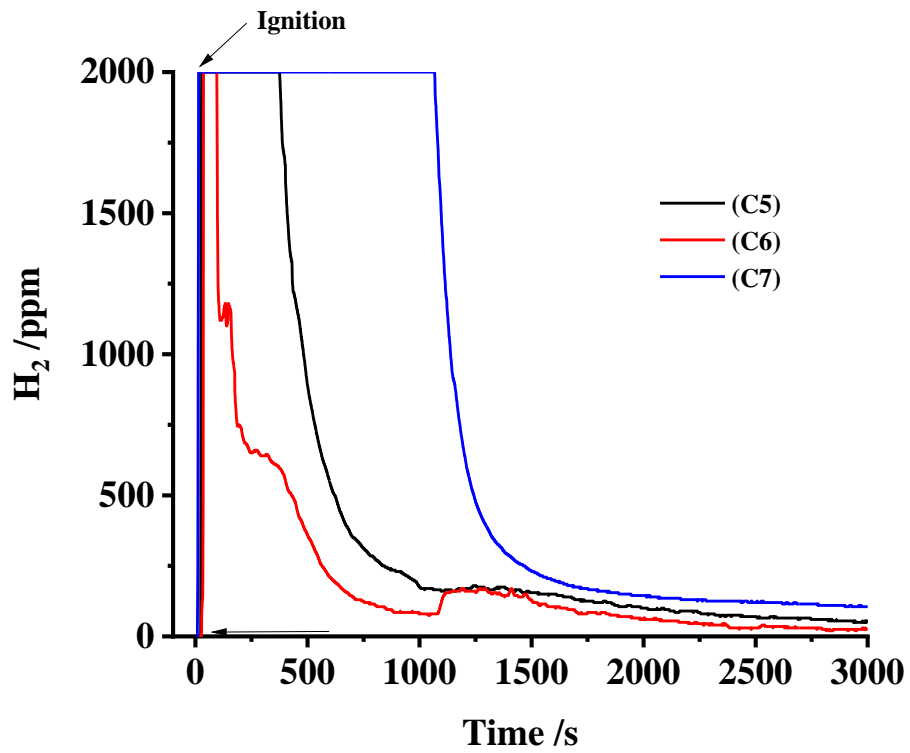
(a)



(b)



(c)



(d)

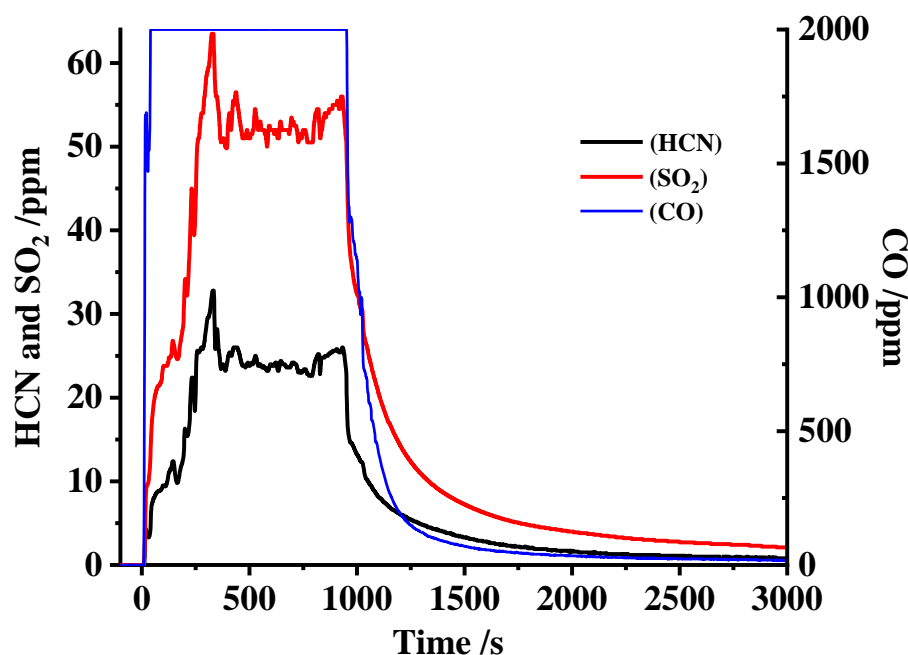


Figure 4.12. Plots comparing the production of (a) HCN, (b) CO, (c) SO₂ and (d) H₂ in experiments C5, C6, and C7. (e) Shows plots of the concentrations of HCN, SO₂ and CO during experiment C7.

The decrease in the concentrations of CO and SO₂ track each other, as has been observed previously, suggesting the two gases had a common origin which was attributed to the pyrolysis of the additive ethylene sulphite (see Chapter 3). The HCN and SO₂ concentrations in Figure 4.12(e) track each other rather suspiciously closely, and this may be due to crosstalk, i.e. the sensor is sensitive to both gases.

Most noticeable (and consistent) is the persistence of the flammable gases HCN, H₂ and CO in experiment C7 when there was no ignition: in fact, it is noteworthy that even after ignition, H₂ and CO concentrations remained saturated for some time at least in experiments C5 and C7: as may be expected they decreased significantly more rapidly following ignition in the ¼ container volume of experiment C6. In contrast, Figure 4.12(c) shows that the variation in the concentration of SO₂ in the three experiments is somewhat more complicated: it is produced prior to ignition and rapidly decreases following ignition: however, in both experiments C5 and C6 it shows a second maximum following ignition. In experiment C7, it is not lost for some time.

Trace amounts of the following organic compounds were detected by a HAPSITE ER GCMS during the vapour cloud emission in experiment C5: the dominant fraction was the electrolyte i.e. diethyl carbonate. The remaining compounds included benzene, dimethylsilanediol, styrene, ethylbenzene, and various hydrocarbons in the range of C9 to

C14 (i.e., 3,3,5-trimethyl-1-hexene, 2,6,6-trimethyl-dodecane, 2,3,6,7-tetramethyl-octane, 2-methyl-decane, 2-methyl-5-propyl-nonane and 4-methyl-undecane). From the literature, as well as the main constituents of the vapour cloud, HCN, HF, HCl etc., traces of C4 – C8 organic compounds have also been detected [27, 30]. Thus, the analytical data obtained during the experiments discussed in this section are not inconsistent with the literature.

Returning to the blue/purple emission observed in experiments C5 and C6, see Figure 4.10 and Figure 4.11(b), it is clear that there is a major inconsistency: during the production of the vapour cloud, the temperatures of the modules in experiments C5 and C6 were clearly too low for pyrolysis [31] or combustion [31, 32] to be responsible for the vapour cloud, as these processes require temperatures in excess of 600 K. These inconsistencies raise the question that, if the reactions responsible for the constituents of the vapour are not thermally driven, what process is responsible for their formation?

One possible, if tentative theory, is as follows. The cells each hold c.a. 81072 Coulombs of charge: over the 60s when the cell pairs 1 & 2 voltages collapse, this equates to a “discharge current” of 1351A. Thus, the blue/purples emission may be due to a DC arc plasma, dominated by emission from metastable electronically-excited nitrogen molecules and ionized species from the air, including the C³P-B³P system [33].

Plasma is generally regarded as the fourth state of matter, and comprises atoms, molecules, ions, electrons, and radicals having internal energies (with the exception of the electrons) unevenly distributed over the three degrees of freedom [34]. The generation of plasma relies on the fact that all neutral gases have stray charges due to, for example, ionisation by cosmic radiation [35]: a DC or AC electric field is then employed across two electrodes in a gas to accelerate the stray electrons to sufficient velocities to cause a cascade of ionizing collisions according to Townsend theory, and the formation of a plasma. The current/voltage characteristics of the plasma determine its type, thus [34]:

$$10^{-7} - 10^{-5} \text{ A} = \text{Corona discharge}$$

$$10^{-5} - 1 \text{ A} = \text{Glow discharge}$$

$$> 1 \text{ A} = \text{Arc discharge}$$

Arc discharge or plasma requires relatively low voltage to maintain once a stable arc is established and requires higher gas pressures than the other plasmas.

Due to the presence of radicals, ions and excited species present in plasma that would require temperatures > 1000 K to be produced thermally, it is generally assumed that plasma chemistry could offer the possibility of opening up highly novel chemical pathways, and this has been the experience of Professor Paul Christensen (see, for example, [36, 37]).

4.3. Conclusions

This Chapter began with electronically abusing lithium-ion batteries by overcharging until thermal runaway commenced which can be a catastrophic event in the case of, for example, a malfunctioning BMS. These experiments, similar to the nail penetrations at DNV 1, emitted an unknown gas which ignited almost immediately, producing flare-like flames. Extinguishing the flames produced a large quantity of white gas, similar to experiment B2 at FSC, which re-ignited and again produced flare-like flames. The realisation that the white gas emitted in B2 could form a flammable vapour cloud and mistaken for smoke or steam made the determination of the emitted gas desirable to know. Further experiments at DNV 2 to sample the emitted vapour and ignition attempts of the vapour cloud in a confined space led to the discovery of a purple/blue light during the vapour emission.

The overcharging of a lithium-ion cell follows a voltage/time curve, where initially the voltage rises rapidly, then rises at a slower rate, rises rapidly again, plateaus, drops and then thermal runaway commences. At the beginning of thermal runaway, a white gas is emitted from the cell which quickly ignites in the presence of molten hot material being ejected from the cell, producing flare-like flames. Heat propagation then sends neighbouring cells and modules into thermal runaway.

The extinguishing of a lithium-ion battery fire was achieved with a foam extinguisher; however, it did re-ignite producing the same flare-like flames. Once the flames were extinguished the temperature between the modules stayed at 100 °C, most likely due to water surrounding the thermocouples until it evaporated, and a large amount of white vapour was produced, easily confused for steam. Once the water evaporated the temperature began to rise as the self-sustaining exothermic reactions inside the module continued, eventually igniting the white vapour, demonstrating that solely extinguishing flames is not enough to cease thermal runaway.

Analysis of the white vapour showed it contains flammable materials, such as: CO, H₂, diethyl carbonate, benzene, and other hydrocarbons from C₉ – C₁₄. Diethyl carbonate is a known component of the electrolyte. A purple/blue light was observed during the vapour emission, a hypothesis for the creation of this is: the formation of a plasma.

References

1. Yuan, Q., et al., Overcharge failure investigation of lithium-ion batteries. *Electrochimica Acta*, 2015. 178: p. 682-688.
2. Feng, X., et al., Thermal runaway mechanism of lithium ion battery for electric vehicles: A review. *Energy Storage Materials*, 2018. 10: p. 246-267.
3. Zhu, X., et al., Overcharge investigation of large format lithium-ion pouch cells with Li (Ni_{0.6}Co_{0.2}Mn_{0.2})O₂ cathode for electric vehicles: Thermal runaway features and safety management method. *Energy*, 2019. 169: p. 868-880.
4. Jiang, L., et al., Overcharge behavior and early warning analysis of LiNi_{0.5}Co_{0.2}Mn_{0.3}O₂/C lithium-ion battery with high capacity. *Journal of The Electrochemical Society*, 2019. 166(6): p. A1055.
5. Shan, T., et al., Explosion behavior investigation and safety assessment of large-format lithium-ion pouch cells. *Journal of Energy Chemistry*, 2022. 72: p. 241-257.
6. Freunberger, S.A., et al., Reactions in the rechargeable lithium–O₂ battery with alkyl carbonate electrolytes. *Journal of the American Chemical Society*, 2011. 133(20): p. 8040-8047.
7. Feng, X., et al., Thermal runaway features of large format prismatic lithium ion battery using extended volume accelerating rate calorimetry. *Journal of power sources*, 2014. 255: p. 294-301.
8. Li, T., et al., Degradation mechanisms and mitigation strategies of nickel-rich NMC-based lithium-ion batteries. *Electrochemical Energy Reviews*, 2020. 3: p. 43-80.
9. Tomaszewska, A., et al., Lithium-ion battery fast charging: A review. *ETransportation*, 2019. 1: p. 100011.
10. Hill, D. and A.P.S. Company, McMicken Battery Energy Storage System Event: Technical Analysis and Recommendations. 2020: DNV GL Energy Insights USA, Incorporated.

11. Swart, J., K. White, and M. Cundy, APS McMicken Progress Report. 2020, Exponent, Inc.
12. Wang, H., et al., The efficiency of Aqueous Vermiculite Dispersion fire extinguishing agent on suppressing three typical power batteries. *Journal of Electrochemical Energy Conversion and Storage*, 2021. 18(2).
13. Christensen, P., et al., Thermal and mechanical abuse of electric vehicle pouch cell modules. *Applied Thermal Engineering*, 2021. 189: p. 116623.
14. Christensen, P.A., et al., Risk management over the life cycle of lithium-ion batteries in electric vehicles. *Renewable and Sustainable Energy Reviews*, 2021. 148: p. 111240.
15. Barone, T.L., et al., Lithium-ion battery explosion aerosols: Morphology and elemental composition. *Aerosol Science and Technology*, 2021. 55(10): p. 1183-1201.
16. Huang, L., et al., Uncovering LiH triggered thermal runaway mechanism of a high-energy LiNi_{0.5}Co_{0.2}Mn_{0.3}O₂/graphite pouch cell. *Advanced Science*, 2021. 8(14): p. 2100676.
17. Liao, Z., et al., Hazard analysis of thermally abused lithium-ion batteries at different state of charges. *Journal of Energy Storage*, 2020. 27: p. 101065.
18. Wang, H., et al., Fire and explosion characteristics of vent gas from lithium-ion batteries after thermal runaway: A comparative study. *eTransportation*, 2022. 13: p. 100190.
19. Rosewater, D. and A. Williams, Analyzing system safety in lithium-ion grid energy storage. *Journal of power sources*, 2015. 300: p. 460-471.
20. Jin, Y., et al., Explosion hazards study of grid-scale lithium-ion battery energy storage station. *Journal of Energy Storage*, 2021. 42: p. 102987.
21. Abbott, K.C., et al., Comprehensive gas analysis of a 21700 Li (Ni_{0.8}Co_{0.1}Mn_{0.1}O₂) cell using mass spectrometry. *Journal of Power Sources*, 2022. 539: p. 231585.
22. Sturk, D., et al., Analysis of li-ion battery gases vented in an inert atmosphere thermal test chamber. *Batteries*, 2019. 5(3): p. 61.
23. Said, A.O., C. Lee, and S.I. Stolarov, Experimental investigation of cascading failure in 18650 lithium ion cell arrays: impact of cathode chemistry. *Journal of Power Sources*, 2020. 446: p. 227347.

24. Koch, S., A. Fill, and K.P. Birke, Comprehensive gas analysis on large scale automotive lithium-ion cells in thermal runaway. *Journal of Power Sources*, 2018. 398: p. 106-112.
25. Hoelle, S., et al., Analysis on thermal runaway behavior of prismatic Lithium-ion batteries with autoclave calorimetry. *Journal of The Electrochemical Society*, 2021. 168(12): p. 120515.
26. Gully, B., et al., Technical Reference for Li-ion Battery Explosion Risk and Fire Suppression. DNV GL, 2019. 1025.
27. Zhang, Q., et al., Research on the effect of thermal runaway gas components and explosion limits of lithium-ion batteries under different charge states. *Journal of Energy Storage*, 2022. 45: p. 103759.
28. tl, T.V. Dad, daughter and dog flee as electric scooter explodes in Beijing living room while charging. 2018 [cited 2023 04/03/2023];. Available from: <https://www.dailymotion.com/video/x6r3mkf>.
29. Industry, B. Mackinac Island bans E-bikes from certain buildings after battery explosion, house fire. 2022; Available from: https://www.linkedin.com/posts/battery-industry_mackinac-island-bans-e-bikes-from-certain-activity-6961369406308278272-K3G-/?utm_source=linkedin_share&utm_medium=ios_app.
30. Chen, S., et al., Lower explosion limit of the vented gases from Li-ion batteries thermal runaway in high temperature condition. *Journal of Loss Prevention in the Process Industries*, 2020. 63: p. 103992.
31. Kanayama, K., et al., Study on oxidation and pyrolysis of carbonate esters using a micro flow reactor with a controlled temperature profile. Part I: Reactivities of dimethyl carbonate, ethyl methyl carbonate and diethyl carbonate. *Combustion and Flame*, 2022. 237: p. 111810.
32. Sinha, A. and M. Thomson, The chemical structures of opposed flow diffusion flames of C3 oxygenated hydrocarbons (isopropanol, dimethoxy methane, and dimethyl carbonate) and their mixtures. *Combustion and flame*, 2004. 136(4): p. 548-556.
33. Deng, X., et al., Direct current plasma jet at atmospheric pressure operating in nitrogen and air. *Journal of Applied Physics*, 2013. 113(2): p. 023305.
34. Gicquel, A., S. Cavadias, and J. Amouroux, Heterogeneous catalysis in low-pressure plasmas. *Journal of Physics D: Applied Physics*, 1986. 19(11): p. 2013.

35. Wong, C.S., et al., Methods of plasma generation. Elements of plasma technology, 2016: p. 15-48.
36. Christensen, P.A., et al., The production of methane, acetone, "Cold" CO and oxygenated species from isopropyl alcohol in a Non-thermal plasma: An in-situ FTIR study. The Journal of Physical Chemistry A, 2018. 122(17): p. 4273-4284.
37. Christensen, P., et al., The production of ketene and C₅O₂ from CO₂, N₂ and CH₄ in a non-thermal plasma catalysed by earth-abundant elements: An in-situ FTIR study. Plasma Chemistry and Plasma Processing, 2018. 38: p. 461-484.

Chapter 5 . Calculating Heat Release Rates from Lithium-Ion Battery Fires: A Methodology Using Digital Imaging

5.1. Introduction

This chapter reports the determination of Heat Release Rates from video images using the expression [1]:

$$\text{HRR [kW]} = 0.009489 \times \text{flame area (cm}^2\text{)} + 0.014722 \quad (1)$$

However, measuring flame lengths and areas from turbulent flame flares developing from lithium-ion battery failures is complex due to the varying directions of the flares, the thin flame zone, the spatially & temporally rapid changes of the thermal runaway event and the hazardous nature of the event. A method was developed using digital cameras and a newly developed numerical code to process the distortion of the flame size based on distance, direction, and shape. The model was tested with the data obtained in experiment C9 and validated with a reference set of measurements using calibration boxes, a method commonly used in the reconstruction of flame areas.

Experimental studies of failure of energy intensive objects such as lithium-ion batteries are becoming more widely used to understand the consequences of failure which can lead to combustion events [2-4]. These experiments provide an effective method of measuring temperature, pressure, off gassing, chemical composition, and the use of visual imaging to attempt to study flame flares is becoming more widespread [5, 6]. However, as with most combustion phenomena, visualization of a flame is helpful to try and interpret its behaviour and possible quantification of heat release rate, if the images obtained from the experimental setup can be processed and calibrated correctly [7-10].

Digital images can be used to make dimensional measurements and when recorded in video format these can be made as a function of time. This can be extremely beneficial when measuring spatially or temporally rapidly changing events, where there is insufficient time to make measurements or the position where the intended measurement is being taken changes, e.g.: unsteady flames, hazardous events where it is not safe to get close enough to make measurements, or where instrumentation modifies the experimental measurements or behaviour of the system such as

thermocouples locally quenching a flame [11]. Another advantage is that as the burning velocities of the different gases vary, there has been extensive work in modelling such velocities [12, 13], depending on conditions a camera can make measurements over a larger field of view. Recently, image processing tools have been implemented in estimating heat release rates for façade fires, with the use of two cameras [14].

There are challenges associated with the application of digital images as a viable option to match the measurement sensitivity of more invasive options, such as heat flux gauges and thermocouples. First, it is important to define a flame, in this thesis a flame is the zone in space where fuel and oxygen react together in a process called combustion to produce heat and visible light. The inside of the flame zone contains unburnt fuel, the outside of the zone is air, with exhaust gases emitted from the uppermost tip of the flame. The flame zone is assumed to be thin (e.g. 0.4 – 1.4 mm (methane), 0.6 – 1.6 mm (60% methane 40% hydrogen mix) [15]) as combustion reactions are faster than the diffusion of fuel gases (5.1 mm/s methane in air) and oxygen. A cross section of a candle flame with the flame zone is shown in Figure 5.1.

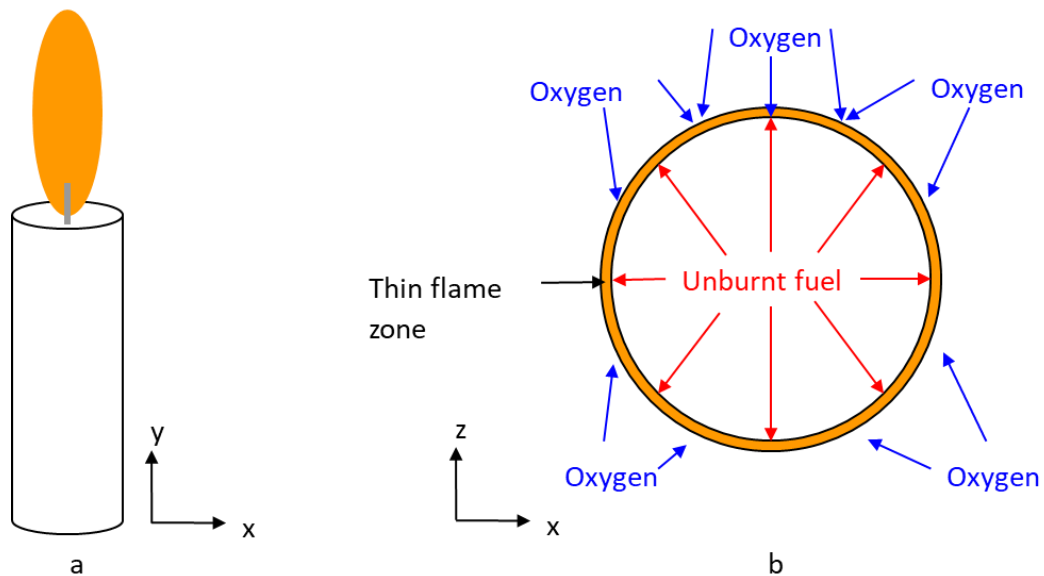


Figure 5.1. (a) A diagram of a candle and flame and (b) a cross section of the flame, showing the flame zone, unburnt fuel and oxygen moving towards the flame zone, not to scale.

In the flame, oxygen molecules migrate towards the flame zone from the surrounding air, whilst unburnt fuel molecules migrate towards the flame zone from within. For a fire to start it needs oxygen, fuel, and an ignition source, but once a fire has started the

ignition source is the flame itself, creating a self-sustaining flame zone [16]. The flame zone can appear to be stationary, as with a candle flame in a motionless atmosphere, or a rapidly changing shape, for example, in a draft. To measure the external dimensions of a stationary candle flame is relatively simple, it is regularly shaped, i.e. it is the same from all angles at the same altitude if the viewer is normal to the vertical direction of the wick, does not change with time, allowing a ruler or other metric device to be placed behind it at a known distance and the observer only needs to use a single equation to calculate the size of the flame (see Figure 5.1(b)) it is small and does not produce large quantities of gases or heat, i.e. it does not pose a significant safety risk to a person or measuring equipment in close proximity to the flame. Figure 5.2 shows a method for measuring the dimensions of a candle flame using a camera and measuring device.

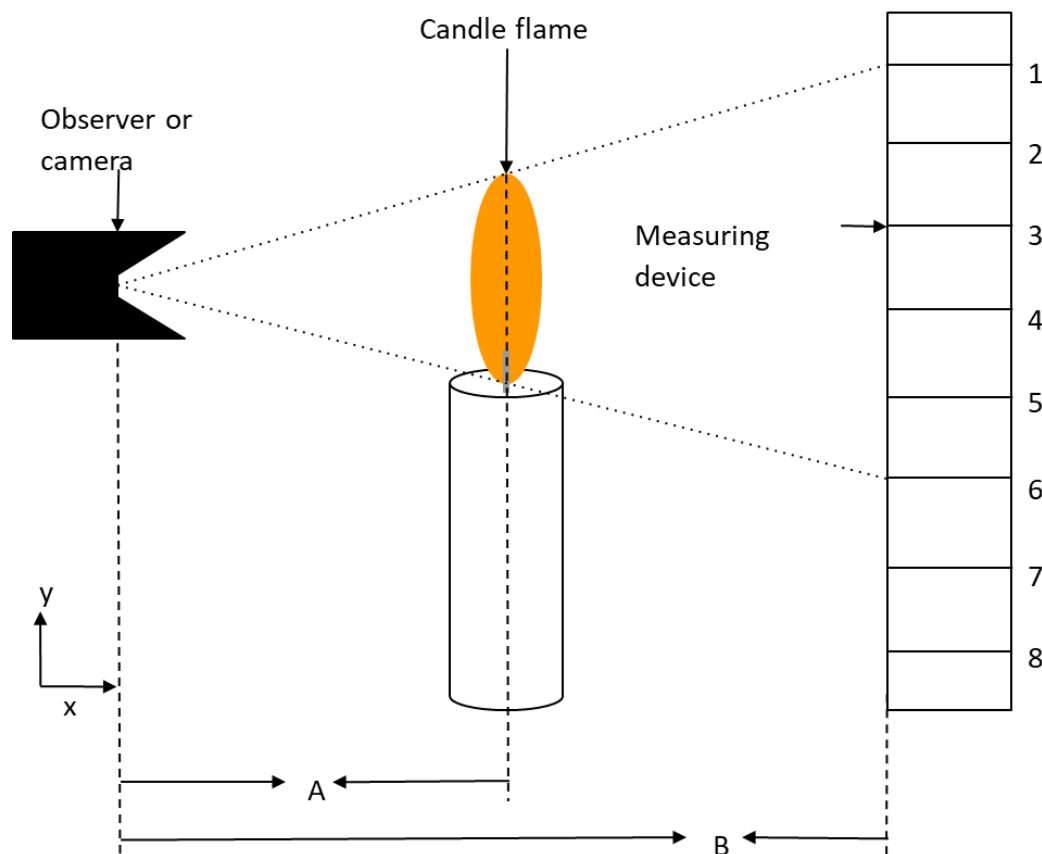


Figure 5.2. A schematic showing how to measure the height of a candle flame.

In Figure 5.2, the distance from the camera/observer to the flame is 'A' and the distance from the camera to the measuring device is 'B'. The dotted lines show how much of the measuring device is blocked by the flame, 5 units, but the flame is not 5 units high. The actual height of the flame (H) is given by:

$$\text{Flame height} = \frac{\text{number of units} \times A}{B} \quad (2)$$

So, if the measuring device is twice the distance from the camera as the flame, $B = 2A$, and the height of the flame in Figure 5.2 will be:

$$\text{Flame height} = \frac{5 \times A}{2 \times A} = 2.5 \text{ units}$$

The width of the flame can be measured in the same way by rotating the measuring device 90 degrees whilst keeping it in the line of sight, behind the flame from the camera/observer, see Figure 5.3.

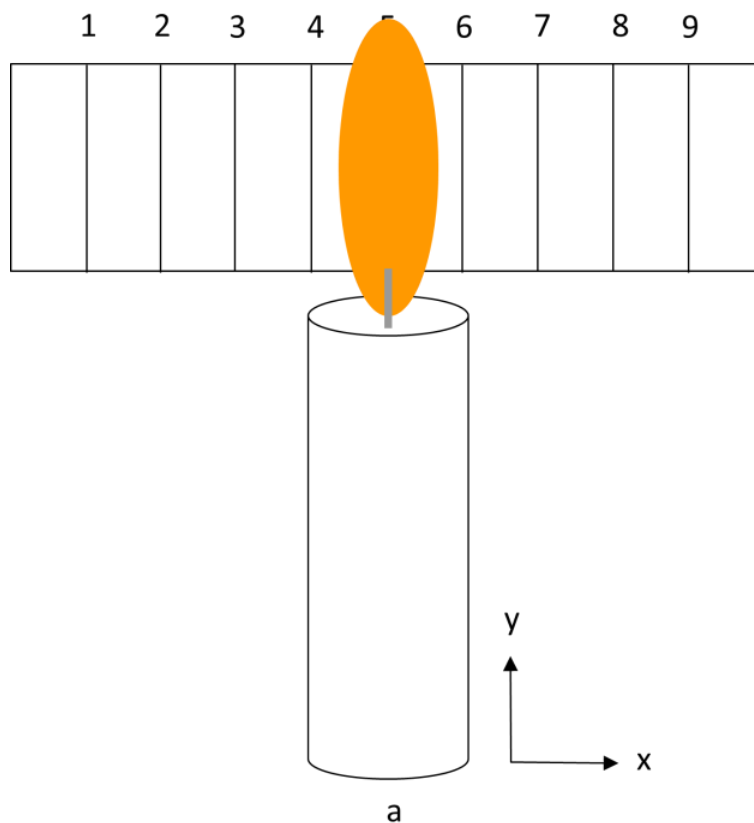


Figure 5.3. The camera/observer view of measuring the width of a candle flame.

To measure a rapidly changing, irregularly shaped and large flame, a method is needed which keeps the surveyor and equipment away from the maximum reach of the flame, fumes and hot gases being generated. Cameras combined with a measuring device offer a solution to these problems. A camera replaces the person, saves images at small intervals of time, and when the measuring device is in the camera's field of view, equation (1) is employed. Cameras do, however, present an additional problem in obtaining accurate measurements because the view can be distorted by the lens, in what is commonly referred to as the “fish-eye effect”. Calculating Heat Release

Rates from Lithium-Ion Battery Fires: A Methodology Using Digital Imaging presents a novel methodology for capturing and analysing flame data in complex phenomena such as lithium-ion battery failures, and then tests the methodology with real experimental setups and validates the results with reference measurements. The experiments were conducted at the DNV site at RAF Spadeadam in April and May 2021 using Envision-AESC modules comprising 8 x 56.3Ah lithium nickel manganese cobalt (NMC532) pouch cells. Fire was initiated by nail penetration using a purpose-built steel rig as described in Chapter 2.

5.2. Image Processing

This section highlights the different options for processing digital images for the purposes of correctly measuring flame lengths, flame areas, and the location of flames. A digital image is a two-dimensional recording of a scene from a set point. It is stored in a grid or ‘matrix’ configuration with each cell commonly called a pixel. The number of rows of pixels gives the height of the image and the number of columns gives the width. These numbers are often quoted to give the resolution of an image, for example, a 1080p HD image (1920p x 1080p) is 1920 pixels in width (columns) and 1080 pixels in height (rows). These are numbered from the top left corner of the image, with the top left pixel given a location of (1,1), as shown in Figure 5.4 and in the case of a 1080p HD image the bottom right pixel location is (1080,1920), as the row number is quoted before the column number.

$(1,1)$	$(1,2)$	$(1, \dots)$	$(1,1919)$	$(1,1920)$
$(2,1)$	$(2,2)$	$(2, \dots)$	$(2,1919)$	$(2,1920)$
$(\dots, 1)$	$(\dots, 2)$	(\dots, \dots)	$(\dots, 1919)$	$(\dots, 1920)$
$(1079,1)$	$(1079,2)$	$(1079, \dots)$	$(1079,1919)$	$(1079,1920)$
$(1080,1)$	$(1080,2)$	$(1080, \dots)$	$(1080,1919)$	$(1080,1920)$

Figure 5.4. Representation of pixels for a given location in an image.

The light sensor employed in a digital camera is a charge coupled device (CCD). At the microscopic level, a CCD is made of many small squares, also called pixels, arranged in a grid formation. These are numbered in the same manner as the pixels in the image and correspond to each other. A CCD takes advantage of the photoelectric

effect, where an electron is ejected from an atom if a photon of light hits it at a high enough energy, however a CCD only emits electrons when photons between certain wavelengths strike it, as shorter wavelengths (higher energy photons) are blocked by the lens [17], and longer wavelengths do not contain the required energy to eject an electron, leaving the CCD sensitive only to the visible part of the electromagnetic spectrum. If the CCD is connected to an electrical circuit, an electrical current is produced which is proportional to the number of photons that are incident on the pixel in a unit of time: thus, measuring the current measures the light intensity. The possible recording methods available from digital imaging, with the concomitant advantages and disadvantages, are presented in the next section.

5.2.1 Black and White recording method

The simplest method to record an image is as ‘black and white’. This is where each pixel in the CCD either receives light with both a wavelength in the working range of the CCD, and a high enough intensity of these to create a current above a minimum threshold to record a ‘1’ in the corresponding pixel in the digital image matrix; or, if neither of these events occur, a ‘0’ is recorded. When this image is displayed the pixels that contain a ‘1’ are white and the pixels that contain a ‘0’ are black. The resulting image from using this method can be hard to decipher, and vary depending on the minimum threshold, due to the quantity of information that is lost in recording, however, this method can be useful for identifying objects with a high contrast such as barcodes and QR codes. An example of this can be seen by comparing Figure 5.5, which is a colour photo comparable to what the human eye sees, with Figure 5.6(a-f) which are black and white images of the same scene but have different minimum thresholds. The images were collected during experiment C9 at the DNV site at RAF Spadeadam during April and May 2021.



Figure 5.5. A colour still photo taken from an observation camera.

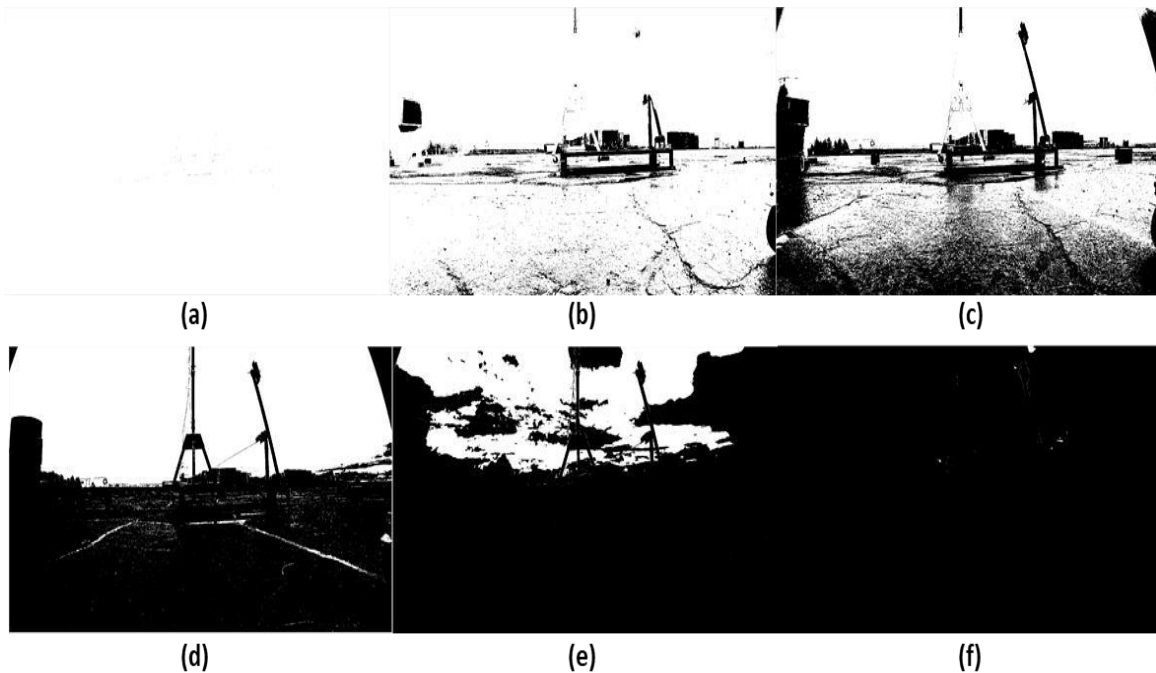


Figure 5.6. The image in figure 5.5 in black and white with different thresholds for light detection: threshold of: (a) 0, (b) 200, (c) 400, (d) 600, (e) 800 and (f) 1000.

Comparing the images in Figure 5.5 & Figure 5.6, at a minimum threshold of 0, Figure 5.6(a), there are still a few black pixels in the centre of the image with a value of '0' as '0' is not above the minimum threshold these pixels. The black appears grey, because each pixel is small, so to the observer they converge with the surrounding white pixels and appear lighter. When the threshold is increased to 200, Figure 5.6(b), the rig becomes visible in the centre of the image, along with other dark

areas of Figure 5.5. The sky, clouds, and turret, are however, still indistinguishable from each other. When the threshold is increased to 400, Figure 5.6(c), more of the concrete pad comes over the threshold and the rough surface can now be seen more clearly, the rig arm can now be seen, but the sky and clouds are still indistinguishable from one another. When the threshold is increased to 600, Figure 5.6(d), the concrete has become largely black, the turret is clearly distinguishable against the sky and clouds, but these are still indistinguishable from one another. When the threshold is increased to 800, Figure 5.6(e), the sky and clouds are now distinguishable, but at the expense of almost every other part of the image becoming black, the rig and turret can no longer be distinguished from the concrete. When the threshold is increased to 1000, Figure 5.6(f), almost all of the image is black, the maximum value is 1024, so only the brightest pixels in figure 5 are now '1's' or white.

Figure 5.7 shows a plot of the number of pixels in the image recorded as a 1 against the minimum light intensity threshold. From the figure it can be seen that there is a nonlinear dependency between the minimum light intensity threshold and the number of pixels that are recorded as a '1'. This is because an image has bright and dark areas, and it is possible that a whole area of the picture can change from a '0' to a '1' by changing the minimum threshold by 1. Figure 5.7 was created using Figure 5.5, changing the minimum threshold from 0 to 1000 and counting the number of '1's' each time, the image has 2160 rows and 3840 columns, producing a maximum number of pixels of $2160 \times 3840 = 8,294,400$ pixels.

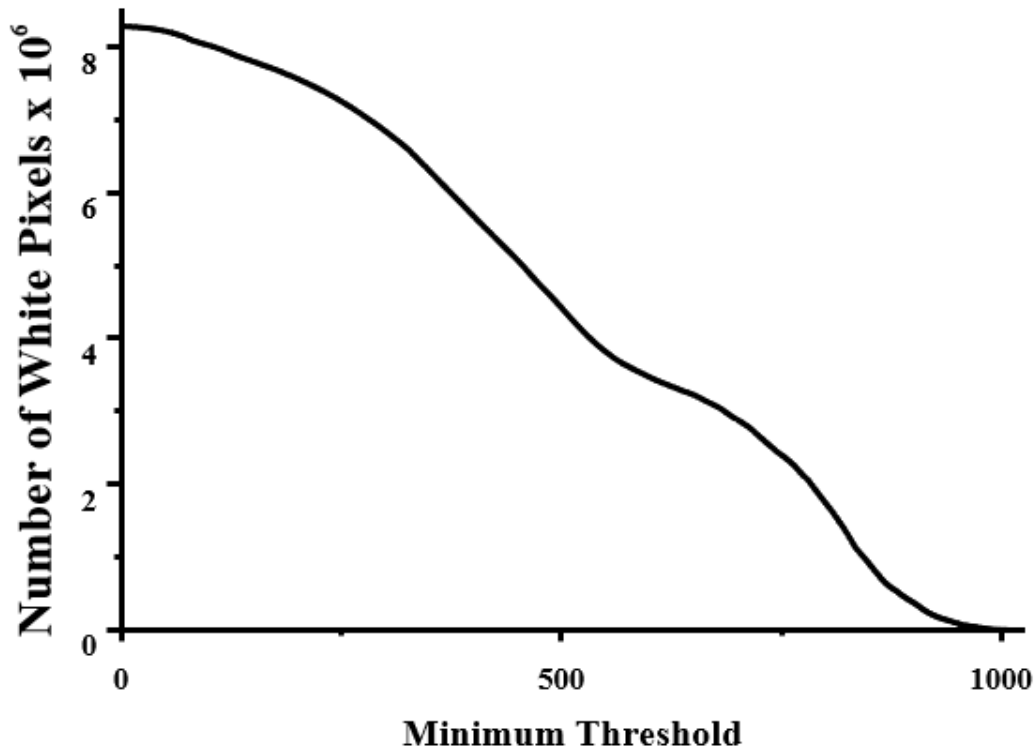


Figure 5.7. A plot of the effect of minimum threshold on the outputted number of pixels with thresholds from 0 to 1000.

5.2.2 Greyscale recording

The next simplest method is to record an image as ‘monochrome’, often called ‘greyscale’. This is where each sensor grades the light intensity that falls onto it using a scale between 0 and 255, with 0 being black, i.e. no light, then getting brighter at each increment until 255, which is displayed as white. The image obtained using this method requires more digital storage, but gives a much clearer representation of the original scene, as shown in Figure 5.5. In Figure 5.8, there are three methods shown for recording an image. All three use the general equation for calculating each pixel’s intensity:

$$\text{pixel intensity} = rR + gG + bB \quad (3)$$

With the condition, $r + g + b = 1$, and where r is the coefficient for the red light intensity (R), g is the coefficient for the green light intensity (G) and b is the coefficient for the blue light intensity (B).

Figure 5.8 shows three results for different r , g , and b values: (a) treats each colour equally ($r = g = b = 0.3333$), (b) gives G twice the importance of R and B ($r = b =$

0.25, $g = 0.5$), (c) uses $r = 0.2126$, $g = 0.7152$, $b = 0.0722$. The coefficients can be changed to any that the user desires, but as can be seen in Figure 5.8, all three methods show an image with greater detail than using black and white, with little difference between the three methods.

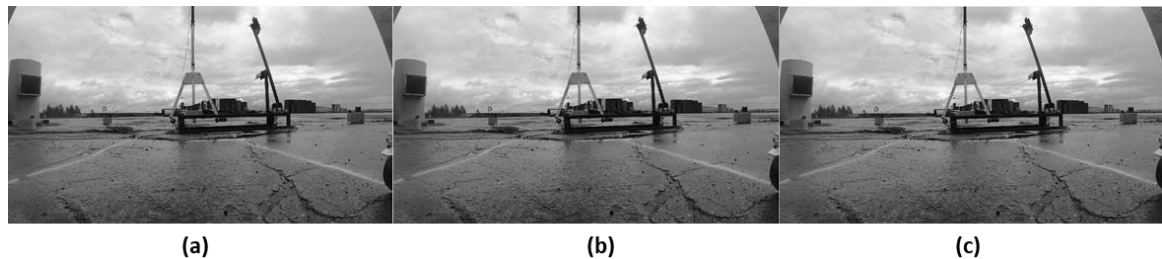


Figure 5.8. Three methods for accounting for the intensities of red, green and blue light: (a) all colours equal, (b) green twice the importance of blue and red and (c) a weighted scaling.

5.2.3 RGB Recording

Images can be recorded in colour, using a red, green, and blue method (RGB). This method uses a colour filter as shown in Figure 5.9, which is placed over the CCD. There are twice as many green pixels as red or blue, because the human eye has evolved to recognise green light the most, this makes the resulting display appear a better quality. As only red light can pass through the red filter, green light through the green filter and blue light through the blue filter, so the CCD now measures the intensity of a single colour on each pixel. However, digital screen pixels are made up of 3 parts, a red, a green and a blue, so a value for each of the three colours must be stored in each pixel. So, when saving the image, a value for the 2 missing colours is estimated from the surrounding pixels of the same colour, for example pixel (4,4) in Figure 5.9 will only record a value for green light intensity, to get a value for blue light intensity, for example, pixels (2,3), (2,5), (4,3), (4,5), (6,3) and (6,5) may be used, similarly for red light intensity, pixels (3,2), (3,4), (3,6), (5,2), (5,4), and (5,6) may be used. The resulting image from using this method requires more digital storage (3 times more than greyscale) but produces a colour representation of the original scene, as shown in Figure 5.5.

(1,1)	(1,2)	(1,3)	(1,4)	(1,5)	(1,6)	(1,7)
(2,1)	(2,2)	(2,3)	(2,4)	(2,5)	(2,6)	(2,7)
(3,1)	(3,2)	(3,3)	(3,4)	(3,5)	(3,6)	(3,7)
(4,1)	(4,2)	(4,3)	(4,4)	(4,5)	(4,6)	(4,7)
(5,1)	(5,2)	(5,3)	(5,4)	(5,5)	(5,6)	(5,7)
(6,1)	(6,2)	(6,3)	(6,4)	(6,5)	(6,6)	(6,7)
(7,1)	(7,2)	(7,3)	(7,4)	(7,5)	(7,6)	(7,7)

Figure 5.9. An example of a colour filter used with a CCD to produce colour digital images.

5.3. Image Processing of lithium-ion battery fires

Using the different digital imaging techniques presented in Section 5.2, the objectives of the processing of flame images are to: (i) determine the impact of image resolution and flame capturing speeds on quality of outputted flame measurement (Section 5.3.1), (ii) remove the ‘fisheye’ effect from images (Section 5.3.2), (iii) measure the surface area of a rapidly changing, irregularly shaped flame (Section 5.3.3) and (iv) calculate the heat release rate as a function of time in a battery fire (Section 5.4).

5.3.1 Comparing different camera resolutions and camera speeds

If the change in shape and size of an object of interest (m s^{-1} or $\text{m}^2 \text{s}^{-1}$) is much faster than the camera speed (frames s^{-1}), there will be a large jump in measurements between images (m frame^{-1} or $\text{m}^2 \text{frame}^{-1}$), meaning approximations of these dimensions will have to be made, causing a loss of accuracy.

Clearly, for accurate measurements of an object of interest, a clear image is required: however, for example, if a low shutter speed (s^{-1}) is used, the parts of the object of interest that move will be recorded by multiple pixels, generating a blurry image.

Each pixel in an image should represent a small area in the plane of interest, this is achieved with a high pixel density (pixels per m^2), the smaller the pixel area the greater the precision. If a pixel represents a large area, edges of the object of interest, e.g. a flame, may not be recorded, as the pixel it is recorded in, by the CCD, will take an average of everything in that pixel, including the background.

An experimental setup (C9) was assembled as shown in Figure 2.23, with imaging for lithium-ion module failures caused by mechanical abuse by nail penetration, based on

previous experiments (experiment groups A and B). The setup included GoPro Hero 9 Black digital cameras with SanDisk Ultra 256GB A1 micro SD memory cards. The cameras have settings for resolution, camera speed and shutter speed. To test the effect of different resolutions and flame capture speeds, the cameras were setup with different settings: three cameras were employed as shown in Figure 2.23, with two different settings, camera 'G' had a resolution of 3840p (pixels) x 2160p with a camera speed of 60FPS (frames s⁻¹), cameras 'A' and 'I' had resolutions of 1920p x 1080p with a camera speed of 240FPS. All three cameras had their shutter speeds set to 'AUTO' as this setting allowed the camera to adjust the shutter speed to allow for changing light conditions, caused by the cloud coverage on the day.

Figure 5.10(a) –(e) show images taken from camera 'G' during experiment C9, where a single Envision-AESC module, secured to the battery rig, was penetrated by a steel nail. Figure 5.10(g) – (i) show images taken from camera 'A'. In Figure 5.10(a) and (b) were taken the moment before and after ignition, respectively, the images were taken by camera 'G', 1/60 seconds = 0.0167 seconds apart. Comparing them, the moving parts of the images are the vapour cloud and ignition [18]. The vapour cloud is moving too slowly for there to be an appreciable difference in the images, and the ignition shows only a small flame. Figure 5.10(c) is the magnified ignition from (b), it is 64p x 36p and the high resolution used clearly shows the flame edges. However, even though the flame that appears in Figure 5.10(b) is small it cannot be presumed to show that the camera speed is high enough to produce images close enough together in time not to cause a large jump in measurements, as the flame could have been produced from any time after (a) was taken until just before (b) was taken.

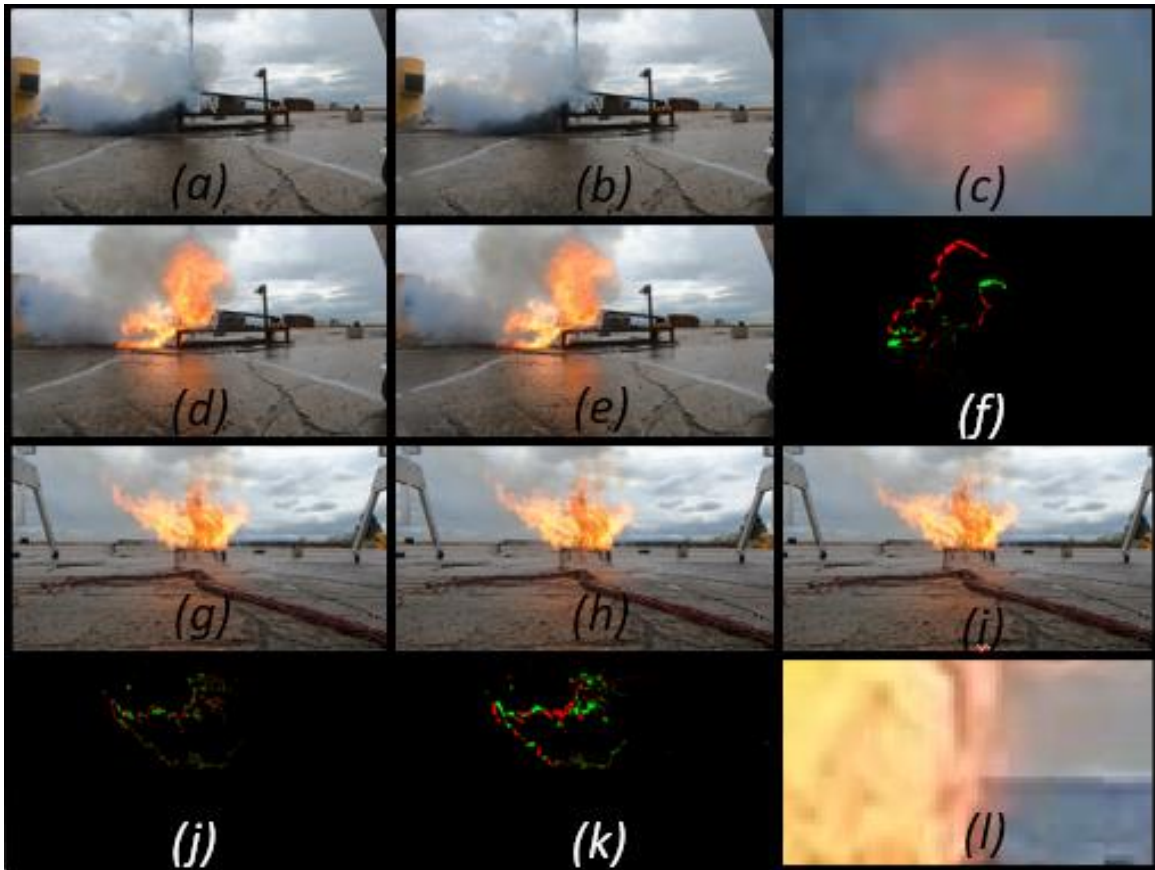


Figure 5.10. Camera G: (a) pre ignition; (b) ignition; (c) zoomed in (b); (d) & (e) thermal runaway; (f) differences in (c) & (d); Camera A: (g), (h) & (i) thermal runaway; (j) differences in (g) & (h); (k) differences in (g) & (i); and (l) zoomed in (g).

To check the camera speed image, Figure 5.10(d) and (e) were also recorded 0.0167 seconds apart but show images with different flame edges. Figure 5.10(f) shows the difference between these images, the black colour represents no change in that pixel, the red colour represents a new flame in that pixel, i.e. there is no flame in (d) but there is in (e), the green colour represents a flame disappearing in that pixel, i.e. there is a flame in (d) but not in (e). Therefore, (f) shows that the flame has mainly grown at the top edge and shrunk in the bottom left corner, but the amount is small compared to the body of the flame, showing that the camera speed is at a high enough rate for this experiment. Figure 5.10(g) and (h) are 2 frames taken by camera 'A' at a moment in time where there is a large flame present in the frame and were taken 0.004167 seconds apart. Comparing them is more difficult than Figure 5.10(a) and (b) as less movement of the flame edges happens in the shorter time period, but from (j), the red pixels, showing the new flame, and the green pixels, showing disappearing flames, makes the comparison easier. The main difference is the top edge to the left hand side, with red and green mixed, it shows the fluttering nature of the flame. Now

looking at Figure 5.10(k), which is the difference between images from (g) and (j) and were taken 0.0167 seconds apart, the same time interval as in (f), the difference in camera speed becomes apparent, however, this is still a small change when compared to the body of the flame, so even though a higher camera speed is desirable, it is not essential in this experiment to obtain the required degree of accuracy. Comparing Figure 5.10(c) and (l), both contain an equal number of pixels, therefore the magnification is different, with (c) having a magnification of c.a. 60 times and (l) having a magnification of ca. 30 times, which is one of the reasons it looks clearer, with different parts of the flame visible, and the horizon can be distinguished in the right hand side, overall a higher resolution is desirable but the lower resolution still provides good precision.

5.3.2 Removing the fish-eye effect from recorded images

It can be seen from Figure 5.5 that the yellow turret on the right hand side appears to be curved, and also, although not immediately obvious, the right hand side of the rig appears to be further from the camera than the left; however, from Figure 2.23 it can be seen that the rig was set perpendicular to the camera. These are examples of the fisheye effect on images, which occurs when the camera lens distorts the image, usually to obtain a wide field of view. To remove this effect, a calibration box was used to provide exact reference points, as shown in Figure 5.11. This is a method previously used in other works [19, 20].

The calibration box was 2200 mm x 600 mm x 600 mm and comprised 200 mm x 200 mm black and white squares. The box was made of an internal steel frame made from 25 mm box section steel, covered in plastic chequered panelling on each of the 6 faces, the four large faces were black and white, and the two smaller (end) faces were green and red plastic chequered panelling. The use of the box allowed the distortion of the image to be seen more easily. Thus, from Figure 5.11(a), given the fact that the box is perpendicular to the camera, and all the squares are the same size, the distortion of the lens becomes apparent: the box appears to be shorter and further away from the camera on the left hand side compared to the right.

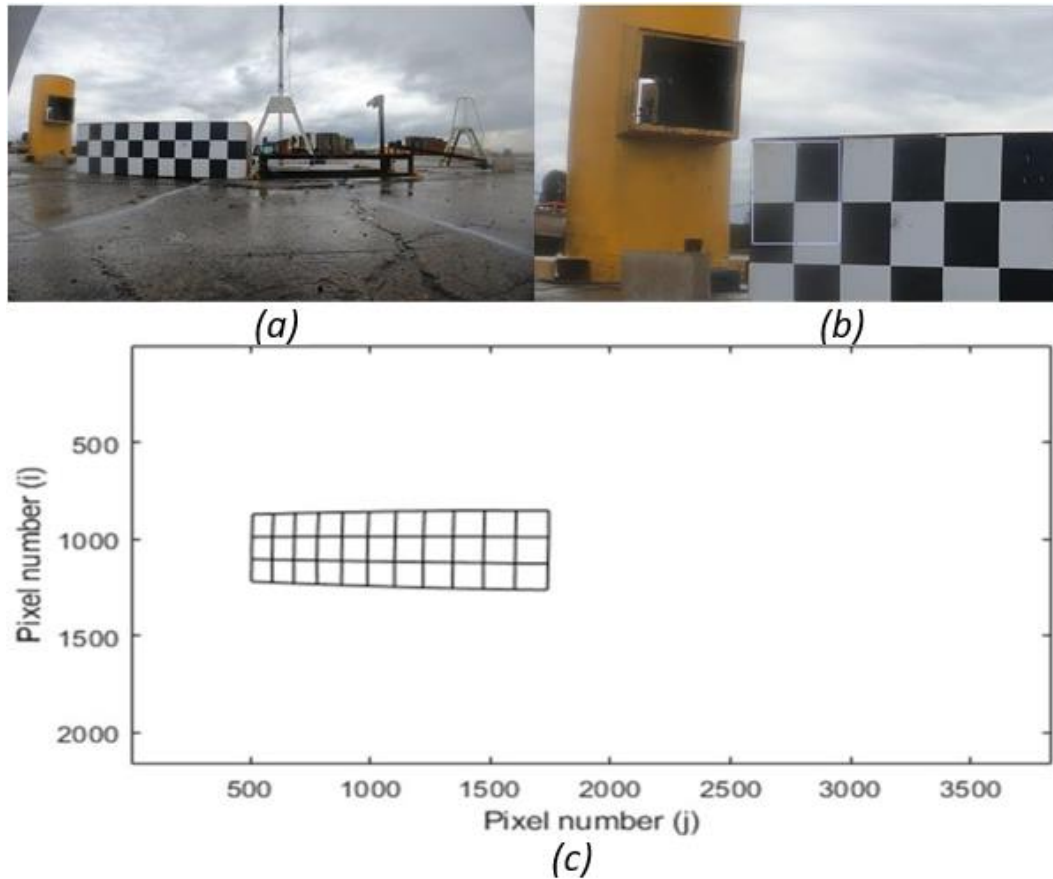


Figure 5.11. (a) The calibration image showing the full calibration box; (b) zoomed in version showing that the box has stretched in image and (c) calibration grid to account for image distortion.

Figure 5.11(b) is the same image as (a) but zoomed in around the top left corner of the calibration box, with a square outline superimposed on the image. The curvature of the turret becomes more apparent, the squares on the calibration box appear to be rectangles, i.e. they are longer than they are wide, and the right edge of the superimposed square outline shows how the calibration squares appear to be curved. The superimposed square is used to find the co-ordinates of the chequers of the calibration box, in this case the top left corner of the calibration box, as that is the point where the top left corner of the superimposed square is over. The top left corner has coordinates of (870, 508). Once all the coordinates have been found they can be plotted, as shown in Figure 5.11(c).

Figure 5.11(c) is a scale plot of where the calibration box sits in (a), it is a useful redundancy, built in as a check that the data has been entered correctly, i.e. there are no erroneous points in the plot. The points have been joined horizontally and vertically to make it easier for the user to see if there is a pattern in any distortions of the image. In Figure 5.11(c), the left hand side of the plot looks shorter than the right,

as does the calibration box in (a) and the squares do not look of equal width along a horizontal line, i.e. they are narrower on the left hand side than the right.

The next step is to stretch the image in one direction, any direction can be first, as long as it is stretched in a direction perpendicular to this afterwards. In this case, the image is stretched vertically first, then horizontally. With the squares being shorter on the left, the vertical stretch for each pixel is greater on the left side than the right, to make the squares of equal height.

For ease of processing, polynomial equations were used with MATLAB. MATLAB has an inbuilt function that uses the least squares method for finding trend lines, for example, a horizontal line fits the equation $y = c$, where c is a constant. A straight line with a gradient fits the equation $y = ax + c$, where a and c are constants, with the coefficient of x being a , which is the gradient of the line. A curved line has a term with a power of at least 2, for example, $y = ax^2 + bx + c$, where a , b and c are constants. MATLAB can generate equations up to and including a power of 9, for example, $y = ax^9 + bx^8 + cx^7 + dx^6 + ex^5 + fx^4 + gx^3 + hx^2 + ix + j$, where a , b , c , d , e , f , g , h , i , and j are all constants (but this requires a minimum of 10 points), the vertical trend line in this example are limited to a power of 3, as there are only 4 vertical points. The number of points could be quadrupled by adding imaginary lines of symmetry (mirrors), horizontally and vertically, running through the centre of the image, or doubled by using one 'mirror', this assumes that the image is equally distorted by the lens around the centre of the image.

Once horizontal trend lines have been found, they can be overlaid on the horizontal lines in Figure 5.11(c), to check that they are a good fit, and to obtain an insight as to how the image is distorted on the right-hand side. The plots for each power considered is found in the Appendix 5.1, for the nine options for fitting trend lines to the points of the calibration box. In these results, it was found that it is not necessarily the case that a higher power fit increases accuracy. Figure 5.12 shows the results for horizontal powers of 1 to 9 (when a vertical power of 1 is used, this pattern was similar for all vertical powers and is explained in more detail in Appendix 5.3). In Figure 5.12 the ideal result is 1, and as can be seen this occurs when the horizontal power is 2, this was then used for the remaining calculations.

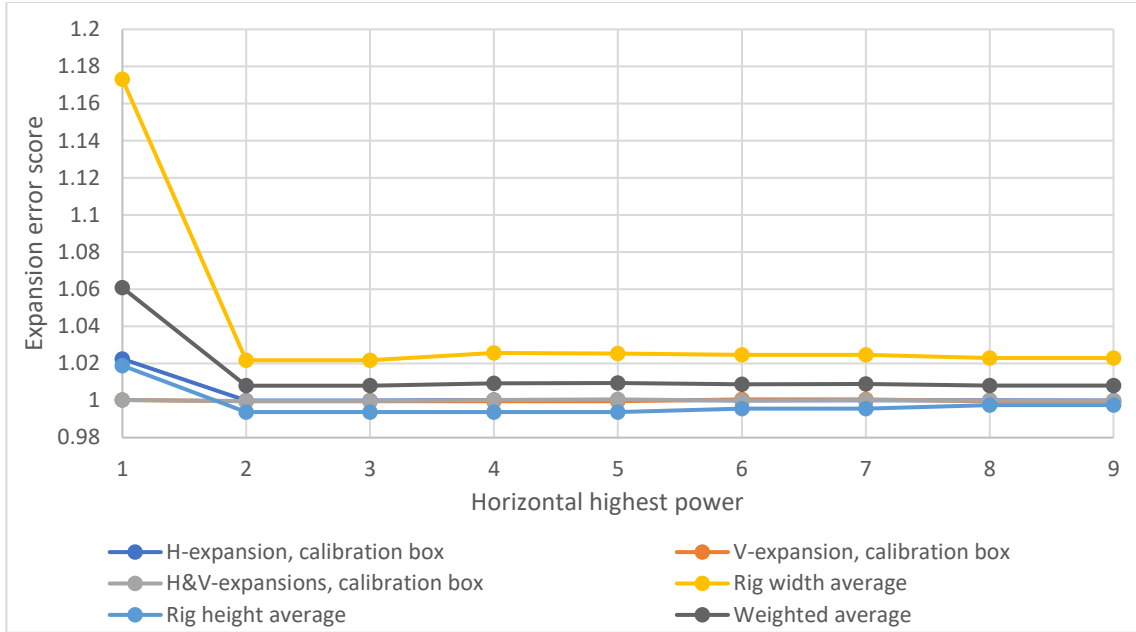


Figure 5.12. The errors for horizontal powers from 1 to 9 and a vertical power of 1.

The next step is to find how much each pixel needs to be stretched so that each pixel represents the same height. It was decided that each pixel should represent an area of 1 mm x 1 mm on the plane where the calibration box lies, as this size is acceptable for both precision and accuracy, as 1 mm² is much smaller than the flame area. To achieve this a factor was calculated between each horizontal trend line on every column of pixels. As the calibration squares on the calibration box were 200 mm in height, 200 can be divided by the number of pixels in a column between the trend lines to give a vertical expansion factor in the middle of the trend lines. For example, if at column 50, two trend lines are at row 600 and row 750, then a vertical expansion factor of:

$$\frac{200}{750 - 600} = \frac{4}{3} \quad (4)$$

would be needed at row:

$$600 + \frac{750-600}{2} = 675 \quad (5)$$

This was done for various powers and full detail of all possibilities analysed below, with the outcome being that a vertical expansion above a power of 2 does not give realistic results. This analysis was expanded to all directions, for all cameras, with the option of using imaginary mirrors, and the fisheye effect was removed from all imaging, full details are shown below.

Once the vertical expansion factors were found between the trendlines, these were used to calculate the vertical expansion factors for every other pixel in the image. The previously

calculated expansion factors were assigned to the pixel between the trendlines they were calculated from, then vertical trendlines were calculated for each column, but only with the option of using a highest power of 2, as there are only 3 points in each column. The vertical expansion factors for the whole image are shown in Figure 5.13. The results of each vertical expansion are shown in Figure 5.14. The same method was then applied for a horizontal expansion and the results combined to eliminate the lens distortion ‘fish-eye effect’.

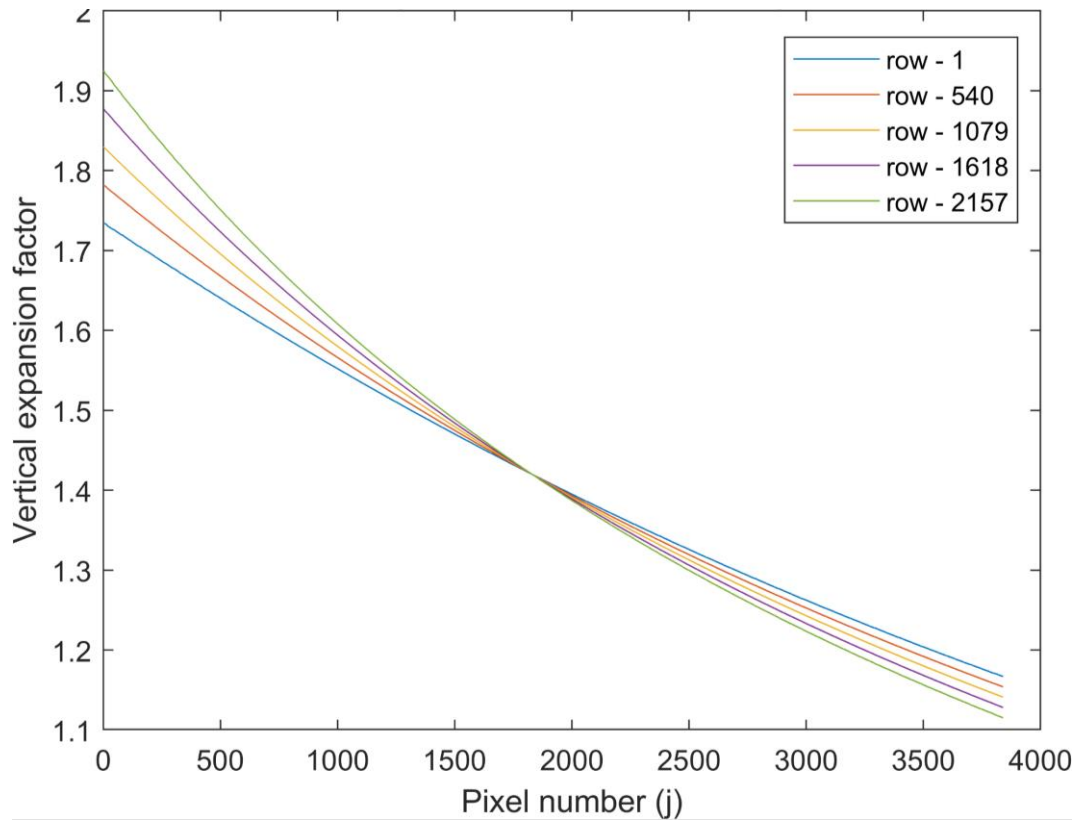


Figure 5.13. Vertical expansion factors for the whole image when using a highest power of 1 for the trendlines as described in Appendix 5.1, and a highest vertical power of 1 for the trendlines as described above.

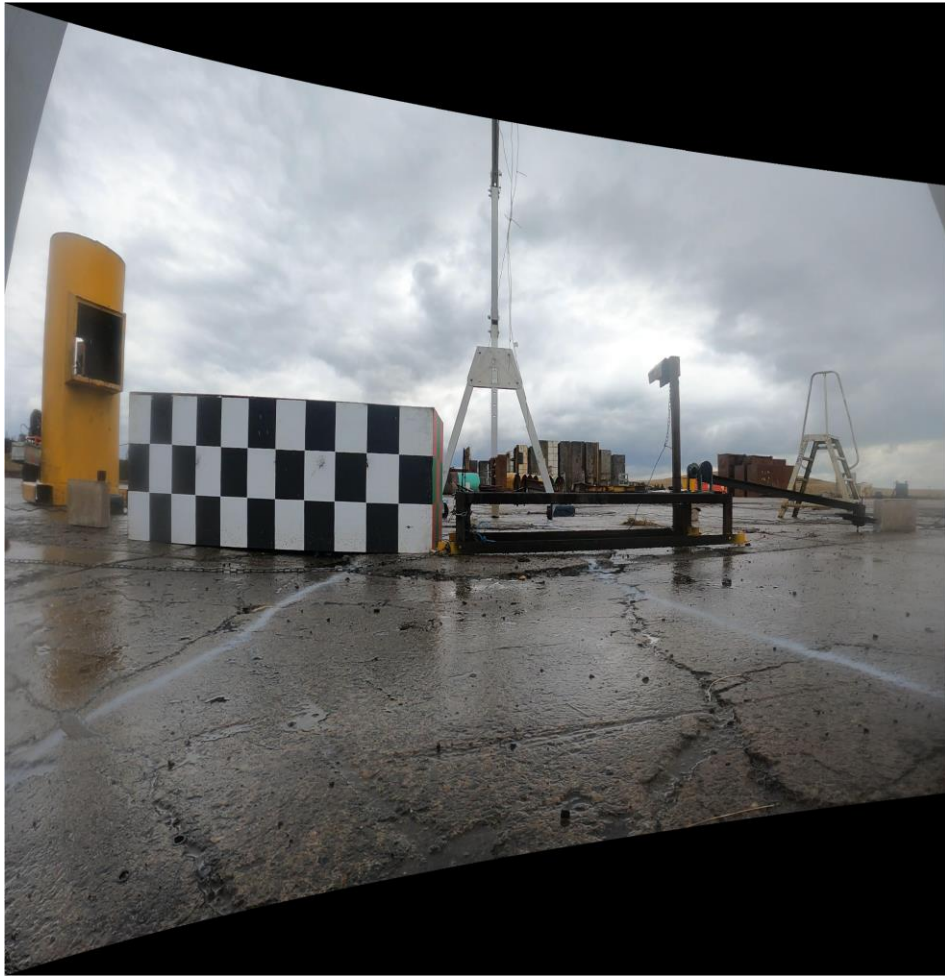


Figure 5.14. Result of the expansion method used in Figure 5.28.

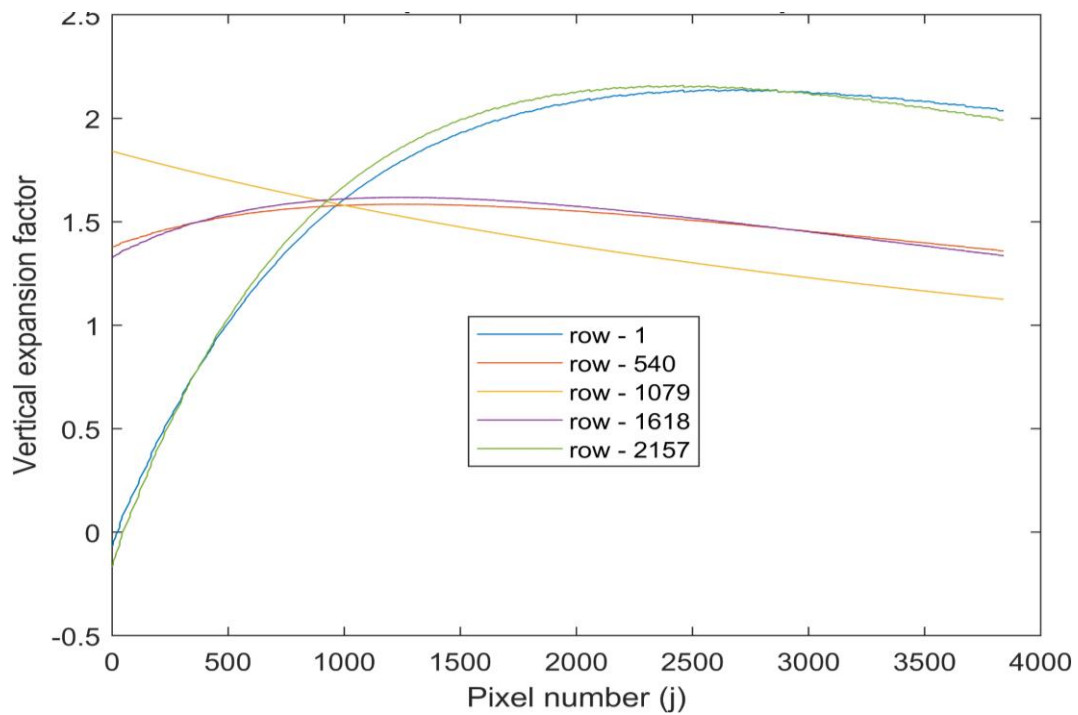


Figure 5.15. Vertical expansion factors for the whole image when using a highest power of 1 for the trendlines as described in Appendix 5.1, and a highest vertical power of 2 for the trendlines as described above.



Figure 5.16. Result of the expansion method used in Figure 5.30.

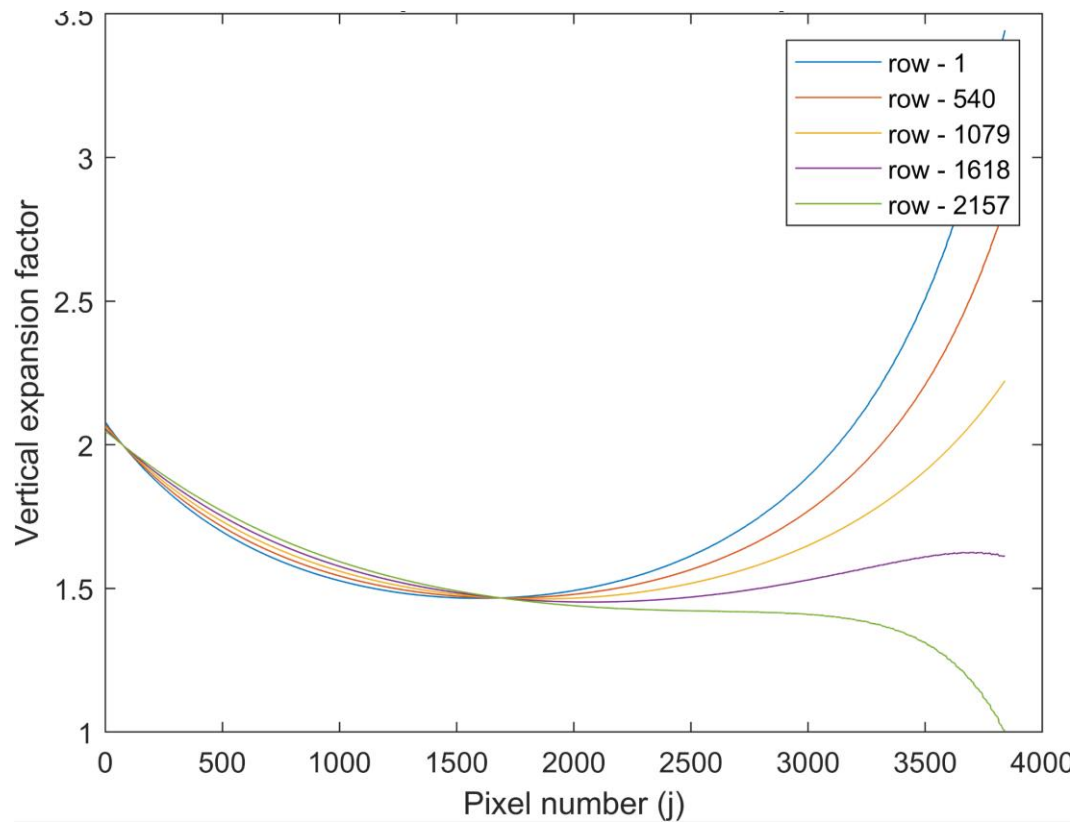


Figure 5.17. Vertical expansion factors for the whole image when using a highest power of 2 for the trendlines as described in Appendix 5.1, and a highest vertical power of 1 for the trendlines as described above.

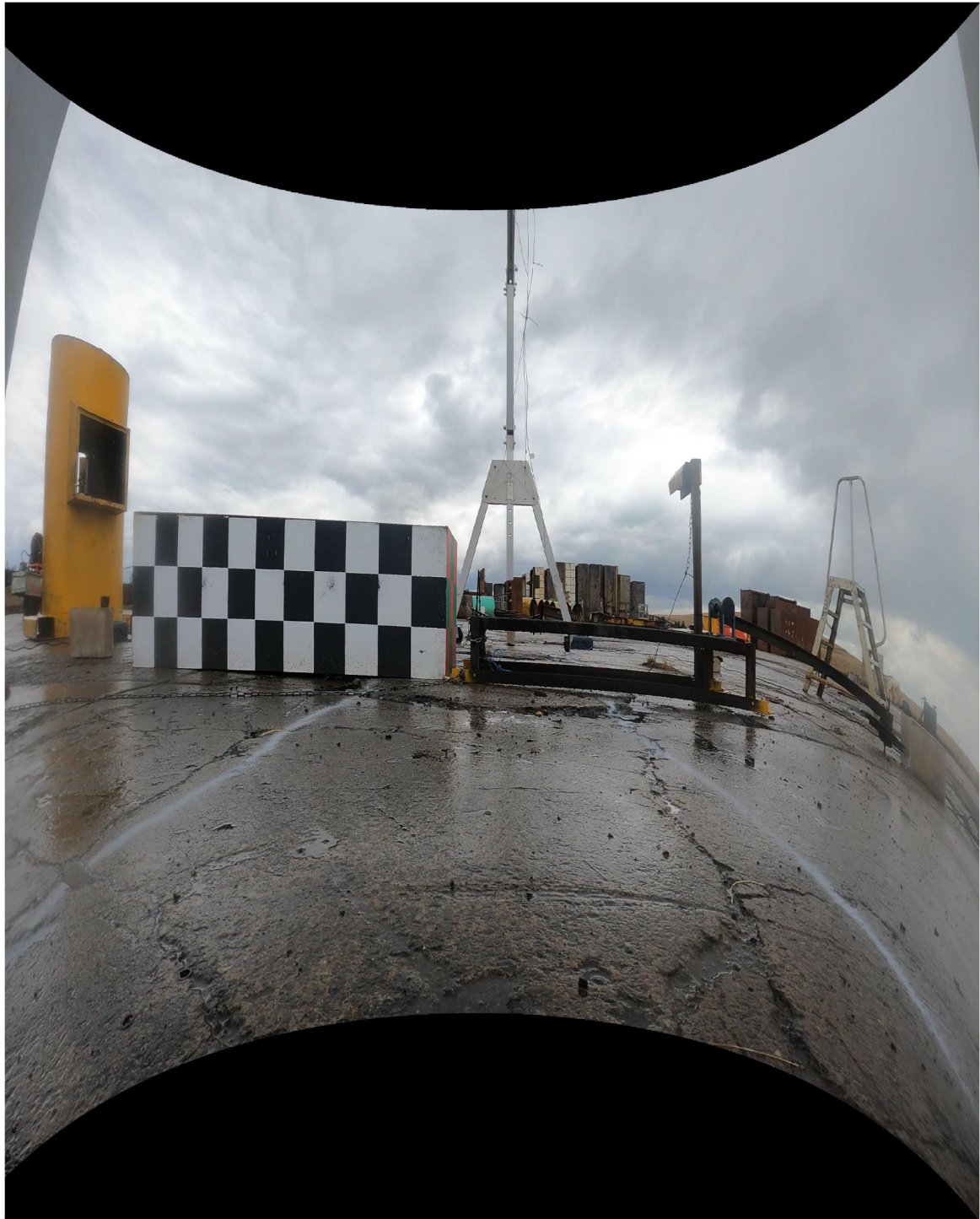


Figure 5.18. Result of the expansion method used in Figure 5.32.

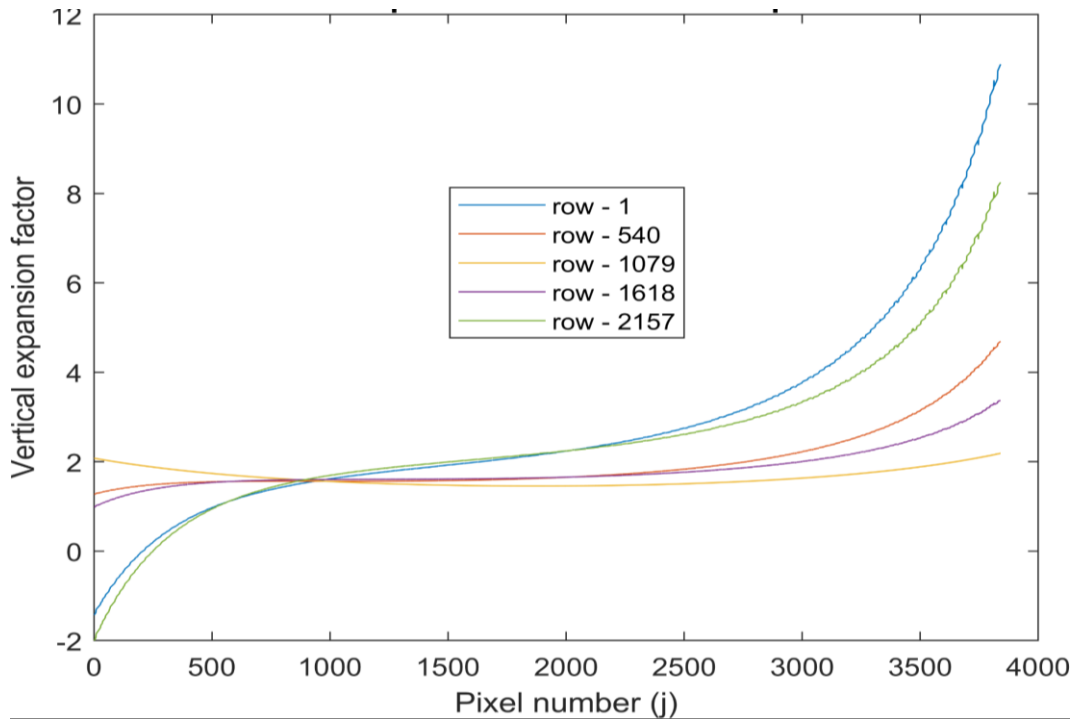


Figure 5.19. Vertical expansion factors for the whole image when using a highest power of 2 for the trendlines as described in Appendix 5.1, and a highest vertical power of 2 for the trendlines as described above.



Figure 5.20. Result of the expansion method used in Figure 5.34.

Another option was found, to introduce imaginary mirrors, this presumes that the distortion is symmetrical around the centre of the lens. **Error! Reference source not found.** show the effect of using an imaginary vertical mirror in the vertical expansion.

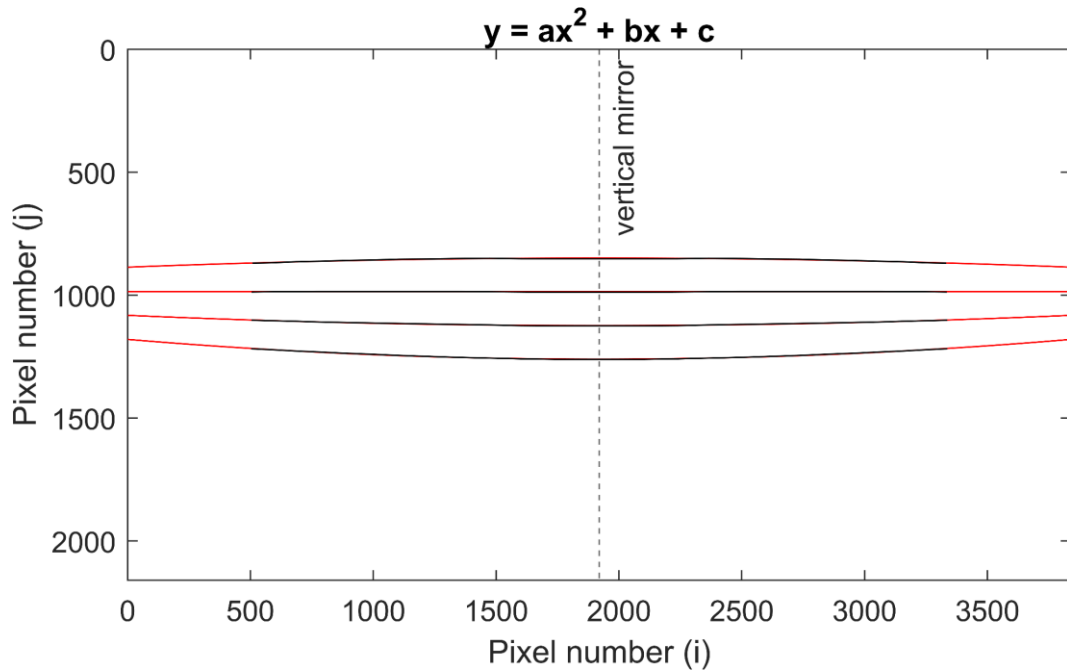


Figure 5.21. The same trendlines as in Figure 5.17, but with an imaginary mirror to reflect the points to the other side of the image.

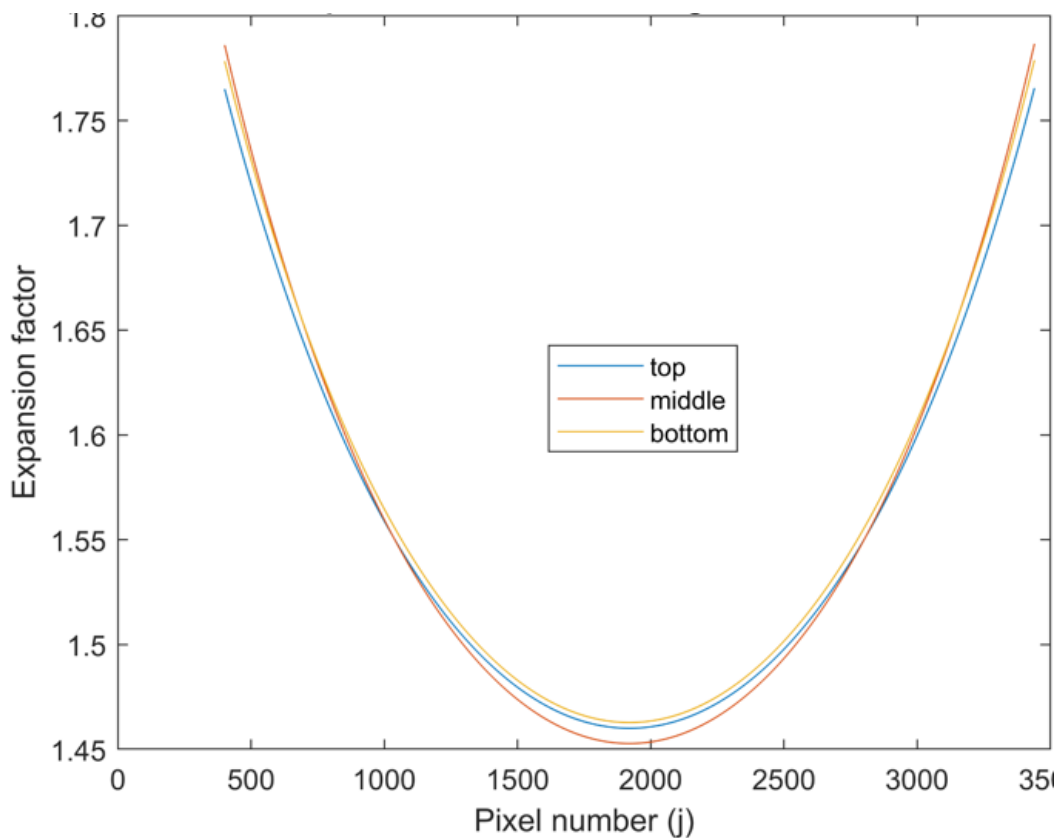


Figure 5.22. The resulting expansion factors form Figure 5.36.

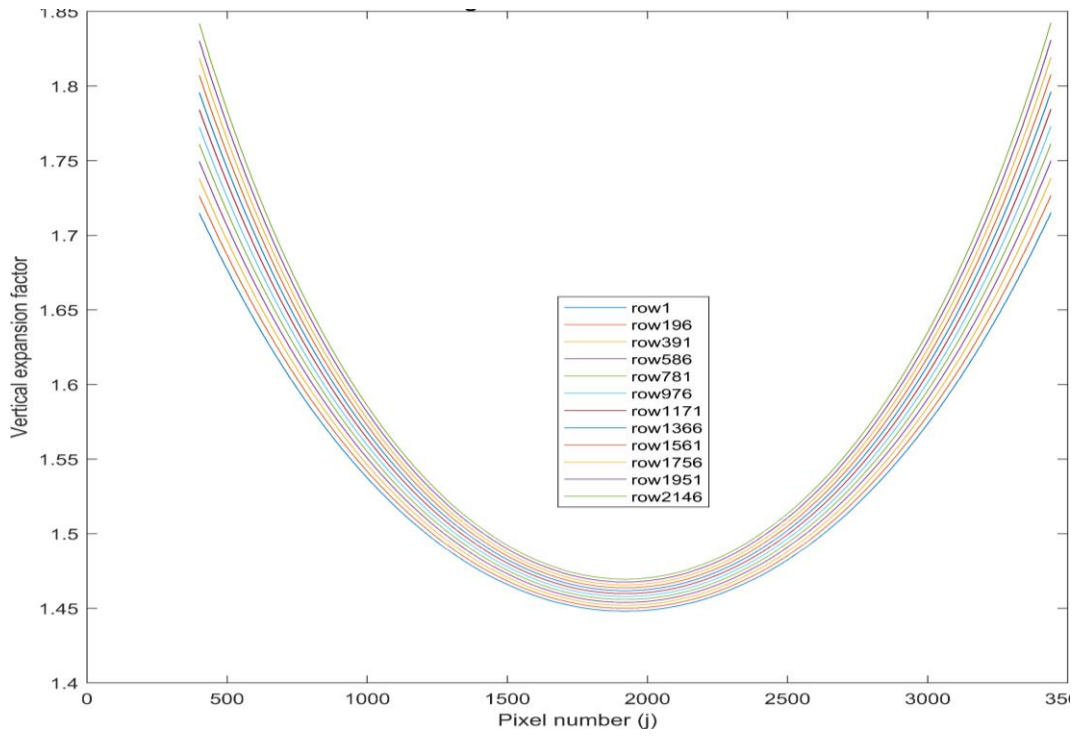


Figure 5.23. The resulting expansion factors from Figure 5.37, for the whole image.



Figure 5.24. The result of the expansion with an imaginary vertical mirror, for comparison see Figure 5.33

It was found that higher powers could be used in the initial trendline calculations, as the convergence problem was reduced by the use of an imaginary mirror, **Error! Reference source not found.** show how this technique allowed an initial trendline to be calculated with a highest power of 6.

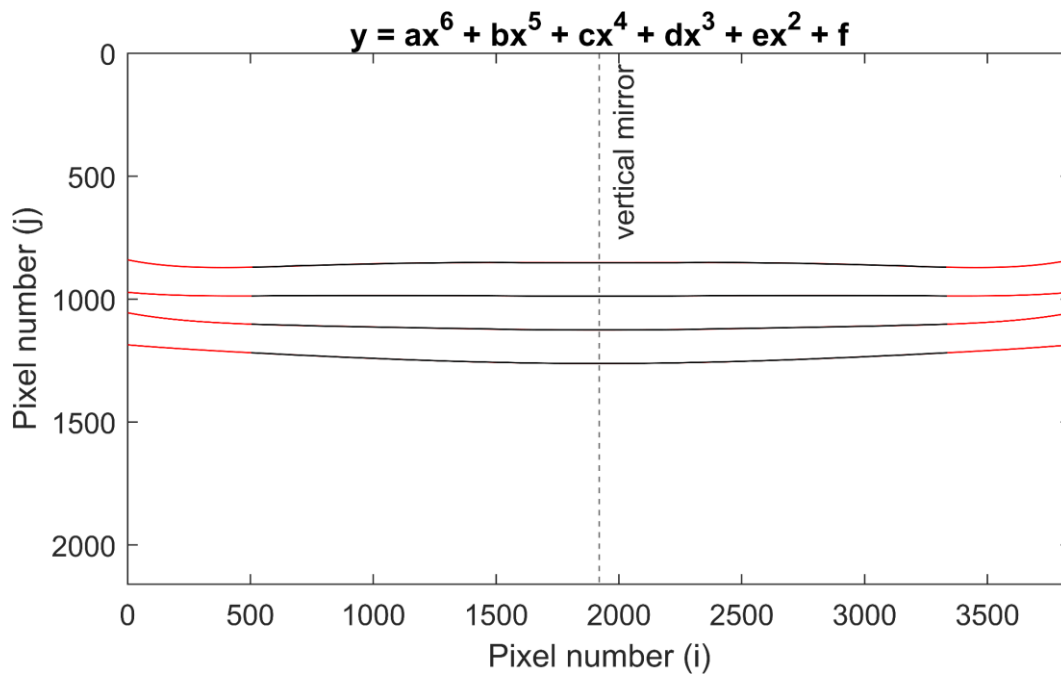


Figure 5.25. The same trendlines as in Figure 5.21, but with an imaginary mirror to reflect the points to the other side of the image., note how the trendlines no longer converge.

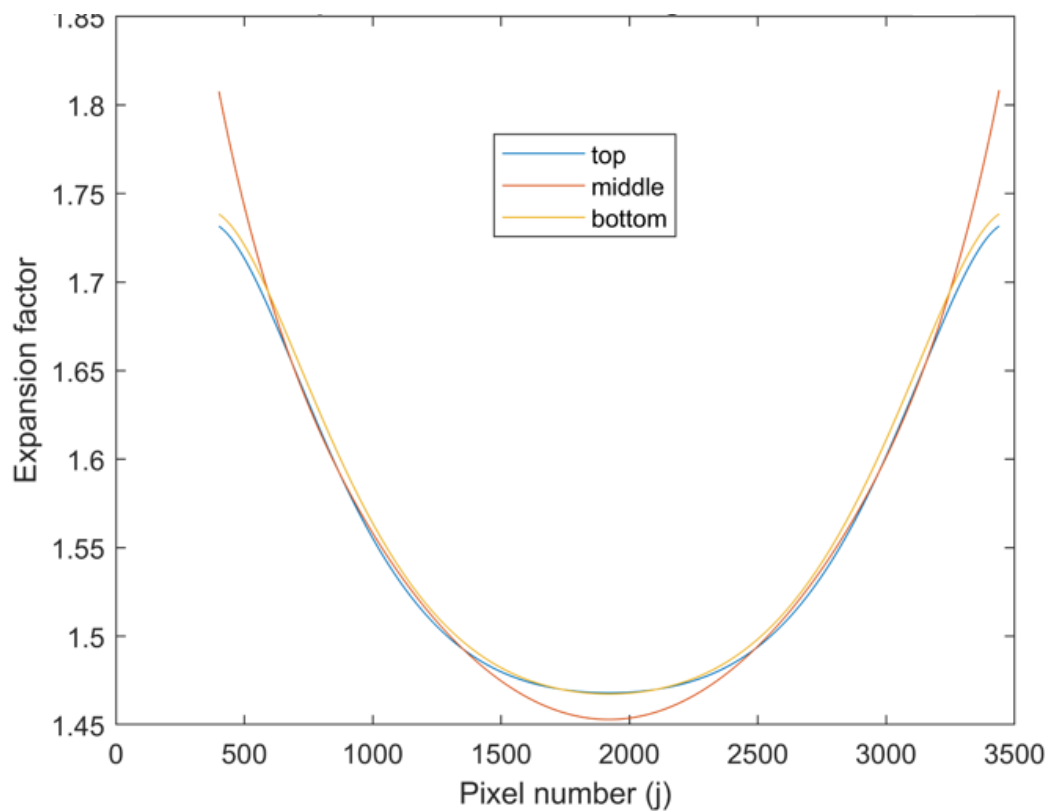


Figure 5.26. The resulting expansion factors from Figure 5.40.

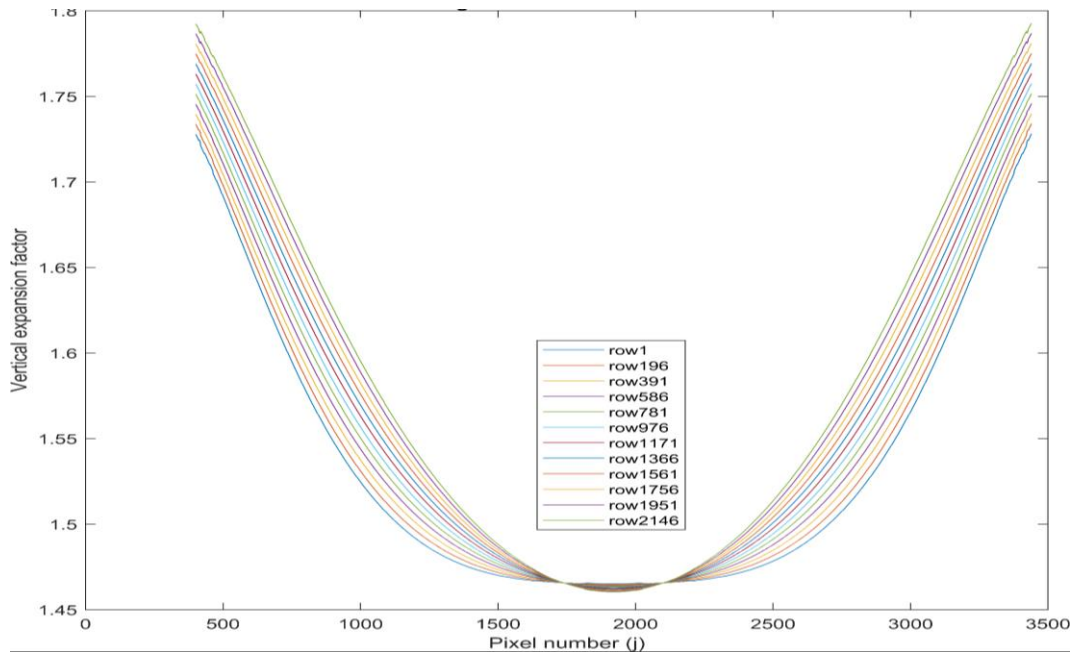


Figure 5.27. The resulting expansion factors from Figure 5.41, for the whole image.

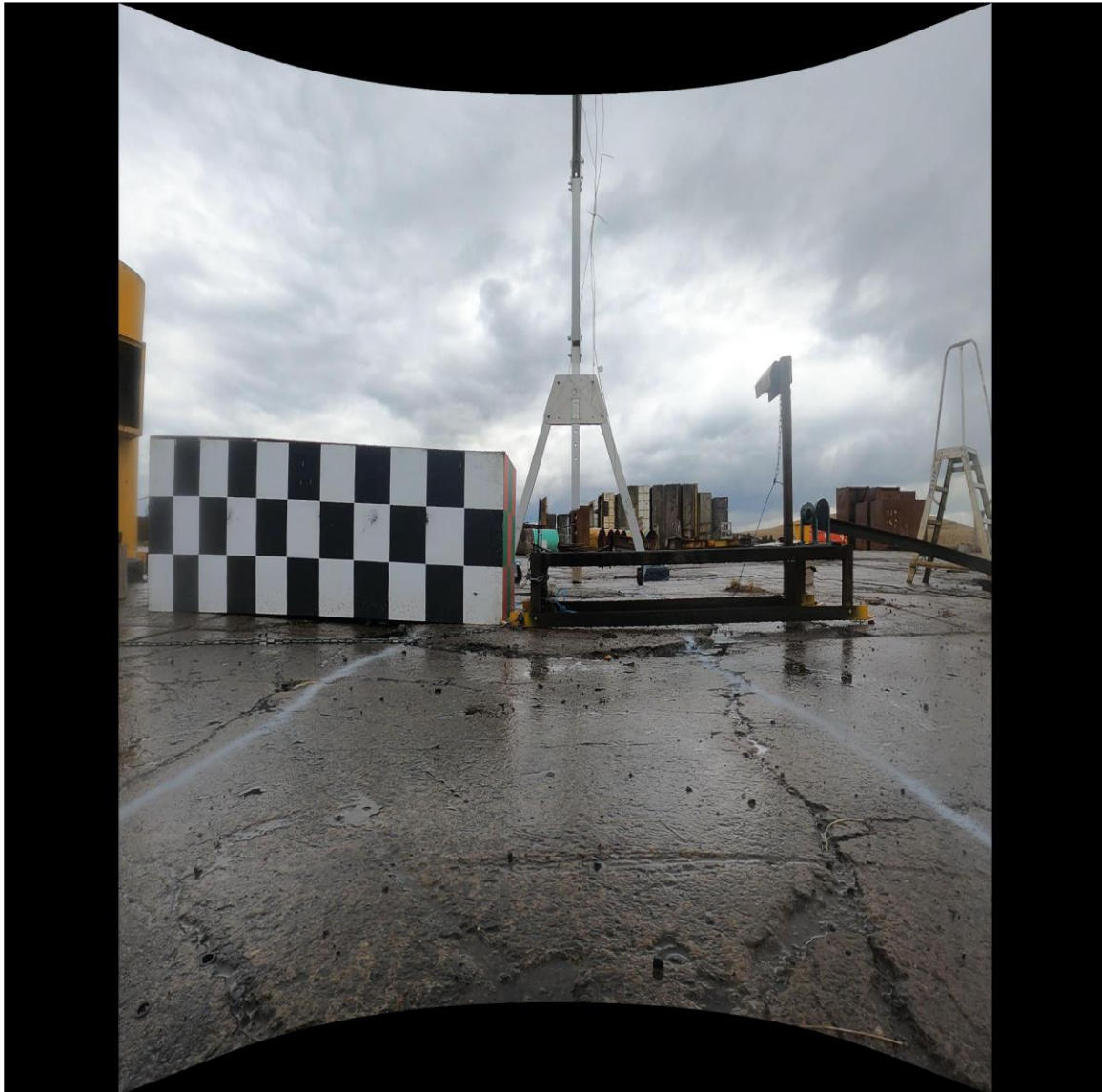


Figure 5.28. The result of the expansion in Figures 5.40 to 42, with an imaginary vertical mirror.

5.3.3. Surface area of a rapidly changing, irregularly shaped flame

To calculate precision measurements compared to referencing, a score was assigned to each image compared to what the actual size was in the reference images. A score of '1' meant that the measurements were perfect, above '1' means that the measurement was too large and below '1' it was too small. For example, a score of 1.1 means that if the actual measurement was 1000 mm the measurement after the analysis was 1100 mm. This was done for all physical reference points, namely: (i) on the calibration box after the horizontal expansion when only using one mirror; (ii) on the calibration box after the vertical expansion when only using one mirror, (iii) on the calibration box after the horizontal and vertical expansions when using both

mirrors; (iv) on the rig widths measuring how accurately the expansions have expanded the width of the rig, at various heights, after both expansions, when using both mirrors, and averages these into a single score; (v) on the rig heights measuring how accurately the expansions have expanded the height of the rig, at various widths, after both expansions, when using both mirrors, and averages these into a single score; (vi) is a weighted average of the xy result and both rig scores, and is the score used to determine the best combination of powers. The results are shown in detail in Appendix 5.5, but the best accuracy is when using a horizontal power of two and a vertical power of three, the weighted average score was 1.007357, meaning there was an average overestimation of 0.736 % in the measurements.

Finally, the aspect of error not yet addressed is the numerical error that can arise from the code. For example, the code may not always correctly recognise pixels which are flames and may falsely mark pixels which are not flames as flames, i.e. generate false positives. This is of particular concern on the perimeter of a flame body, as this is where the flames become thinner and from the viewpoint of the camera, merge with the background, which is made worse by the fluctuating nature of these flames.

Recognising that no measurement is perfect a maximum and minimum range is also measured in the analysis, the maximum adds a set number of pixels around the flame perimeter, the minimum only records a flame if that pixel is surrounded by flames of the set number of pixels. The set number of pixels can be changed by the user, in this analysis it was set at '2', which represents 2 mm in length or 4 mm² in area. Figure 5.29(b) – (d) show the measured, minimum, and maximum flames from (a). The differences in the perimeter measurements are that when the maximum perimeter is used (c), more interference becomes recorded, for example the reflection of the flames from the wet concrete floor, also the body of the flame has small areas where no flame was recorded, whereas the minimum (d) is the opposite. These are shown in Figure 5.29(e) and (f), where the red in (e) shows new pixels that have recorded a flame in (c) compared to the original (b), and the green in (f) shows pixels that have not recorded a flame in (d) compared to the original (b).

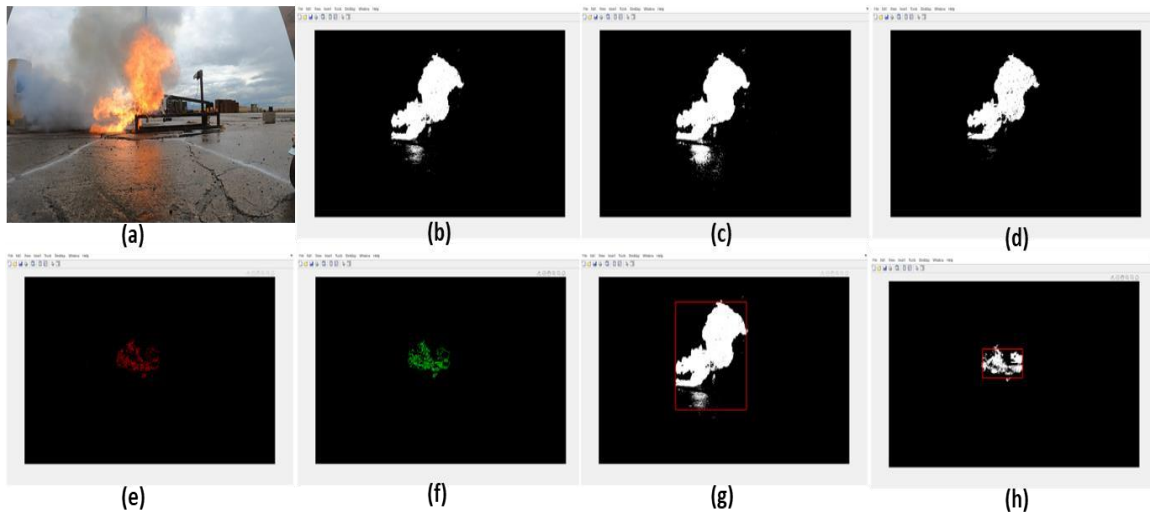


Figure 5.29. (a) image of flame; (b) flame image in black and white; (c) maximum flame body; (d) minimum flame body; (e) differences in (b) and (c); (f) differences in (b) and (d); (g) and (h) changing red box based on flame body.

Another source of error is interference in the background, e.g. when a rough surface is wet with a thin film of water, the film can reflect sunlight to the camera, direct sunlight has R, G and B parameters similar to those used to identify flames, therefore, Matlab marks these pixels as flames. To reduce this effect an assumption can be made that the flame edge is connected to a flame body and only summing pixels that are within a body that is above minimum dimensions. This is complicated by the irregular shape of a flame, so a box cannot be drawn around an area at the beginning of the analysis, but a box that constantly changes shape and size with the changing flame is required. To achieve this a minimum pixel number which contained flames was required for the horizontal and vertical axis: only if these were above the minimum would a pixel be counted as a flame.

(g) and (h) show a box (in red) drawn around the area, which was being measured, it changed size and location depending on the body of the flame. The very tips of the flames can be omitted from the analysis, but this can be counteracted by using the maximum value from the perimeter errors.

5.4. Measuring the flames and resulting Heat Release Rate

The flames were isolated from the images as described in Section 5.3, each pixel was then multiplied by the horizontal and vertical expansion matrices to get the area of each pixel. These were then summed to get a total area for each image. However, as the flame edges move towards the cameras the distance between the camera and the

calibration plane reduces, meaning the flame areas are underestimated. To counteract this, the calibration was changed depending on the distance to the flame edge. For example, see Figure 2.23, camera 'G' can be used to measure how far the flame has moved towards cameras 'A' and 'I': likewise camera 'A' can be used to measure how far the flame has moved towards cameras 'G' and 'I', and camera 'I' can be used to measure how far the flame has moved towards cameras 'G' and 'A'. As shown in Figure 5.2, this involves multiplying all the pixels by a new constant which changes at each interval in time.

Once the areas have been calculated the heat release rate (HRR) and heat released (HR) can be calculated, by multiplying the area by the known HRR per unit area. The conversion factor [1] was that employed for methane:

$$\text{HRR [kW]} = 0.009489 \times \text{flame area (cm}^2\text{)} + 0.014722 \quad (5)$$

which is a hydrocarbon as is the bulk of the electrolyte that is ignited in the experiment [18]. The HRR for most of the hydrocarbon fuels found in the ejecta of the battery are all in a similar range, so for the purposes of this analysis the same conversion factor was used for all hydrocarbons emitted.

30 shows the heat release rates calculated without applying the correction factors presented in Section 5.3. The minimum, normalised, and maximum are shown in the figure, where the minimum and maximum areas are produced using the same method as that in Figure 5.29(e) and (f), and the normalised is the actual value used. No adjustment has been made for the flame being closer or further away from the cameras in Figure 5.30, the analysis assumes the whole flame is in the same plane as the calibration box.

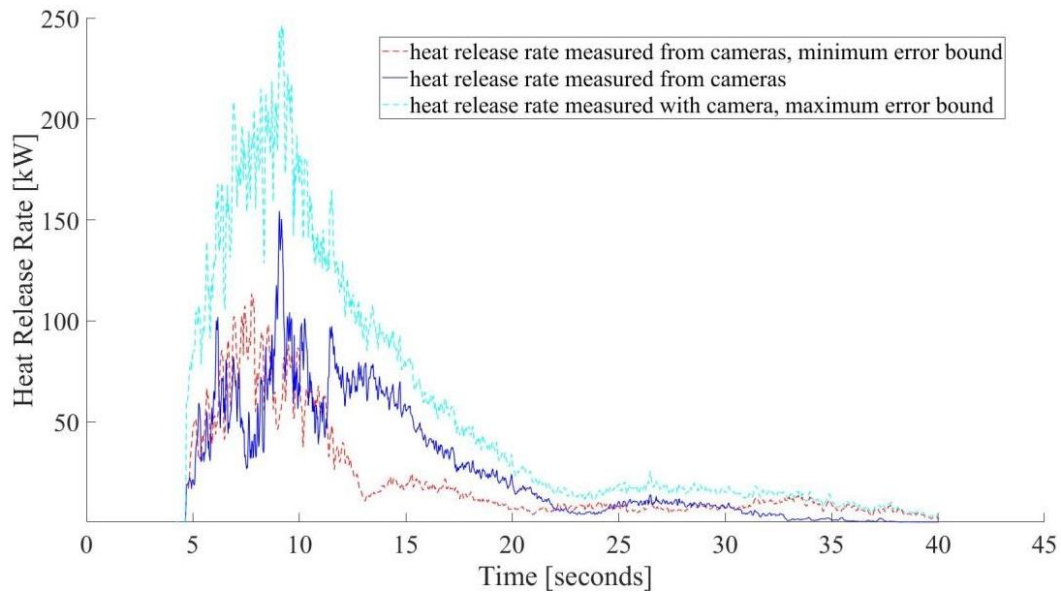


Figure 5.30. Plots of the heat release rate normalised, maximum, and minimum areas that can be calculated from the measured pixels of the flame. No correction factors were used.

When applying the correction factors presented in Section 5.3 to account for flame distances, the heat release rate found was significantly higher than as in Figure 5.30, as can be seen in Figure 5.31. This shows the importance of accounting for the position of each flame flare, pixel by pixel, which cannot be done with invasive measurement techniques, especially once multiple flares occur.

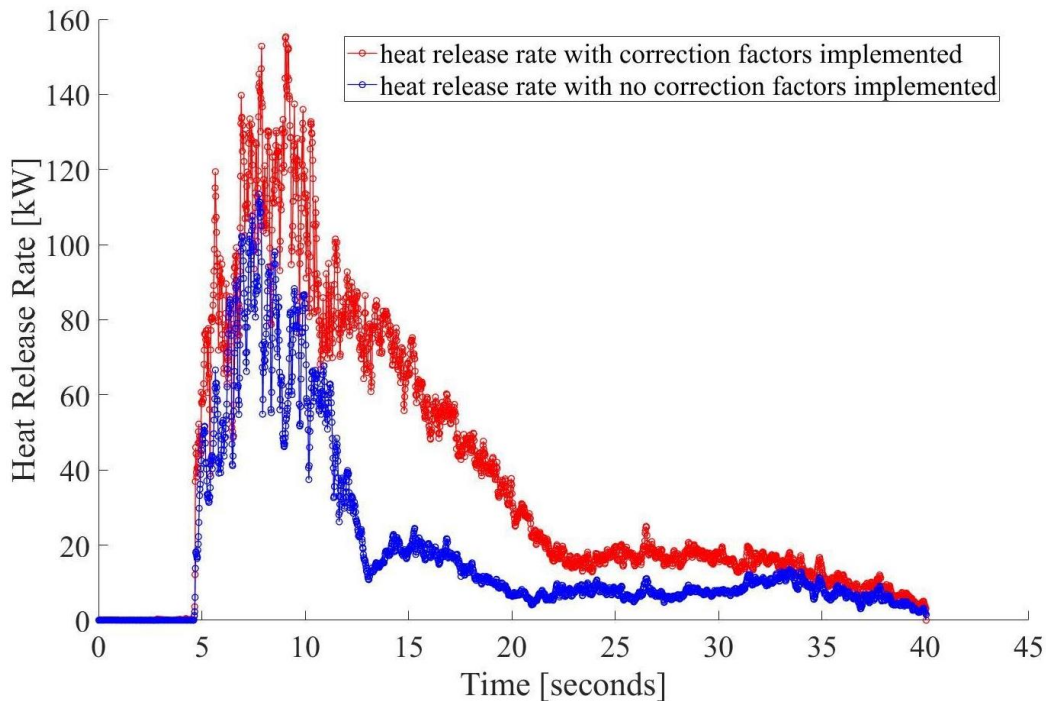


Figure 5.31. Plots of the heat release rate (mean) with and without the correction factor implemented.

The effect of the error without the calibration is compounded when trying to calculate the total heat release rate from a lithium-ion battery fire: as can be seen in Figure 5.32 the total heat release rate, once calibration is taken into account, is almost twice what which would have been calculated without the calibration. This shows that, because flames are thin regions in space, the error in pixel measurements deriving from spatial resolution can create very large errors in the analysis, and shows why the methodology to fully correct the errors in measurement presented in Section 5.3 was essential for the use of digital imaging for the processing of heat release rate calculations for systems like lithium-ion battery pack fires where there can be multiple flame flares and simultaneously changing in different directions.

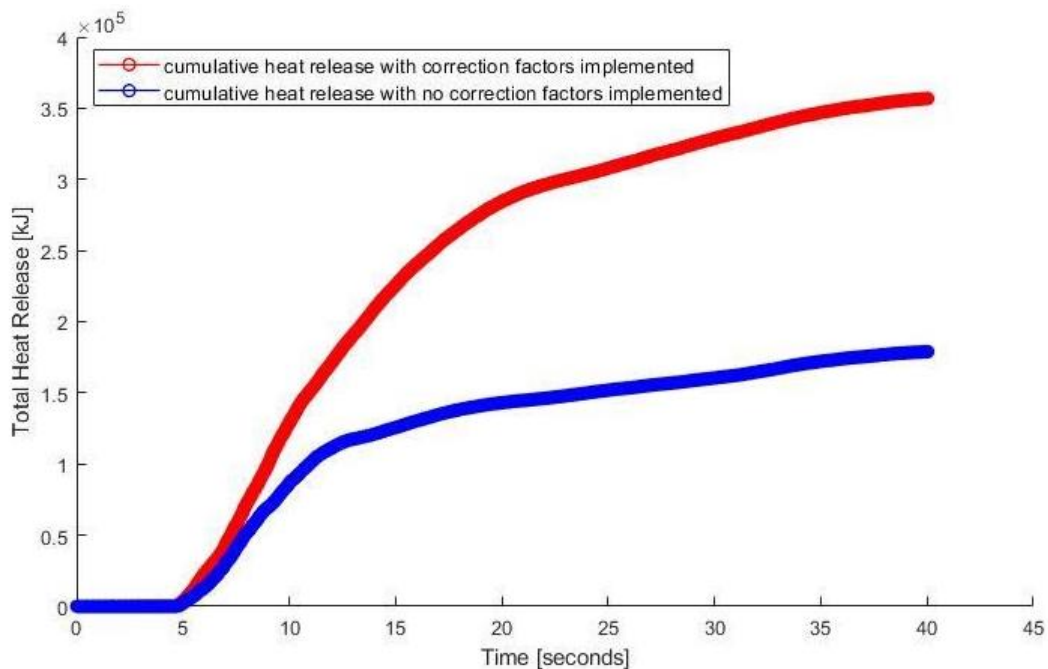


Figure 5.32. Plots of total heat release with and without correcting for flame movement.

Figure 5.32 shows that the total heat release is approximately doubled by taking into account the movements of the flame, and so without the correction method developed in this Chapter, using imaging for heat release estimation would very much under-estimate the total heat released from the battery fire.

The difference is mainly due to the constant calibration of the images as the flame front moves towards/away from the camera, each pixel represents a changing area as the flame front moves, and this method calibrates the images for that.

5.5. Conclusions

This Chapter proposed and tested a new methodology to capture images of flames generated from the ignition of a lithium-ion module, post-process them to remove distortions and errors as well as background image noise, and finally use the images to reconstruct the total flame areas generated from the failure, even when multiple flares occurred simultaneously. Without appropriate calibration and error correction, using raw images of flame flares can give an error almost 50%, significantly underestimating the actual heat release rate and total heat release of the flame flares by more than half. The extensive calibration and testing of this newly-developed image processing method presented in this paper ensures that a crucial non-invasive tool such as visual imaging can be used more widely in the measurements and quantification of the effects of fire from lithium-ion batteries. The tool can be further adapted to be used in scenarios where the fuel is drastically different, by altering the fuel conversion factor as long as the flame generated from the reactions is visible and an appropriate heat release rate relation between flame area and heat produced is known.

5.6. References

1. Linteris, G.T. and I. Rafferty, Flame size, heat release, and smoke points in materials flammability. *Fire Safety Journal*, 2008. 43(6): p. 442-450.
2. Baird, A.R., et al., Explosion hazards from lithium-ion battery vent gas. *Journal of Power Sources*, 2020. 446: p. 227257.
3. Chen, H., et al., An experimental study on thermal runaway characteristics of lithium-ion batteries with high specific energy and prediction of heat release rate. *Journal of Power Sources*, 2020. 472: p. 228585.
4. Hoelle, S., et al., Analysis on thermal runaway behavior of prismatic Lithium-ion batteries with autoclave calorimetry. *Journal of The Electrochemical Society*, 2021. 168(12): p. 120515.
5. Li, W., et al., Fire boundaries of lithium-ion cell eruption gases caused by thermal runaway. *Iscience*, 2021. 24(5): p. 102401.
6. Fernandes, Y., A. Bry, and S. De Persis, Identification and quantification of gases emitted during abuse tests by overcharge of a commercial Li-ion battery. *Journal of power sources*, 2018. 389: p. 106-119.

7. Xin, Y., Estimation of chemical heat release rate in rack storage fires based on flame volume. *Fire safety journal*, 2014. 63: p. 29-36.
8. Li, K., S. Mao, and R. Feng, Estimation of heat release rate and fuel type of circular pool fires using inverse modelling based on image recognition technique. *Fire Technology*, 2019. 55: p. 667-687.
9. Stratton, B.J., Determining flame height and flame pulsation frequency and estimating heat release rate from 3D flame reconstruction. 2005.
10. Koch, S., A. Fill, and K.P. Birke, Comprehensive gas analysis on large scale automotive lithium-ion cells in thermal runaway. *Journal of Power Sources*, 2018. 398: p. 106-112.
11. Carmignani, L., Flame Tracker: An image analysis program to measure flame characteristics. *SoftwareX*, 2021. 15: p. 100791.
12. Henriksen, M., et al., Laminar burning velocity of gases vented from failed Li-ion batteries. *Journal of Power Sources*, 2021. 506: p. 230141.
13. Mao, B., et al., Experimental and modeling analysis of jet flow and fire dynamics of 18650-type lithium-ion battery. *Applied Energy*, 2021. 281: p. 116054.
14. Bonner, M., W. Węgrzyński, and G. Rein, Visual Fire Power: An Algorithm for Measuring Heat Release Rate of Visible Flames in Camera Footage, with Applications in Facade Fire Experiments. *Fire Technology*, 2022: p. 1-25.
15. Lafay, Y., et al., Experimental and numerical investigation of the effect of H₂ enrichment on laminar methane–air flame thickness. *Combustion and Flame*, 2008. 153(4): p. 540-561.
16. Turns, S.R., Introduction to combustion. Vol. 287. 1996: McGraw-Hill Companies New York, NY, USA.
17. Li, F. and A. Nathan, CCD image sensors in deep-ultraviolet: degradation behavior and damage mechanisms. 2005: Springer Science & Business Media.
18. Christensen, P., et al., Thermal and mechanical abuse of electric vehicle pouch cell modules. *Applied Thermal Engineering*, 2021. 189: p. 116623.
19. Rackauskaite, E., et al., Fire experiment inside a very large and open-plan compartment: x-ONE. *Fire Technology*, 2021: p. 1-35.
20. Graham, D., Tomographic reconstruction of a swirling flame. MEng thesis. Imperial College London, 2016.

5.7. Appendix 5.1

Once the points of the squares on the calibration box were found, they were entered into MATLAB and to stretch the image in the vertical direction, horizontal trendlines were calculated using equations $y = ax + b$ up to $y = ax^9 + bx^8 + cx^7 + dx^6 + ex^5 + fx^4 + gx^3 + hx^2 + ix + j$, where $a, b, c, d, e, f, g, h, i,$ and j are constants and x is the horizontal or column pixel number. In Figure 5.33 the black lines are the points of the calibration box joined horizontally and the red lines are the calculated trendlines, by overlaying them the user can quickly check the quality of the trendline to the known points.

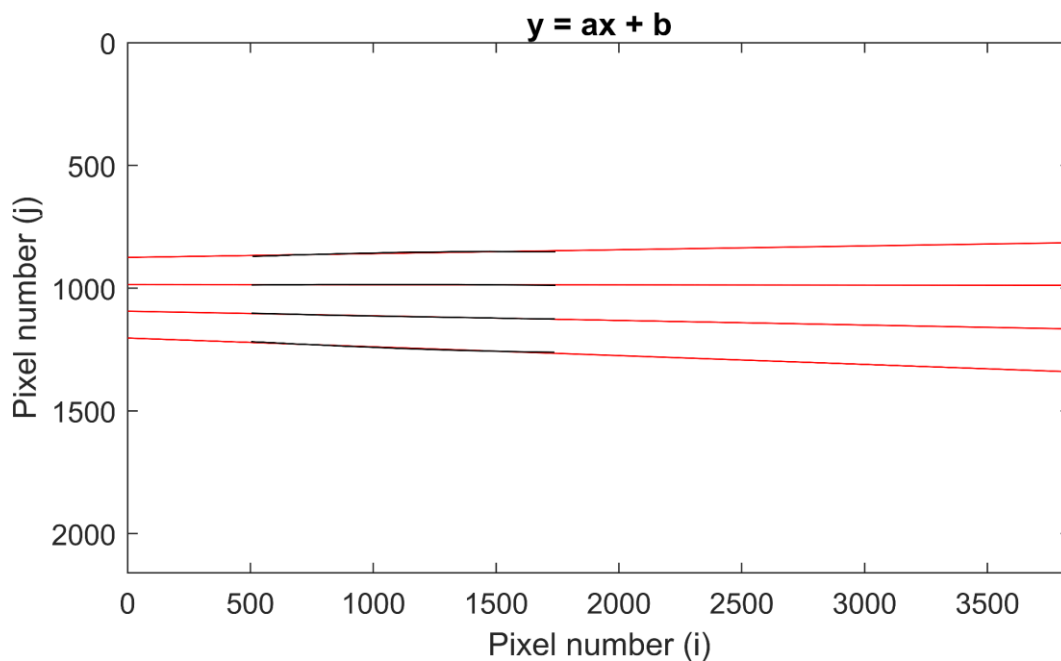


Figure 5.33. The horizontal lines of the calibration box (black lines), with trendlines (red lines) overlaid when the equation shown was used to calculate the trendlines.

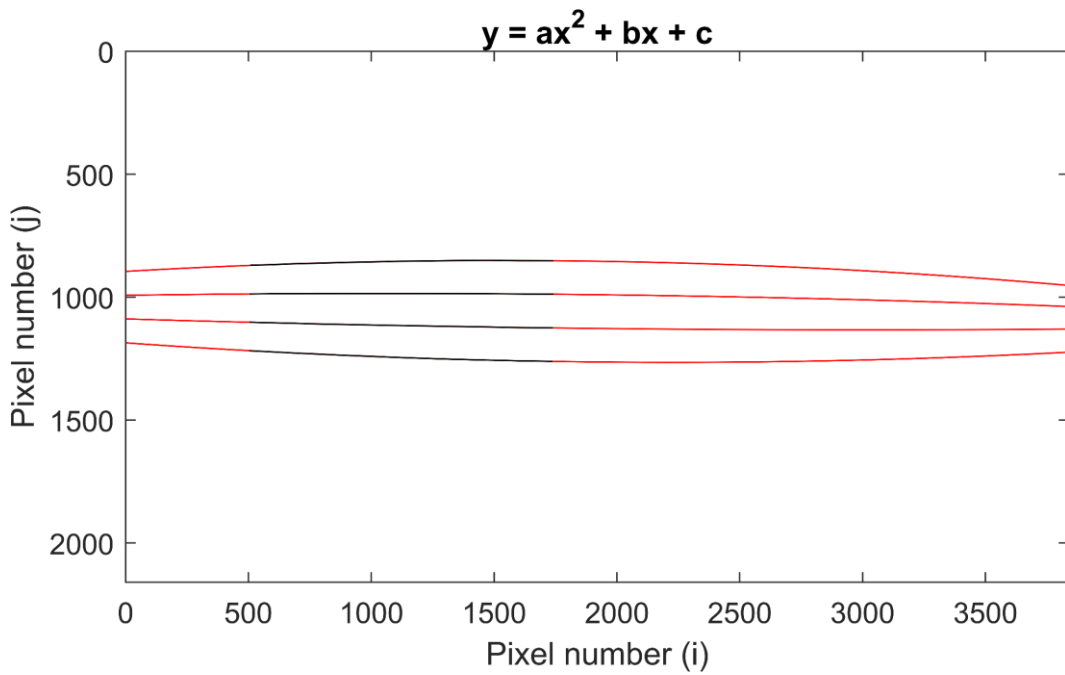


Figure 5.34. The horizontal lines of the calibration box (black lines), with trendlines (red lines) overlaid when the equation shown was used to calculate the trendlines.

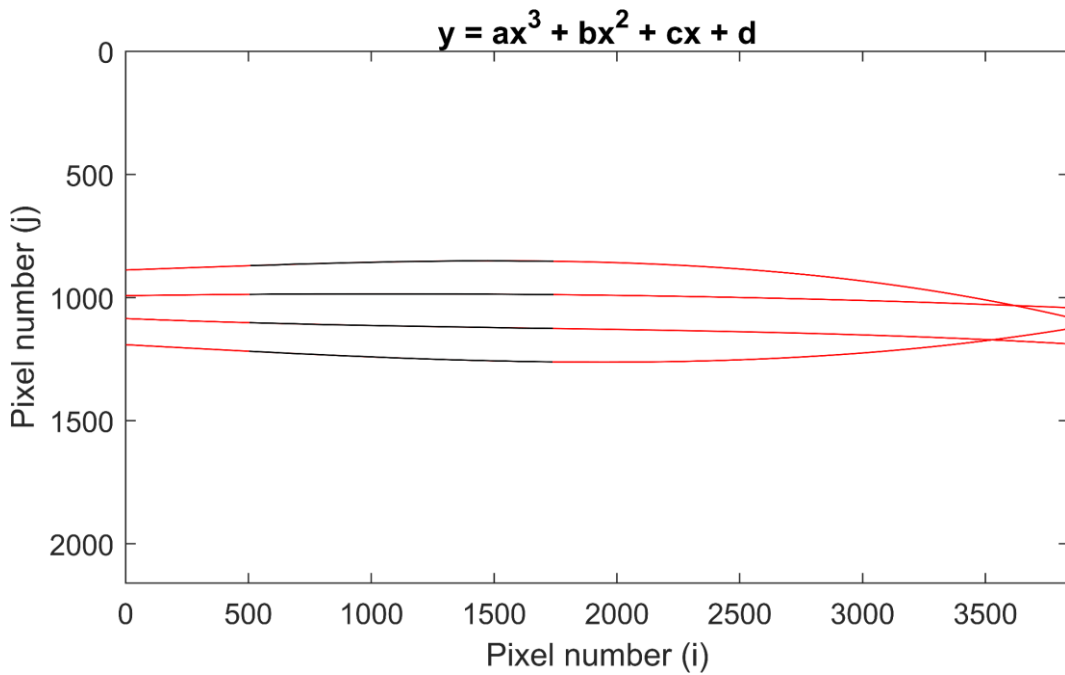


Figure 5.35. The horizontal lines of the calibration box (black lines), with trendlines (red lines) overlaid when the equation shown was used to calculate the trendlines.

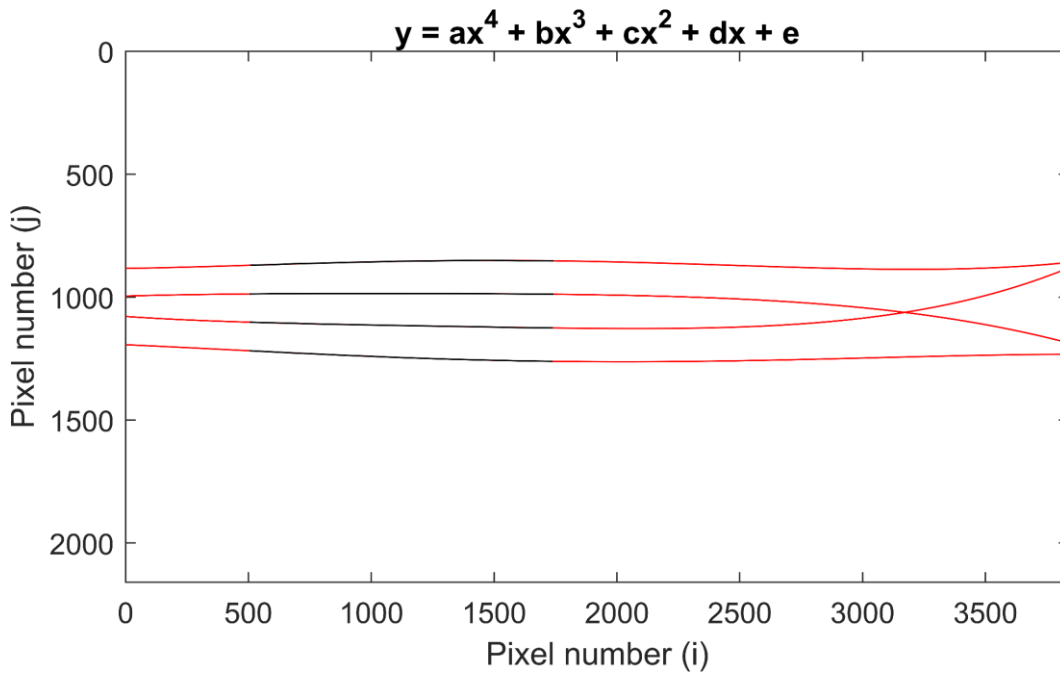


Figure 5.36. The horizontal lines of the calibration box (black lines), with trendlines (red lines) overlaid when the equation shown was used to calculate the trendlines.

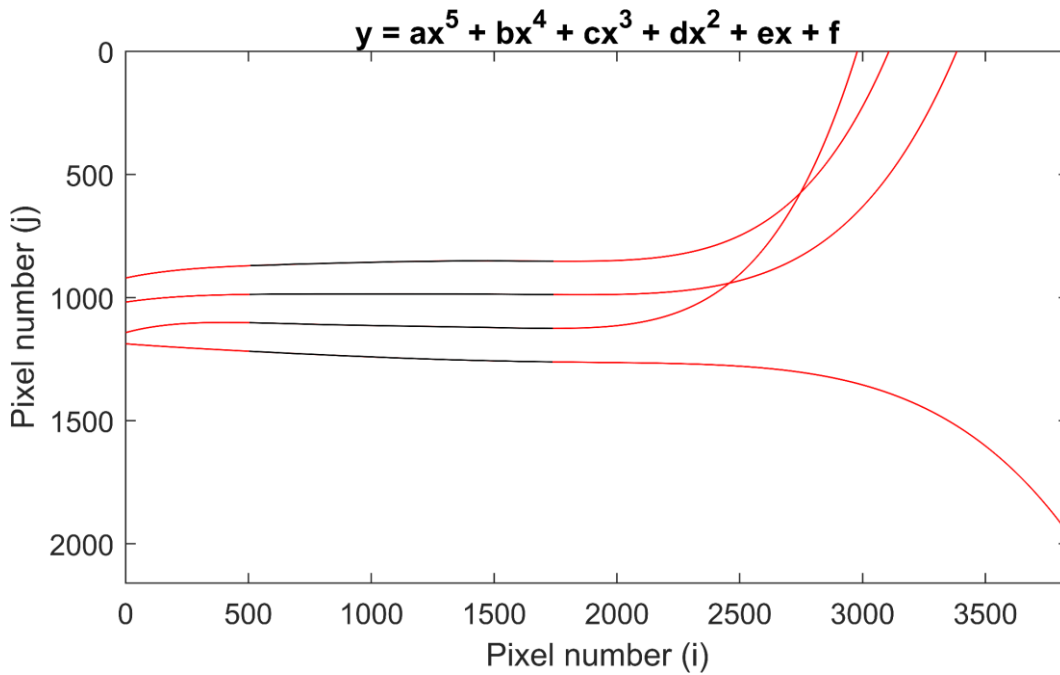


Figure 5.37. The horizontal lines of the calibration box (black lines), with trendlines (red lines) overlaid when the equation shown was used to calculate the trendlines.

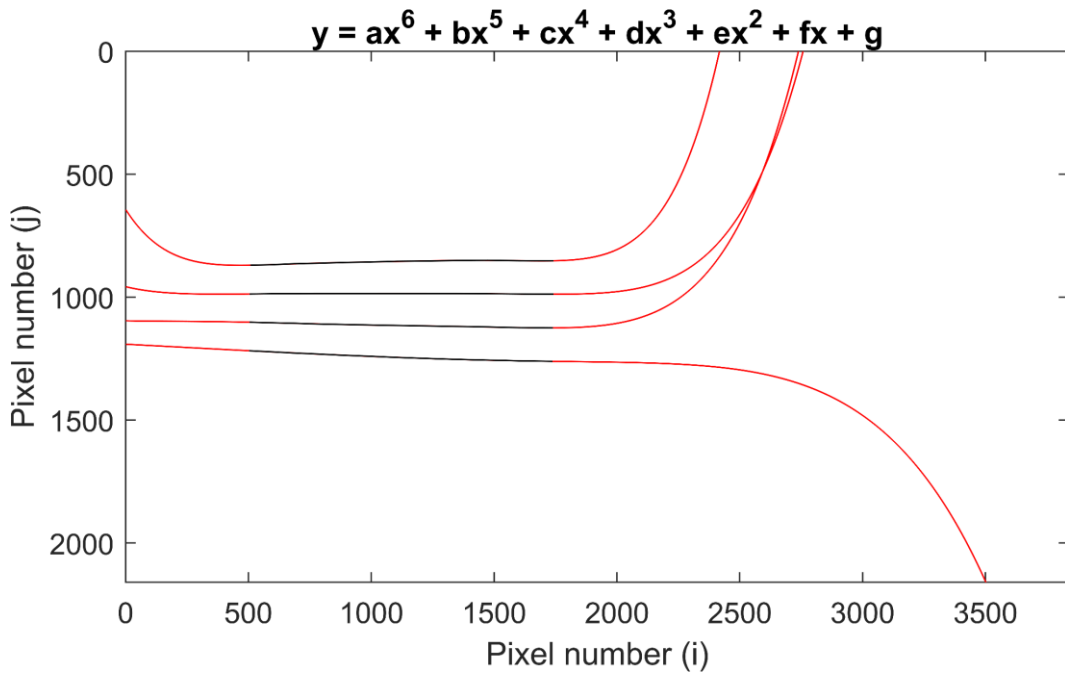


Figure 5.38. The horizontal lines of the calibration box (black lines), with trendlines (red lines) overlaid when the equation shown was used to calculate the trendlines.

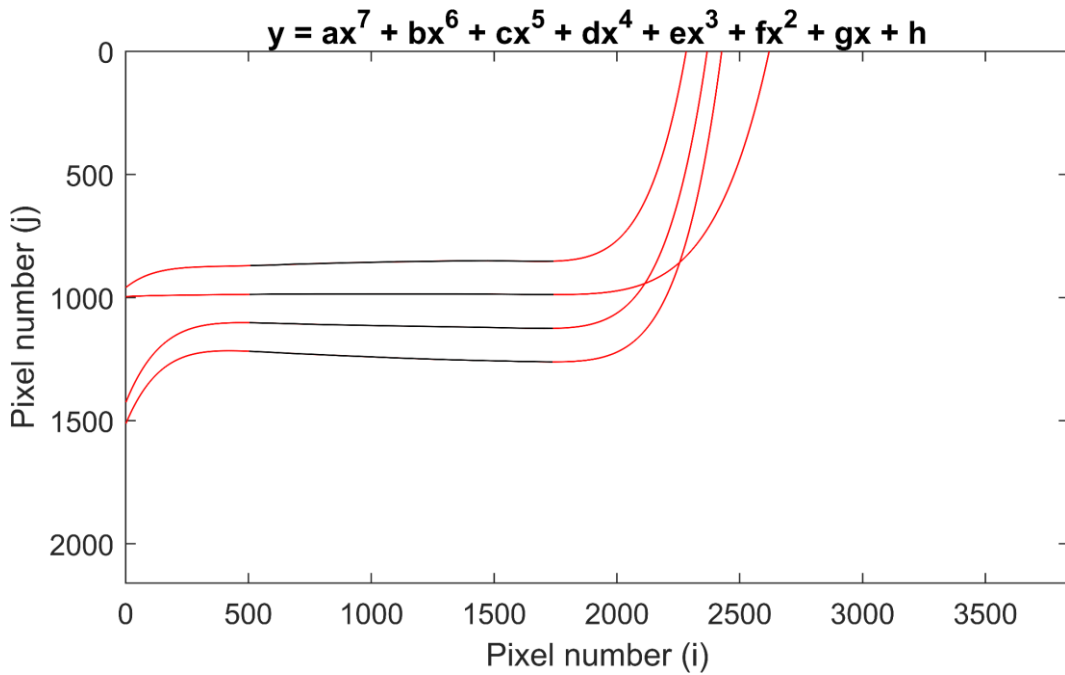


Figure 5.39. The horizontal lines of the calibration box (black lines), with trendlines (red lines) overlaid when the equation shown was used to calculate the trendlines.

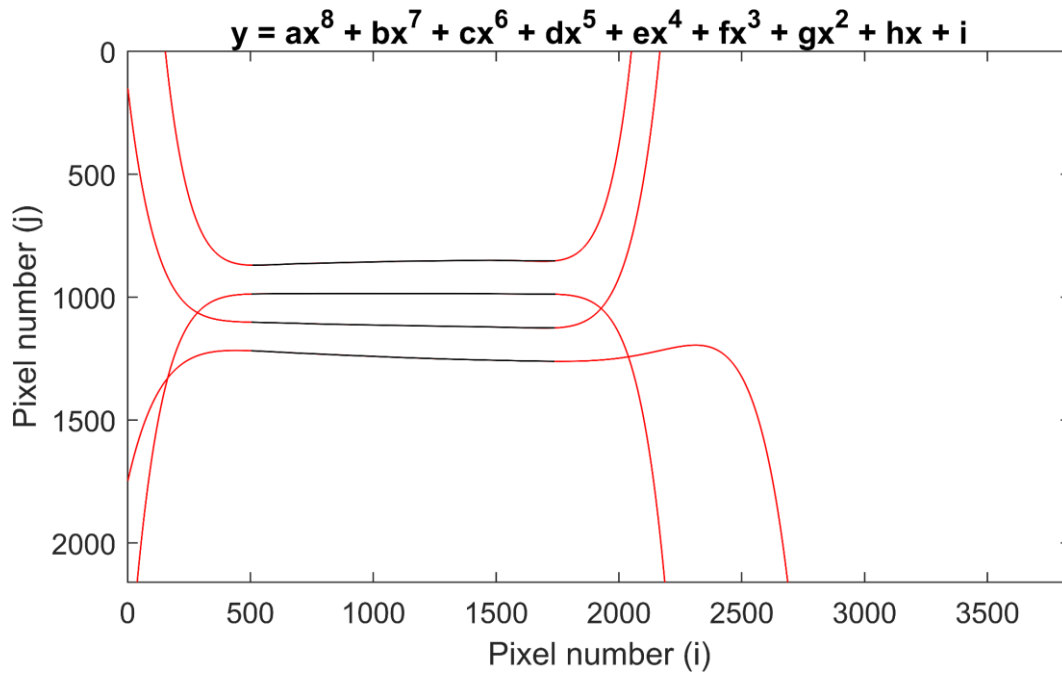


Figure 5.40. The horizontal lines of the calibration box (black lines), with trendlines (red lines) overlaid when the equation shown was used to calculate the trendlines.

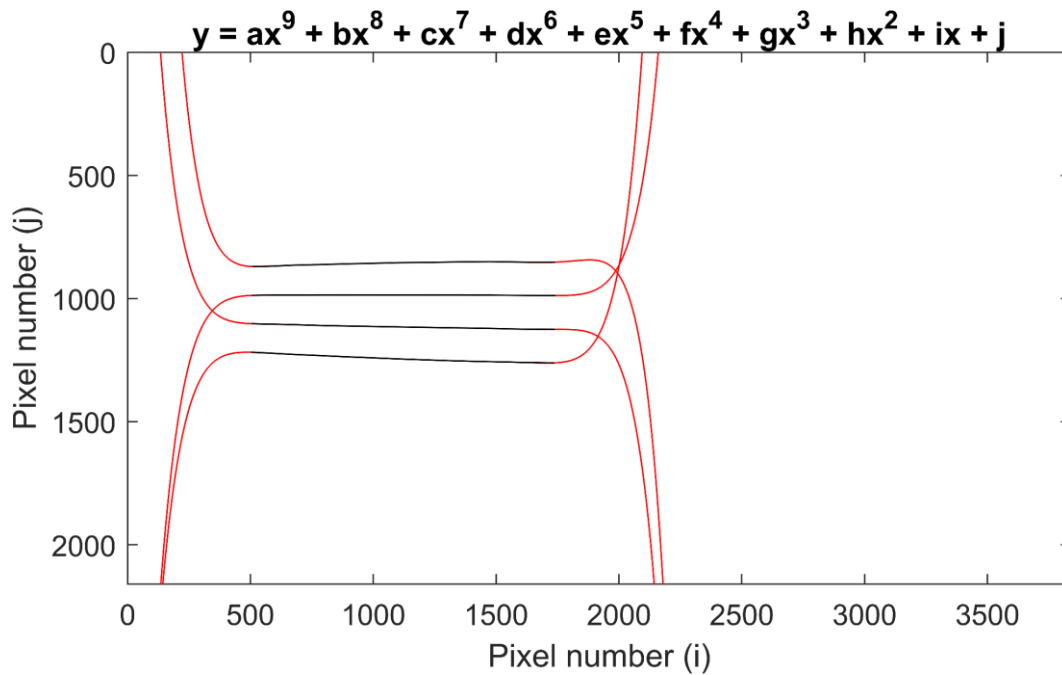


Figure 5.41. The horizontal lines of the calibration box (black lines), with trendlines (red lines) overlaid when the equation shown was used to calculate the trendlines

5.8. Appendix 5.2

Once the trendlines have been calculated, an expansion factor between these can be calculated. The expansion factor is the amount the image needs to be stretched in between these lines to get the pixels to represent 1 mm in height along the plane of space where the calibration box was positioned. The equation:

$$\frac{200}{\text{Number of pixels between trendlines}} \quad (6)$$

Was used, as the squares on the calibration box were 200 mm in height. This was done across the whole length of the image, i.e. for every column three factors were found.

Figure 5.42 to 27 are plots of the expansion factors needed for a vertical expansion of the image, as the trendlines converge when powers of 3 and higher are used, shown in **Error! Reference source not found..1**, they cannot be taken further, Figure 5.44 shows the expansion factors becoming excessively large at the convergence as the distance between the trendlines approaches zero leading to unrealistic results.

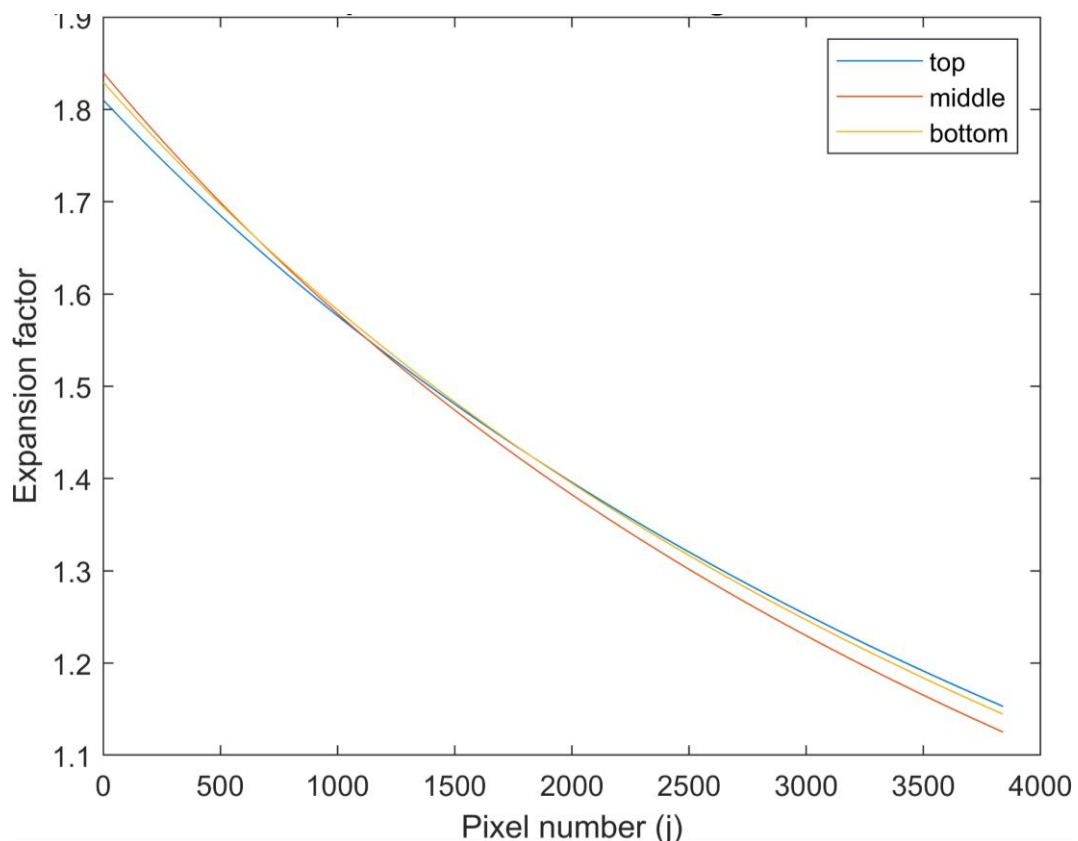


Figure 5.42. The expansion factors for each column when a trendline equation of $y = ax + b$ was used.

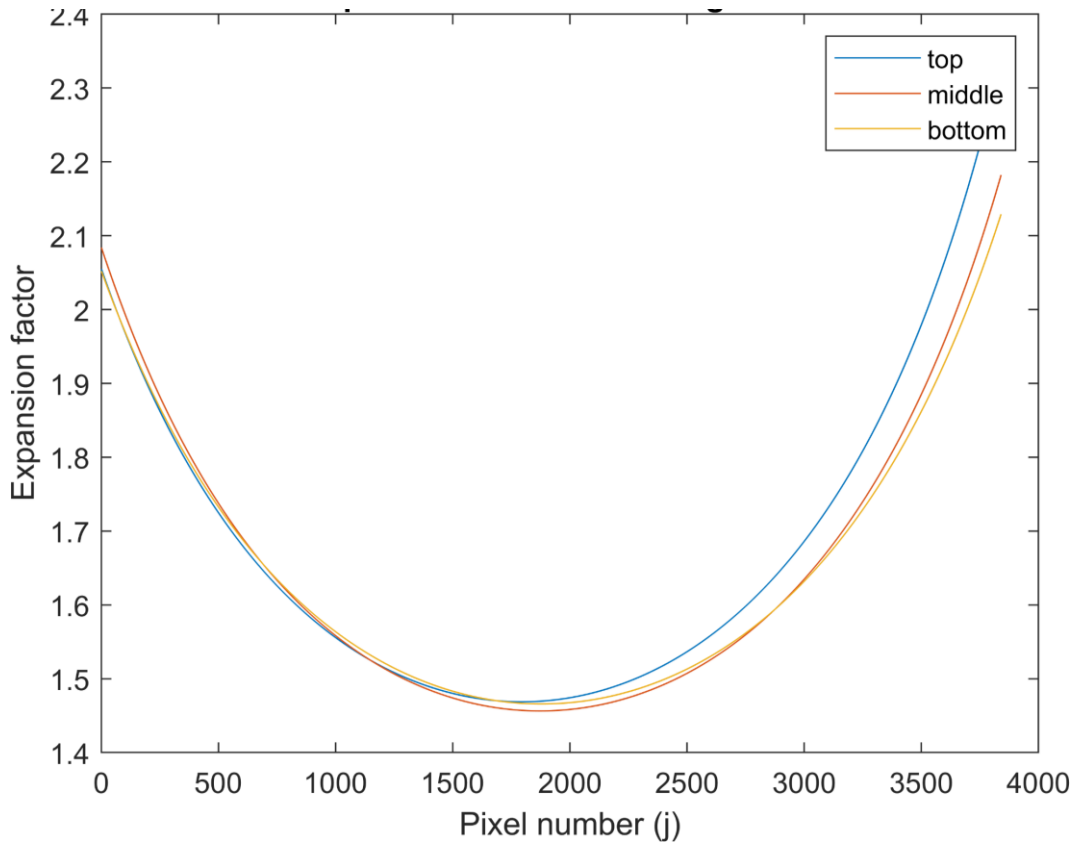


Figure 5.43. The expansion factors for each column when a trendline equation of $y = ax^2 + bx + c$ was used.

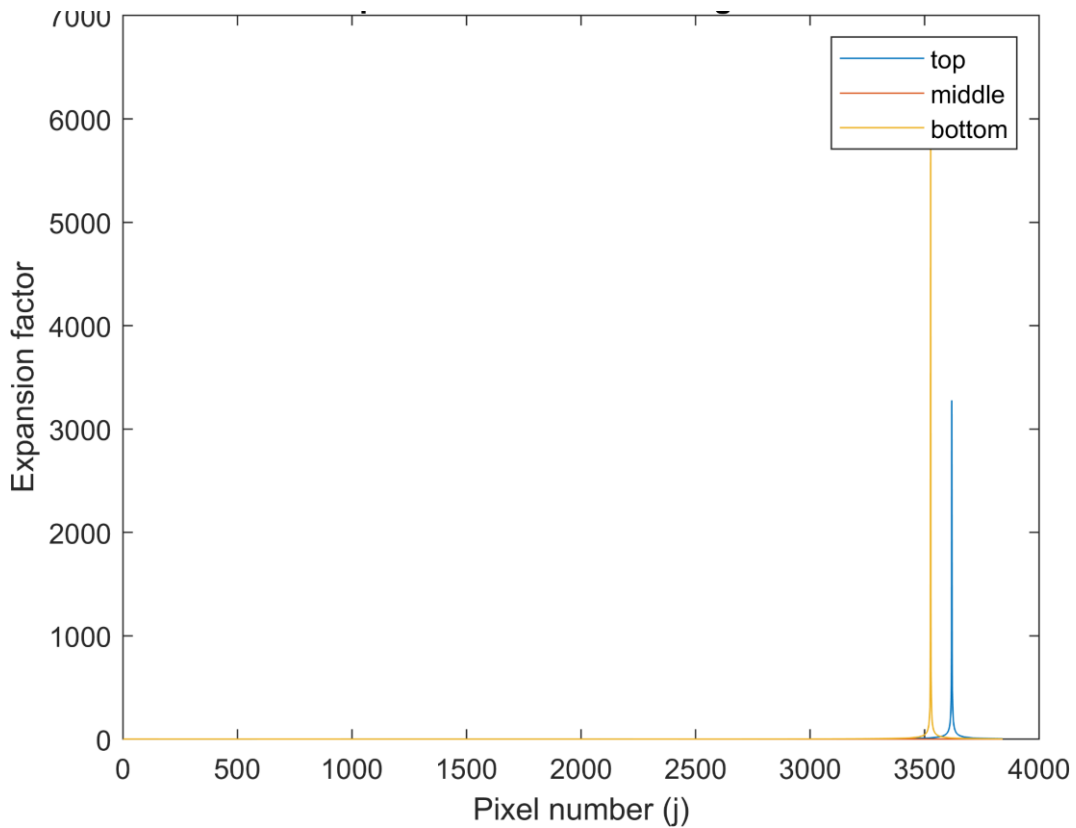


Figure 5.44. The expansion factors for each column when a trendline equation of $y = ax^3 + bx^2 + cx + d$ was used

5.9. Appendix 5.3

For a vertical expansion there are up to 18 different powers for the first trendline (highest power of 9, with or without an imaginary mirror), then 7 different powers for a vertical trendline (up to a highest power of 2 without a mirror and up to a highest power of 5 with an imaginary mirror), giving $18 \times 7 = 126$ different combinations of the trendlines, therefore, a method is needed to find the best combination. By measuring the calibration box after the expansions and other objects of known sizes, the error in the expansions can be measured to these objects and the best combination chosen for the video analysis.

Figure 5.45 show the errors when using horizontal powers up to 9 and (5.44) a vertical power of 1, (5.45) a vertical power of 2, and (5.46) a vertical power of 3. In the figures ‘H-expansion, calibration box’ measures how accurately the calibration box was expanded in the horizontal direction; ‘V-expansion, calibration box’ measures how accurately the calibration box was expanded in the vertical direction; ‘H&V-expansion, calibration box’, measures how accurately the calibration box was expanded in both the horizontal and vertical directions; ‘Rig width average’ measures how accurately the rig was expanded in the horizontal direction (measured at various heights); ‘Rig height average’

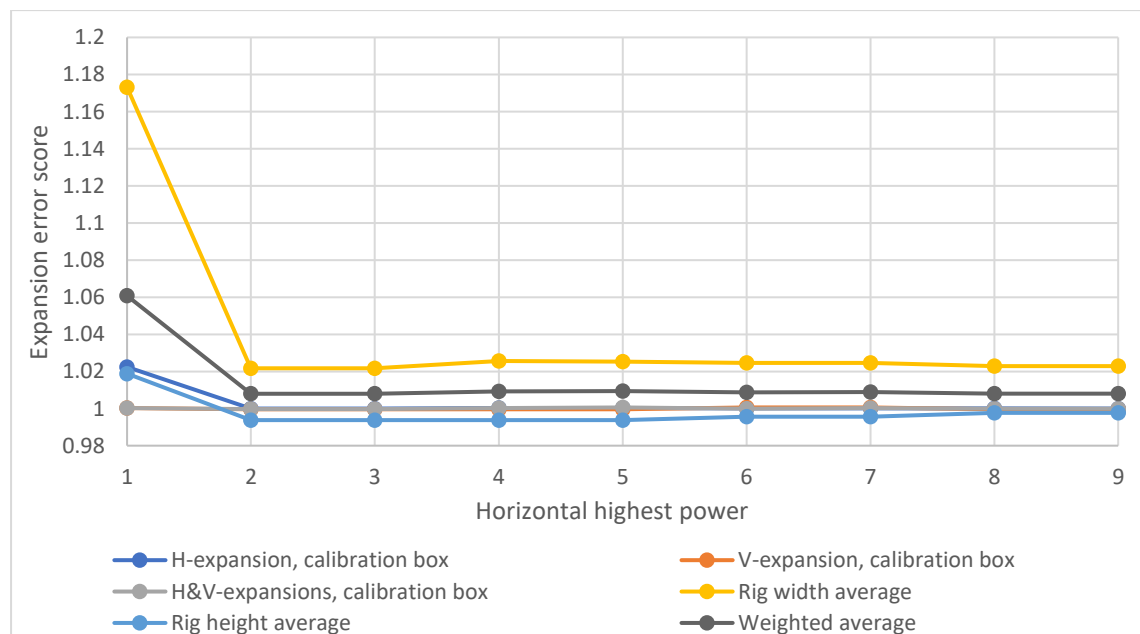


Figure 5.45. The errors for horizontal powers from 1 to 9 and a vertical power of 1.

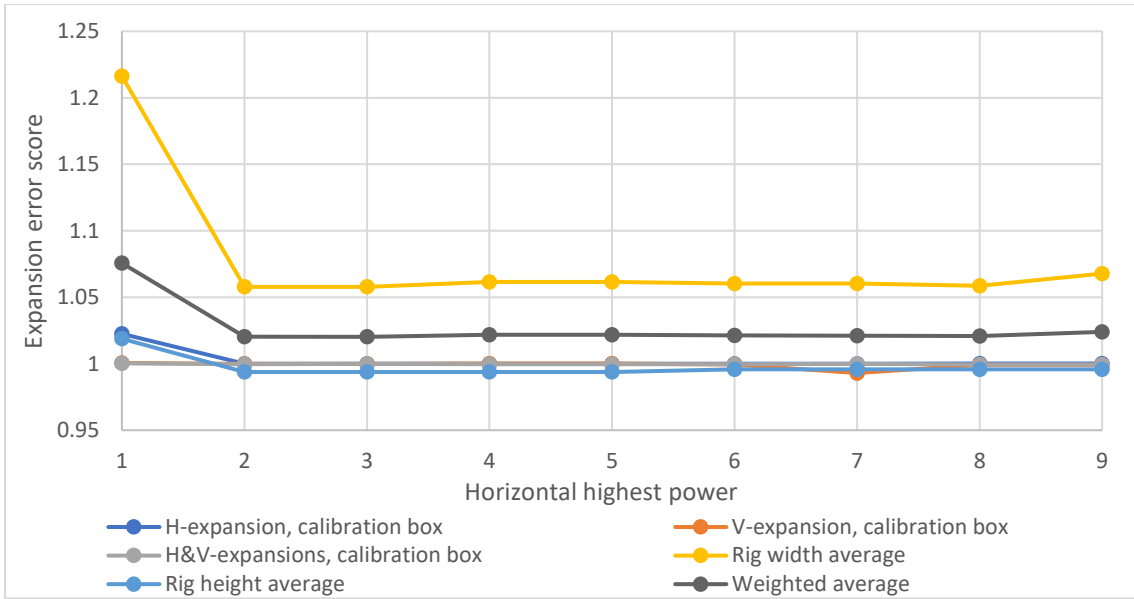


Figure 5.46. The errors for horizontal powers from 1 to 9 and a vertical power of 2.

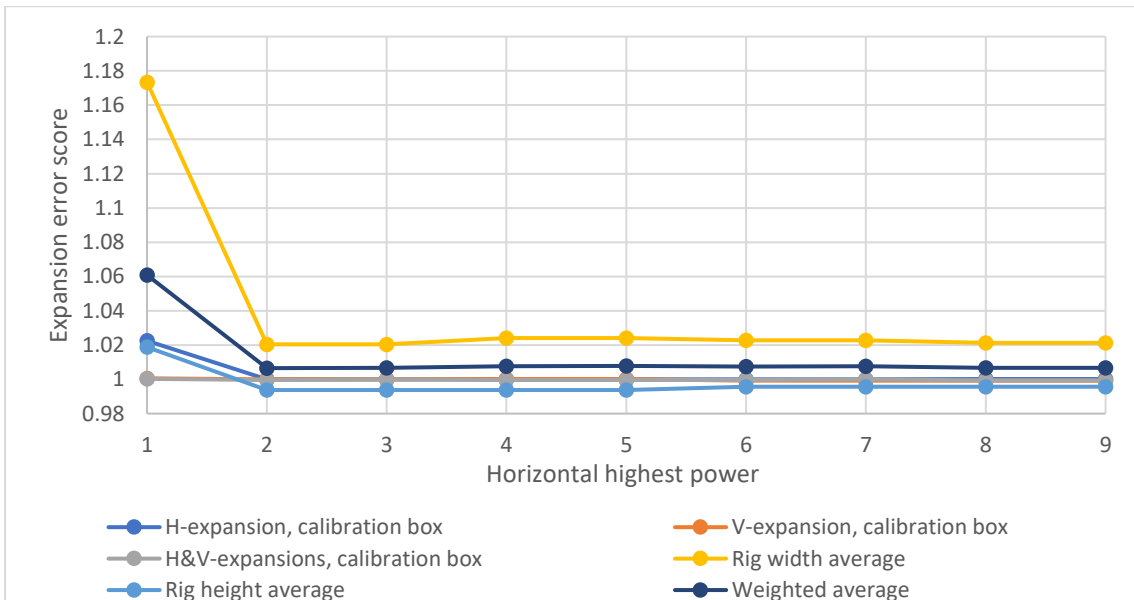


Figure 5.47. The errors for horizontal powers from 1 to 9 and a vertical power of 3.

In Figure 5.45 to 46, the same pattern is seen where a horizontal power of 1 is the least accurate, with the others approximately the same, but the accuracy score closest to 1 (1 is a perfect expansion) is when a horizontal power of 2 and a vertical power of 2 is used, with a weighted average of 1.007357, or an over estimation of 0.736 %, therefore, that was the combination taken forward in the flame measurements.

Chapter 6 Department of Business Energy & Industrial Strategy Report: A Study on the Safety of Second-life Batteries in Battery Energy Storage Systems.

Electrical energy storage will be a critical source of flexibility needed to transform and decarbonise the energy system. These systems allow for the storage of energy for times when it is needed and increase the flexibility of the grid, which is key for integrating variable renewable generation. From a consumer perspective, domestic lithium-ion battery energy storage systems (DLiBESS) are becoming an attractive option, particularly when installed alongside onsite generation such as solar photovoltaic (PV), enabling the consumer to maximise the use of this generation and to buy and sell electricity at times that are financially advantageous. This is particularly beneficial when used in conjunction with Demand Side Response (DSR).

Although few incidents of thermal runaway with DLiBESS are known in the public domain, such an event could present hazards such as fire, toxic gas release or explosion. The safety risks, best practice and standards associated with the use of new lithium-ion batteries (LiBs) in domestic systems are covered in BEIS research paper 2020/037, “*Domestic battery energy storage systems: a review of safety risks*” [1].

The current study follows on from this, as it addresses the use of second-life lithium-ion batteries in DLiBESS driven by the significant increase in the availability of second-life electric vehicle (EV) batteries resulting from the global drive to decarbonisation. However, there is a concern that second-life LiBs may have a greater risk of failure if steps are not taken to adequately mitigate this risk. Therefore, the aim of this study is to improve the evidence base available on the safety risks and hazards associated with the application of second-life lithium-ion batteries in domestic LiBESS and measures to mitigate these, including an assessment of best practice and standards. This report contains findings from a literature review and is supplemented by consultations with key stakeholders, listed below:

Altium	Bombus Energy	BVES (German Energy
Aviva	Solutions (ESL/120)	Storage Association)
Birmingham University	British Standards	Cawleys
(ReLiB project)	Institute	Cert-Fi
		Certsure

Cleevely Electric Vehicles	Johnson Controls Inc	Regen
Connected Energy	Levelise Ltd	Ricardo
Department for Environment, Food & Rural Affairs	London Fire Brigade	Siemens
Direct Line	National Fire Chiefs Council	Silver Power Systems
Electrical Safety First	Newcastle City Council	Solarwatt
Environment Agency	Newcastle University (ReLiB project)	UL
EV Recycling	Nissan Motor	Varta
IFV (Netherlands)	Manufacturing UK	Vehicle Certification Agency
INERIS (TC/120)	National Physical Laboratory	Warwick Manufacturing group
Jaguar Land Rover	Renewable Energy Association	XMS Capital
		Xtralis

The market for second-life DLiBESS (SLDLiBESS) is difficult to predict which was evident by the absence of detailed market information. While a number of stakeholders consulted as part of this study use second-life batteries in their LiBESS, these are predominantly for industrial applications and evidence suggests there is currently limited use in domestic systems. Therefore, in order to assess the potential market for SLDLiBESS, the following drivers and barriers were reviewed as reasonable indicators:

- **The market for DLiBESS.** Market analysis suggests that the UK DLiBESS market is a nascent but growing industry, with estimated capacity at 38 MWh in 2019 expected to rise to between 128 – 339 MWh by 2024 [2]. Consumer drivers are likely to be maximising use of onsite generation, such as solar, in addition to buying and selling electricity. This should be considered in light of rising electricity costs and the falling costs of LiBs.
- **Environmental and economic drivers for second-life LiBs.** The extraction and processing of the metals required by LiBs is both expensive and harmful to the environment. Additionally, it is estimated that there could be 75,000 to 105,000 end of first-life (EoFL) EV LiBs in the UK by 2025, which represent potential

environmental and safety waste hazards. In contrast, reuse, remanufacture or repurposing could extend battery life by 7 – 10 years, minimising waste and delaying or reducing materials recovery which is currently both energy intensive and limited in capacity.

- **Availability of second-life LiBs.** While the projected surplus of second-life LiBs is good news for the DLiBESS industry, the latter is unlikely to soak up the surplus and there will have to be significant innovation and investment in materials recovery. This will likely be driven by material supply and/or regulation, with the 2022 EU Batteries Regulation proposing to significantly increase the recovery of certain metals from LiBs in addition to requirements to incorporate certain levels of these recyclates into new LiBs. While likely to drive materials recovery, this could be at the expense of second-life.
- **Price of second-life LiBs.** It is currently both costly and labour intensive to test and triage EoFL batteries due to a lack of standardisation among EV OEMs. In addition, the falling cost of new LiBs means the economic incentive for reuse and repurposing may become less attractive.

The hazards represented by LiBs can be severe if they are not properly mitigated. The hazards associated with second-life LiBs are broadly the same as for new LiBs, but the probability of failure may be higher with the former due to the effects of ageing and unknown stress and/or abuse during the LiBs first life application. However, this remains an ongoing area of research and there is currently insufficient information available to determine either the likelihood of an age related failure or the effect of that failure with confidence.

The capacity loss of LiBs is generally considered to be linear, with EoFL typically around 75-80% state of health (SoH) and final end-of-life around 50-60% SoH. However, at some point there is a change in and/or an additional ageing mechanism which leads to an increased ageing rate. The time at which this occurs is referred to as the “knee” where severe and potentially dangerous deterioration is expected to occur, and the battery has reached its final end-of-life. Currently this point is difficult to predict but can occur at a higher SoH than expected. Cycling at normal rates or calendar ageing does not have a significant impact on safety; however, cycling at low temperatures or high rates can have a detrimental effect upon stability and can significantly reduce the temperate at which

thermal runaway occurs and consequently increases the risk of thermal runaway. In addition, this is shown to increase the risk of internal short circuits and joule heating.

It is for this reason, and due to the variance of SoH between EoFL LiBs (including within the same pack), that a sample of second-life LiBs should not be taken to be representative of the batch. Therefore, the **safety of second-life LiBs cannot be reliably assured by type tests**, which form the basis of all current international and European standards. Instead, an assessment is required for each LiB.

The re-purposing of LiBs is a nascent global market which has led to some uncertainty amongst respondents in terms of the codes, standards and regulations governing their testing, fitness for purpose, and transport. There are currently no UK or European standards specifically for second-life LiBs; however, both IEC 63330 and IEC 63338 are being developed to address this gap. IEC 63330 will specify the procedure for assessing the safety of second-life LiBs to be employed in applications other than that of their first life, and IEC 63338 provides high-level guidance on the safe and environmentally benign re-use of LiBs. Additionally, the EU Batteries Regulation contains requirements for second-life LiBs, including for first-life data to be made available in the battery management system (BMS) to facilitate re-use. Outside of the UK and Europe, UL 1974 (Standard for Evaluation for Repurposing Batteries) covers the sorting and grading process of LiBs that are intended for a repurposed use application.

Current practices include a variety of methods to measure state-of-health and/or reliance on detailed information retained in the BMS employed during first life (i.e. the EV BMS). The engagement of EV OEMs in the latter has yet to be assessed but is a critical factor. This information may include parameters such as: extreme values of temperature, charge and discharge current and charge & discharge voltage, details of insulation failure, accidents and storage conditions, total times or number of instances at extremes or out of specification, total number of charges and discharges, total times or numbers under charge and under discharge and total number or type of error messages. Gateway testing to assess the health of second-life LiBs includes: measuring capacity, internal resistance and self-discharge and performing a discharge/charge cycle test. However, **there is currently no widely-accepted test methodology for assessing the safety of second-life LiBs and this is a major gap in international standards**. Additionally, there remains uncertainty amongst stakeholders around the transportation of second-life LiBs.

Additional considerations for best practice when using second-life LiBs in DLiBESS include use of a dedicated BMS for the new application and monitoring as close to cell level as possible, the importance of which was highlighted by the incident in Surprise, Arizona, and is a requirement in the German standard VDE-AR-E 2510: 2017.

Extensive discussions with stakeholders have revealed two opposing views on second-life batteries: firstly, that a safety framework can be put in place to allow the use of second-life LiBs in DLiBESS, so long as the full history of the batteries in their first life applications is known and/or they can be tested effectively. A second, more radical view shared by some respondents is simply that the safety of such cells can never be guaranteed, and hence that second-life LiBs should not be employed under any circumstances in DLiBESS.

Lastly, due to the fire and electrical hazards associated with LiBs, the availability of potentially untested second-life LiBs and the potential lack of knowledge (for example, with LiB ageing) and skills of consumers to mitigate the risk through testing and good system design, consideration should also be given to whether stricter requirements are needed for home-built (“DIY”) DLiBESS that use second-life batteries, similarly to the USA.

6.1. Introduction

This document is the final report of the “Study on the Safety of Second-life Batteries used in Domestic Battery Energy Storage”. The work was commissioned from Newcastle University by the Office for Product Safety and Standards (OPSS) and work commenced in February 2021. The report was published in February 2023¹.

The project commenced with in-depth research of academic, commercial, and regulatory sources which was supplemented by consultations with key stakeholders. In total, representatives from 40 organisations responded, including electric vehicle (EV) and battery energy storage system (BESS) manufacturers/suppliers and industry associations, battery recyclers, research institutes, public and government bodies, product safety experts and standards bodies. Following assessment by OPSS and amendment, a virtual

¹<https://www.gov.uk/government/publications/safety-of-second-life-batteries-in-battery-energy-storage-systems>.

workshop was held with all respondents to test and validate the findings. This is the final report.

The report commenced with an overview of the market for second-life batteries, followed by a review of hazards for lithium-ion batteries and risks specific to second-life batteries along with a description of gateway testing and other mitigating measures. It then provided a detailed analysis of the relevant codes, standards and regulations and considered best practice when using second-life batteries in battery energy storage systems.

6.1.1. Overview

Electrical energy storage is seen as a key source of flexibility which will be needed to transform and decarbonise the energy system. These systems allow for the storage of energy for a time when it is needed and increase the flexibility on the grid, which is key for integrating variable renewable generation. Electrochemical battery technology, particularly lithium-ion, is a significant contributor to UK storage capacity, with 1 GW of capacity installed since 2017 and 8 GW of capacity in the planning pipeline [3]. Energy storage systems can also be installed in the home, with domestic battery energy storage systems (DLiBESS) allowing the user to buy and sell electricity at times that are financially advantageous. This is particularly beneficial when used in conjunction with solar power and/or Demand Side Response (DSR). Some systems can also offer limited off-grid capability in the event of a mains power failure.

Although few incidents of thermal runaway with DLiBESS are known to date in the public domain, such an event could present hazards such as fire, toxic gas release or explosion. The safety risks, best practice and standards associated with the use of new lithium-ion batteries in domestic systems are covered in BEIS research paper 2020/037, “Domestic battery energy storage systems: a review of safety risks” [1]. The authors of the report suggested that, if manufacturers and installers follow best industry practices and standards, they can significantly mitigate risks in the residential application of BESSs.

The current study follows on from this, as it addresses the use of second-life lithium-ion batteries in DLiBESS driven by the significant increase in the availability of second-life

electric vehicle batteries resulting from the global drive to decarbonisation. While still considered safe and usable, their capacity is typically 75-80% that of a new battery. This reduction in capacity makes them inadequate for satisfactory car use, but the additional weight/volume: energy ratio of these used batteries is not a problem in stationary applications. It is estimated that LiBs used in second-life stationary storage applications can be of service for a further 10 years before reaching their absolute end-of-life [4].

However, there is a concern that second-life batteries may have a higher risk of failure if steps are not taken to adequately mitigate this risk, due either to the poor condition of the individual cells, the design quality of the new battery assembly, or a new duty that is different to that for which the battery was originally intended. Additionally, there is some evidence to suggest that consumers are building their own DLiBESS using second-life modules purchased online and as EV batteries become more accessible it is foreseeable that this activity will increase.

6.1.2. Study objectives and scope

The aim of this study is to understand best practice in the design and installation of DLiBESS that use second-life batteries and to provide OPSS with a clear understanding of the safety risks to consumers and typical methods used by manufacturers to reduce these risks. This breaks down into the following objectives:

- **Objective 1:** Analyse the current and forecasted market for second-life batteries in DLiBESS.
- **Objective 2:** Assess the safety risks and hazards of second-life batteries.
- **Objective 3:** Review best practice and mitigating measures for the assessment of second-life batteries and the design of DLiBESS that use second-life batteries.

Table 6.1 provides an overview of the research framework, linking the three study objectives to research questions and signposting where in this report each issue is discussed.

Table 6.1. An overview of the research framework.

<i>Study objective</i>	<i>Research questions</i>	<i>Final report section</i>

1	<i>What does the current and forecasted future market look like for second-life domestic LiBESS?</i>	6.2 & 6.3
2	<i>What are the consequences of including damaged or lower performing cells in a battery pack?</i>	6.4 & 6.5
	<i>What are the risks to the consumer of purchasing or building their own second-life battery?</i>	6.5
3	<i>What are the safety issues that should be taken into consideration if creating a new battery pack from second-life cells?</i>	6.6, 6.7 & 6.8
	<i>How can used cells, modules and packs be individually assessed for condition, performance and safety? What will be the impact of future codes, standards and regulations?</i>	6.6 & 6.8
	<i>Do existing testing regimes sufficiently assure safety for the end-product?</i>	6.8

6.2. Overview of lithium-ion cells

6.2.1. Physical characteristics

Lithium-ion batteries (LiBs) are devices for storing electrical energy: they are secondary batteries as, once discharged, they can be recharged by supplying electricity.

The lowest unit of a LiB is the cell. Cells are combined in series and parallel to form a module or string and a number of modules or strings comprise a battery or battery pack. Cells come in three common forms, or form factors [5]: cylindrical, pouch and prismatic, see Figure 6.1.

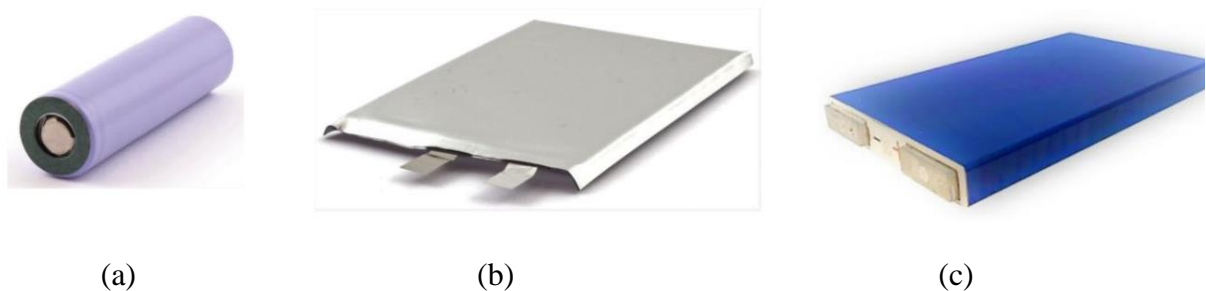


Figure 6.1 The common lithium-ion cell form factors: (a) cylindrical, (b) pouch and (c) prismatic. © Intertek.

Cylindrical cells are typically 18 mm in diameter and 65 mm long (18650): other dimensions include 26650 (26 mm diameter and 65 mm long) and 21700 (21 mm diameter and 70 mm long). Prismatic cells come in a range of sizes depending upon application. Pouch cells are typically the size of an A4 or A5 sheet and about 16 mm

thick. In Tesla EVs, over 7000 cylindrical cells form the battery pack: in the post-2018 Nissan Leaf, there are 8 A4 sized pouch cells per module and 24 modules per pack [6]. The number of cells in industrial LiBESS depends upon the rated energy of the cells and the system (in MWh), but as an example, the 2 MW McMicken LiBESS that exploded in Surprise, Arizona in April 2019 comprised 10,584 64 Ah pouch cells [7]. For domestic scale LiBESS, the 13.5 kWh Tesla Powerwall 2, for example, employs 750 – 900 21700 NMC cells [8].

6.2.2. Applications

The first application of LiBs was in portable electronics, specifically Sony camcorders in 1991 [9], but this expanded rapidly into mobile phones and laptops using all three form factors. The next paradigm shift was the use of LiBs in EVs heralded by the 1st production battery EV, the Tesla Roadster in 2008 [10]. This also triggered very large-scale production of LiBs in gigafactories. Plug-in hybrid EVs were followed by the Nissan Leaf in 2010 and a significant increase in the LiB market in 2015 due to the introduction of Chinese EV buses [11]. The first LiB Energy Storage System (LiBESS) was installed in 2008 in Guadeloupe in a collaboration between SAFT, Tenesol, ADEME and EDF SEI and was actually a number of residential or domestic LiBESS (DLiBESS), consisting of 15 SAFT 11 kWh units each connected to a 2 kW photovoltaic (PV) system [12]. The first large scale (5MW) LiBESS was commissioned for Portland General Electric in 2012 [13].

6.2.3. Composition and electrochemistry

A LiB cell comprises two electrodes, the anode and cathode, pressed either side of a porous polymer separator soaked in electrolyte. The electrolyte is a mixture of organic compounds with an added salt, lithium hexafluorophosphate or LiPF_6 , that dissociates in the organic mixture to produce free lithium and hexafluorophosphate ions (Li^+ and PF_6^-). The separator prevents the electrodes from touching each other, which would cause an internal short circuit and significant Joule heating but allows free movement of the ions. When fully discharged, all the lithium-ions are present inside the crystal structure of the cathode (see Figure 1.9) which is typically a mixed-metal oxide (MMO) such as NMC

111 (Nickel Manganese Cobalt, $\text{LiNi}_{0.33}\text{Mn}_{0.33}\text{Co}_{0.33}\text{O}_2$) or LFP (Lithium iron [Ferrous] Phosphate, LiFePO_4) [14]. The vast majority of LiBs employ graphite anodes and hence they are discriminated between, and the cells known by, the cathode composition (NMC; LFP, LMO, etc). On charging, the lithium-ions move out of the cathode, move through the electrolyte and into the anode, which is typically made up of very small particles of graphite. By definition, oxidative processes take place at the anode and reductive processes at the cathode. The anode is the graphite electrode during discharge and the mixed metal oxide is the cathode: on charging, these terms should switch (i.e. the MMO should become the anode). However, by convention, the terms retained are those specified for discharge.

Typical separators are polyethylene, polypropylene, or a combination of both. The separators typically employed in LiBs [15] are ca. 20-30 μm thick, which is about $1/5$ to $1/3$ of the thickness of a standard sheet of A4 paper: i.e. very thin, and this should be considered in the discussions later in the document concerning abuse and the consequent internal short-circuiting of anode and cathode.

LiBs have energy densities hitherto not seen for conventional batteries such as lead acid, nickel-cadmium (NiCd) etc, with EV batteries having densities [16] up to 250 Wh kg^{-1} and long cycling life.

6.3. The market for second-life LiBESS

The market for SLDLiBESS is difficult to predict which was evident from the absence of detailed market information. However, the DLiBESS original equipment manufacturers (OEMs) consulted during this project all held the view that the demand for domestic LiBESS in general was set to increase significantly over the next decade. This includes two EV OEMs who stated they were repurposing second-life LiBs for portable energy storage applications [17, 18] (e.g. on building sites), while only one company was repurposing these for use in SLDLiBESS [19]. The low number of existing SLDLiBESS on the market correlates with an economic analysis presented in the European ELSA project (Energy Local Storage Advanced system, 2015 - 2018) which stated that the potential market for second-life batteries for domestic use is “low” [20]. Similarly, market analysis from Zhu et al. [21] shows that while the number of industrial applications using second-life LiBs is increasing rapidly, only 3 out of the 41 projects identified were for domestic purposes.

In general, there is a lack of detailed information on the market for second-life LiBs: hence this section analyses the market for DLiBESS more broadly, along with the drivers, supply, and demand for second-life EV batteries, as a reasonable indicator of the potential market for SLDLiBESS.

6.3.1. The market for DLiBESS

Industrial scale LiBESS are seen as the major market for second-life LiBs with the total global market predicted to be up to 2857 GWh by 2040 due to their wide application and the falling price of LiBs [22-24]. These energy storage systems have a number of functions including [25]: frequency regulation, replacing spinning reserves, voltage or reactive power support, load following, peak shaving, load management and arbitrage, and are ideal for supporting renewable energy generation and storage².

In general, the consumer drivers [26] behind the use of DLiBESS and SLDLiBESS³ may include environmental concerns, but are more likely to be economic. Solar energy generation globally in 2021 was the cheapest [27] (\$37/MWh) compared to wind (\$40/MWh), coal (\$112/MWh) and nuclear power (\$163/MWh) [28]. This, when considered along with rising electricity costs [29] and falling LiB prices [30], would be expected to see a significant uptake of PV arrays combined with LiBESS to help consumers maximise the use of their onsite generation and avoid importing electricity from the grid in peak periods.

According to a study from Solar Power Europe, the UK currently ranks 3rd in Europe for the uptake of such DLiBESS after Germany and Italy, however, its share of the market was only 38 MWh in 2019 compared to 496 MWh for Germany. Further, by 2024 the UK DLiBESS capacity is expected to rise to 128 – 339 MWh, slipping to 4th in the ranking compared to 2378 – 4028 for Germany, 430 – 900 (Italy) and 242 – 435 MWh (Austria) [2]. The top 3 countries provide incentives to encourage the uptake of PV + DLiBESS systems. Instead, the UK approach for facilitating domestic storage is to remove barriers and reform markets through actions taken in the 2021 Smart Systems and Flexibility Plan [3]. For solar PV the UK's Feed-in Tariff closed to new applicants in

² Spinning reserves, named after the turbines employed, are coal or gas-fired power stations kept active but idling (as starting up a “cold” station can take days or even weeks) to supply rapid grid support.

³ DLiBESS is generally used for commercial domestic systems using new cells and SLDLiBESS for commercial and Do-It-Yourself (DIY) domestic systems employing second-life cells. The latter are assembled by homeowners with lithium-ion modules or packs purchased from online suppliers.

March 2019 and was replaced by the Smart Export Guarantee (SEG) in January 2020. As a market-led mechanism, where suppliers are responsible for the setting and payment of export tariffs, SEG is designed to allow room for the market to develop options, promoting innovation and competition as part of the transition to a smart and flexible energy system. The SEG framework is designed to maximise the benefits of solar PV and storage combinations by encouraging onsite consumption and agile, time of use tariffs. However, two DLiBESS manufacturers consulted as part of this study argued that this shift has slowed the uptake of domestic energy storage in the UK⁴: and a UK not-for-profit centre of energy expertise and market insight estimated that a PV + DLiBESS system would require a more than 20 year payback period, whilst the owner of a DLiBESS system alone would struggle to achieve any payback at all. Currently, therefore, this is a nascent market. However, electricity is easier to store than heat and the UK domestic storage market is expected to increase significantly due to owners of PV arrays retrofitting DLiBESS, homeowners wishing to exploit behind-the-meter-storage/time of use (TOU) billing and participation in Virtual Power Plants (VPPs) which support the grid.

VPPs can include a network of wind farms, solar arrays, combined heat and power units, but in the context of this report they are clusters of solar arrays and/or DLiBESS remotely managed and operated with the intention of supporting the grid, e.g. by frequency stabilisation, but also with the intention of providing some return to homeowners, who are known as prosumers: producers and consumers of electricity. VPPs are typically cloud-based platforms and the DLiBESS are fully automated. Consumption of electricity by the prosumer and generation by the grid are monitored in real time in order to facilitate the operator to offer the best value electricity to its customers. When demand by the grid is less than production, the energy stored in the VPP is available in seconds to provide grid support and enable smart energy management. The latter is the ability to, for example, utilise rapid response, distributed energy generation and storage systems to deal with uncertainty and rapidly changing demand. One VPP operator stated that 70% of revenue and savings were provided to prosumers, representing 20% more than if the prosumers were benefitting from TOU billing alone.

⁴ This was partly responsible for one major DLiBESS manufacturer pulling out of the UK DLiBESS market.

An extreme example of the emerging VPP market is the “Rent a Roof” concept [31] where a company pays for the installation of a PV + DLiBESS system and the feed-in tariff is assigned to the company. Some return is provided to the homeowner, but otherwise the latter has no significant engagement with, nor have any knowledge of, the DLiBESS.

Finally, one possible driver not linked to economic considerations is protection against power outages. Such events are relatively rare in the UK: however, Tesla introduced the Powerwall DLiBESS following outages in California to allow both home usage and EV charging when the domestic electricity supply fails [32].

6.3.2. Environmental and economic drivers for second-life LiBs

By the early 2030s, there could be 20 M EVs on European roads and more than 100 M by 2040 [33], with an estimated 112 – 1000 GWh of second-life EV LiBs available by 2030 [34-36] as the first significant wave of end-of-first-life (EoFL) battery packs occurs. In response to this challenge, China, South Korea and Japan are developing robust recycling (i.e. materials recovery) and second-life infrastructures [37]. However, there is only a limited LiB recycling industry in the UK at the present time [38] yet it is estimated that there will be 75,000 to 105,000 EoFL EV lithium-ion batteries in the UK by 2025 [39] and these represent potential environmental and safety risks and hazards [6]. However, there are UK companies poised to take up the recycling/repurposing challenge [40-42].

The extraction of the metals required by LiBs is material-rich and costly, and labour, time and carbon-intensive. Thus, 1 ton of lithium ions requires 250 tons of the Li-rich mineral ore Spodumene or 750 tons of Li-rich brine [43]: in addition, each ton of lithium requires 1900 tons of water [44] and each kWh of LiB produced requires 50 – 65 kWh of electricity and generates 55 kg CO₂ if the electricity comes from a coal-fired power station [45]. Needless to say, the extraction and processing of metals is also harmful to the environment [6, 46]. On the other hand, reuse, remanufacture or repurposing could extend battery life by 7 – 10 years [47-49] thus contributing to waste minimisation, delaying or reducing materials recovery (which is currently energy intensive [6]) and reducing gross energy demand and Global Warming Potential by 15 – 70 % [50] by reducing greenhouse gas emissions [51]. The World Economic Forum Battery Alliance estimates that moving from the current linear economy in EV LiBs to a circular economy could reduce global CO₂ emissions by 35 Mt with an attendant economic gain of \$35bn.

With respect to the latter, reusing or repurposing EV LiBs, for example, could lower the cost of the EV charging infrastructure by 90% by 2030 [52].

However, it may be that the global uptake of LiBs places major pressure on the supply of essential material, hence driving recycling (materials recovery) over re-use, remanufacture or repurposing. Thus, it has been estimated that, by 2030, materials recovery from end-of-life LiBs could produce approximately 10% of Europe's cobalt consumption by the automotive sector [39].

6.3.3. The availability of second life LiBs

The EoFL of an EV battery pack is generally taken as 75 – 80 % State-of-Health (SoH, one definition being the ratio of the current charge when fully charged to the initial, rated full charge, expressed as percent [53]⁵). Apart from recycling, EoFL EV battery packs can be reintroduced into the supply chain as follows:

- **Reuse** is defined as using all or part (i.e. modules) of a battery for the same application as its first life, see Figure 6.2.
- **Remanufacturing** involves replacing multiple defective modules and reusing the pack in its original application.
- **Repurposing** is the disassembly of the original pack, assessment and replacement of modules and assembly into a battery for use in a different application to the original pack [54]. At the present time, the most likely destination for repurposed batteries is in stationary energy storage.

End-of-Second-Life (EoSL) is generally stated as 50-60 % SoH (with respect to rated SoC at Beginning-of-Life, BoL) and is limited by concerns over very significant degradation at lower SoH and the attendant safety implications including spalling of the electrodes, lithium metal plating and dendrite formation [54-57].

The current assumption that all second-life LiBs come from end-of-life EVs is incorrect. There are three common routes to market for these batteries [58]:

1. The battery pack is replaced on warranty,

⁵ This figure is increasingly being questioned as it was formulated by the US Advanced Battery Consortium in 1996 (J. Zhu et al., Cell Reports Phys. Sci., 2 (2021) 100537. <https://doi.org/10.1016/j.xcrp.2021.100537>.) prior to the emergence of LiBs.

2. An EV is an insurance write-off and the Authorised Treatment Facility (ATF) dealing with the scrapping of the EV sells the battery and
3. A pack is upgraded [58].

At the time of writing most second-life LiBs in large and mid-sized SLDLiBESS come from (1) and (3) [59]. An important aspect of the write-off of EVs or warranty replacement of EV battery packs was raised by an EV OEM which was the loss of the connection between the Vehicle Identification Number (VIN) and the serial numbers on modules in packs. As a result, all the information stored in the battery management system (BMS) essential to ascertain if the modules were fit for use in second-life applications is lost. This loss of connection between pack and vehicle was also reported by a second EV OEM that repurposes packs from EV vehicles in the company's own prototype testing fleet for use in industrial scale LiBESS⁶. Both these EV OEMs, and manufacturers repurposing batteries for storage which were consulted as part of this research, expressed strong faith in the safety and durability of their second-life batteries based on a significant body of statistical data on 1st and second-life failures rates as well as customer satisfaction.

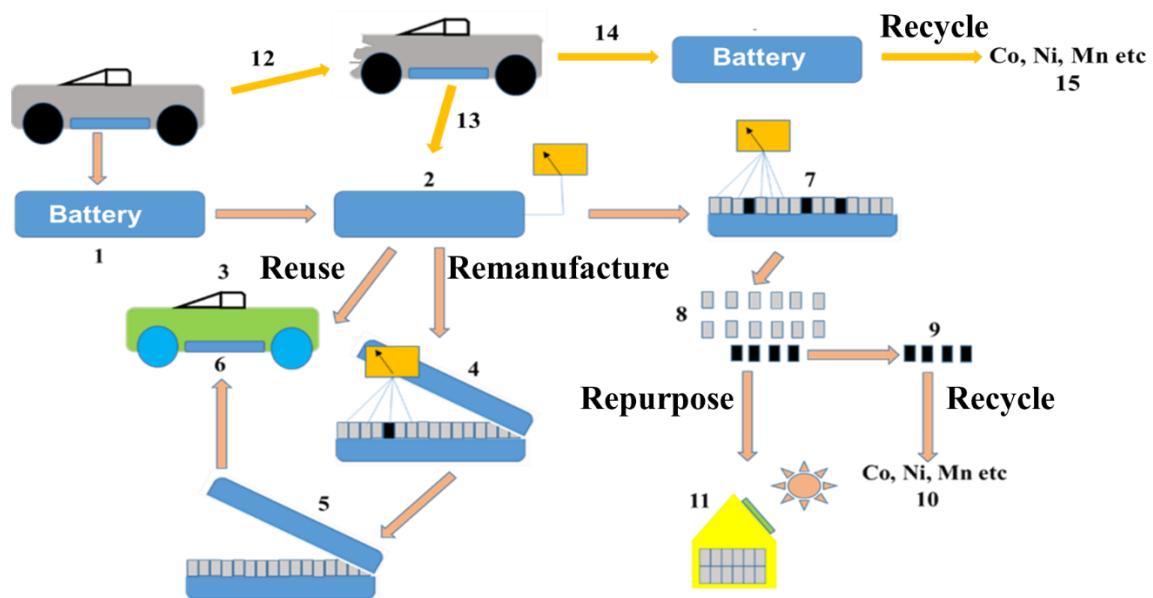


Figure 6.2. Reuse, remanufacturing, and repurposing.

⁶ In addition to the important implications of the loss first life history for second-life applications of LiBs, when an EV is sent to an ATF, the original EV OEM has no way of ascertaining the fate of the EV pack, but retains extended producer responsibility for that pack[59].

In Figure 6.2, (1) EV to be scrapped and battery pack removed. (2) Gateway testing on the pack, if the pack passes the testing criteria it is (3) reused in a second EV. If the pack does not pass it is (4) opened, modules tested individually, defective modules replaced and the modules rebalanced (5). The remanufactured pack is then used in a second EV (6). (7) If multiple modules are defective the pack is opened and (8) the modules tested. Defective modules are (9) separated and (10) sent for materials recovery. (11) The remaining modules are repurposed into a LiBESS. Steps (12) – (15) concern the possible re-use or recycling of packs from damaged EVs.

With respect to the future, scrapped EVs are set to be a significant source of second-life LiBs as the current EVs reach EoFL or are scrapped after being sold on as a used vehicle. Scrapage will also increase as owners upgrade to new, more efficient EVs with greater functionality and longer range, and as a result of the drive by the UK Government to replace new diesel and petrol cars by EVs in 2030. Thus, the International Renewable Energy Agency (IRENA) estimates that the 6 M EVs globally on the roads in 2019 must increase to 745 M by 2040 if the requirements of the Paris Climate Agreement are to be met [60].

In general, car scrappage, as well as driven by economic and legislative factors, is also a function of the total number of cars on the road (known as the “*parc*”) and the rate of new car sales. By taking such factors into account, Skeete and co-workers [39] estimate a stockpile of ca. 75,000 to 105,000 EoFL EV batteries in the UK by 2025. This should be considered in the light of the following:

1. Globally, ATFs are not yet ready to process such volumes of large LiBs primarily because the commercial imperative is not yet clear, the development of the necessary technology is still very much in its infancy and there is a plethora of cell form factors and pack topologies, all of which present their own challenges [6]. In addition, EVs that have been involved in road traffic accidents, or the batteries damaged require, c.a. 20 m exclusion zone at the present time which will place severe pressure on ATFs in terms of space⁷.
2. According to experts consulted as part of this study, there is currently only a very limited EV battery service, maintenance, and repair infrastructure in the UK, this

⁷ Professor Paul Christensen, Senior Advisor to the National Fire Chiefs Council and member of the Cross-government Technical Steering Group for EV Fire Safety, private communication, 8 March 2023.

is due to two factors: firstly, the current very low volumes of batteries requiring repair does not justify the cost of training, and second due to the extreme caution of OEMs to give access to the BMS data of EV battery packs. However, it does not seem unreasonable to expect this to grow.

3. The falling cost of new LiBs. Prices have fallen by ca. 90% since 2010, such that the average price for a new LiB across all markets was ca. \$137 per kWh in the first quarter of 2021 [58, 61], and EV OEMs predict price parity with diesel and petrol cars in 2024 [37]. As a result, the economic incentive for reuse and repurposing of LiBs is less attractive [61]: however, fluctuations in the price of, for example, lithium carbonate and Spodumene could have a major influence on this.
4. Leading research from McKinsey and Co. [62] suggests that there will be between 112 -227 GWh of second-life LiBs available per year by 2030, whereas the demand for industrial LiBESS is expected to be 183 GWh. Therefore, it could be that 60-100 % of the demand for industrial LiBESS could be satisfied by second-life EV LiBs [21, 63]. However, as the uptake of EVs increases it is predicted that global LiB demand could reach 2000 - 3900 GWh y⁻¹ by 2030 [62, 64, 65], with a comparable number of EV batteries, which make up the majority of these, reaching EoFL 8 - 10 years later. This may then exceed global industrial LiBESS demand with a total of 2850 GWh having been deployed by 2040 according to BloombergNEF forecasts [66].

On one hand the projected surplus of second-life batteries is good news for the DLiBESS industry. However, if the surplus 2nd life LiBs are not to be utilised, then the UK Waste Batteries and Accumulators Regulations 2009 [67] prohibits the disposal of EoL LiBs in landfill, and hence there will have to be significant innovation and investment in materials recovery if the consequences of illegal dumping of LiBs is to be avoided [68].

Experience of lead acid battery recycling dictates that recycling is driven by regulation. To this end, the EU Batteries Regulation (discussed in detail in Section 6.6.3) seeks to increase the recovery of key metals including lithium, nickel, and cobalt from scrapped LiBs. The current requirement is 50% by mass, and the draft regulation requires this to increase to 85%. In addition, LiB OEMs will be required to incorporate minimum levels of these recyclates into new LiBs. In the view of a major EV battery research

organisation, whilst likely to drive the much needed innovation, there is also the danger that it will drive materials recovery at the expense of second-life.

6.3.4. Factors determining the price of second-life LiBs

In the view of a major EV battery research organisation, the economics of second-life are on a knife-edge due, amongst other factors, to the fact that the disassembly, assessment & sorting of modules and packs is labour intensive and costly. This is caused by the lack of standardisation among EV OEMs, for example the use of glue and different cell form factors which prevents automation and requires manual disassembly: the latter can require 2 operatives and 8 – 16 hours per pack [69]. It has been predicted that there will be 250 new EV models from more than 15 EV OEMs by 2025 [21]. Currently, the cost of disassembling a pack to module level has been estimated as \$71/kWh with an additional \$16/kWh to disassemble to cell level, i.e. a total cost comparable to the price of new LiBs [21].

A second major factor is the relative price of new LiBs and, as stated in the previous section, this has fallen very significantly over recent years. Unfortunately, estimates of prices of second-life batteries are subject to very wide variation (for a review of this, see research from Haram et al. [70]): e.g. £32/kWh⁸ to £218/kWh [63, 71, 72]. It has been reported that using second-life LiBs in DLiBESS would become profitable at £32.3/kWh [73], but this has also been questioned as too optimistic [74] and it has been predicted that new LiBs become more profitable than second-life LiBs if the price of the latter rises from the break-even point of 60% of the cost of new batteries to 80% [75].

Overall, attempting to predict the future market for second-life LiBs, and hence for SLDLiBESS, is extremely challenging due to the lack of data and information: in addition, the market will be driven to a large extent by the pace of regulatory intervention which is extremely challenging to predict.

⁸ Rates: £1 = \$0.73 and €0.84.

6.4. Summary of the general hazards associated with LiBESS

While the inherent risks may be different for second-life compared with new LiBs, the type of hazards remain the same. This section therefore provides an overview of the general hazards associated with LiBESS to establish a baseline of understanding, before discussing the particular risks of second-life LiBs in Section 6.5.

6.4.1. Electric shock

Batteries cannot be shut down and hence accidental contact with both poles of a charged EV battery (ca. 300 – 600V [76]) can lead to electric shock or electrocution. If LiBESS are installed by accredited engineers, any such risks will be low. However, incorrectly installed systems (for example incorrectly gauged wiring) could result in failures leading to partial discharge or arcing, which are potential ignition sources.

6.4.2. Electrolyte spillage

The electrolyte in new lithium-ion cells contains a mixture of organic cyclic and linear carbonates, the LiPF_6 and up to 5% by volume additives. LiPF_6 is harmful if swallowed, toxic in contact with skin and causes severe skin burns and eye damage: in contrast, the organic carbonates comprising the solvent are generally regarded as having about the same toxicity as ethanol. The additives are commercial secrets but include some extremely toxic chemicals [77]. It is generally accepted that calendar and cycling ageing of LiBs leads to gas evolution (or so-called ‘gassing’), producing solids, liquids and gases [78]. There is insufficient analytical data in the public domain to make definitive statements of the products from gassing, but alkanes, alkenes, CO_2 , CO and HF have all been detected [79-83] as well as alkylfluorophosphates [84]: the latter posing a significant chemical hazard. Thus, contact with the electrolyte from a second-life battery could represent a greater hazard in terms of toxicity than from a new LiB. However, LiBs are sealed and therefore the chances of accidental skin contact with electrolyte from a SLDLiBESS must be considered to be slight and the associated risk low.

6.4.3. Thermal runaway

LiBs are the first batteries to employ an organic solvent in the electrolyte (typically a mixture of ethylene carbonate and other cyclic or linear organic carbonates [85]) rather than water, as the very high cell voltages available (currently up to 4.2V) would result in the electrolysis of an aqueous electrolyte and the production of hydrogen and oxygen. The combination of flammable organic electrolyte with high energy density (as with diesel or petrol) can lead to fire or even explosion if the energy is released in an uncontrolled manner, e.g. by abuse.

Lithium-ion cells are regarded as stable unless abused: such abuse is generally caused by heating, metal penetration, blunt trauma (crushing) or overcharging [86]. With respect to DLiBESS, the most likely abuse is heating (e.g. poor ventilation: this is believed to be one of the causes of the LiBESS fire in Flagstaff, Arizona in 2012 [87, 88]) or overcharging due to, for example, failure of the BMS. Additional factors compromising SLDLiBESS could be poor selection of cells or modules such that one or more cells have passed the “knee” in terms of ageing, after which ageing accelerates (see Section 6.3), cells with mismatched SoH and/or an inappropriate BMS (for example, in a DIY SLDLiBESS).

To demonstrate the potential impact of physical abuse, Figure 6.3 shows frames from a video taken from an experiment conducted by the Commonwealth Scientific and Industrial Research Organisation⁹ (CSIRO) in 2019 simulating the reversing of a vehicle with towbar into a DLiBESS at 100% SoC at 10 km h⁻¹. As can be seen from the figure, the penetration of the DLiBESS results initially in black “smoke” (see Figure 6.3(b), probably the release of toxic metal oxide nanoparticles from the cathode [89]) followed by the white vapour, Figure 6.3(c). There is a small glow in the lower right quadrant of Figure 6.3(c) that may be the ignition source for the subsequent explosion in figure 6.3(d), c.a. 20 seconds after impact.

⁹ CSIRO is an Australian Government agency responsible for scientific research. The test was conducted on 13 November 2019 using a 6.4kWh NMC battery. The test was intended to inform the AS 5139 standard “Electrical installations — Safety of battery systems for use with power conversion equipment”. The towbar was driven at 10 km/h.

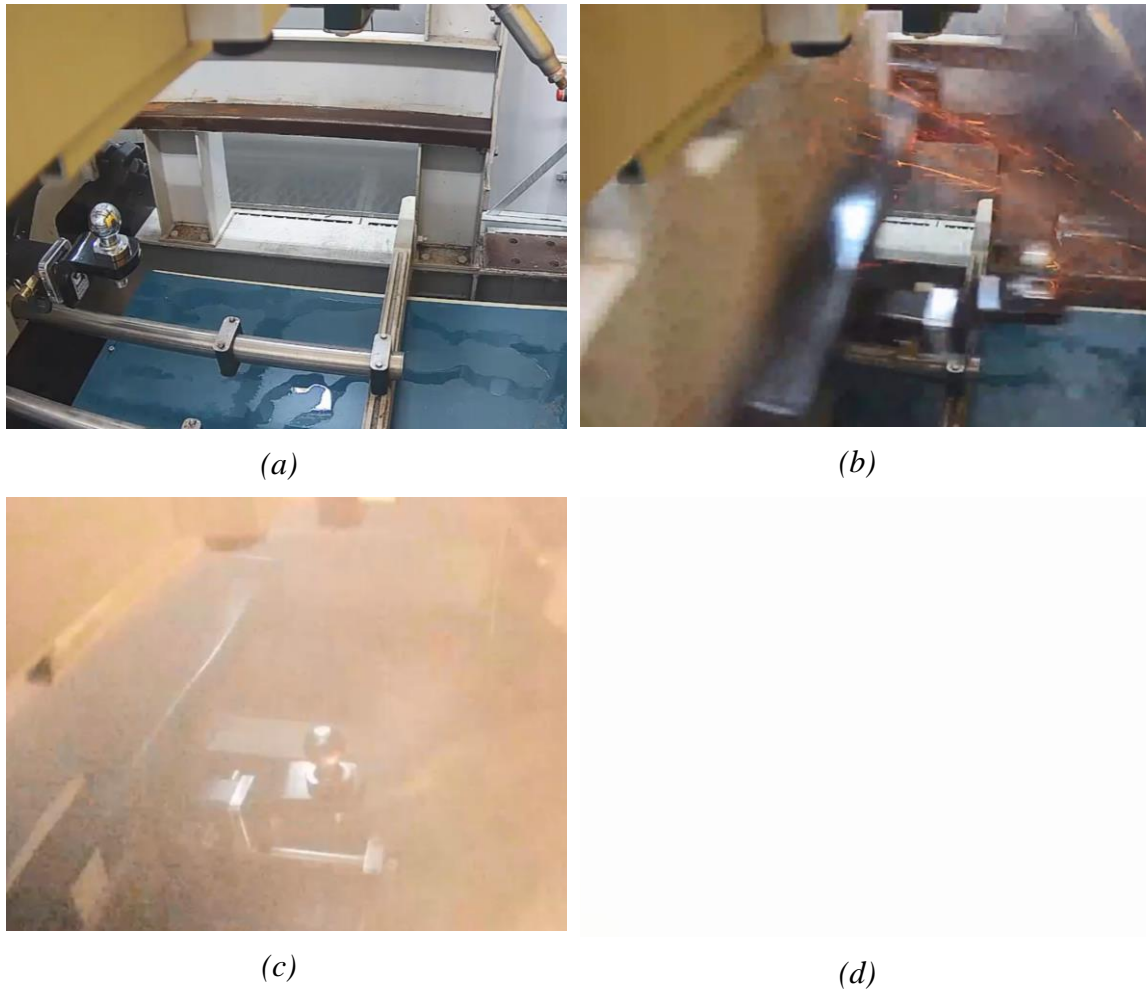


Figure 6.3. Frames from an experiment by CSIRO simulating a vehicle reversing with a towbar into a DLiBESS at 10 kmh-1. (a) before impact; (b) a few seconds after the moment of impact, (c) 13 s after impact, and (d) vapour cloud explosion.

Spontaneous ignition of LiBs can also occur, as seen with electric vehicles [90], the cause of which is uncertain [86], and is generally postulated as due to defects or contamination introduced during manufacturing [78, 91]. The probability of these defects occurring is often given as 1 in a million to 1 in 40 million [79-81] nevertheless, such defects were responsible for a general UK recall of LG Energy Solutions residential units manufactured between April 2017 and September 2019 in May 2021: this followed similar recalls in Australia in March 2021 and the USA. The recalls followed reports of the units overheating which was ascribed to problems with the electrode manufacturing process by the company [92].

Thus: (1) even the most highly experienced manufacturers may inadvertently allow defective cells to be placed on the market and (2) there is much uncertainty around the statistics.

In broad terms, thermal runaway can be described as uncontrolled positive feedback. However, the precise definition of thermal runaway remains a matter for discussion: thus, some authors define it as the point at which a fixed rate of temperature increase is surpassed, e.g. $1\text{ }^{\circ}\text{C min}^{-1}$ [93] or $10\text{ }^{\circ}\text{C s}^{-1}$ [94], whereas a more accurate (but less easy to measure) definition is that of a self-sustaining heating process, i.e. once the temperature of a cell passes a point of no return, the exothermic reactions continue to generate heat and the cell will progress inevitably to an exponential increase in temperature [95].

The events leading up to and including thermal runaway are also still a matter for research. Taking abuse by heating as a starting point: the first stage is generally accepted to be the breakdown of the Solid Electrolyte Interface or SEI, a protective layer that forms on the graphite anode particles during the first charge. This layer prevents further contact between the anode and solvent but allows free passage of lithium ions. The breakdown of the SEI is stated as commencing around $90\text{ }^{\circ}\text{C}$ [78, 89, 96] or as low as c.a. $60\text{ }^{\circ}\text{C}$ [97]. The onset is dependent on the degree of lithiation of the anode: this process is exothermic and has been associated with the onset of self-heating [98]. The breakdown of the SEI results in the production of small chain alkanes, CO_2 and oxygen [78]. In general, it is accepted that the SEI can self-heal up to ca., $80 - 120\text{ }^{\circ}\text{C}$ [91, 97] forming a “secondary SEI” [96] that is less compact than the initially-formed layer and hence may allow exothermic reactions with the organic solvent of the electrolyte, again generating small chain alkanes, heat, and CO. In addition, hydrogen gas is produced from the reduction of the binders employed in the anode (e.g. polyvinylidene fluoride or polyvinylidene difluoride, PVDF [78]).

Between ca. $120\text{ }^{\circ}\text{C}$ and $240\text{ }^{\circ}\text{C}$ internal short circuit and the accompanying catastrophic release of heat can take place depending upon the composition of the separator. Typical separators are made of polyethylene, polypropylene or a mixture of polymers, the latter may be coated with a ceramic layer. Thus, the melting point of polyethylene is 130°C , polypropylene 170°C , and ceramic-coated polymer/mixed polymer separators c.a. 200°C [78, 91]. The collapse of the separator was previously believed to be the trigger for thermal runaway: however, at temperatures above 150°C exothermic collapse of the cathode structure takes place to generate oxygen and, in some cases, highly oxidising oxides: the onset temperature of this process depends upon composition, e.g. from 150°C for NMC cathodes to c.a. 310°C for LFP [89, 91, 94] cathodes. The oxygen produced can cross over to the anode where it is consumed in a highly exothermic reaction, sufficiently

exothermic to initiate thermal runaway at temperatures significantly less than that needed for separator collapse [98]. LiBs having LFP cathodes are generally considered to be more stable due to the higher onset temperature for the collapse of the cathode structure [80]: however, this may simply delay ignition and hence facilitate explosion. With respect to this, it is worth noting that the explosions of the LiBESS in Brisbane [99] and Beijing [100] both employed LFP cells.

As the temperature of a cell rises, the solvents comprising the electrolyte will vaporise, e.g. the boiling point of dimethyl carbonate (DMC) is 91 °C and that of ethylene carbonate (EC) is 248 °C [101], and eventually vent as a result of burst caps activating (in cylindrical and prismatic cells) or a pouch cell rupturing. It is not unreasonable to assume that such an event would terminate thermal runaway [102]: however, Feng and co-workers [91, 97, 103] have shown that lithiated graphite and NMC cathode powders undergo direct, solid-state electrochemical reaction at temperatures \geq c.a. 250 °C that is highly exothermic and generates sufficient heat to raise the temperature of the cell up to 800 °C and perpetuate thermal runaway.

The mechanism of thermal runaway initiated by overcharge involves the same stages as described above but commences with the over-lithiation of the graphite anode, causing lithium metal to deposit on the surface [104]. The accompanying over-delithiation of the cathode and the collapse of its structure increases the cell resistance and causes Joule heating. The metallic lithium reacts exothermically with the solvent in essentially the same way as the lithiated graphite anode and can form dendrites that grow through the separator [105, 106] to the cathode and cause an internal short circuit with attendant and very significant Joule heating. However, it has been suggested that most dendrites will melt due to the very high current density being passed and the attendant Joule heating [107].

The exothermic reactions following abuse generate a mixture of gases that includes on venting: H₂ (up to 45 % [108]), SO₂, NO₂, HF, HCl, HCN, CO, CO₂, droplets of organic solvent and a range of small chain alkanes and alkenes, in other words, a vapour cloud. It appears that, in very general terms, the composition of this vapour cloud does not vary with chemistry, form factor or manufacturer [104]. The vapour has been routinely confused with smoke [81, 109], but is actually the pre-ignition phase: there is insufficient oxygen inside cells undergoing exothermic reactions to sustain ignition [91], but the vapour may ignite immediately on venting, in which flare-like flames can be produced. If

the vapour does not ignite immediately, due to low SoC or insufficient oxygen, then a vapour cloud explosion could result ([86] and references therein). The hazardous chemicals alkylfluorophosphates have also been detected, but such studies are limited and the implications of the emission of these species yet to be researched in detail [110]. Further details on the toxic gases released can be found in BEIS “Domestic battery energy storage systems: a review of safety risks” [1].

Once a cell has passed the point of no return, it is critical to prevent this cascading to adjacent cells which can be challenging. However, codes and standards require design for safety, which includes preventing propagation, see Section 6.10.

The first confirmed vapour cloud explosion caused by LiBs in thermal runaway occurred on 19 April 2019 and involved the McMicken 2 MWh LiBESS in Surprise, Arizona, see Appendix 6.1 for a case study. Thermal runaway was apparently triggered in two cells in a module in one of the racks by an electrical arc and propagated to all the remaining modules in the rack. The modules went into thermal runaway without ignition and produced copious amounts of white vapour. One of the reports on the incident, quoting a fire officer who was first on the scene, draws attention to the production of a heavier-than-air white cloud. The DNV GL report quotes its expert as stating that “the composition of gases is constant across all form factors, chemistries and manufacturers” [105] – an extremely important statement if correct. The literature is certainly full of reports of white vapour or “smoke” being produced from cells with a range of chemistries as a result of thermal runaway. Research conducted by Newcastle University as part of the ReLiB project [111] and the literature has shown that if LiBs are abused at $\leq 50\%$ SoC the white vapour does not necessarily ignite [112]. As stated in Section 6.7.3, in addition to HF, HCl, HCN, hydrocarbon gases, CO, H₂ [78, 105, 113] it is well-established that the vapour also contains droplets of the organic carbonates employed in the cell electrolyte [78]. Figure 6.4(a) – (f) show frames from a video taken during one of the Newcastle University joint ReLiB [111] and SafeBatt [114] experiments at the DNV site at RAF Spadeadam in April 2021 in which a single 1.67 kWh EV module was penetrated by a nail at 40% SoC. As was observed in previous experiments involving nail penetration at SoC $\leq 50\%$ [86] a dense, white vapour was produced: in fact two types of vapour can clearly be seen, one buoyant and one heavier than air, red arrowed in Figure 6.4(d) and clearly visible as a layer on the floor in (e): it is not clear what determines the relative amounts of these gases, but it may be a function of the cathode chemistry and the

temperature of the cell or module. HF concentrations up to 120 ppm and hydrogen & CO concentrations up to 2000 ppm were recorded in the container. The lower explosion limit for the white vapour is c.a. 6 – 12 % [108].

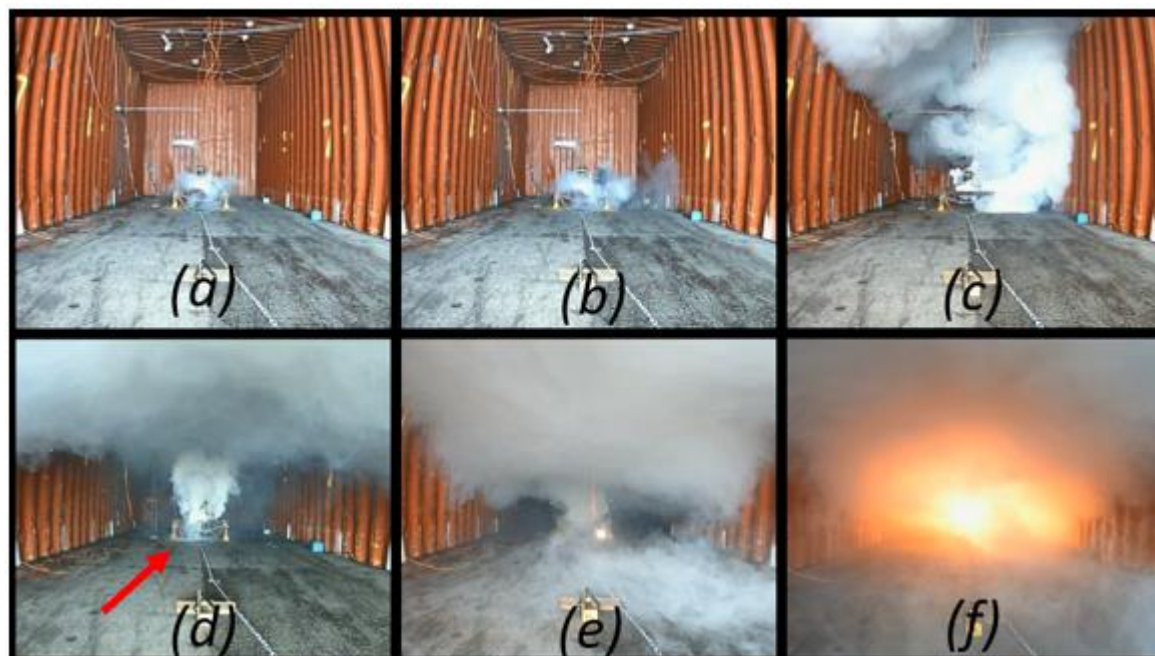


Figure 6.4. Frames from the video taken during one of the Newcastle University joint ReLiB and SafeBatt [114] experiments at the DNV site at RAF Spadeadam in April 2021.

A single 1.67 kWh EV module was penetrated by a nail at 40% SoC. Figure 6.4(a) Nail penetration, (b) less than one second later pouch cell(s) burst ejecting black cathode particles, (c) 17 s after penetration, (d) 56 s and (e) 79 s after penetration and evolution of second, heavier than air vapour, and (f) 87 s after penetration and module self-ignites, consuming vapour cloud and drawing it back. The experiment was conducted in a standard 76.8 m³ sea container.

It should be noted that the experiment depicted in Figure 6.4 was part of a project aimed at researching the relative effects of immediate vs delayed ignition of the white vapour cloud, as well as facilitating the education and training of first responders. Hence the module employed was not protected by a BMS and it was subjected to abuse significantly above industry norms in order to ensure that the cells were driven into thermal runaway.

The module in Figure 6.4(a) - (f) contained 8 x 56.3Ah NMC pouch cells: the 14 LG Chem modules in the McMicken LiBESS that first went into thermal runaway each contained 28 x 64 Ah pouch cells, a 55-fold difference. Further, the contention of the DNV GL report [105] is that the release of the Novac 1230 suppressant prevented ignition

of the gases produced by the cells in thermal runaway by displacing air from the container, and so allowed the gases to build up to dangerous levels.

The cells in the McMicken LiBESS were initially all at > 90% SoC but the vapour did not ignite due to the displacement of the air from the container by the suppressant [105].

Hence if LiBs of any cathode chemistry, form factor or manufacturer are abused at a low SoC and/or the concentration of oxygen is reduced below that necessary for ignition in some way (irrespective of the form of abuse), the toxic white vapour so produced can build up and hence there could be a possibility of a flash fire, fire balls developing, or in extreme cases even a vapour cloud explosion [86]. This explosion hazard, along with the toxicity of the white vapour, could be faced by the occupiers and first responders called to a fire in a home containing a DLiBESS or SLDLiBESS.

6.5. The risks and hazards specific to second-life LiBs

The thermal stability of LiBs is generally assessed on the basis of: the onset temperatures for exothermic reaction, self-heating and thermal runaway, as well as the time taken to reach thermal runaway, maximum temperature and the activation energy for thermal runaway [115-119].

The hazards associated with second-life LiBs are broadly the same as for new LiBs, i.e. toxic gas [1], fire and explosion. However, the literature on the effect of ageing on the thermal stability of LiBs is limited and largely focussed at the cell level. Most such papers concern 18650 cells, presumably for reasons of cost: studies on larger cells or modules are rare and studies on the ageing of cells from actual EV packs extremely so, see for example [120-122]. Given that heat is dissipated through the surfaces of a LiB, but is generated throughout its volume, the extrapolation of data obtained from cells to predict the thermal behaviour of modules or EV battery packs should be considered with caution. In addition, the response of cells to abuse is highly dependent upon the conditions [102] and hence the same cells in different test facilities may vary in their responses. Finally, the definition of thermal runaway in terms of a measurable temperature rise is highly subjective [86]. As a result of all such factors, it is currently challenging to predict the impact of ageing on the thermal stability of EV battery packs, or the intensity or magnitude of the fires and explosions arising from thermal runaway. To do so will require a significant body of further work including studies on the effect of

cycling as a function of temperature, cell form factor, chemistry, and capacity as well as calendar ageing¹⁰ as a function of these parameters and SoC, on the thermal stability of cells, modules, and packs.

The following sections are an assessment of the literature to date which often highlights the need for further understanding of the long-term performance of second-life LiBs.

6.5.1 The effect of ageing and unknown stress and/or abuse

It is generally accepted that the capacity loss with use (cycling) in first life in an EV is essentially linear, although the rate of ageing has been shown to depend upon cell chemistry: for example, LFP cells degrade slowly even up to 50 % SoH [83] whereas NMC cells deteriorate rapidly after 70-80 % SoH [123]. At some point, however, there is a change in and/or an additional ageing mechanism which leads to an increased ageing rate. The time at which this occurs is referred to as the “knee”, the battery has reached its final end-of-life [83, 124] (see Figure 6.5) and should be immediately retired from operation for safety reasons.

Lithium-ion cells may pass the knee during their first life: if NMC cells do so, there is no slowdown in ageing, even in less demanding applications [83, 124]. Under normal circumstances the final EoL is taken as 50 – 60 % SoH [54], after which severe and potentially dangerous deterioration is expected to occur; however, there is an indication that even at 70 % SoH, serious structural damage may have already occurred on the cathode that can lead to accelerated ageing [117, 125].

¹⁰ Calendar ageing simply refers to the changes in the cells of a LiB when in the charged but passive state, i.e. not charging or discharging.

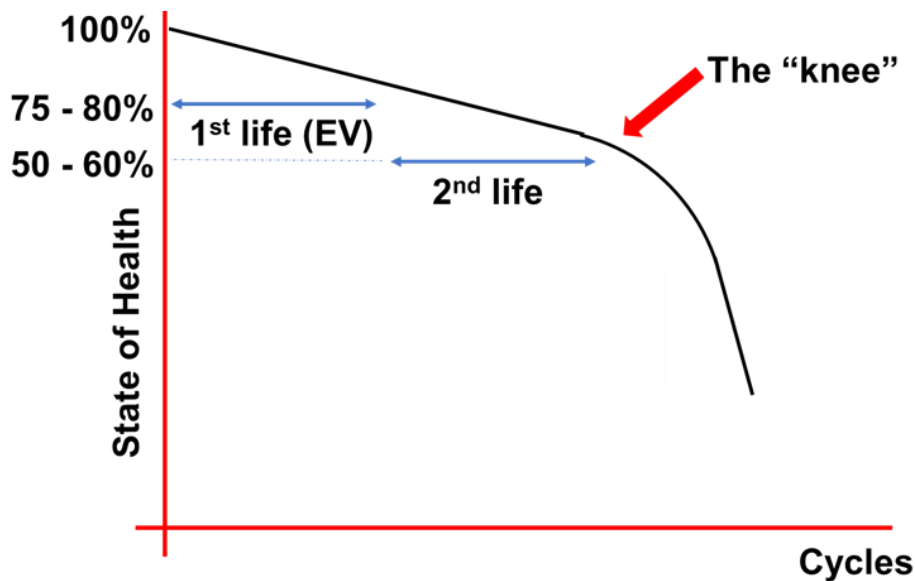


Figure 6.5. Representation of the “knee”: the time at which ageing accelerates and lithium-ion batteries reach final EoL

While it is generally considered difficult to predict the point at which the knee occurs, recent developments mean that it may be possible and has been achieved using capacity degradation and machine learning [126], and capacity fade data along with nonlinear autoregressive network modelling [127], albeit these methods are not currently chemistry agnostic.

Research shows that second-life LiBs will also have greater cell-to-cell variability than new batteries and that this will increase with ageing. Additionally, the SoH of modules recovered from EV battery packs may vary according to location in the pack (see Figure 6.8 below) [120], and this can result in accelerated ageing [83, 117, 125].

It is generally accepted that calendar ageing and cycling under the conditions and between the potential limits set by the manufacturer, simply reduces the lithium inventory in cells as a result of the reduction of electrolyte, thickening of the SEI and attendant trapping and isolation of lithium cations in the SEI [120]. This does not reduce the thermal stability of the LiB [89][96] and may even improve stability slightly, as the lithium cations are then unable to participate in the reduction of the solvent at the lithiated anode particles when the SEI breaks down [97][118].

However, calendar ageing and the normal operation of an EV pack within the limits specified by the manufacturer could also decrease stability. During ageing, other structural changes take place which affect the degradation process. With a decrease of SoH, there is higher inhomogeneity of lithium in the anode and a reduction of the

graphitization of the anode. This leads to the fragmentation of the anode which can lead to increasing resistance and Joule heating. The cathode itself does not change much during benign ageing, however the mixed metal oxide gradually spalls and may finally fall off [128]. Therefore, it is believed the greatest impact on battery safety is by the anode. There is also a decrease in the separator pores that increases the internal resistance [129, 130]. Additionally, dry spots in cells, where the electrolyte has been consumed during use, can result in Joule heating [93].

In contrast, any process that removes lithium inventory as lithium metal, such as cycling at low temperatures or high C-rates, can have a marked and detrimental effect upon thermal stability [96][115][118][121][128]. In these scenarios, the lithium metal reacts exothermically with the electrolyte producing gaseous products and the deposition of solids from the electrolyte on the anode takes place, as well as the precipitation of solvent fragments in the electrolyte which could block the pores of the separator [129].

As a result of these processes, there is an increase in internal resistance and the formation of non-electrochemically active lithium dendrites: these thin tendrils of lithium metal are formed when significant lithium metal plating occurs [125][130]. The dendrites reduce the temperature of the self-sustaining exothermic processes (from 80 °C to about 50 °C) and the temperature of thermal runaway from 170 °C to about 100 °C. Therefore, there is a much shorter time needed for the battery to reach thermal runaway [89][125] and the lithium metal dendrites can penetrate the separator and cause catastrophic internal short circuit. Currently, methods to detect lithium metal plating in first life are still at the experimental stage [106].

Lithium metal plating occurs during charging when the flux of lithium ions to the anode is, for any reason, insufficient to match the charging current, and those lithium ions at the anode are then reduced to the metal. A number of factors can cause lithium metal plating: the low solvent viscosity and low ion diffusion coefficients at low temperatures will demand low charging C-rates, and even at ambient temperatures, high charging currents can cause plating if the flux of lithium ions is insufficient.

A natural extension of this theory concerns operation under normal conditions: thus, normal operation under the conditions specified by the LiB manufacturer continually removes the lithium inventory as benign lithium ions. However, at some point, it is not unreasonable to postulate that the concentration of the remaining lithium ions in the

electrolyte will be insufficient to provide sufficient ion flux during charging even under normal C-rates, and lithium metal plating will occur. It could be that this is the point at which the knee occurs, though further research is needed to support this theory.

Thus, in their study of Nissan Leaf modules taken out of the vehicle at EoFL at 62.8 – 71.2 % SoH and prior to the knee, Braco and co-workers [122] employed accelerated ageing on 6 modules within the potential limits specified by Nissan, which caused 5 of the 6 modules to pass the knee. The accelerated ageing associated with the knee as specifically attributed to lithium metal plating by the authors.

A simple example can highlight the extremes of ageing of LiBs that are likely to be seen in practice during first life: private EVs will be charged at most once per day and probably at low C-rates overnight, whilst taxis are charged far more often, and generally using fast charging, both of which may accelerate ageing, the possibility of lithium metal plating and hence thermal instability [128].

Additionally, battery packs may have suffered physical abuse during first life (e. g. via a road traffic collision) and/or disassembly, and this can result in cells being crushed or coolant leakage (larger energy density EV packs in particular require active cooling, usually using liquid cooling loops [131]), either of which can lead to thermal runaway and fire [121].

However, there is a need for more research to gain a clearer understanding of the effect of ageing on thermal stability, particularly with respect to cell chemistry. This is highlighted in the study by Wang and co-workers [121] who tested both new and aged batteries. To begin with, they cycled 14 Ah LFP pouch cells after calendar ageing for 10 years (SoH at start of tests 84%). The cells were cycled at -10, 0 and 25 °C: capacity loss, lithium metal plating and dendrite formation were observed in the cells cycled at -10°C and at C-rates ≥ 0.2 . In contrast, fresh 19 Ah LFP pouch cells from the same manufacturer showed little or no capacity loss after cycling at 1C and 25 °C for 10 weeks, followed by 50 weeks cycling at 1C at -10 °C then 10 weeks cycling at 25 °C again. The SoH dropped to 70 % after the cycling at -10C, but recovered to 98 % after the second cycling at 25 °C. This indicates that the age of the cell can also have an impact on the effect of low temperatures and draws attention to the complexity of the ageing phenomenon.

Extensive discussions with stakeholders have revealed two opposing views on second-life batteries: firstly, that a safety framework can be put in place to allow the use of second-

life LiBs in DLiBESS, so long as the full history of the batteries in their first life applications is known and/or they can be tested effectively. Discussions with INERIS representatives reinforced the critical nature of first life information in second-life applications, a point made very clearly in a recent report from the organisation [36].

The second, more radical, view shared by some respondents is simply that the safety of such cells can never be guaranteed, and hence that second-life LiBs should not be employed under any circumstances in DLiBESS.

6.5.2. Consumers purchasing or building their own SLDiBESS

Cells, modules, and battery packs are freely available from, for example, online sites (see Appendix 6.3). The source of second-life modules is most likely to be EV battery packs, but it is unlikely that a typical home will require a full EV battery pack, see Section 6.8.6. Hence consumers building DIY SLDLiBESS are likely to buy cells and/or modules directly, or packs which they can disassemble, online or directly from e.g. ATFs. Where this is the case, it raises concerns over the potential lack of skills, knowledge, and training of consumers if they are to avoid electrocution, arc flash explosion (the disassembly of EV packs is complicated and hazardous), thermal runaway (and hence toxic gas release, fire and/or explosions inside the domestic environment) or chemical hazards when handling EV batteries and being exposed to the electrolyte. In addition, any information consumers may have acquired is likely to have come from hobbyists (such as social media groups) comprised of people who may lack knowledge of LiB technology¹¹ [132] and the associated risks and hazards. A knowledge of system-level safety is key here and highlighted by e.g. the industrial scale LiBESS incidents in South Korea, many of which were due to system-level failures [133].

The issue of variability of second-life LiBs is addressed in Section 6.8.1, and it is not clear if consumers will know the importance of matching SoH. If there is variability in SoH across the modules and cells of a SLDLiBESS, cell balancing would be critical to avoid overcharge [134], or overdischarge: hence the design and operation of the BMS of such packs would also be safety-critical. A key question would then be, if the BMS was supplied with the pack, was it repurposed by competent personnel? If the BMS was built

¹¹ As a simple example, a common misconception is that a lithium ion battery discharges to 0V: in fact, the cell voltage should not be taken below c.a. 2.4V (so even a discharged battery still retains considerable electrical energy) to avoid overdischarge and the attendant copper dissolution and re-deposition.

by the homeowner, would they have the appropriate knowledge and expertise to ensure the BMS is fit-for-purpose? For example, the explosion of the McMicken LiBESS in Surprise (see Appendix 6.1) clearly showed the importance of cell-level rather than module or stack-level monitoring. It is also not clear if consumers will realise the necessity for maintenance or have the necessary knowledge to effect it if they do.

Finally, modules and packs acquired by consumers may be damaged, at SoH < 50 % and/or have lithium metal plating and hence have a greater potential for failure. Thus, in February 2021, a mid-terraced house in Western Avenue in Acton [135] was badly damaged by fire caused by the failure of LiBs being charged for two electric bicycles: the bicycles had been converted using kits sourced from the internet. The Western Avenue fire was the second such major fire involving LiBs in London within 3 months. This shows the inherent risks of the public purchasing lithium-ion cells or modules from less reputable vendors and assembling energy storage devices from them¹².

6.6. Gateway testing of second-life LiBs

6.6.1. State of health, state of safety and remaining useful life

Gateway testing is employed for two reasons: (1) to assess if a pack or modules are suitable for reuse, remanufacture or repurposing in terms of the requirements of the 2nd life application, i.e. to assess Remainder-of-Useful-Life (RUL) and (2) to assess if the pack or its modules are safe for 2nd life application, i.e. to assess State-of-Safety (SoS).

Gateway testing initially involves (see Figure 6.6) visual inspection of the pack and modules for damage such as dents or perforations, leakage of coolant (if employed) or electrolyte: such defects render the pack suitable only for recycling. Assessing RUL can be achieved through access to the first life data stored in the EV BMS providing it is sufficiently comprehensive and there is a strong link to the EV OEM. The BMS data are also regarded as essential with respect to ascertaining SoS, e.g. to determine the number of times overcharged & overdischarged or operated at extremes of temperature [21]. However, as pointed out in Zhu et al [21], the ability to accurately determine the RUL based on the historical information will depend on the role of the company that is responsible for repurposing. For example, LiB manufacturers are likely to have more

¹² Such fires are an increasing problem, see <https://www.london-fire.gov.uk/news/2021-news/july/fire-investigators-issue-urgent-warning-over-fires-involving-e-bike-batteries/>; <https://www.nyl.com/nyc/all-boroughs/news/2021/12/18/fire-officials-say-e-bike-battery-caused-deadly-fire-in-east-village>

information on the degradation of their LiBs to base an assessment on compared to third-party repurposers, which is why a relationship with the EV OEM is desirable.

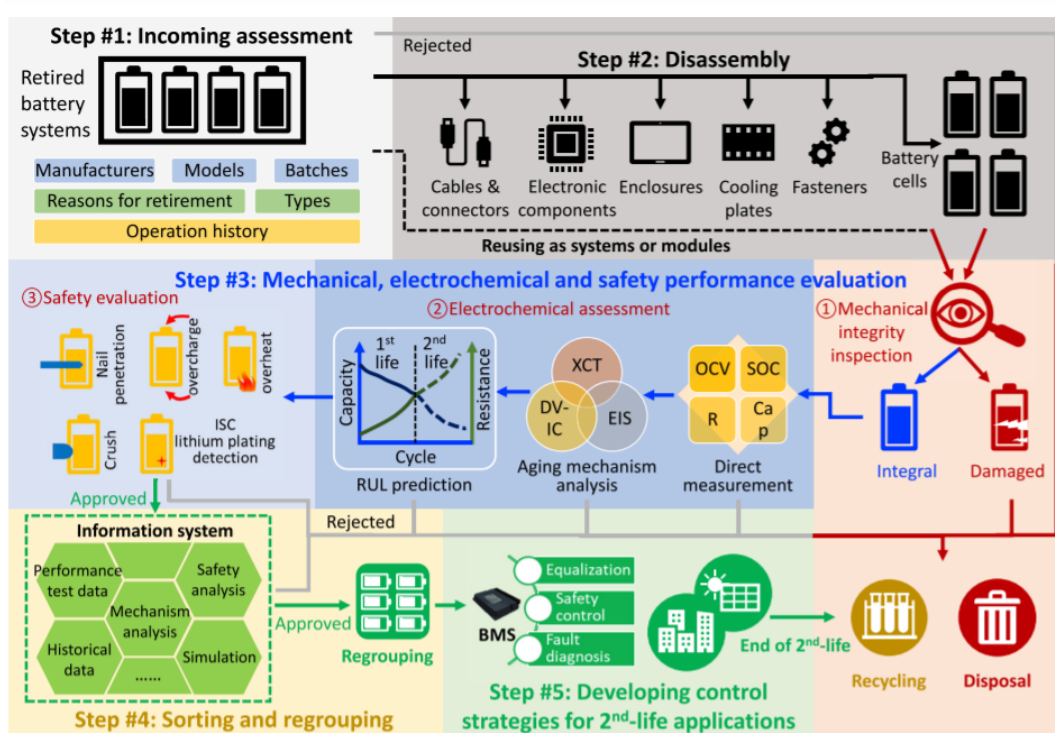


Figure 6.6. Schematic illustrating the gateway assessment of 2nd life lithium-ion batteries. From [21].

As part of assessing RUL, the SoH is also generally determined: as was stated in Section 1.4.2, the most common definition of SoH is the ratio of the current maximum capacity of a cell, module or battery, Q_C , to the maximum capacity when new, at BoL, Q_{BoL} , expressed as a percentage (see Figure 1.12):

$$\text{SoH} = (Q_C/Q_{BoL}) \times 100\% \quad (1)$$

The SoC of a new cell is determined from a calibration curve of cell voltage vs charge (known as capacity, in Ah): this is produced by detailed testing and only valid as a result of rigorous quality control producing cells with extremely tight specifications. The determination of the SoH of a cell once it has been used is extremely challenging [136] as the charge corresponding to 100% SoC cannot be determined.

An alternative numeric definition is in terms of the internal resistance, or impedance which can be measured for both new and used cells. In alternating current (AC) theory, the impedance, Z , is given by Ohm's Law:

$$Z = V/I \quad (2)$$

Where V is the voltage and I the current. The resistance R is the specific case of (2) when applying a direct current (DC):

$$R = V/I \quad (3)$$

The internal resistance or impedance of a cell is that of all the components of the cell, current collectors, electrodes, separator, electrolyte, and wires. When measured by DC techniques it is the internal resistance and when measured by AC techniques it should be referred to as the internal impedance, but resistance is the term most usually employed. Increasing internal resistance causes power fade and eventual EoFL [137, 138].

A typical technique employed to measure internal resistance, along with other critical parameters, is Electrochemical Impedance Spectroscopy (EIS) [139]. This involves applying a sinusoidal voltage perturbation (with a fixed max amplitude of 3 – 10 mV) between the anode and cathode of a cell. The equipment then measures the current response in terms of the time-dependence of the magnitude of the current and its phase shift as a function of the frequency of the imposed signal. The cell is modelled as an assembly of electrical components, known as the equivalent circuit approach, e.g. resistors (the internal resistance and the resistance to charge transfer at the interfaces), capacitors (representing the electrode/electrolyte interfaces or “double layers”), constant phase elements (“leaky capacitors”) and inductances (the wires). By varying the parameters of the components in an iterative manner, the actual EIS response of the cell is compared and finally matched to that produced by the equivalent circuit model, and values for the various cell components extracted. The method relies on the testing of a significant number of modules at a number of temperatures and SoC. The data so obtained is then employed to create a look-up database to inform the formulation of the equivalent circuit model [140]. This is specific to the cell under test: the procedure has to be repeated for each cell type.

SoH is then defined in terms of the current internal resistance R_{IRC} and the resistance at BoL, R_{IRBoL} :

$$SoH = (1 - [R_{IRC}/R_{IRBoL}]) \times 100\% \quad (4)$$

One DC approach to measure internal resistance is the current off method in which the cell is charged, and the current supply switched off: the ratio of the drops in voltage and current are then employed to determine the resistance via Ohms Law (3). Similarly, the current switching method measures the ratio of the changes in current and voltage when switching from charge to discharge.

Additional tests include measurement of the open circuit voltage and battery capacity, the latter typically via cycling between charge and discharge.

With respect to the State of Safety (SoS) of a LiB there are no clear definitions, one problem is that there are currently no generally accepted tests to measure SoS (making it hard to quantify), as will be discussed in Section 6.6.2. In addition, there are currently no UK codes, standards or regulations relating to the safety and fitness-for-purpose of second-life lithium-ion modules or packs to be employed in SLDLiBESS, but this situation will change with the introduction, and adoption by the UK, of the IEC standards currently being drafted (see Section 6.8.2).

Future developments and the state of the art for gateway testing are discussed further in the paper by Zhu et al [21] which reviews promising developments such as automatic battery disassembly and inspection, non-destructive testing using acoustic waves and data-driven machine learning approaches.

6.6.2. Examples of gateway testing

In general, companies employing second-life LiBs were understandably reluctant to disclose the gateway testing methods they employ to assess the safety and SoH of modules and packs, but praiseworthy exceptions were a recycling company (EVRC) and the UK Energy Storage Laboratory (UKESL) project [141, 142]. Visual inspection is invariably the first check to assess any physical abuse and hence possible crushing of cells, coolant, or electrolyte leakage, as well as corrosion (and hence water penetration).

Case study: EVRC approach to gateway testing

EVRC takes EoFL EV packs and remanufactures LiBESS from them for use in a variety of applications from construction to marine but excluding SLDLiBESS. The testing the company employs is noteworthy as it is fairly extensive:

- A Safe System of Work is created.
- The EV pack is disassembled.
- The modules are inspected visually for obvious signs of damage.

- A series of current/voltage tests are performed followed by internal measurements of module resistances, using DC methodology, and the determination of SoH using power and capacitance measurements.
- Insulation and isolation of the modules are then assessed.
- If necessary, pressure tests are also carried out.
- The BMS is replaced by an application-appropriate system as, in the company's view, retaining or revising the original BMS could be dangerous.

The company offers this testing to customers and selected outside organisations.

Case study: UKESL approach to gateway testing

The aim of the UKESL project was to investigate the value and commercialisation of Nissan Leaf EV batteries for the stationary and portable (“roaming”) electricity storage markets but did not include domestic storage. The project produced workflows that NMUK could follow and train shop floor people to do which consisted of a series of pass/fail gateway tests, which included visual checks for corrosion and damage, pressure tests and a BMS test. The project facilitated the repurposing of the Leaf packs into a commercial operation.

A pack is assessed as grade 1 if it passes all these gateway tests and is then reused directly in an industrial scale LiBESS. If the pack fails any tests, it is opened and examined to see whether it can easily be repaired. If so, it is retested and classed as grade 1. If the pack still fails, it is disassembled, and the modules graded using EIS. The process and associated algorithms have been patented. This includes assessing parameters such as charge transfer resistance and internal resistance to check against look-up data to assess if there are any electrochemical or electrical problems with the module, within 3 minutes. If the module fails the EIS tests, it is sent for materials recovery, although such failures have been minimal. Passed modules are sent to the battery remanufacturer, and NMUK pass on the required information on the modules along with producer responsibility. The respondent, representing a major EV battery research organisation, stated that Extended Producer Responsibility is in urgent need of clarification, and it should move with the second-life cells/modules/packs from the EV OEM to the remanufacturer: further there needs to be flexibility and clarity over who carries what level of liability and when.

The same respondent replied to concerns that type tests are not valid for second-life cells, modules, and packs: in their view, this critically depends upon how product safety and standards are set, and it is largely down to the remanufacturer/repurposer to ensure that the second-life batteries are safe, not just using tests, but also through rigorous control of the remanufacturing/repurposing process and system design. The risk of failure should be minimised, and containment should be in place to prevent thermal runaway propagating, and it should be possible to warrant safety based on this design-for-failure concept. Overall, it would be a mistake to be too prescriptive as this would give a false sense of security and seriously restrict the flow of second-life material into a potentially important market, the technical feasibility of which has been thoroughly proven with respect to the Nissan modules and packs which have 5 – 10 years of useful life in their second-life applications and many satisfied customers. An EV OEM also expressed strong faith in the safety and durability of its second-life batteries, based on a significant body of statistical data on 1st and second-life failure rates and its customer satisfaction.

6.7. Analysis of mitigating measures for LiBs and DLiBESS

It should be stated that apart from the gateway testing discussed in Section 6.6, there is currently limited information available on best practice in design for mitigating risks specific to second-life LiBs and DLiBESS. Therefore, this section builds on mitigating measures from [1] and, where possible, their relevance to second life LiBs and LiBESS.

There are four key categories of safety systems in new LiBs: the Solid Electrolyte Interface, the Battery Management System, physical safety systems and chemical additives, see Figure 6.7. These are described below alongside safety systems external to the DLiBESS and installation and maintenance, which should also be considered for domestic BESS. The previous BEIS report [1] presents a detailed discussion of the system-level safety strategies by DLiBESS manufacturers including measures to prevent thermal propagation between cells and control of temperature during normal operation and is therefore not discussed further in this report.

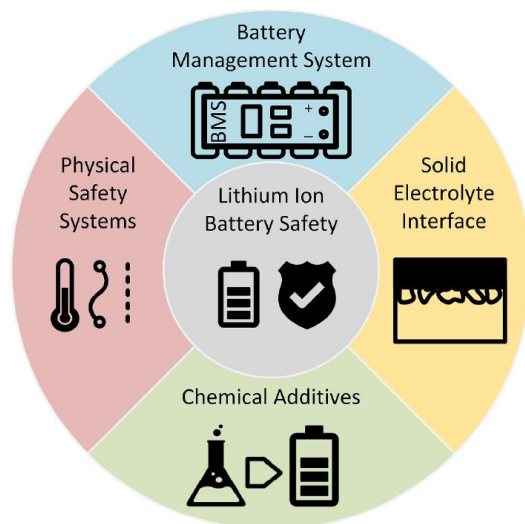


Figure 6.7. Safety systems in LiBs [68].

6.7.1. Safety systems at cell level

The SEI is the first safety “system” and is internal to the cell. When fully charged LiBs should be inherently unstable, as the graphite anodes have essentially the same potential as metallic lithium and hence should immediately and exothermically reduce the organic carbonates employed in the electrolyte [143] and continue to do so. The reason that this process stops is the formation of the SEI during the first charge. Thermal runaway is generally initiated when this protective barrier is damaged in some way. In the manufacturing process, LiB cells are usually held at low states of charge (SoC) for long periods of time during the cell manufacture to ensure complete SEI formation.

The physical and chemical safety systems employed at cell level in LiBs are designed to cut one of the two circuits in a battery: the internal ionic circuit (movement of lithium-ions) and the external, electronic circuit (movement of electrons). Physical safety systems include: safety vents, thermal fuses such as temperature cut-off (TCO) circuitry (e.g. protection circuit modules, PCM’s) which form part of the BMS, positive temperature coefficient (PTC) thermistors and shutdown separators [16]. As the temperature approaches the melting point of a shutdown separator, the pores close and become blocked, preventing the movement of lithium-ions, and hence shutting down the electrochemical processes in the cell.

Blast caps are typically manufactured from aluminium-ferrum alloy which has a weakened area defined by engraving, designed to break under excessive gas pressure. The gas vents to the outside of the cell via vent holes. As well as releasing gas, by positioning the vent foil below and linked to the cathode connector, when the vent breaks it breaks the connection to the external circuit (acting as a current interrupt device, CID) hence stopping electrochemical reactions from taking place.

An example of a PTC comprises conducting ceramic particles in a crystalline, non-conducting polymer matrix. Under normal circumstances, the ceramic particles form a conducting path. However, if the temperature of the thermistor increases due to the local temperature rising, or due to the passage of out-of-range current (causing Joule heating), the polymer matrix softens and the particles move apart, increasing the resistance: eventually the PTC becomes non-conducting.

Chemical additives form up to 5% of the solvent [16, 144] are usually commercially secret and are critically important to the safe functioning of LiBs. They have a number of functions, which include: facilitating SEI formation and/or improving SEI structure, enhancing the thermal stability of LiPF_6 , improving the conductivity, viscosity and wettability of the solvent or protecting the Al current collector from corrosion. Perhaps most importantly, they are a key aspect of the in-built safety systems in an LIB along with the physical systems, in that they can: reduce solvent flammability, provide overcharge protection/toleration and terminate battery operation under abuse conditions (shutdown additives). Some specific examples of additives are presented below.

The electrolyte, LiPF_6 , exists in chemical equilibrium with PF_5 :



The PF_5 so produced can attack both the organic solvent and the SEI, producing gaseous products and reducing the stability of the latter. A simple solution to this problem exploits Le Chatalier's Principle by adding low concentrations of LiF to the electrolyte (e.g. 0.05 wt.%) to force the equilibrium (5) to the left [145].

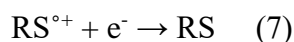
The alkyl carbonate solvents employed in lithium-ion cells are the most thermally sensitive component of these devices, and their reaction with exposed lithiated anodes and/or with the oxygen produced as cathode structures collapse are responsible for the heat and gas generation. The flashpoints of the typical solvents dimethylcarbonate

(DMC), ethylmethylcarbonate (EMC) and ethylenecarbonate (EC)¹³ are 15, 22 and 33°C [145], and flame retardant additives can be employed to lower the flammability of the electrolyte. Both halogenated and non-halogenated organic phosphorous compounds have been used, but toxicity and environmental concerns have led to more focus on the latter: the organophosphorus compounds generate radical scavenging species in fire which remove the hydrogen and hydroxyl radicals essential to maintain combustion. They can also act to form a char which acts as a barrier between the liquid and gas phases to inhibit combustion [16, 145].

Overcharge protection is achieved using redox shuttles (RS). If the BMS malfunctions, redox shuttles can provide additional protection against overcharge. These species are reversibly oxidised and reduced (i.e. the shuttle is rapidly oxidised to the cation radical $RS^{\bullet+}$ which in turn can be rapidly reduced back to the neutral species) at the cathode and anode, respectively, during charging, providing a safe ionic internal short circuit which converts the current supplied to heat. Once the potential of the cathode surpasses the reduction potential of the shuttle, the shuttle is oxidised:



where e^- is an electron. The radical cation then diffuses to the anode where it is reduced back to RS:



The potential of the cathode is pinned at that of the shuttle: at lower potentials, the redox shuttle is inactive. Examples of redox shuttles are phenothiazines, triphenylamine, metallocenes and dimethyl benzene. Thermal runaway typically occurs at SoC > 140% [146] and hence potentials for overcharge protection can be significantly higher than the nominal voltage of the cell, and range from 3.52V to 4.90V ([16, 145] and references therein).

Shutdown additives are oxidised at high potentials to release a gas (typically CO₂) which triggers a CID or safety vent: they may also polymerize on the cathode surface to prevent further overcharge ([16, 145] and references therein). Examples of these species include xylene, cyclohexylbenzene, biphenyl and 2,2-diphenylpropane.

Another major safety system is the BMS. The purpose of the BMS is to ensure as far as possible (i.e. BMS are known to fail, as may be seen, for example, from incidents

¹³ All solvents contain EC as it is believed to be essential for the formation of the SEI.

involving the overcharge of EVs [16]) safe operation and to facilitate longevity, monitor state of function in the form of SoC and SoH, provide alerts for causes of concern such as high temperatures and cell imbalance, and indicate EoFL [147]. The BMS should prevent overcharge (thus, when charging a smart phone, the BMS disconnects the battery from the charger when 100% SoC is attained) and overdischarge, both of which can lead to potentially catastrophic failure [145]. The BMS should prevent cell imbalance: e. g. cells with lower SoH in terms of lower capacity and/or higher internal resistance tend to show a higher voltage than other cells when the battery is fully charged. This means that they can be repeatedly overcharged, leading to accelerated ageing and possible thermal runaway. Thus, selecting cells or modules with similar SoH is critical in reusing, remanufacturing, and repurposing batteries.

The sophistication and functionality of the BMS depends strongly upon the application: hence reuse and remanufacturing of a pack will not require the BMS to be replaced or modified, however, repurposing will require replacement or modification to an application-specific BMS. Thus, the BMS would have to adjust the operational limits at the cell level to take into account ageing. Ideally, the BMS of a battery employing second-life cells should ensure that as far as possible individual cells were monitored and maintained within their operational limits (as opposed to monitoring just at module or rack level: such low monitoring granularity relies on the very high quality control over the manufacture of new cells) e. g. as with VDE-AR-E 2510: 2017 (See Section 6.8.2) and DNV RP43. The latter is quite specific on the granularity of monitoring: “For Li-ion batteries ... the voltage measurement of each cell is crucial for a reliable operation. If the voltage measurement fails, overcharging or deep discharge of certain cells in a battery module cannot be detected. In some cases, this can lead to thermal runaway. For this reason, the voltage measurement of every cell should be checked for plausibility and if this plausibility check fails, the operation must be stopped immediately.” [148].

However, disassembly to cell level after EoFL is generally regarded as too expensive and in many cases not practicable (see Section 6.3.4), and hence will be stopped at module level. The granularity of monitoring will then depend on the wiring of the modules: for example, the Envision-AESC modules employed in 2018 and after Nissan Leafs will only allow monitoring down to parallel pairs of cells [149].

In the view of a major EV battery research organisation, the economics of second-life LiBs are on a knife edge not least because the gateway testing/triangling of modules and

packs is labour intensive, but also the potential requirement to replace EV BMS with a second-life application-specific system are costly. However, the same organisation estimates that around 90% of the functionality of the EV BMS is focussed on the functioning of the EV, which is not relevant to second-life and the remaining 10% simply concerns reporting parameters (such as voltage, current and temperature) and simple switching functions. Thus, it was suggested that, with respect to reuse and remanufacturing, if it were possible to embed a simple code into the BMS to allow repurposers access to this reporting & switching functionality via a simple interface it would reduce costs significantly. In contrast, an INERIS report [54], questions whether this would be possible given the disparity in language employed by different EV OEMs in their controller area networks (CAN) protocols, and the fact that CANs are almost non-existent in stationary storage applications, where Modbus and Ethernet protocols are common.

There are also several other control and energy management strategies specific to second-life LiBs to consider [21]. As a result of the difference in energy and power capabilities between first and second-life LiBs, optimal battery sizing and appropriate control strategies are necessary to smooth the power output, to avoid overcharge/ overdischarge, and to extend the cycle life of the second-life battery systems. Additionally, although the challenge of cell and module balancing and inconsistencies are generally considered during gateway testing and assembly of the second-life application based on the LiBs current status, growing inconsistencies during future operations needs to be solved by active equalization strategies that can quickly reduce cell/module inconsistencies during use. Lastly, advanced fault-diagnosis algorithms for fast detection of internal short circuits, lithium plating, gas generation, etc., are also particularly relevant for second-life LiBs due to the increased risk. According to Zhu et al [21] several fault diagnosis methods have been developed for EVs but their effectiveness for second-life applications requires further validation.

6.7.2. Safety systems external to DLiBESS

Given the risk of fire, or the explosion of the white vapour produced by cells in thermal runaway in a DLiBESS, then the question arises of whether DLiBESS systems should be co-located with some form of smoke detector and/or gas sensor and fire detection. One

European DLiBESS manufacturer does require a volatile organic compound (VOC) sensor to be co-located with its DLiBESS: however, this was not the case in general. One manufacturer that employs both new and second-life cells stated that such sensors were unnecessary as the supplier of its second-life cells had an excellent safety record and this was supported by its own gateway testing. Additionally, the manufacturer provides information on safe operation of its DLiBESS to homeowners, and safe installation guidelines to installers as well as operating an approved installer scheme.

The only EV LiB manufacturer at the time of writing in the UK employs conventional aspirated smoke detection in its plant. However, there are three sensor systems specifically marketed for LiBs, two of which are relevant to DLiBESS.

The first is a non-aspirated system and relies on the detection of vented gases via solid-state VOC sensors to provide early warning of thermal runaway (defined as a rapid temperature rise).

The second is an aspirated system drawing air through a pipe with perforations at appropriate places down its length. The air sample is then drawn past blue and red light emitting diodes (LEDs): the blue light is scattered from small droplets/particles and the red from large, respectively, with both forward scattered and backscattered light being detected and providing information.

Both systems rely on the release of gases via blast caps prior to ignition: as such they cannot provide any forewarning with pouch cells as these generally tend to simply burst with no pre-venting of gases. The detection of gases vented from prismatic and cylindrical cells depends upon the pressure setting of the vents: if too high, the cell could already be beyond the point of no return and hence in thermal runaway.

It has been suggested [21] that combining results from these gas sensors with information from voltage, current and temperature could allow multi-sensor based algorithms to help achieve better safety management.

6.7.3. Installation and maintenance

It is also important to consider the locations in the home to avoid placing a DLiBESS¹⁴. This includes any location with a significant fire load, a main access route, bedrooms or roof spaces, in addition to ensuring that air can circulate around the DLiBESS to avoid overheating. As a result of the potential consequences of the hazard, rather than the risk, of thermal runaway in LiBs, the US NFPA 855 standard and the AS/NZS 5139:2019 Australian and New Zealand standard do not permit DLiBESS in the domestic space, and NFPA 855 does not permit DIY SLDLiBESS at all (see Section 6.8.3). Currently, there are no requirements for the location of DLiBESS in the UK, which is generally left up to installers. If the cells in a DLiBESS go into thermal runaway and the system is located in a confined space such as a roof or the fuse cupboard under the stairs, a vapour cloud explosion could be the result. Discussions with various fire and rescue services revealed that roof voids provide an effective means of spreading fire to rooms beneath as well as adjacent houses. Further, the presence of a DLiBESS in a loft or cupboard on an upper floor could provide an unknown hazard to the fire and rescue services (FRS), as there is currently no requirement on householders to inform their local FRS of the installation of a domestic energy storage system. Thus, a fire on the floor below could send the storage system into thermal runaway posing a major hazard to both occupants and first responders in terms of fire, toxic gases, and explosion. DLiBESS in under-stair locations could represent a significant obstruction to emergency egress.

In general, roof spaces and lofts do not have fire detection systems and are often employed as storage spaces that incorporate significant fire loads: in addition, the ventilation systems in modern properties often have units in the loft that take, filter, and distribute air around the house, and hence would facilitate the effective distribution of battery gases from cells in thermal runaway.

There was some confusion amongst respondents as to whether or not local building control should be informed when a domestic LiBESS system had been installed. It was stated that such notification was required by one person who was Head of Building Control at a major city council, whilst other qualified persons stated this was not the case. Section 11.1.1 of the IET Code of Practice Electrical Energy Storage Systems (2nd

¹⁴ UK FRS are concerned that DLiBESS have been located under the main staircase and in the loft.

edition) seeks to clarify this and states that “Larger projects will require notification”, however, “larger” is not defined.

There is some requirement for signage associated with LiBESS. Thus, the IET Code of Practice Electrical Energy Storage Systems (2nd edition), Appendix C states: “In many circumstances, particularly for larger installations, a suitable warning sign at the main incomer (and other generators where fitted) should also be considered to warn the emergency services that a battery pack is installed on the premises.” Suggested signs are given including “Battery installed on premises” to be located at main incoming switchgear and a battery voltage warning sign if the voltage exceeds 60 V DC. Additionally, although there is currently no requirement for signs to provide shut-down instructions, nor is there any requirement in the code for the installation of an audible alarm to alert homeowners to an emergency, these have been identified as further mitigating measures in the literature [150, 151].

Monitoring and maintenance are other key aspects of ensuring safe operation of DLiBESS. According to correspondence with installers, some DLiBESS are subjected to regular maintenance, while other installers monitor the performance of the system via the BMS, and engineers are sent to the home to repair or replace the system as required. The recently published BS EN 62485-5 standard, discussed in Section 6.8.2, provides recommendations and guidance for maintaining DLiBESS.

6.8. Codes, standards, and regulations

The safety of most second-life LiBs falls under the scope of the UK General Product Safety Regulations 2005. A summary of the codes, standards and regulations relevant to DLiBESS employing new LiBs is presented in a previous BEIS report [1]. This section reviews these in relation to second-life batteries along with codes, standards and regulations developed specifically for second-life batteries. Based on stakeholder consultation, and considering the nascency of the market, there was some uncertainty amongst respondents in terms of the codes, standards, and regulations governing their testing and fitness for purpose, and the legality of their transport.

It should be noted that this section deals only with those codes, standards and regulations that are directly applicable or relevant to second-life LiBs, it is not an exhaustive list of all standards relevant to DLiBESS.

A description of the BSI committees and their remits can be found in Appendix 6.2.

6.8.1. Second-life LiBs and type tests

At the present time, there are two methods of assessing batteries and their component cells and modules. The first approach is typified by the Underwriters Laboratories (UL)¹⁵ standard UL1974 which covers the sorting and grading process of battery packs, modules, and cells (and electrochemical capacitors) that were originally configured and used for other purposes, such as electric vehicle propulsion, and that are intended for a repurposed use application. UL1974 requires that all the cells or modules to be employed in a repurposed battery are tested, and that any that fall out of specification are discarded (see Section 6.6.3).

In contrast, all relevant European and International Electrotechnical Commission (IEC) standards (which currently cover only new LiBs) are founded upon “type tests”. Such tests rely on a sample of cells, modules, and/or packs being representative of the type, an assumption that is largely valid when dealing with LiBs produced by OEMs where strict quality control standards ensure conformity with respect to performance and physical characteristics such as cell impedance and SoH. Such type tests are the cornerstone of EU and UK product safety, and hence CE/UKCA marking. The majority of these tests were formulated before the concept of second-life. However, type tests on second-life cells, modules or packs from a batch cannot be taken as representative of others in the batch due to the wide variability in ageing and its consequences, and the possibility that disassembly from the original pack and reassembly during remanufacturing/repurposing has introduced defects and/or unbalanced units. In essence, an EV LiB has a demanding life, e.g. 1000 charge/discharge cycles over 5 – 10 years, operating at temperatures that can be between -20C and +70C and with routine fast charging [152].

As a simple illustration of the effect of ageing, see Figure 6.8, which shows data from research conducted by the Newcastle University ReLiB team. The modules at BoL had a capacity at 100 % SoC of 66.2Ah: as can be seen, the modules at EoL showed capacities from 49.4 to 57 Ah (75 % - 86 % SoH defined as the ratio of nominal maximum capacity

¹⁵ UL is an accredited standards developer in the US and Canada.

to the maximum capacity at BoL). A single module from the pack is thus clearly not representative of the “type” in this case.

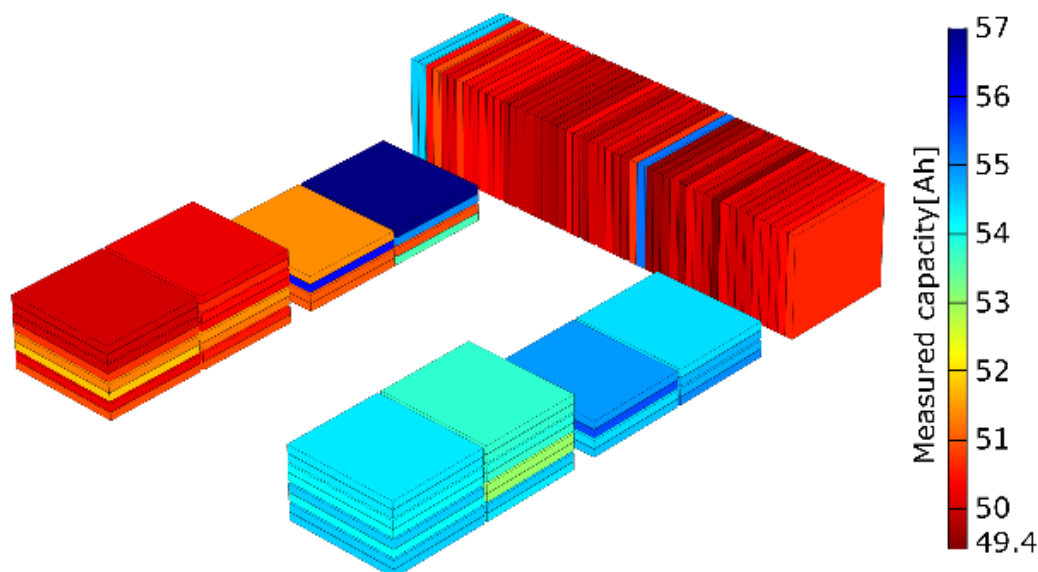


Figure 6.8. SoH of the modules in a 2011 Nissan Leaf battery pack, purchased second hand in 2018. P. Das, M. Ahmeid, S. M. Lambert and Z. Milojevic, Faraday Institution ReLiB project unpublished results.

6.8.2. Standards in the UK and Europe

No EU, UK or IEC standards currently address the use of second-life batteries specifically, though there are several standards in development. This section therefore begins by discussing the range of existing standards applicable to systems employing both new and second-life cells.

BS EN 62933¹⁶ covers electrical energy storage (EES) systems: parts 1 - 5 define terms, cover testing, environmental issues, specify safety considerations and describe human safety aspects. BS EN 62933-5-2 covers the safety of DLiBESS, but not explicitly SLDLiBESS; though it is foreseeable that this could incorporate second-life LiBs in the future.

The first edition of BS EN 62933 states that a system test program for domestic BESS (indoor use) needs to be addressed in a different manner to that of a large complex (outdoor) utility system. According to the standard, a mass-produced domestic BESS in a

¹⁶ When a standard exists as a British standard (BS) based on a European (EN) or international (IEC) standard, the BS version is referenced.

single enclosure would be evaluated in a similar way to an appliance in that it would be subjected to a type test program.

BS EN 62619 (Secondary cells and batteries containing alkaline or other non-acid electrolytes - Safety requirements for large format secondary lithium cells and batteries for stationary and motive applications) specifies type tests at cell, module, pack, and system level for the safe operation of LiBs in industrial scale applications, including stationary applications. Most DLiBESS manufacturers test their LiBs according to BS EN 62619. The standard includes external and internal short circuit, impact, drop, thermal abuse, overcharge, and forced discharge tests: to pass these tests, no fires or explosions should occur following failure. In order to pass the system level tests, the BMS should prevent overcharging and should terminate charging when the temperature exceeds safe limits: in addition, inducing thermal runaway in a single cell should not cause propagation to other cells. Given the rigour of the BS EN 62619 test standard, it is therefore often recommended to apply BS EN 62619 instead of BS EN 62133-2 (this specifies the requirements and tests for the safe operation of portable sealed secondary lithium cells and batteries containing non-acid electrolyte, under intended use and reasonably foreseeable misuse) for the LiB part of domestic energy storage systems (using new LiBs). Currently, second-life LiBs are not covered under BS EN 62619, and the standard relies on type tests. The standard is currently being amended, but is not expected to include second-life LiBs [153].

BS EN 62619 covers various applications and therefore includes requirements that are common and minimum to the applications. To cover specific LiB risks for electric energy storage systems, IEC has recently published IEC 63056 (adopted as BS EN 63056: Secondary cells and batteries containing alkaline or other non-acid electrolytes - Safety requirements for secondary lithium cells and batteries for use in electrical energy storage systems) which complements BS EN 62619 and includes specific safety requirements and tests for LiBs used in electrical energy storage systems under the assumption that the battery has been tested according to BS EN 62619. BS EN 63056 does not cover the use of second-life batteries.

BS EN 62485-5 (Safety requirements for secondary batteries and battery installations. Part 5: safe operation of stationary lithium-ion batteries) was published recently and is highly relevant to DLiBESS in general, whether employing new or 2nd life lithium-ion cells. It applies to stationary storage systems connected to the grid having a maximum

DC voltage of 1500 V. The standard concerns primarily electrical safety, including protection against electric shock and prevention of faults such as short circuits. Section 9 is focussed on the enclosures employed to accommodate LiBs but concerns larger LiBESS rather than DLiBESS, as does section 11 on identification labels and warning notices. However, a number of sections make explicit reference to LiBs: thus section 7 makes explicit reference to preventing lithium metal plating caused by operation at low temperatures, overcharging and preventing overdischarge. Section 8 discusses the safety measures to be taken in the event of the release of electrolyte, smoke, and fire. Section 13 states explicitly: “To ensure the safe operation of a stationary battery, regular inspection is required” and lists the signs of deterioration of LiBs that could signal a “safety critical state” and should trigger the withdrawal of the battery from use. However, the same section states “Regular inspection and monitoring of batteries in service shall be performed in accordance with the recommendations contained in the battery manufacturer's instructions” and, as was discussed in Section 6.7.6, routine maintenance including visual inspection, is not carried out by all DLiBESS manufacturers.

In contrast to existing UK and EU standards, the German national standard VDE-AR-E 2510-50:2017 [154] seeks to address DLiBESS directly and is compliant with EU practice. This standard also addresses potential gaps in the current international standards regarding LiBESS. Thus, for example, it was stated by a DLiBESS manufacturer that no international standards require mandatory tests to account for spontaneous internal failures (very much specific to LiBs). Only one of the DLiBESS suppliers consulted require an audible alarm and VOC detector¹⁷ [154] to be installed with a DLiBESS, and VDE-AR-E 2510: 2017 is the only European standard requiring the BMS to monitor all cells and to shut down the DLiBESS if one or more cells are operating outside of their safe parameters. The revised VDE-AR-E 2510 standard is also likely to include this requirement, which is especially relevant to systems using second-life LiBs. The standard explicitly excludes second-life batteries, as these are to be specifically covered by new standards.

Additionally, there is a notable German guide that covers the safety aspects of DLiBESS (although not SLDLiBESS). The voluntary guide “Safety guidelines for Li-ion home battery storage systems” was released in 2014 [155] and was prepared with the

¹⁷ A co-located VOC sensor is also required by the Austrian standard OIB Richtlinie 2 – Brandschutz 2019

participation of many institutions including the German industry association for electrical manufacturers (BVES), the German Solar Industry Association (BSW-Solar), and the International Solar Energy Society, German section (DGS, Deutsche Gesellschaft für Sonnenenergie E.V.). Together these associations represent the majority of stakeholders for LiBs. The guide seeks to educate installers and other stakeholders about the hazards associated with DLiBESS at cell, battery, and system level by listing the hazards, the acceptable outcome if there is an incident caused by the hazard, preventative and corrective measures and the relevant codes, standards, or regulations. The guide is focussed only on the DLiBESS itself and does not cover any wider issues such as location in the home or emergency planning.

IEC Committee TC21 is drafting IEC 63330 (Requirements for reuse of secondary batteries) which will link to IEC 62933-5-3. A new standard, IEC 63338 (The reuse of secondary lithium and nickel metal-hydride cells and batteries after extraction from the application they were first placed on the market with) is also under development. Both IEC 63330 and IEC 63338 will cover the use of second-life LiBs.

IEC 63330 specifies the procedure for assessing the safety of second-life LiBs to be employed in applications other than that of their 1st life (assumed to be in EV battery packs). The current draft provides a simple, high level flow chart of the route from the initial production of the cells and assembly into the 1st life battery, through EoFL, and assessment for second-life through to ultimate end-of-life and recycling/disposal. The assessment includes suitability for second-life application as well as safety. IEC 63338 provides high-level guidance on the safe and environmentally benign re-use (intended as a general term for second-life application) of LiBs.

A 2021 BSI report [136] identified second-life testing as a gap in standards, and the invalidity of type tests on second-life batteries is made explicit in Clause 6.3 of BS EN IEC 63338 (19 Jan. 2021 draft). However, both it and BS EN IEC 63330 rely completely on the BMS data collected during first life, without any gateway testing, to ensure the safety of reused, remanufactured, and repurposed LiBs. Clause 6.3 states that non-destructive (i.e. non-type) testing of batteries is “not established at the time of publication”: and this remains a major gap in the standards. The information required by BS EN IEC 63330 includes (but is not restricted to): extreme values of temperature, charge and discharge current and charge & discharge voltage. BS EN IEC 63338 requires

more information: as well as explicitly requiring information on overcharge and overdischarge (which is implied in the information required by BS EN IEC 63330) and overcurrent & overtemperature, details of insulation failure, accidents and storage conditions (e.g. storage period, environment, etc.) are also required.

The reliance on EV OEMs to make BMS data freely available to repurposers (the re-use and remanufacture of EV battery packs is likely to involve the OEM directly and may be carried out by the OEM, see Section 6.3.3) was greeted by considerable scepticism by a number of respondents from EV manufacturers. Further, the failure to keep the link between the VIN and battery serial numbers by the EV OEMs discussed in Section 6.3.3 **Error! Reference source not found.**, is a challenge that needs to be addressed. Both BS EN IEC 63330 and 63338 require the company looking to place second-life LiBs on the market to form direct links with the EV OEM, and BS EN IEC 63338 goes further in requiring contractual links to be sought where the OEM intended the batteries for reuse. In fact, EV OEMS are forming collaborations with repurposers to ensure the smooth transfer of information and materiel to produce a range of products including: SLDLiBESS [152] industrial LiBESS [153] and solar nanogrids [153]. Some EV OEMs are going even further and incorporating the principle of whole life from production through 1st and 2nd life to recycling [153] into battery design. BS EN IEC 63338 also introduces the novel concepts of “intended” and “unintended” reuse, and requires the original manufacturer (e.g. the EV OEM) to label their batteries accordingly: finally, if any of the required information is not available, the cells, modules or batteries are not to be reused.

Lastly, BS EN 62933-5-3 is currently a draft standard under development and specifies the requirements for prevention of safety deterioration caused by initially non-anticipated modifications to electrochemical based EES systems. The standard is essentially concerned with the retrofitting of cells, modules, or other parts to an *existing* BESS, but does include the “loading (of) reused batteries”, although details are yet to be publicly available. It was suggested by one respondent that it is important that the difference between repair and modification should be made plain in this standard: thus, a repair is the like-for-like replacement of faulty components (such as cells, modules, inverters) for remanufacture, as opposed to a modification for repurposing. BS EN 62933-5-3 is to be applied in addition to the requirements in BS EN 62933-5-2.

6.8.3. Codes, standards, and regulations outside the UK and Europe

While no standards currently address second-life LiBs in the UK and Europe, standards do exist elsewhere, most notably the first edition of UL1974 (Standard for Evaluation for Repurposing Batteries) which was published in 2018. Similarly, to the UK, UL has a suite of standards concerning LiBs and LiBESS which are discussed below in addition to notable codes, standards, and regulations in other countries.

UL1974 is a manufacturing process standard and, as stated in Section 6.6.1, it is the factory repurposing or remanufacturing the batteries that is certified under the standard, not the batteries themselves. An important definition in UL1974 is the "incoming sample" or battery pack when dealing with first life LiBs in an EV. This is the battery pack at EoFL and prior to disassembly and subsequent repurposing. UL1974 requires that the tests carried out on the cells in the pack when new conform to the appropriate standards, e.g. UL2580 and IEC62660-3. The EoFL pack is visually examined and the information on the pack, e.g. reason for withdrawal from service, length and nature of storage and handling history also assessed. The SoH of the pack is also assessed using data from the BMS, which includes:

- Average and extreme values of current, voltage and temperature.
- Out of specification values of these.
- Total times or number of instances at extremes or out of specification.
- Total number of charges and discharges.
- Total times or numbers under charge and under discharge
- Total number or type of error messages.

This reflects the fact that the SoH of a battery is far more complex than represented by the simple in equations (1) and (4) in Section 6.6.1. The information required for compliance with UL 1974 is more comprehensive than that required by the draft BS EN IEC 63330 but omits the additional requirements of BS EN IEC 63338 (insulation failure, accidents and storage conditions) although these may be encompassed in the information contained in the specified error messages. If the BMS data offers no cause for concern (and hence

rejection of the pack into materials recovery) then the next stage of the assessment is employed which is the following tests:

- Open circuit voltage.
- High voltage isolation check.
- Capacity.
- Internal resistance.
- Check BMS controls and protection components (if BMS to be re-used).
- Discharge/charge cycle test whilst monitoring temperature, voltage and current.
- Self-discharge.

These tests may also provide reason for rejection of the pack: if the tests are passed then the pack is disassembled to the smallest unit that will be employed in the repurposed battery, typically the module. The modules and the bus bars, wires etc, are inspected for damage. The modules from the disassembled pack are then subjected to the same tests and the standard recommends a 6σ limit (i.e. the tested parameters of 99.99966% of the cells or modules are within the acceptable range) or narrower for the repurposed battery specification values: modules that fall within the same 6σ range are placed in the same grade and hence are “balanced and appropriately matched” and used in the same repurposed battery. Batteries and/or parts falling outside the specification set by the repurposing manufacturer will be rejected. The standard gives suitable tests to assess each parameter should the manufacturer not have its own tests. Cells assembled into repurposed batteries should be of the same model and from the same original manufacturer.

The standard does not cover the process for remanufactured batteries, which are also referred to as refurbished or rebuilt batteries. If the cells or modules conform to UL1974 then the LiBESS comprised of these must meet standard UL1973. As with BS EN 62619, UL1973 allows for the simple fact that failures will occur and hence the tests include assessment of the ability of the system to withstand failure.

UL 1973 is a comprehensive safety standard for batteries that includes the cell, pack, BMS and system criteria. It requires a Failure Mode and Effect Analysis (FMEA), the BMS is required to go through a functional safety investigation and there is a

comprehensive suite of tests including single cell propagation. UL 1973 is similar to an end product standard.

In addition to the UL standards for second-life LiBs, the US organisation SAE International is drafting J2997 (Standards for Battery secondary use). The aim is to “develop standards for a testing and identity regimen to define batteries for variable safe reuse. Utilize existing or in process standards such as Transportation, Labelling, and State of Health”.

Another relevant test method, applicable to both new and second-life DLiBESS, is UL9504A. This was developed to address safety concerns identified by the building codes and the country’s fire service, namely: BESS installation instructions; installation ventilation requirements; effectiveness of fire protection (integral or external) and fire service strategy and tactics. The test method is aimed at determining the capability of battery technology to undergo thermal runaway and to allow the subsequent evaluation of the fire and explosion hazards & hence the fire and explosion protection required, rather than focussing on assessing the safety of the cells. It is applicable to DLiBESS as well as industrial LiBESS and could be applied to SLDLiBESS as it is assessing the safety of the system, rather than cells or modules, and provides data that can be used to mitigate or prevent propagation of thermal runaway between cells and modules.

The test method involves a sequential series of destructive tests at cell, module, and LiBESS level, each test carried out a total of four times to assess reproducibility. Individual cells are heated using a heating pad: if they go into thermal runaway, then modules are tested: if they also fail then full LiBESS level testing is carried out. In each case, tests are fully monitored on a tick-list basis, e.g. thermocouples are employed to monitor temperature, and gasses are monitored to ascertain composition. The tests facilitate a number of design strategies and standard operating procedures to be developed. For example, the determination of: separation distances between units to minimize fire propagation; separation distances between units and enclosure walls; potential of fire spread to overhead cabling; fire protection strategies; ventilation requirements via the measurement of deflagration potential and heat generation and fire service strategy and tactics. It is worth re-iterating that UL9540A is intended to inform the development of safety systems and procedures, it does not demand action be taken on the basis of the tests. Thus, it can be claimed that a LiBESS “conforms to” UL9540A in

that the tests have been carried out but may not actually have been acted upon in terms of addressing any issues arising from the tests.

A number of countries are addressing the issue of the hazards specifically represented by the location of DLiBESS – but none currently specifically address SLDLiBESS. For example, the US NFPA 855 states that [156]:

“BESS shall only be installed in the following locations:

1. In attached garages separated from the dwelling unit living area and sleeping units in accordance with the local building code.
2. In detached garages and detached accessory structures.
3. Outdoors on exterior walls or on the ground located a minimum of 3 ft from doors and windows.
4. In enclosed utility closets and storage or utility spaces.”

However, NFPA855 assigns the prevention of thermal runaway entirely to the BMS: but once the chemical reactions responsible for thermal runaway have replaced the electrochemical processes of normal operation, thermal runaway cannot be prevented by any form of electrical intervention under the control of the BMS such as switchgear, or physical intervention by e.g. thermal fuses.

Of direct relevance to this report is that DIY (home-built) DLiBESS and SLDLiBESS are not permitted in the USA, and Authorities Holding Jurisdiction can insist on the removal of such systems. In addition, cities in Arizona have introduced new laws requiring a monitoring panel to be located outside of a building containing a DLiBESS [157].

The Australian AS/NZS 5139:2019 “Electrical installations — Safety of battery systems for use with power conversion equipment” standard states that [158] “Pre-assembled integrated BESS shall not be installed: (i) in ceiling spaces; (ii) wall cavities; (iii) on roofs not specifically deemed suitable; (iv) under stairways; or (v) under access walkways. In areas of domestic or residential electrical installation, pre-assembled integrated BESS shall not be located in habitable rooms. Suitable areas may include garages, storage rooms, dedicated battery system room and verandas”. If DLiBESS are excluded from the domestic space in the UK, their protection against water ingress will have to conform to BS EN 60529.

A final, notable development is that on 21 June 2021, the Chinese government proposed regulations to prohibit the use of second-life EV LiBs in large industrial stationary storage systems following a number of industrial LiBESS fires, although they will still be allowed in small industrial LiBESS [157]. According to reports this will be under review until a 'breakthrough in battery consistency management technology and a sound power battery performance testing and evaluation system' is developed [158].

6.8.4. Second-life LiBs as waste

The Waste Batteries and Accumulators Regulations 2009 require individuals or companies who place batteries on the UK market to register as producers, and this then requires them to take back waste batteries. However, there is considerable confusion as to whether second-life LiBs should be considered as waste under these regulations, which were drawn up before LiBs became ubiquitous in society and before their use in second-life applications was conceived. The Environment Agency, as part of the consultation process, stated that there is a general misunderstanding that second-life batteries employed in an application such as a LiBESS are not waste. The Agency's view is that LiBs removed from an EV, or other device, are waste. They may or may not achieve End-of-Waste status if they meet the End-of-Waste test in Article 6 of the EU Waste Framework Directive¹⁸ [159]. Due to the confusion, any queries concerning LiBs as waste are currently dealt with on a case-by-case basis by DEFRA, the Environment Agency and OPSS. This is not considered by these organisations to be a sustainable practice as battery reuse increases. Reuse is due to be considered as part of domestic regulation reforms, and is also covered, as discussed below, by the EU Batteries Regulation which was passed by the EU Parliament in March 2022.

In the consultation process, the Environment Agency expressed concerns over the safe disposal of batteries from DLiBESS. The DLiBESS manufacturers will be responsible for this at the end of the systems' life¹⁹: the concern is where consumers have built their own system, and whether or not they understand their responsibilities. Thus, once the modules in a DIY SLDLiBESS have to be replaced, they will become waste. If the waste

¹⁸ The Waste Framework Directive explains when waste ceases to be waste and becomes a secondary raw material, and how to distinguish between waste and by-products. The Directive also introduces the "polluter pays principle" and "extended producer responsibility".

¹⁹ The regulations also allow for other producers to take responsibility under certain circumstances.

weighs more than 4 kg (as an example, a 2018 Nissan Leaf module weighs more than 8 kg) it would be classified as an industrial battery. As such, they must be transported to a suitable ATF for recycling in accordance with the regulations covering the transport of dangerous goods (see Section 6.8.5 below).

6.8.5. The sale and transport of second-life LiBs

The market in second-life LiBs, and hence the remanufacture and repurposing of LiBs, depends critically on the transport of the batteries. This includes start-up companies and consumers assembling DIY SLDLiBESS who rely on online sites. In general, there was considerable uncertainty amongst respondents regarding the application of transport requirements on second-life LiBs.

LiBs are classified as dangerous goods under UN 3480 [160] and hence require transportation in accordance with the requirements of the agreement “Accord relatif au transport international des marchandises dangereuses par route” (ADR [161]). Any LiBs classified under UN3480 (lithium-ion batteries) and UN3481 (lithium-ion batteries contained in equipment) must pass the type tests detailed in the UN Manual of Tests and Criteria Part III sub-section 38.3 (UN38.3). There are eight of these type tests, including thermal, vibration, shock, external short circuit, impact, and overcharge, which are tests to destruction. All cells, including those used in equipment, are required to have passed these tests, although certain tests are waived when the batteries are to be installed in a vehicle that offers suitable protection. UN38.3 requires a number of batteries to be tested, half of which are subjected to one test cycle and 25 half cycles: this is based entirely on new LiBs as these are known to change with further cycles after the first. Moreover, as discussed in Section 6.8.1, type tests are not suitable for second-life LiBs.

At the time that UN38.3 was formulated, the possibility that LiBs would have a second-life was not envisaged: it was assumed that, as was the case with lead-acid batteries, their use (in EVs) would be followed by recycling. Hence UN38.3 testing only applies to new LiBs as a design type test to allow for classification (a lithium battery may only be transported once it has passed the 38.3 tests, although there are some exceptions): it does not apply to second-life LiBs. However, where a battery is reworked, the changes may result in it being considered a new battery as defined in 38.3.2.2.

The ADR is transposed into UK law as Regulation 5 of the UK Carriage of Dangerous Goods and Use of Transportable Pressure Equipment Regulations 2009 [162]: “No person is to carry dangerous goods, or cause or permit dangerous goods to be carried, where that carriage is prohibited by ADR ..., including where that carriage does not comply with any applicable requirement of ADR or RID [163].”. The ADR regulations have a number of exemptions depending on battery size; however, if the total load of LiB on a vehicle weighs more than 333 kg, then the transport must conform fully with the requirements of ADR:

- The driver needs to hold an ADR licence and have received the relevant training.
- The packaging must have the correct markings and labels.
- Transportation documents are required.
- Vehicle marking and equipment, and driver equipment are required.
- The LiB must be packed according to the appropriate packing instruction.

There are three packing groups in the UN recommendations for solids and liquids (Packing group I – high hazard, II – medium hazard, and III – low hazard). As lithium batteries are articles, they are not assigned a packing group. However, where UN tested packaging is required, packaging for articles will be tested to the packing group II level for solids unless otherwise indicated:

- III. **Undamaged** batteries require packing according to packing instruction P903.
- II. **Damaged and defective** batteries require packaging in accordance with packing instruction P908 that has passed the required UN tests (drop and stack tests).
- I. **Damaged, defective and batteries liable to rapidly “disassemble”** require packaging in accordance with P911 at the packing group I level and additional testing as agreed with the Vehicle Certification Authority (VCA) on behalf of the Department of Transport. Essentially, a test must be done that demonstrates that with the LiB content in thermal runaway, any fire/explosion

and excessive heat is contained by the package. This is an expensive test to do.

Critically for DIY SLDLiBESS, the ADR requirements do not apply to the public collecting and transporting LiBs.

6.8.6. The EU batteries regulation

Representatives from across the UK battery industry attending DEFRA consultations expressed strong support for the EU Batteries Regulation (EU BR) when published as a draft, and hence it is likely that the UK will broadly align with the regulations [164].

The Eurobat organisation which represents companies covering all aspects of the LiB value chain also welcomed the draft EU BR, but expressed concerns over restrictive aspects of the proposed regulation, including the requirements to use minimum levels of recycled materials and materials recovery targets, and the incorporation of design for second life application [165].

The German Energy Storage Association (BVES) has also suggested that “The proposed EU Batteries Regulation are far-reaching, progressive and likely to shape the battery market in the EU in the 2020s” [166]. However, the same association expressed significant concern over the fact that the draft regulation does not cover the testing of second-life LiBs and, along with other German national organisations, has also expressed concern at the apparent drive to reuse EV batteries inherent in the proposed regulation at the expense of considerations of safety. In 2020, BVES published a position paper on the proposed EU Battery Regulations in which it raised its concerns that type tests were not valid for 2nd life LiBs [166].

The full weight of the EU BRs will be applied to battery energy storage systems with capacities greater than 2 kWh which will be classified as “ industrial batteries”: as the average annual domestic electricity demand for a Profile Class 1 home in the UK is 1800 – 4300 kWh (i.e. 5 – 12 kWh of electrical energy per day [167, 168]), it is likely that DLiBESS will be classified as industrial batteries and hence be governed by UK versions of the EU BRs if adopted. Of the 13 UK DLiBESS systems listed on the Solarguide website [168], only one is less than 2 kWh and eight are scalable to 10 kWh or more.

Focussing only on the LiB-specific safety aspects of the EU BRs: under Article 12, stationary BESS will require documentation showing that the systems are safe via a number of type tests, ranging from evaluation of resilience to thermal shock, thermal cycling, mechanical shock and internal short circuit, to overcharge, over-discharge and over-temperature protection systems. This is highly reminiscent of the UL 9540A test standard employed in the USA. However, the EU BRs relies on type tests. Additionally, Article 14 requires that BMS can store the data deemed to be required to determine the SoH and expected lifetime (including remaining capacity, capacity fade, remaining power capacity and power capacity fade, round trip efficiency, cooling demand, self-discharge history and Ohmic resistance or impedance) and that such data are made available to facilitate re-use, repurposing or remanufacturing, but there is no explicit requirement for this information to have been employed to ascertain if second-life LiBs are fit-for-purpose for use in BESS. Furthermore, the data required does not include parameters that can indicate abuse such as maximum/minimum temperature, maximum charging current, as required by IEC 63330.

Article 64 states that the Commission will implement an electronic information exchange system to store and make available battery information: operators who place industrial LiBs on the market will make the information on the battery available through this resource. However, the information to be stored appears to be only beginning-of-life data, and there is no explicit link to the data discussed under Article 14.

Article 59 explicitly concerns the repurposing and remanufacture of industrial and EV batteries with respect to the availability of data and particularly information on safety relevant to handling and testing. It also seeks to broadly address the key question of whether LiBs at the end of their first life are classified as waste, and hence subject to the appropriate regulations. Thus, the article requires that an operator proposing to employ a battery in a second-life application proves that the battery is not waste by providing evidence that the SoH has been evaluated or tested in a member state, that the purpose of the battery is validated by an invoice or contract of sale or transfer of ownership, and that evidence is provided of the appropriate protection against damage during transport.

Under Article 65, by January 2026 every industrial battery, irrespective of application, will have to have an “associated battery passport”, linked to the EU data system described in Article 64. When the battery “changes status” responsibility for the information held on the data system transfers to the new owner.

The EU BR will not cover millions of industrial batteries in use now and in the immediate future, and its relevance to second-life LiBs is not clear. However, once the regulation is in force, it may be that changing the application from EV to industrial may require a new producer declaration and the batteries would be covered.

As stated at the start of this section, the broad acceptance of the draft EU BR in the UK is not shared elsewhere. Whilst welcoming in principle the EU BR, the German Energy Storage Association (BVES), along with the German Association of the Automotive Industry E.V. (VDA) and the German Electrical and Electronic Manufacturers' Association (ZVEI) have responded at various levels [167] to a standardisation request from the EU which, in the group's view, has deficiencies in many safety topics relevant to second-life batteries. This includes the testing of second-life LiBs which remain a gap in standards and, in particular, the validity of type testing as discussed in Section 6.8.1.

Lithium-ion cells must operate within strict operational limits if catastrophic loss via thermal runaway is to be avoided through e.g. lithium plating, lithium dendrites, copper deposition and internal short circuit, excessive heat etc. In addition, as discussed above, a LiB, unlike its lead-acid counterpart, has chemical, electrical and mechanical safety systems, and these require monitoring as do current, temperature and voltage. Thus, unlike a lead-acid battery, a LiB requires a BMS, and is an electrical device that should, in the view of the German industry group, have equivalent requirements for electrical safety as the Low Voltage Directive (implemented as Electrical Equipment Safety Regulations in GB). This was a view widely shared by stakeholders consulted as part of this research.

The group raises particular challenges with article 59, whereby independent operators would be given access to the BMS for “the purpose of assessing and determining the SoH and remaining lifetime”. In addition to concerns over OEMs' willingness to release such potentially valuable intellectual property, the group was concerned that it may not always be the case that operators would have the necessary skills and expertise to be able to use the information for the purposes specified.

With respect to LiB energy storage systems employing new cells, the German industry group believes that, although a lithium-ion-specific standard is overdue, there is no gap, the existing standards just need to be applied intelligently. However, there are a number

of gaps in the current relevant international codes, standards and regulations for second-life lithium-ion batteries.

Key challenges for the success of the EU BRs, and the use of second-life modules and packs in general, will be: how effectively first life information will be retained with the modules and packs during their life journeys; whether EV OEMs will grant access to this intellectual property and whether there will be a general acceptance that the gateway testing and/or access to key first life information of these devices is fit for purpose.

6.9. Conclusions

The market for second-life DLiBESS (SLDLiBESS) is difficult to predict which was evident by the absence of detailed market information. While a number of stakeholders consulted as part of this study use second-life batteries in their LiBESS, these are predominantly for industrial applications and evidence suggests there is currently limited use in domestic systems. Therefore, in order to assess the potential market for SLDLiBESS, the following drivers and barriers were reviewed as reasonable indicators:

- **The market for DLiBESS.** Market analysis suggests that the UK DLiBESS market is a nascent but growing industry, with estimated capacity at 38 MWh in 2019 expected to rise to between 128 – 339 MWh by 2024[2]. Consumer drivers are likely to be maximising use of onsite generation, such as solar, in addition to buying and selling electricity. This should be considered in light of rising electricity costs and the falling costs of LiBs.
- **Environmental and economic drivers for second-life LiBs.** The extraction and processing of the metals required by LiBs is both expensive and harmful to the environment. Additionally, it is estimated that there could be 75,000 to 105,000 end of first-life (EoFL) EV LiBs in the UK by 2025, which represent potential environmental and safety waste hazards. In contrast, reuse, remanufacture or repurposing could extend battery life by 7 – 10 years, minimising waste and delaying or reducing materials recovery which is currently both energy intensive and limited in capacity.
- **Availability of second-life LiBs.** While the projected surplus of second-life LiBs is good news for the DLiBESS industry, the latter is unlikely to soak up the

surplus and there will have to be significant innovation and investment in materials recovery. This will likely be driven by material supply and/or regulation, with the draft EU Battery Regulations proposing to significantly increase the recovery of certain metals from LiBs in addition to requirements to incorporate certain levels of these recyclates into new LiBs. While likely to drive materials recovery, this could be at the expense of second-life.

- **Price of second-life LiBs.** It is currently both costly and labour intensive to test and triage EoFL batteries due to a lack of standardisation among EV OEMs. In addition, the falling cost of new LiBs means the economic incentive for reuse and repurposing may become less attractive.

The hazards represented by LiBs can be severe if they are not properly mitigated. The hazards associated with second-life LiBs are the same as those found with new LiBs, but the probability of failure is likely to be higher with the former due to the effects of ageing and unknown stress and/or abuse during the LiBs first life application. The capacity loss of LiBs is generally considered to be linear, with EoFL typically around 75-80% state of health (SoH) and final end-of-life around 50-60% SoH. However, at some point there is a change in and/or an additional ageing mechanism which leads to an increased ageing rate. The time at which this occurs is referred to as the “knee” where severe and potentially dangerous deterioration is expected to occur, and the battery has reached its final end-of-life. Currently this point is difficult to predict but can occur at a higher SoH than expected. Cycling at normal rates or calendar ageing does not have a significant impact on safety; however, cycling at low temperatures or high C-rates can have a detrimental effect upon stability and can significantly reduce the temperature at which thermal runaway occurs and consequently increase the risk of thermal runaway. In addition, this is shown to increase the risk of internal short circuits and joule heating.

It is for this reason, and due to the variance of SoH between EoFL LiBs (including within the same pack), that a sample second-life LiB should not be taken to be representative of the batch. Therefore, the safety of second-life LiBs cannot be assured by type tests, which form the basis of all current international and European standards. Instead, an assessment is required for each LiB.

The re-purposing of LiBs is a nascent global market which has led to some uncertainty amongst respondents in terms of the codes, standards and regulations governing their

testing, fitness for purpose, and transport. There are currently no UK or European standards specifically for second-life LiBs; however, both IEC 63330 and IEC 63338 are being developed to address this gap. IEC 63330 will specify the procedure for assessing the safety of second-life LiBs to be employed in applications other than that of their first life, and IEC 63338 provides high-level guidance on the safe and environmentally benign re-use of LiBs. Both these standards seek to address the need to assess second-life LiBs without relying on type tests. Additionally, the EU Batteries Regulation contains requirements for second-life LiBs, including for first-life data to be made available in the battery management system (BMS) to facilitate re-use. Outside of the UK and Europe, UL 1974 (Standard for Evaluation for Repurposing Batteries) covers the sorting and grading process of LiBs that are intended for a repurposed use application.

Current practices include a variety of methods to measure state-of-health and/or reliance on detailed information retained in the BMS employed during first life (i.e. the EV BMS). The engagement of EV OEMs in the latter has yet to be assessed but is a critical factor. This information may include parameters such as: extreme values of temperature, charge and discharge current and charge & discharge voltage, details of insulation failure, accidents and storage conditions, total times or number of instances at extremes or out of specification, total number of charges and discharges, total times or numbers under charge and under discharge and total number or type of error messages. Gateway testing to assess the health of second-life LiBs includes: measuring capacity, internal resistance and self-discharge and performing a discharge/charge cycle test. However, there is currently no widely-accepted test methodology for assessing the safety of second-life LiBs and this is a major gap in international standards. Additionally, there remains uncertainty amongst stakeholders around the transportation of second-life LiBs.

Additional considerations for best practice when using second-life LiBs in DLiBESS include use of a dedicated BMS for the new application, and monitoring as close to cell level as possible, the importance of which was highlighted by the incident in Surprise, Arizona, and is a requirement in the German standard VDE-AR-E 2510: 2017.

Extensive discussions with stakeholders have revealed two opposing views on second-life batteries: firstly, that a safety framework can be put in place to allow the use of second-life LiBs in DLiBESS, so long as the full history of the batteries in their first life applications is known and/or they can be tested effectively. A second, more radical view

shared by some respondents is simply that the safety of such cells can never be guaranteed, and hence that second-life LiBs should not be employed under any circumstances in DLiBESS.

Lastly, due to the fire and electrical hazards associated with LiBs, the availability of potentially untested second-life LiBs and the potential lack of knowledge (for example, with LiB ageing) and skills of consumers to mitigate the risk through testing and good system design, consideration should also be given to whether stricter requirements are needed for home-built (“DIY”) DLiBESS that use second-life batteries, similarly to the USA.

6.10. References

1. Intertek, Domestic battery energy storage systems a review of safety risks. 2020, BEIS <https://www.gov.uk/government/publications/domestic-battery-energy-storage-systems>.
2. SolarPower Europe, European Market Outlook For Residential Battery Storage 2020-2024. 2020: <https://www.solarpowereurope.org/european-market-outlook-for-residential-battery-storage/>.
3. ofgem, Transitioning to a net zero energy system. Smart Systems and Flexibility Plan 2021. 2021, BEIS: <https://www.gov.uk/government/publications/transitioning-to-a-net-zero-energy-system-smart-systems-and-flexibility-plan-2021>.
4. Neubauer, J., et al., Identifying and Overcoming Critical Barriers to Widespread Second Use of PEV Batteries. 2015, National Renewable Energy Lab: <https://www.osti.gov/biblio/1171780-identifying-overcoming-critical-barriers-widespread-second-use-pev-batteries>.
5. Maiser, E., Battery packaging - Technology review. AIP Conference Proceedings, 2014. 1597(1): p. 204-218.
6. Harper, G., et al., Recycling lithium-ion batteries from electric vehicles. Nature, 2019. 575(7781): p. 75-86.
7. McKinnon, M.B., S. DeCrane, and S. and Kerber, Four Firefighters Injured In Lithium-Ion Battery Energy Storage System Explosion – Arizona. 2020, Underwriters Laboratories report,:

- https://d1gi3fvbl0xj2a.cloudfront.net/files/2021-07/Four_Firefighters_Injured_In_Lithium_Ion_Battery_ESS_Explosion_Arizona_0.pdf.
8. Clean Energy Reviews. Tesla Powerwall Review. 2021 [cited 2021 15 Sep].
 9. Sony. Keywords to understanding Sony Energy Devices. 2015 [cited 2021 15 May].
 10. Gold, R. and B. Foldy. The Battery Is Ready to Power the World. 2021 [cited 2021 01 May].
 11. Adesanya-Aworinde, V. 2015 - A great year for large-sized lithium-ion batteries. 2016 [cited 2021 3 Apr].
 12. Melin, H.E., The lithium-ion battery end-of-life market 2018-2025. 2018, Circular Energy Storage: United Kingdom.
 13. Vernacchia, J. A Brief History of Utility-Scale Energy Storage. 2017 [cited 2021 27 Apr].
 14. Väyrynen, A. and J. Salminen, Lithium ion battery production. *The Journal of Chemical Thermodynamics*, 2012. 46: p. 80-85.
 15. Weber, C.J., et al., Material review of Li ion battery separators. *AIP Conference Proceedings*, 2014. 1597(1): p. 66-81.
 16. Sun, P., et al., A Review of Battery Fires in Electric Vehicles. *Fire Technology*, 2020. 56(4): p. 1361-1410.
 17. Stoker, L. Jaguar Land Rover latest EV manufacturer to take aim at second-life batteries. 2017 [01/05/2021)].
 18. Clements, S. and R. Ruf, UK Energy Storage Lab Project. 2020, Element Energy Ltd: http://www.element-energy.co.uk/wordpress/wp-content/uploads/2020/01/UKESL-Non-technical-Public-Report_2020.pdf.
 19. PowerVault, Powervault and Renault give EV Batteries a “Second-Life” in Smart Energy Deal. 2017: <https://www.powervault.co.uk/article/powervault-and-renault-give-ev-batteries-a-second-life-in-smart-energy-deal/>.
 20. ELSA. Energy Local Storage Advanced system 2015.
 21. Zhu, J., et al., End-of-life or second-life options for retired electric vehicle batteries. *Cell Reports Physical Science*, 2021. 2(8): p. 100537.
 22. Henze, V., Energy Storage is a \$620 Billion Investment Opportunity to 2040. 2018, BloombergNEF: <https://about.bnef.com/blog/energy-storage-620-billion-investment-opportunity-2040/>.

23. Engel, H., P. Hertzke, and G. Siccardo, Second-life EV batteries: The newest value pool in energy storage 2019, McKinsey & Company: <https://www.mckinsey.com/industries/automotive-and-assembly/our-insights/second-life-ev-batteries-the-newest-value-pool-in-energy-storage>.
24. Ambrose, H., The Second-Life of Used EV Batteries. 2020, Union of Concerned Scientists: <https://blog.ucsusa.org/hanjiro-ambrose/the-second-life-of-used-ev-batteries/>.
25. Nigon, P., et al., Battery Storage. 2019, Battery Storage: <https://www.imia.com/wp-content/uploads/2020/01/IMIA-WGP-112-19-Battery-Storage.pdf>.
26. Ambrose, H., et al., Battery Second-life: Unpacking opportunities and barriers for the reuse of electric vehicle batteries. 2020: <https://pdfslide.net/documents/battery-second-life-unpacking-opportunities-and-2020-05-27-battery-second-life.html>.
27. IRENA, Renewable Energy Statistics 2021. 2021, The International Renewable Energy Agency: Abu Dhabi <https://irena.org/publications/2021/Aug/Renewable-energy-statistics-2021>.
28. SolarPower Europe, Global Market Outlook for Solar Power 2017-2021. 2017: <https://resources.solarbusinesshub.com/solar-industry-reports/item/global-market-outlook-2017-2021>.
29. statista, Electricity prices for households in the United Kingdom (UK) from 2010 to 2020, semi-annually 2021: <https://www.statista.com/statistics/418126/electricity-prices-for-households-in-the-uk/>.
30. The Economist, Lithium battery costs have fallen by 98% in three decades. 2021: <https://www.economist.com/graphic-detail/2021/03/31/lithium-battery-costs-have-fallen-by-98-in-three-decades>.
31. Roberts, S. Rent-a-roof solar PV schemes. 2020.
32. TESLA. Vehicle Charging During Power Outage. 2021 [cited 2021 1 Jun].
33. Baltac, S. and S. Slater, Batteries on wheels: the role of battery electric cars in the EU power system and beyond. 2019, Element Energy report: <https://www.transportenvironment.org/discover/batteries-wheels-role-battery-electric-cars-eu-power-system-and-beyond/>.

34. Jiao, N., Second-life Electric Vehicle Batteries 2020-2030. Key players, value opportunities, business models and market forecast. 2018, IDTechEx: <https://www.idtechex.com/en/research-report/second-life-electric-vehicle-batteries-2019-2029/626>.
35. Stringer, D. and M. Jie, Where 3 Million Electric Vehicle Batteries Will Go When They Retire. 2018, Bloomberg Quint: <https://www.bloombergquint.com/technology/where-3-million-electric-vehicle-batteries-will-go-when-they-retire>.
36. Reid, G. and J. Julve, Second Life-Batteries As Flexible Storage For Renewables Energies. 2016, Bundesverbandes Erneuerbare Energie e.V. und der Hannover Messe: https://www.bee-ev.de/fileadmin/Publikationen/Studien/201604_Second_Life-Batterien_als_flexible_Speicher.pdf.
37. Energy Sector Management Assistance Program (ESMAP), Reuse and Recycling : Environmental Sustainability of Lithium-Ion Battery Energy Storage Systems. 2020, Washington, D.C. : World Bank Group.: <http://documents.worldbank.org/curated/en/593961599738208006/Reuse-and-Recycling-Environmental-Sustainability-of-Lithium-Ion-Battery-Energy-Storage-Systems>.
38. Catapult_Energy_Systems, Storage and Flexibility Net Zero Series Second-life Batteries. 2020: <https://es.catapult.org.uk/report/storage-and-flexibility-net-zero-series-second-life-batteries/>.
39. Skeete, J.-P., et al., Beyond the EVent horizon: Battery waste, recycling, and sustainability in the United Kingdom electric vehicle transition. Energy Research & Social Science, 2020. 69: p. 101581.
40. <https://www.reuters.com/world/uk/glencore-britishvolt-team-up-uk-ev-battery-recycling-plant-2022-02-03/#:~:text=The%20plant%20will%20be%20built>, I.D. [cited 2021 5 Jun].
41. <https://www.veolia.co.uk/press-releases/veolia-announces-its-first-electric-vehicle-battery-recycling-plant-uk>. [cited 2021 30 Apr].
42. <https://www.discoverev.co.uk/ev-news/uk-car-recycling-preparing-for-wave-of-evs>. [cited 2021 10 May].

43. Meshram, P., B.D. Pandey, and T.R. Mankhand, Extraction of lithium from primary and secondary sources by pre-treatment, leaching and separation: A comprehensive review. *Hydrometallurgy*, 2014. 150: p. 192-208.
44. Katwala, A., The spiralling environmental cost of our lithium battery addiction. 2018, WIRED: <https://www.wired.co.uk/article/lithium-batteries-environment-impact>.
45. Davidsson Kurland, S., Energy use for GWh-scale lithium-ion battery production. *Environmental Research Communications*, 2019. 2(1): p. 012001.
46. Balach, O. The curse of 'white oil': electric vehicles' dirty secret. 2020.
47. Venkatapathy, K., E. Tazelaar, and B. Veenhuizen. A Systematic Identification of First to Second Life Shift-Point of Lithium-Ion Batteries. in *2015 IEEE Vehicle Power and Propulsion Conference (VPPC)*. 2015.
48. Tang, Y., et al., Economic Analysis on Repurposed EV batteries in a Distributed PV System under Sharing Business Models. *Energy Procedia*, 2019. 158: p. 4304-4310.
49. Cusenza, M.A., et al., Reuse of electric vehicle batteries in buildings: An integrated load match analysis and life cycle assessment approach. *Energy and Buildings*, 2019. 186: p. 339-354.
50. Richa, K., et al., Environmental trade-offs across cascading lithium-ion battery life cycles. *The International Journal of Life Cycle Assessment*, 2017. 22(1): p. 66-81.
51. Schulz-Mönninghoff, M., et al., Integration of energy flow modelling in life cycle assessment of electric vehicle battery repurposing: Evaluation of multi-use cases and comparison of circular business models. *Resources, Conservation and Recycling*, 2021. 174: p. 105773.
52. Global Battery Alliance (GBA), A Vision for a Sustainable Battery Value Chain in 2020: Unlocking the Full Potential to Power Sustainable Development and Climate Change Mitigation. 2019, Insight Report; World Economic Forum http://www3.weforum.org/docs/WEF_A_Vision_for_a_Sustainable_Battery_Value_Chain_in_2030_Report.pdf .
53. Liu, P., et al., Progress of State of Health Evaluation Methods for Lithium-ion power Battery. *IOP Conference Series: Materials Science and Engineering*, 2018. 452: p. 032033.

54. INERIS, DRA06 – Opération B3, Seconde vie des batteries Li-ion. 2020, INERIS: MINISTERE DE LA TRANSITION ECOLOGIQUE ET SOLIDAIRE.
55. Lacey, G., et al., The effect of cycling on the state of health of the electric vehicle battery, in 48th International Universities' Power Engineering Conference (UPEC). 2013, IEEE. p. 1-7.
56. Bobba, S., et al., Sustainability Assessment of Second Life Application of Automotive Batteries (SASLAB). 2018, JRC Exploratory Research (2016-2017): https://www.researchgate.net/publication/327690459_Sustainability_Assessment_of_Second_Life_Application_of_Automotive_Batteries_SASLAB_JRC_Exploratory_Research_2016-2017_Final_technical_report_August_2018. .
57. Casals, L.C., et al., PHEV battery aging study using voltage recovery and internal resistance from onboard data. IEEE Transactions on Vehicular Technology, 2015. 65(5): p. 4209-4216.
58. Circular Energy Storage. Prices for used batteries are higher than for new batteries – this is why. 2021 [23/11/2021)].
59. Guidance., Waste batteries: producer responsibility. <https://www.gov.uk/guidance/waste-batteries-producer-responsibility>. .
60. Prescient & Strategic Intelligence, Lithium-Ion Battery Recycling Market to Witness Robust Growth in Coming Years: P&S Intelligence. 2020, GlobeNewswire: <https://www.globenewswire.com/news-release/2020/05/06/2028156/0/en/Lithium-Ion-Battery-Recycling-Market-to-Witness-Robust-Growth-in-Coming-Years-P-S-Intelligence.html>.
61. Melin, H.E., State-of-the-art in reuse and recycling of lithium-ion batteries – A research review. 2019, The Swedish Energy Agency: Circular Energy Storage.
62. <https://www.mckinsey.com/business-functions/operations/our-insights/unlocking-growth-in-battery-cell-manufacturing-for-electric-vehicles>. . [05/05/2021)].
63. Melin, H.E., The lithium-ion battery end-of-life market – A baseline study 2019, Global Battery Alliance: https://www3.weforum.org/docs/GBA_EOL_baseline_Circular_Energy_Storage.pdf.
64. Statista, Projected global battery demand from 2020 to 2030, by application 2020: <https://www.statista.com/statistics/1103218/global-battery-demand-forecast/>.
65. InternationalBanker, The Outlook for the Global Battery Market. 2021: <https://internationalbanker.com/brokerage/the-outlook-for-the-global-battery->

- https://warwick.ac.uk/fac/sci/wmg/business/automotive_batteries_101_wmg-apc.pdf.
77. Haregewoin, A.M., A.S. Wotango, and B.-J. Hwang, Electrolyte additives for lithium ion battery electrodes: progress and perspectives. *Energy & Environmental Science*, 2016. 9(6): p. 1955-1988.
 78. Wang, Q., et al., A review of lithium ion battery failure mechanisms and fire prevention strategies. *Progress in Energy and Combustion Science*, 2019. 73: p. 95-131.
 79. Zilio, S., et al., Gas release mitigation in LiFePO₄-Li₄Ti₅O₁₂ Li-ion pouch cells by an H₂-selective getter. *Electrochimica Acta*, 2019. 294: p. 156-165.
 80. Sturk, D., L. Hoffmann, and A. Ahlberg Tidblad, Fire tests on e-vehicle battery cells and packs. *Traffic injury prevention*, 2015. 16(sup1): p. S159-S164.
 81. Chen, S., et al., Lower explosion limit of the vented gases from Li-ion batteries thermal runaway in high temperature condition. *Journal of Loss Prevention in the Process Industries*, 2020. 63: p. 103992.
 82. Sun, J., et al., Toxicity, a serious concern of thermal runaway from commercial Li-ion battery. *Nano Energy*, 2016. 27: p. 313-319.
 83. Martinez-Laserna, E., et al. Evaluation of lithium-ion battery second life performance and degradation. in 2016 IEEE Energy Conversion Congress and Exposition (ECCE). 2016.
 84. Menzel, J., et al., Quantification of ionic organo(fluoro)phosphates in decomposed lithium battery electrolytes. *RSC Advances*, 2017. 7(62): p. 39314-39324.
 85. Eshetu, G.G., et al., In-depth safety-focused analysis of solvents used in electrolytes for large scale lithium ion batteries. *Physical chemistry chemical physics*, 2013. 15(23): p. 9145-9155.
 86. Christensen, P.A., et al., Thermal and mechanical abuse of electric vehicle pouch cell modules. *Applied Thermal Engineering*, 2021: p. 116623.
 87. Hering, G., Burning concern: Energy storage industry battles battery fires. 2019, S&P Global Market Intelligence:
<https://www.spglobal.com/marketintelligence/en/news-insights/latest-news-headlines/51900636>.
 88. Mai, H., APS storage facility explosion raises questions about battery safety 2019, Utility Dive: <https://www.utilitydive.com/news/aps-storage-facility-explosion-raises-questions-about-battery-safety/553540/>.

89. Abada, S., et al., Combined experimental and modeling approaches of the thermal runaway of fresh and aged lithium-ion batteries. *Journal of Power Sources*, 2018. 399: p. 264-273.
90. Bravo Diaz, L., et al., Review—Meta-Review of Fire Safety of Lithium-Ion Batteries: Industry Challenges and Research Contributions. *Journal of The Electrochemical Society*, 2020. 167(9): p. 090559.
91. Feng, X., et al., Thermal runaway mechanism of lithium ion battery for electric vehicles: A review. *Energy Storage Materials*, 2018. 10: p. 246-267.
92. Grundy, A., Overheating reports prompt LG Energy Solution battery recall. 2021, *Energy Storage News*: <https://www.energy-storage.news/overheating-reports-prompt-lg-energy-solution-battery-recall/>.
93. Ren, D., et al., A comparative investigation of aging effects on thermal runaway behavior of lithium-ion batteries. *eTransportation*, 2019. 2: p. 100034.
94. Li, C., et al., An Experimental Study on Thermal Runaway Behavior for High-Capacity Li(Ni_{0.8}Co_{0.1}Mn_{0.1})O₂ Pouch Cells at Different State of Charges. *Journal of Electrochemical Energy Conversion and Storage*, 2020. 18(2).
95. He, X., et al., Experimental Study of Self-heating Ignition of Lithium-Ion Batteries During Storage: Effect of the Number of Cells. *Fire Technology*, 2020. 56(6): p. 2649-2669.
96. Fleischhammer, M., et al., Interaction of cyclic ageing at high-rate and low temperatures and safety in lithium-ion batteries. *Journal of Power Sources*, 2015. 274: p. 432-439.
97. Feng, X., et al., Investigating the thermal runaway mechanisms of lithium-ion batteries based on thermal analysis database. *Applied Energy*, 2019. 246: p. 53-64.
98. Liu, X., et al., Thermal Runaway of Lithium-Ion Batteries without Internal Short Circuit. *Joule*, 2018. 2(10): p. 2047-2064.
99. Dannien, M. Firefighter 'knocked on his back' in fire blast at Griffith University. 2020 [cited 2021 7 Jul].
100. Shaw, V. Two firefighters killed after Beijing battery blaze. 2021 [cited 2021 9 Jul].
101. Bertilsson, S., et al., Lithium-ion battery electrolyte emissions analyzed by coupled thermogravimetric/Fourier-transform infrared spectroscopy. *Journal of Power Sources*, 2017. 365: p. 446-455.

102. Larsson, F., et al., Gas explosions and thermal runaways during external heating abuse of commercial lithium-ion graphite-LiCoO₂ cells at different levels of ageing. *Journal of power sources*, 2018. 373: p. 220-231.
103. Feng, X., et al., Mitigating thermal runaway of lithium-ion batteries. *Joule*, 2020. 4(4): p. 743-770.
104. Yuan, Q., et al., Overcharge failure investigation of lithium-ion batteries. *Electrochimica Acta*, 2015. 178: p. 682-688.
105. Arizona Public Service, McMicken Battery Energy Storage System Event Technical Analysis and Recommendations. 2020:
<https://www.aps.com/en/About/Our-Company/Newsroom/Articles/Equipment-failure-at-McMicken-Battery-Facility>. .
106. Tomaszewska, A., et al., Lithium-ion battery fast charging: A review. *eTransportation*, 2019. 1: p. 100011.
107. Santhanagopalan, S., P. Ramadass, and J. Zhang, Analysis of internal short-circuit in a lithium ion cell. *Journal of Power Sources*, 2009. 194(1): p. 550-557.
108. Baird, A.R., et al., Explosion hazards from lithium-ion battery vent gas. *Journal of Power Sources*, 2020. 446: p. 227257.
109. Luo, W.-t., et al., Research and Development of Fire Extinguishing Technology for Power Lithium Batteries. *Procedia Engineering*, 2018. 211: p. 531-537.
110. Bergström, U., et al., Vented Gases and Aerosol of Automotive Li-ion LFP and NMC Batteries in Humidified Nitrogen under Thermal Load 2015, Swedish Civil Contingencies Agency, report FOI-R-4166-SE:
<https://www.msb.se/siteassets/dokument/publikationer/english-publications/vented-gases-and-aerosol-of-automotive-li-ion-lfp-and-nmc-batteries-in-humidified-nitrogen-under-thermal-load.pdf>.
111. <https://relib.org.uk/>. [cited 2021 8 Apr].
112. Jiang, F., et al., Theoretical analysis of lithium-ion battery failure characteristics under different states of charge. *Fire and Materials*, 2018. 42(6): p. 680-686.
113. Lai, X., et al., Investigation of thermal runaway propagation characteristics of lithium-ion battery modules under different trigger modes. *International Journal of Heat and Mass Transfer*, 2021. 171: p. 121080.
114. <https://www.safebatt.ac.uk/>. [cited 2021 10 Aug].
115. Friesen, A., et al., Impact of cycling at low temperatures on the safety behavior of 18650-type lithium ion cells: Combined study of mechanical and thermal abuse

- testing accompanied by post-mortem analysis. *Journal of Power Sources*, 2016. 334: p. 1-11.
116. Lian, T., et al., Changes in Thermal Stability of Cyclic Aged Commercial Lithium-Ion Cells. *ECS Transactions*, 2019. 89(1): p. 73-81.
 117. Liu, J., et al., Aging mechanisms and thermal stability of aged commercial 18650 lithium ion battery induced by slight overcharging cycling. *Journal of Power Sources*, 2020. 445: p. 227263.
 118. Wang, Z. and J. Wang, An experimental investigation of the degradation and combustion behaviors associated with lithium ion batteries after different aging treatments. *Journal of Cleaner Production*, 2020. 272: p. 122708.
 119. Geisbauer, C., et al., Review—Review of Safety Aspects of Calendar Aged Lithium Ion Batteries. *Journal of The Electrochemical Society*, 2020. 167(9): p. 090523.
 120. Lebedeva, N.P., et al., Amount of Free Liquid Electrolyte in Commercial Large Format Prismatic Li-Ion Battery Cells. *Journal of The Electrochemical Society*, 2019. 166(4): p. A779-A786.
 121. Wang, S., et al., Effects of lithium dendrites on thermal runaway and gassing of LiFePO₄ batteries. *Sustainable Energy & Fuels*, 2020. 4(5): p. 2342-2351.
 122. Braco, E., et al., Experimental assessment of cycling ageing of lithium-ion second-life batteries from electric vehicles. *Journal of Energy Storage*, 2020. 32: p. 101695.
 123. Swierczynski, M., D. Stroe, and S.K. Kær. Calendar ageing of LiFePO₄/C batteries in the second life applications. in 2017 19th European Conference on Power Electronics and Applications (EPE'17 ECCE Europe). 2017.
 124. Martinez-Laserna, E., et al., Technical Viability of Battery Second Life: A Study From the Ageing Perspective. *IEEE Transactions on Industry Applications*, 2018. 54(3): p. 2703-2713.
 125. Ilieș, A.I., I. Ciascai, and D. Pitică. Methods for Reusing Li-Ion Cells from Discarded Battery Packs. in 2019 42nd International Spring Seminar on Electronics Technology (ISSE). 2019.
 126. Fermín-Cueto, P., et al., Identification and machine learning prediction of knee-point and knee-onset in capacity degradation curves of lithium-ion cells. *Energy and AI*, 2020. 1: p. 100006.

127. Hosen, M.S., et al., Battery lifetime prediction and performance assessment of different modeling approaches. *iScience*, 2021. 24(2): p. 102060.
128. Raj, A., M.-T.F. Rodrigues, and D.P. Abraham, Rate-Dependent Aging Resulting from Fast Charging of Li-Ion Cells. *Journal of The Electrochemical Society*, 2020. 167(12): p. 120517.
129. Ma, T., et al., Study on lithium plating caused by inconsistent electrode decay rate during aging of traction batteries. *Solid State Ionics*, 2020. 345: p. 115193.
130. Wang, C.-j., et al., Morphology, Structure, and Thermal Stability Analysis of Aged Lithium-Ion Battery Materials. *Journal of The Electrochemical Society*, 2020. 167(14): p. 140550.
131. Hu, D., et al., Unrevealing the effects of low temperature on cycling life of 21700-type cylindrical Li-ion batteries. *Journal of Energy Chemistry*, 2021. 60: p. 104-110.
132. Fear, C., et al., Elucidating Copper Dissolution Phenomenon in Li-Ion Cells under Overdischarge Extremes. *Journal of The Electrochemical Society*, 2018. 165(9): p. A1639-A1647.
133. Energy Solution Company, Causes of ESS fires in Korea: Recommended actions for customers. LG Chem: August 16 2019.
134. Hemavathi, S., Overview of cell balancing methods for Li-ion battery technology. *Energy Storage*, 2021. 3(2): p. e203.
135. <https://www.fsrmatters.com/Fire-investigators-issue-warning-over-e-bikes.> . 03/03/2022)].
136. BSI, Battery manufacturing and technology standards roadmap July 2021: <https://www.bsigroup.com/en-GB/industries-and-sectors/energy-and-utilities/faraday-battery-challenge/battery-manufacturing-and-technology-standards-roadmap/>.
137. Amine, K., et al., Factors responsible for impedance rise in high power lithium ion batteries. *Journal of Power Sources*, 2001. 97-98: p. 684-687.
138. Edge, J.S., et al., Lithium ion battery degradation: what you need to know. *Physical Chemistry Chemical Physics*, 2021. 23(14): p. 8200-8221.
139. Attidekou, P.S., et al., A New Time Constant Approach to Online Capacity Monitoring and Lifetime Prediction of Lithium Ion Batteries for Electric Vehicles (EV). *Journal of The Electrochemical Society*, 2017. 164(9): p. A1792-A1801.

140. Lambert, S.M., et al., Rapid Nondestructive-Testing Technique for In-Line Quality Control of Li-Ion Batteries. *IEEE Transactions on Industrial Electronics*, 2017. 64(5): p. 4017-4026.
141. <http://www.element-energy.co.uk/2020/01/element-energy-led-project-ukesl-demonstrates-grading-and-sorting-of-end-of-life-nissan-ev-batteries-for-the-first-time-in-the-uk/>. 2020 07/08/2021)].
142. University of Warwick, Used Nissan LEAF batteries given “second life” thanks to WMG, University of Warwick 2020: https://warwick.ac.uk/newsandevents/pressreleases/used_nissan_leaf/.
143. Balakrishnan, P.G., R. Ramesh, and T. Prem Kumar, Safety mechanisms in lithium-ion batteries. *Journal of Power Sources*, 2006. 155(2): p. 401-414.
144. Zhang, S.S., A review on electrolyte additives for lithium-ion batteries. *Journal of Power Sources*, 2006. 162(2): p. 1379-1394.
145. Samadi, M.F. and M. Saif, Integrated Battery Management System, in *Integrated Systems: Innovations and Applications*, M. Fathi, Editor. 2015, Springer International Publishing: Cham. p. 173-193.
146. Juarez-Robles, D., et al., Overcharge and Aging Analytics of Li-Ion Cells. *Journal of The Electrochemical Society*, 2020. 167(9): p. 090547.
147. Chombo, P.V. and Y. Laonual, A review of safety strategies of a Li-ion battery. *Journal of Power Sources*, 2020. 478: p. 228649.
148. DNV, Considerations for ESS Fire Safety. 2017, DNV GL AS(2) for Consolidated Edison and NYSERDA: <https://www.dnv.com/Publications/considerations-for-energy-storage-systems-fire-safety-89415>.
149. https://www.marklines.com/en/report_all/rep1786_201811#report_area_3. 30/09/2021)].
150. Wenger, M., et al. Investigation of gas sensing in large lithium-ion battery systems for early fault detection and safety improvement. in *IECON 2014 - 40th Annual Conference of the IEEE Industrial Electronics Society*. 2014.
151. Guidance on Li Ion Battery Fires. December 2020, Fire Industry Association Guidance Note: <https://www.fia.uk.com/static/2a999c49-760b-47e3-b02f96a2ca89ecd9/Guidance-Document-on-Li-Ion-Battery-Fires-12-20-v1.pdf>.
152. Chen, B.-R., et al., A machine learning framework for early detection of lithium plating combining multiple physics-based electrochemical signatures. *Cell Reports Physical Science*, 2021. 2(3): p. 100352.

153. Draft (21A/722/CDV). IEC 62619 second edition.
154. VDE, VDE-AR-E 2510-50 Anwendungsregel:2017-05 - Standards - VDE Publishing House (vde-verlag.de) <https://www.vde-verlag.de/standards/0500098/vde-ar-e-2510-50-anwendungsregel-2017-05.html>.
155. OIB, OIB Richtlinie 2 – Brandschutz 2019 2019: Austria, <https://www.oib.or.at/en/node/5699261>.
156. <https://www.nfpa.org/>. [cited 2021 5 Sep].
157. Fifield, J., After APS explosion injures 4 firefighters, Arizona cities enact battery storage laws for utilities, homeowners. 2019, azcentral.com: <https://eu.azcentral.com/story/news/local/surprise/2019/09/30/phoenix-peoria-and-surprise-enact-battery-storage-laws/2305933001/>.
158. https://www.erac.gov.au/wp-content/uploads/2021/03/Battery_Energy_Storage_System_02Feb2021.pdf. [10/10/2021].
159. European Commission, Directive 2008/98/EC of the European Parliament and of the Council of 19 November 2008 on waste and repealing certain Directives 2008: https://ec.europa.eu/environment/topics/waste-and-recycling/waste-framework-directive_en.
160. <https://www.gwp.co.uk/guides/un3480-regulations/>. [cited 2021 30 Aug].
161. UNECE. About the ADR. Agreement concerning the International Carriage of Dangerous Goods by Road. 2021 (09/23/2021)].
162. The Carriage of Dangerous Goods and Use of Transportable Pressure Equipment Regulations 2009. 2009: <https://www.legislation.gov.uk/uksi/2009/1348/introduction/made>.
163. OTIF, Convention concerning International Carriage by Rail (COTIF)Appendix C – Regulations concerning the International Carriage of Dangerous Goods by Rail (RID). 2021: https://otif.org/fileadmin/new/3-Reference-Text/3B-RID/RID_2021_e_01_July_2021.pdf.
164. RICARDO, “Supply of Batteries – Review of United Kingdom (UK) Legislation”, . 2021: presentation to the DEFRA Batteries Consultation Group, 26 April 2021.
165. EuroBat, Joint industry position paper on the Batteries Regulation. 2022: https://www.eurobat.org/images/Joint_industry_paper_future_Batteries_Regulation_January_2022_FINAL.pdf.

166. BVES, BVES position paper: EU Regulation proposal concerning batteries and waste batteries -COM(2020) 798/3. 2020: <https://www.bves.de/wp-content/uploads/2021/03/BVES-Positionpaper-EU-Regulation-proposal-concerning-batteries-and-waste-batteries.pdf>.
167. ofgem. Decision on revised Typical Domestic Consumption Values for gas and electricity and Economy 7 consumption split. 6 Jan 2020 [cited 2021 8 May].
168. <https://www.solarguide.co.uk/solar-batteries#/>. [cited 2021 15 Aug].

6.11. Appendix 6.1: A case study: the explosion of the McMicken LiBESS, Surprise, Arizona

At 16:55:20 on 19 April 2019 a smoke alarm was activated by the 2MWh McMicken LiBESS in Surprise, Arizona (comprised of new LiBs). Three hours later, one of the doors of the LiBESS container was opened by first responders: the resulting explosion produced a jet of flame approximately 75 feet long and 20 feet high. Two first responders were thrown against and under the chain-link fence that surrounded the LiBESS, one coming to rest approximately 73 ft from the opened door beneath a bush that had ignited in the event and the second officer came to rest approximately 30 ft from the opened door. A third first responder was also thrown by the blast but remained within the fence. The explosion was caused by the ignition of the white cloud produced by one rack of 14 modules going into thermal runaway and resulting in a vapour cloud explosion. As discussed in Section 6.4.3, the hazard of vapour cloud explosion is directly relevant to DLiBESS.

6.11.1. The LiBESS

The McMicken LiBESS consisted of [1] 36 racks, of which 27 contained a vertical stack of 14 modules: the modules were numbered bottom to top. Each module comprised 14 pairs of 64Ah NMC lithium-ion pouch cells: the cells in the pairs were in parallel and the pairs themselves in series. The racks were held in two rows in a standard 50 ft x 13 ft x 12 ft steel container, very similar to a sea container except with two doors. One door was on the end of the container, the other on the side and farthest away from the first door. The energy storage capacity of the LiBESS was 1/10th of that of the Carnegie Road LiBESS on Merseyside that exploded in September 2020 [2].

6.11.2. Timeline

At 16:54:30 local time, cell pair 7 in module 2 failed in the McMicken LiBESS. The temperature of the electronic systems on top of racks 15 and 17 started to increase at 16:54:44 from 40°C to a peak of 49.8°C over the next 54 s. At 16:55:20 the laser smoke detection system (which would respond to smoke, vapour, or fine droplets of solvent) triggered and opened circuit breakers: 30 s later, as designed, the system deployed the fire

suppression agent, Novac 1230. It is now generally acknowledged that fire suppressants are ineffective with respect to the thermal runaway of LiBs in LiBESS as they offer no cooling ability (the reservoirs of these systems are also typically insufficient for the extended periods of thermal runaway). The Surprise Fire Department received a report of smoke & possible prairie fire from a passer-by at 17:41 and arrived at the scene c.a. 7 minutes later and observed a steady stream of white “smoke” issuing from the container. Unaware that the container was a LiBESS they were met by a technician who informed them that the container housed a lithium-ion battery system. Units from Peoria Fire Service including Hazardous Materials specialist arrived at 18:28 and noted low-lying white clouds of a gas/vapor mixture issuing from the structure and nearby components and drifting through the desert. The container was monitored from the arrival of the Surprise officers until it was decided to open the door around 19:00 at which point “a visible white gas/vapor mixture immediately poured out of the open door” and the explosion took place. Detailed timelines may be found in references [1, 3-5].

6.11.3. The cause of thermal runaway

There are four reports on the McMicken LiBESS explosion: one commissioned by the owners (DNV GL for Arizona Public Services) [1], one for the lithium ion cell suppliers (Exponent for LG Chem [3]) and two by Underwriters Laboratories (UL [4, 5]).

The DNV GL and Exponent reports differ in terms of identifying the cause of the thermal runaway.

The DNV GL report identifies the formation of lithium metal dendrites and the penetration of the separator between anode and cathode of cell pair 7 causing a catastrophic internal short circuit. The primary evidence for this model was the presence of lithium-rich deposits on the anodes of randomly-selected undamaged cells in the McMicken LiBESS and on the anodes of undamaged cells from a sister site, Festival Ranch. The Exponent report disputes this model on the basis of the following points: (1) the separators employed were coated with a ceramic layer that would resist penetration by the dendrites; (2) the deposits were not electronically conducting (and hence could not

cause a short circuit²⁰) and (3) even if they were conducting, the thickness of the dendrites was insufficient to sustain the expected large current flows (i.e. they would act like a fuse).

The Exponent report did not dispute the fact that the deposits contained lithium metal in some form as it acknowledged that they were pyrophoric on contact with air, as would be expected of metallic lithium. The alternative model proposed in the Exponent report is that electrical arcing sent cell pair 7 into thermal runaway, citing the facts as evidence that (1) the position of cell pair 7 was next to arc damage on the rack framework and (2) the cells in rack 15 were being charged at 27A, but this suddenly switched direction to discharging at 4A.

As discussed in Section 6.5.1 **Error! Reference source not found.**, lithium metal plating is associated with the operation of LiBs at extremes of temperature (e.g. $\leq 5^{\circ}\text{C}$) or with systematic overcharging, i.e. abuse of some form, and is regarded as highly undesirable in terms of facilitating thermal runaway. Yet neither report questions why plating occurred in an installation only c.a. 2 years old²¹.

6.11.4. References

1. Arizona Public Service, McMicken Battery Energy Storage System Event Technical Analysis and Recommendations. 2020:
<https://www.aps.com/en/About/Our-Company/Newsroom/Articles/Equipment-failure-at-McMicken-Battery-Facility>. .
2. Colthorpe, A. Fire at 20MW UK battery storage plant in Liverpool. 2020 [cited 2023 25/03/2023]; Available from: <https://www.energy-storage.news/fire-at-20mw-uk-battery-storage-plant-in-liverpool/>.
3. Swart, J., K. White, and M. Cundy, APS McMicken Progress Report. 2020, Exponent, Inc.

²⁰ In fact, metallic lithium would react with the electrolyte in the same way as lithiated graphite anodes on first charging when the SEI is formed: the layer so produced on the metal may have been thick enough to prevent electrical conduction.

²¹ It should be noted that UL have not been able to attribute any field failures of LiBESS to lithium metal plating.

4. McKinnon, M.B., S. DeCrane, and S. Kerber, Four firefighters injured in lithium-ion battery energy storage system explosion-Arizona. 2020: Underwriters Laboratory, Firefighter Safety Research Institute.
5. UL, Battery Energy Storage System Incidents and Safety: A Technical Analysis by UL 2021, UL.

6.12. Appendix 6.2: The BSI committees and their remits

BSI has many national committees that mirror both international (ISO/IEC) and European (CEN/CENELEC) work. **PEL/21** is responsible for the preparation of product standards for all secondary cells and batteries, irrespective of type or application. **ESL/120** is responsible for standardization in the field of grid integrated EES Systems, focussing on system aspects on EES Systems rather than energy storage devices as well as investigating system aspects and the need for new standards for EES Systems. **ESL/120** also focusses on the interaction between EES Systems and Electric Power Systems (EPS).

These committees mirror technical committees within IEC (the International Electrotechnical Commission) and CENELEC (the European Committee for Electrotechnical Standardisation). Most work items are developed at the international (IEC) level, as this has the biggest member input and global co-operation. Some developments may be European specific and so will be developed at CENELEC. The UK is not permitted to endorse IEC standards when they are published: however, most are because they will be useful for users. If an IEC Standard is then adopted into the CENELEC work programme and approved, so it becomes an EN IEC Standard, the UK must endorse it. It will then become a BS EN IEC XX.

The UK mirror committees are entitled to draft new work item proposals (NWIP) and present them to the IEC technical committee, and it is most likely that project will be led by the UK. Alternatively, UK members can sit on the Working Groups developing the various international standards going through development and so UK input is considered in those discussions as well as at comment feedback on ballots. The publishing process is as follows:

1. New Work Item Proposal (NWIP) – comments and vote:
approval/disapproval/abstention
2. Committee Draft (CD) – comments only – best stage to heavily redraft the standard is needed
3. Committee Draft for Vote (CDV) – comments and vote:
approval/disapproval/abstention
4. Final Draft International Standard (FDIS) – comments and vote: approval/
disapproval/abstention

6.13. Appendix 6.3: Survey of LIB suppliers on EBay

As of 4th June 2021, 23 suppliers were found on Ebay, see Table 6.2, some selling multiple and different types of batteries, some with multiple batteries on the same listing. The deliveries have been listed as standard and as ‘other courier’. In the latter case, it was not explicitly stated if the courier was licenced to transport dangerous goods.

<i>Line number</i>	<i>Supplier</i>	<i>Type</i>	<i>Quantity available</i>	<i>Postage or delivery</i>	<i>Collection</i>	<i>Trader type</i>	<i>OEM</i>	<i>Capacity</i>	<i>Last date viewed</i>	<i>Date contacted</i>
1	Supplier 1	Module	5	Standard delivery (£20)	free	Unknown, probably sole trader	Nissan	30kWh (stated)	01/04/21	31/03/21
2a	Supplier 2	Module	10	Standard delivery (Royal Mail)(£15.70)	Not available	Breaker's yard	VW	Not stated	01/04/21	01/04/21
2b	Supplier 2	Module	3	Economy delivery (£19)	Not available	Breaker's yard	BMW	94 Ah	22/04/21	01/04/21
2c	Supplier 2	Module	> 10	Economy delivery (£19)	Not available	Breaker's yard	Outlander	Not stated	22/04/21	01/04/21
2d	Supplier 2	Pack	1	Economy delivery (£100)	Not available	Breaker's yard	Tesla	75 kWh	22/04/21	01/04/21
2e	Supplier 2	Module	10	Economy delivery (£19)	Not available	Breaker	Nissan	56 Ah	04/06/21	01/04/21
3	Supplier 3	Module	≥ 4	None	Free	Breaker's yard	Nissan	30 kWh (stated)	01/04/21	01/04/21
4a	Supplier 4	Pack	1	Standard delivery £40	Free	Breaker's yard	BMW	7613 Wh	31/03/21	31/03/21
4b	Supplier 4	Battery	1	Standard delivery £40	Free	Breaker's yard	SEAT	Not stated	22/04/21	31/03/21
5	Supplier 5	Pack		Courier	Not available		Toyota	73 kWh	31/03/21	31/03/21

6	Supplier 6	Pack	1	Economy delivery (£150)	Lithuania	Breaker's yard	BMW	7613 Wh	20/04/21	31/03/21
7	Supplier 7	Pack	1	Economy delivery (£199)	Free	Breaker's yard	KIA	Not stated	21/04/21	31/03/21
8	Supplier 8	Pack	1	No delivery, they install	Not available	Repair	Honda	Not stated	21/04/21	01/06/21
9a	Supplier 9	Pack	1	Free or express (£10)	Free	Breaker's yard	Honda	Not stated	21/04/21	30/03/21
9b	Supplier 9	Battery	1	Express (Other), Express (Parcelforce)(£10)	Free	Breaker's yard	Suzuki	36 Wh	22/04/21	30/03/21
10	Supplier 10	Pack	1	Standard international (E245)	Not available	Breaker's yard	Mitsubishi	12kWh	21/04/21	30/03/21
11	Supplier 11	Module	> 4	Standard delivery (DPD)(£20)	Not available	Breaker's yard	CATL	2.47 kWh	22/04/21	01/06/21
12	Supplier 12	New starter battery	2	Standard, economy, express	Free	Parts supplier	BMW	69 Ah	22/04/21	01/06/21
13	Supplier 13	Battery	1	No delivery	Free	Possible private seller	Mercedes	Not stated	22/04/21	01/06/21
14	Supplier 14	Battery	1	Express delivery (DPD)(£30)	Free	Possible breakers	Mercedes	Not stated	22/04/21	01/06/21
15	Supplier 15	Battery	1	Standard delivery	Free	Breaker's yard	Mercedes	Not stated	22/04/21	01/06/21

16	Supplier 16	Battery	1	Standard delivery (£622.71 from California)	Not available	Parts supplier	Infiniti	Not stated	22/04/21	03/06/21
17	Supplier 17	Battery	1	No delivery	Free	Parts supplier	Mercedes	Not stated	22/04/21	03/06/21
18a	Supplier 18	Battery	1	Express (other), Express (Royal Mail)	Free	Breaker's yard	Range rover	Not stated	22/04/21	03/06/21
18b	Supplier 18	Battery	1	Express (Other), Express (Royal Mail)(£14.00)	Free	Breaker's yard	Suzuki	36 Wh	22/04/21	03/06/21
19	Supplier 19	Battery	1	Express (Other)	Free	Possible breakers yard	Suzuki	36 Wh	22/04/21	03/06/21
20	Supplier 20	Battery	1	Economy (Other)	Free	Breaker's yard	Suzuki	36 Wh	22/04/21	03/06/21
21	Supplier 21	Battery	1	Express (Other)	Free	Parts supplier	Suzuki	36 Wh	22/04/21	04/06/21
22	Supplier 22	Battery	3	Express (Other)(£8.50)	Not available	Breaker's yard	Suzuki	36 Wh	22/04/21	04/06/21
23	Supplier 23	Battery	1	£59.99 Standard Delivery	Free	Breaker's yard	Toyota	Not stated	04/06/21	04/06/21

Table 6.2. Various listings of second hand lithium-ion batteries found on EBay.com.

Chapter 7 . Future Work

A core theme of this thesis is the vapour cloud with the attendant risk of vapour cloud explosion. However, it is poorly understood in the literature, often referred to as ‘smoke’ or ‘steam’, descriptions which do little to convey the hazards it presents. In addition, there is a large range of values quoted for the volume of vapour cloud produced as well as its composition. Thus, the volume, composition, toxicity and explosibility of the vapour cloud by lithium-ion cells in thermal runaway needs to be understood as a function of form factor, cell chemistry, module/pack topography and SoC.

The optical method for determining heat release rates from lithium-ion battery fires described in Chapter 5 needs first to be checked for reproducibility, and then validated by a completely independent method. For example, further experiments on the same module type would be desirable with the heat release rate results integrated to give total heat release rates (THR). These should then be compared against each other (assuming the total stored energy (electrical + chemical) in each module is consistent), to determine if the method is consistently and accurately measuring the energy released during a fire. The method should then be validated using a conventional method of measuring HRRs, for example, oxygen consumption calorimetry.

Finally, the wholly novel (if tentative) suggestion in Chapter 4 that a DC plasma arc produces the vapour cloud, should be explored using appropriate techniques such as emission spectroscopy to assess if the postulate is valid.